A novel Monte Carlo - Discrete Element Method approach for the micro-mechanics of colloidal
suspensions

(Article begins on next page)

04 August 2020

ScuDo

Scuola di Dottorato ⌣ Doctoral School

WHAT YOU ARE, TAKES YOU FAR

Doctoral Dissertation
Doctoral Program in Chemical Engineering (30thcycle)

A novel Monte Carlo - Discrete Element Method approach for the micro-mechanics of colloidal suspensions

Graziano Frungieri

******

Supervisor:
Prof. Marco Vanni

Doctoral Examination Committee:
Prof. Frédéric Gruy, Referee, École nationale supèrieure des mines de Saint-Étienne
Prof. Marco Lattuada, Referee, University of Fribourg
Prof. Matthäus Bäbler, KTH Royal Institute of Technology
Prof. Valeria Garbin, Imperial College London
Prof. Roberto Pisano, Politecnico di Torino

Politecnico di Torino
2018

Declaration

I hereby declare that, the contents and organization of this dissertation constitute my own original work and does not compromise in any way the rights of third parties, including those relating to the security of personal data.

<div align="right">

Graziano Frungieri
2018

</div>

* This dissertation is presented in partial fulfillment of the requirements for **Ph.D. degree** in the Graduate School of Politecnico di Torino (ScuDo).

Contents

List of Symbols

Roman Symbols

a	primary particle radius
$A.R.$	aspect ratio
a_1, a_2, a_3	inertia semi-axis
A_H	Hamaker constant
b	contact radius
b_0	zero-load contact radius
c^+, c^-	ion concentration
c_0	salt bulk concentration
D	diffusivity
d_f	fractal dimension
d_{32}	average Sauter diameter
dA	area vector module
dt	infinitesimal time interval
E	elastic modulus
$\mathbf{e}$	rate-of-strain vector
$\mathbf{E}$	rate-of-strain tensor
f^a	aggregation frequency
f^e	encounter frequency
$\mathbf{F}$	force
F_{adh}	adhesion force
g	gravitational acceleration
h_ξ^+	birth function
h_ξ^-	death function
h_{po}	pull-off distance

$\mathbf{i}$	identity tensor
$\mathbf{I}$	inertia tensor
J_{ij}	force propagator tensor
k^a	aggregation rate constant
k^b	breakage rate constant
k_B	Boltzmann constant
k_f	power-law prefactor
k_v	viscous damping constant
k_ζ	tangential spring stiffness
k_ϑ	torsional spring stiffness
K_{ijk}	stresslet propagator tensor
L	characteristic length
m	mass
$\mathcal{M}$	mobility matrix
$\mathbf{M}$	first moment of the hydrodynamic force
n	number density function
n_A	number concentration of cationic particles
n_B	number concentration of anionic particles
n_c	coordination number
n_p	number of primary particles in DEM simulations
N_p	number of suspended particles
$\mathbf{n}$	normal unit vector
p	pressure
p^*	dimensionless pressure
P	number of constituent primary particles
Pe	Péclet number
q	breakup exponent
q^+, q^-	ion valence
q_α	particle atomic density
r	radial coordinate
$r_{\alpha\beta}$	particle center-to-center distance
R	cluster outer radius
R_{ij}	torque propagator tensor

R_g	cluster gyration radius
$\mathcal{R}$	resistance matrix
Re	Reynolds number
$\mathbf{s}$	stresslet vector
$\mathbf{S}$	stresslet tensor
t	physical time
T	absolute temperature
T_{rot}	period of rotation
$\mathbf{T}$	torque
U	characteristic velocity
$\mathbf{u}$	linear velocity
V	potential energy
W	stability ratio
$\mathbf{x}$	spatial/external coordinates vector
x_A	number fraction of cationic particles
x, y, z	spatial coordinates
z_0	minimum approach distance

Greek Symbols

α	aggregation efficiency
α_m	molecule polarizability
$\dot{\gamma}$	shear rate intensity
$\dot{\gamma}_{cr}$	critical shear rate intensity
γ_s	surface energy
Γ	probability density function for the fragment mass
δ_{ij}	Dirac delta
Δt	integration time-step
ε	encounter cross section parameter
ε_0	vacuum permittivity
ε_r	relative permittivity
ϵ_{ijk}	Levi-Civita operator
ζ	spring elongation
$\dot{\zeta}$	derivative of the spring elongation
η	dipole moment

ϑ	spring torsional angle
$\dot{\vartheta}$	derivative of the spring torsional angle
$\theta_{\alpha\beta\gamma}$	three-particle angle
κ	Debye length reciprocal
λ_d	Debye length
λ_l	London wavelength
λ^{VdW}	London-Van der Waals constant
μ	medium viscosity
ν	Poisson ratio
ν_f	number of fragments generated upon breakage
$\boldsymbol{\xi}$	internal coordinates vector
ρ	density
ϱ	charge density
$\boldsymbol{\sigma}$	stress tensor
ϕ, θ, ψ	euler angles
φ	volume solid fraction
Ψ	electrical potential
Ψ_0	surface potential
$\boldsymbol{\omega}$	angular velocity vector
Ω_x	domain of external coordinates
Ω_ξ	domain of internal coordinates
$\boldsymbol{\Omega}$	rate-of-rotation tensor

Superscripts

coll	colloidal
H	hydrodynamic

Subscripts

l	liquid
s	solid

Acronyms / Abbreviations

c.o.m	center of mass
DEM	discrete element method
EDL	electrical double layer
FDA	free draining approximation

IQ	interval of quiescence
m.t.r.	mass transfer rate
MC	Monte Carlo
NDF	number density function
PBE	population balance equation
PDF	probability density function
PSD	particle size distribution

Chapter 1

Introduction

Suspensions of colloidal particles are relevant to a wide variety of industrial processes: typical applications involving colloidal suspensions include the production and/or processing of pigments, cosmetics, chemical–mechanical polishing agents, food products, etc. (Matijević, Babu, 2008; Mezzenga et al., 2005). Whatever the nature of the particular suspension is, a special attention is generally paid to control the typical size of the dispersed particles, their shape, their composition and the distribution of these quantities over the entire population of particles. These quantities have in fact profound implications on the macroscopic behavior of the suspension, including its rheological behaviour, appearance, stability and so on. Therefore, the understanding of the typical underlying phenomena occurring in colloidal suspensions and the way of how to manipulate them is of paramount importance.

It has been known for over a century that colloidal particles aggregate upon the addition of salts to the dispersing medium (Hardy, 1900). About seven decades ago, the DLVO theory, named after Derjaguin, Landau, Verwey and Overbeek, was formulated, succeeding in explaining quantitatively this phenomenon. This theory explains the aggregation of colloidal particles as the result of the joint action of two types of interactions: the attractive Van der Waals force and the repulsive electrical double layer force. The relative intensity of such forces (which together are often referred to as DLVO forces) are strongly dependent on the nature of the solvent and the particle. Briefly speaking, for low ionic strength of the medium, the high energy barrier to the coagulation, due to the repulsive electrical double layer interaction, prevent particle to aggregate. As the ionic strength is increased, this energy barrier is reduced and particles can approach each other up to a distance in which the attractive Van der Waals interaction dominates, thus causing their aggregation.

However, for aggregation to take place, particles need to be brought in close proximity. Different mechanisms can be responsible for the encounters between suspended particles. For sufficiently small particle dispersed in a quiescent fluid, the encounters may be promoted by the Brownian motion. The unevenness of the bombardment the particles receive from the molecules of the surrounding medium cause them to randomly move about and eventually meet each other. This mechanism, defined as *perikinetic* aggregation, has been extensively investigated both numerically

and experimentally over the last decades (Kyriakidis et al., 1997; Witten, Sander, 1983); in this context two different limiting aggregation regimes have been identified (Lin et al., 1989): the diffusion-limited cluster aggregation (DLCA) and the reaction limited cluster aggregation (RLCA). DLCA takes place whenever the energy barrier to aggregation has a negligible intensity, so that the aggregation rate is limited by the diffusion rate i.e., by the time needed by two particles to meet each other in the suspension and eventually aggregate. On the contrary, when a substantial but not insurmountable energy barrier exists, the aggregation rate is determined by the time needed by the particles to overcome it, with the Brownian motion acting as a thermal activation. These two regimes have also been referred to as fast and slow coagulation regimes and have been proven to lead to the formation of different cluster morphologies; in the DLCA regime, clusters generally show a open, porous structure characterized by the alternation of void and dense regions; conversely, in the RLCA regime, clusters have a compact and highly coordinate structure. For both cases, it is common to relate the cluster mass m to a characteristic dimension R with a power-law of the following kind $m \propto R^{d_f}$, where the exponent d_f is frequently indicated as fractal dimension. This dimension can thus be seen as a measure of the space filling properties of the cluster and as such it is frequently used to characterize the clusters obtained upon aggregation; for the DLCA regime, d_f was observed to fall in the range 1.7–1.8 (Brasil et al., 2000; Köylü et al., 1995; Meakin, 1984), while in the RLCA regime a larger value (≈ 2.1) was found (Lin et al., 1990), meaning that when an energy barrier holds, more compact structure are generally produced, regardless of the detailed physicochemical nature of the suspension.

A second mechanism can promote the encounters between particles, that is, the difference in their relative velocities; in a sedimenting suspension, for instance, the encounters are triggered by the different settling velocities of the particles, which can arise as a consequence of their different density or size.

However, in engineering applications, suspensions are generally mechanically stirred; in such conditions the particles are brought close to each other by the gradient of the flow field and the rate of aggregation is determined by the frequency of such encounters, in turn dependent on the intensity of the flow field; this mechanism is often referred to as *orthokinetic* aggregation and for intense flow field can substantially speed up the aggregation kinetics compared to a *perikinetic* mechanism. However, in a stirred suspensions, the growth of the clusters is generally bounded by breakage phenomena. Once clusters have attained a large enough size, the viscous stress exerted on their structure by the flow field may be able to overcome the adhesion force that keeps particles in contact, thus causing the failure of one or more internal bonds (Eggersdorfer et al., 2010; Harada et al., 2006; Vanni, Gastaldi, 2011). As a consequence an equilibrium between aggregation and breakage eventually sets in the system, leading the particle size distribution toward a steady state (Oles, 1992; Serra, Casamitjana, 1998; Soos et al., 2008).

The modelling of such phenomena can be dated back to the work by Smoluchowski (1917), who drawn mathematical expressions useful to model the collision frequency of particles for both Brownian coagulation and laminar shear. These expressions, known as aggregation kernels, even though derived relying on several approximations, have

set the basis for the interpretation of the dynamics of aggregation phenomena in the context of Population Balance Equations (PBE). PBE have attracted a widespread attention among scientists who employed them for the most diverse use (Ramkrishna, 2000), such as crystallization, liquid-liquid, gas-liquid systems, cellular processes, etc. They are in fact able to track the evolution of a generic dispersed phase by simply imposing the conservation of mass throughout the process. Traditionally, PBE can be distinguished in mono-variate and multivariate formulation. In the first case only one quantity (often referred to as *internal variable*) is used to describe the state of the system. Conversely, in the second case, a number of variables is considered. These may include the size of the dispersed particles, composition, shape, fractal dimension.

However, due to their complex integro-differential nature especially when more than one internal variable is considered, the solution of PBE by analytical means is possible in a limited number of idealized situations. As a consequence, a number of methods has been developed to numerically solve PBE in applications of practical interests. Most of the developed methods can be ascribed to three main groups: class or sectional methods, moment-based methods and Monte Carlo methods. For the first group method, the PBE are solved by using a discretization of the internal variable space (Hounslow et al., 1988; Kostoglou, Karabelas, 1994; Vanni, 2000). However, this discretization approach may pose some difficulties since the features of the distribution may change in time and may not be predicted in advance. The method of moments solves the PBE by tracking the temporal evolution of the lower-order moments of the size distribution (Buffo et al., 2013; Marchisio et al., 2003; McGraw, 1997). However, the information given by the method of moments is limited to the integral properties of the suspension and as such is poorer compared to what inferable from the method of classes. On the other hand, the lower computational effort represents the main advantage of the method.

Finally, Monte Carlo (MC) methods reside in the realm of the stochastic method class (Liffman, 1992; Shah et al., 1977; Smith, Matsoukas, 1998; Zhao et al., 2007); they do not solve directly the PBE, but they mimic numerically a realization of the process governed by PBE by adopting a limited number of simulated particles. Because of their discrete nature, MC schemes are particularly well suited to simulate an intrinsically discrete process such as aggregation. Their wide use is also due to the ability to follow the history of each simulated particle and handle easily complex multivariate populations. Therefore, in the last years, MC methods have been applied to the modeling of a wide variety of discrete processes, including aerosol agglomeration (Matsoukas, Friedlander, 1991), cloud droplet coalescence (Gillespie, 1975), simultaneous nucleation and surface growth (Maisels et al., 2004), crystallization (Van Peborgh Gooch, Hounslow, 1996), fractal aggregation (Lattuada et al., 2003), simultaneous aggregation and breakup (Lee, Matsoukas, 2000).

In colloidal suspensions, besides aggregation, other phenomena take place such as breakage and restructuring of the aggregates. Therefore, to accurately follow the dynamics of a colloidal suspension, all these phenomena need to be addressed. This is still a challenging task in the framework of PBE: the scarce knowledge of the underlying physics of such phenomena partially hinders the study of colloidal suspensions in terms of PBE. Furthermore, in laminar flows the breakup occurs

almost instantaneously soon after an aggregate grows over a critical dimension. This behavior can hardly be modeled in the framework of PBE, whereas it is feasible to model it in Monte Carlo simulations.

PBE methods reduce the complexity of aggregates to a few global variables, such as size, mass, fractal dimension. Consequently, they are not capable of capturing the features of the typically disordered structures of clusters. Discrete Element Methods (DEM), for instance, represent a valid alternative for this task; DEM simulations assume the clusters to be composed by a number of distinct elements, each one undergoing forces arising from the interaction with nearby elements and with the dispersing medium. Introducing models for such interactions, DEM simulations are capable of tracking the motion of each individual particle of a cluster, providing valuable insight into the suspension dynamics. This approach dates back to the work of Cundall, Strack (1979), who first employed a DEM to simulate dense granular flows. Since then, DEM have been applied to a number of different problems, ranging over an ample spectrum of length scales; typical applications comprise colloidal suspension (Becker et al., 2009; Harshe, Lattuada, 2016; Harshe et al., 2010; Isella, Drossinos, 2010; Vanni, Gastaldi, 2011), fluidized beds (Tsuji et al., 2008), rock mechanics (Jing, 2003), astrodynamics (Sánchez, Scheeres, 2012). However the applicability of such a method is hindered by the high computational cost involved, which so far has restricted the use of DEM to the study of single aggregates or at most of very small populations.

In this work, in order to circumvent the high computational cost typically associated to pure DEM simulations and to deal with the uncertainty which affects the PBE modelling of colloidal suspension phenomena, a novel method has been developed: it is a mixed stochastic-deterministic numerical method which couples the mean-field approach of PBE (solved stochastically with a MC algorithm) with detailed DEM simulations; the basic idea behind such a combination is that the dynamics of a dilute suspension is determined by a sequence of binary encounter events between the suspended particles, each of which can result into an aggregation, a breakage, a restructuring of the aggregates or into any combination of these phenomena. Therefore, the MC is used to sample a statistically expected sequence of such events and the DEM is used to accurately simulate them; the DEM has been developed in the framework of Stokesian Dynamics (Brady, Bossis, 1988) and coupled with proper models for the colloidal interactions and, thanks to its coupling with a MC scheme, it is used to track the motion of just two particles at a time, thereby reducing significantly the computational cost of the method.

The method has been used to follow the dynamics of dilute model colloidal suspensions and it has been proven to address properly the aggregation, breakage and restructuring phenomena of colloidal suspensions and to give significant insights into the suspension dynamics and aggregate morphology.

The present thesis is organized as follows:

- in Chapter 2 the general framework of Population Balance Equation is presented with a special attention to its application to colloidal suspensions. Furthermore, some solution techniques are briefly revisited;

- in Chapter 3 the developed Discrete Element Method is presented, addressing the modelling of both hydrodynamic and colloidal interactions;

- in Chapter 4 the strategy adopted for the coupling of the Monte Carlo algorithm and the Discrete Element Method is described;

- in Chapter 5 the resulting MC-DEM is applied to investigate the shear-induced aggregation of a fully destabilized suspension of colloidal particles; in particular, simulations are performed to evaluate the effect of the model of colloidal interactions on the aggregation behaviour;

- in Chapter 6 the DEM method is employed to estimate in a predictive manner the aggregation efficiency of porous clusters;

- in Chapter 7 the MC-DEM method is applied to study the dynamic behaviour of suspensions subject to severe viscous stress, with a particular attention the analysis of the aggregation-breakage equilibrium;

- in Chapter 8 the MC-DEM method is used to investigate the shear-induced aggregation of mixed populations of colloidal particles with different surface potentials.

References

Becker, V., Schlauch, E., Behr, M., Briesen, H. 2009. "Restructuring of colloidal aggregates in shear flows and limitations of the free-draining approximation". *Journal of Colloid and Interface Science* 339. 362–372.

Brady, J. F., Bossis, G. 1988. "Stokesian dynamics". *Annual Review of Fluid Mechanics* 20. 111–157.

Brasil, A., Farias, T., Carvalho, M. 2000. "Evaluation of the Fractal Properties of Cluster–Cluster Aggregates". *Aerosol Science & Technology* 33. 440–454.

Buffo, A., Vanni, M., Marchisio, D., Fox, R. O. 2013. "Multivariate quadrature-based moments methods for turbulent polydisperse gas–liquid systems". *International Journal of Multiphase Flow* 50. 41–57.

Cundall, P. A., Strack, O. D. 1979. "A discrete numerical model for granular assemblies". *Geotechnique* 29. 47–65.

Eggersdorfer, M., Kadau, D, Herrmann, H., Pratsinis, S. 2010. "Fragmentation and restructuring of soft-agglomerates under shear". *Journal of Colloid and Interface Science* 342. 261–268.

Gillespie, D. T. 1975. "An exact method for numerically simulating the stochastic coalescence process in a cloud". *Journal of the Atmospheric Sciences* 32. 1977–1989.

Harada, S., Tanaka, R., Nogami, H., Sawada, M. 2006. "Dependence of fragmentation behavior of colloidal aggregates on their fractal structure". *Journal of Colloid and Interface Science* 301. 123–129.

Hardy, W. 1900. "A preliminary investigation of the conditions which determine the stability of irreversible hydrosols". *The Journal of Physical Chemistry* 4. 235–253.

Harshe, Y. M., Lattuada, M. 2016. "Universal breakup of colloidal clusters in simple shear flow". *The Journal of Physical Chemistry B* 120. 7244–7252.

Harshe, Y. M., Ehrl, L., Lattuada, M. 2010. "Hydrodynamic properties of rigid fractal aggregates of arbitrary morphology". *Journal of Colloid and Interface Science* 352. 87–98.

Hounslow, M., Ryall, R., Marshall, V. 1988. "A discretized population balance for nucleation, growth and aggregation". *AIChE Journal* 34. 1821–1832.

Isella, L., Drossinos, Y. 2010. "Langevin agglomeration of nanoparticles interacting via a central potential". *Physical Review E* 82. 011404.1–15.

Jing, L. 2003. "A review of techniques, advances and outstanding issues in numerical modelling for rock mechanics and rock engineering". *International Journal of Rock Mechanics and Mining Sciences* 40. 283–353.

Kostoglou, M., Karabelas, A. J. 1994. "Evaluation of zero order methods for simulating particle coagulation". *Journal of Colloid and Interface science* 163. 420–431.

Köylü, Ü. Ö., Faeth, G., Farias, T. L., Carvalho, M. d. G. 1995. "Fractal and projected structure properties of soot aggregates". *Combustion and Flame* 100. 621–633.

Kyriakidis, A. S., Yiantsios, S. G., Karabelas, A. J. 1997. "A study of colloidal particle Brownian aggregation by light scattering techniques". *Journal of Colloid and Interface Science* 195. 299–306.

Lattuada, M., Wu, H., Morbidelli, M. 2003. "A simple model for the structure of fractal aggregates". *Journal of Colloid and Interface Science* 268. 106–120.

Lee, K., Matsoukas, T. 2000. "Simultaneous coagulation and break-up using constant-N Monte Carlo". *Powder Technology* 110. 82–89.

Liffman, K. 1992. "A direct simulation Monte-Carlo method for cluster coagulation". *Journal of Computational Physics* 100. 116–127.

Lin, M., Lindsay, H., Weitz, D., Ball, R., Klein, R, Meakin, P 1989. "Universality in colloid aggregation". *Nature* 339. 360–362.

Lin, M., Lindsay, H., Weitz, D., Ball, R., Klein, R, Meakin, P. 1990. "Universal reaction-limited colloid aggregation". *Physical Review A* 41. 2005–2020.

Maisels, A., Kruis, F. E., Fissan, H. 2004. "Direct simulation Monte Carlo for simultaneous nucleation, coagulation, and surface growth in dispersed systems". *Chemical Engineering Science* 59. 2231–2239.

Marchisio, D. L., Vigil, R. D., Fox, R. O. 2003. "Quadrature method of moments for aggregation–breakage processes". *Journal of Colloid and Interface Science* 258. 322–334.

Matijević, E, Babu, S. 2008. "Colloid aspects of chemical–mechanical planarization". *Journal of Colloid and Interface Science* 320. 219–237.

Matsoukas, T., Friedlander, S. K. 1991. "Dynamics of aerosol agglomerate formation". *Journal of Colloid and Interface Science* 146. 495–506.

McGraw, R. 1997. "Description of aerosol dynamics by the quadrature method of moments". *Aerosol Science and Technology* 27. 255–265.

Meakin, P. 1984. "Diffusion-limited aggregation in three dimensions: results from a new cluster-cluster aggregation model". *Journal of Colloid and Interface Science* 102. 491–504.

Mezzenga, R., Schurtenberger, P., Burbidge, A., Michel, M. 2005. "Understanding foods as soft materials". *Nature Materials* 4. 729–740.

Oles, V. 1992. "Shear-induced aggregation and breakup of polystyrene latex particles". *Journal of Colloid and Interface Science* 154. 351–358.

Ramkrishna, D. (2000). *Population balances: Theory and applications to particulate systems in engineering.* 1st edition. Academic press, San Diego (CA).

Sánchez, D. P., Scheeres, D. J. 2012. "DEM simulation of rotation-induced reshaping and disruption of rubble-pile asteroids". *Icarus* 218. 876–894.

Serra, T., Casamitjana, X. 1998. "Structure of the aggregates during the process of aggregation and breakup under a shear flow". *Journal of Colloid and Interface Science* 206. 505–511.

Shah, B., Ramkrishna, D., Borwanker, J. 1977. "Simulation of particulate systems using the concept of the interval of quiescence". *AIChE Journal* 23. 897–904.

Smith, M., Matsoukas, T. 1998. "Constant-number Monte Carlo simulation of population balances". *Chemical Engineering Science* 53. 1777–1786.

Smoluchowski, M. V. 1917. "Versuch einer mathematischen Theorie der Koagulationskinetik kolloider Lösungen". *Zeitschrift für physikalische Chemie* 92. 129–168.

Soos, M., Moussa, A. S., Ehrl, L., Sefcik, J., Wu, H., Morbidelli, M. 2008. "Effect of shear rate on aggregate size and morphology investigated under turbulent conditions in stirred tank". *Journal of Colloid and Interface Science* 319. 577–589.

Tsuji, T., Yabumoto, K., Tanaka, T. 2008. "Spontaneous structures in three-dimensional bubbling gas-fluidized bed by parallel DEM–CFD coupling simulation". *Powder Technology* 184. 132–140.

Van Peborgh Gooch, J. R., Hounslow, M. J. 1996. "Monte Carlo simulation of size-enlargement mechanisms in crystallization". *AIChE Journal* 42. 1864–1874.

Vanni, M. 2000. "Approximate population balance equations for aggregation–breakage processes". *Journal of Colloid and Interface Science* 221. 143–160.

Vanni, M., Gastaldi, A. 2011. "Hydrodynamic forces and critical stresses in low-density aggregates under shear flow". *Langmuir* 27. 12822–12833.

Witten, T. A., Sander, L. M. 1983. "Diffusion-limited aggregation". *Physical Review B* 27. 5686.

Zhao, H., Maisels, A., Matsoukas, T., Zheng, C. 2007. "Analysis of four Monte Carlo methods for the solution of population balances in dispersed systems". *Powder Technology* 173. 38–50.

Chapter 2

Population Balance Equation

In this chapter the Population Balance Equation (PBE) framework is introduced. Starting from the derivation of the generic PBE, the discussion will move afterwards to the case of colloidal suspensions, whose dynamics is determined exclusively by aggregation and breakup phenomena. The most commonly used kernels to model such phenomena will be analysed.

Finally, an overview of the solution methods of PBE is presented with a particular attention to the discrete formulation and to the Monte Carlo approach.

2.1 PBE for colloidal systems

Colloidal suspensions are characterized by the coexistence of a dispersed phase, in the form of small solid particles, and a continuous liquid phase, acting as dispersing medium. Each single element of the disperse phase can be characterized by a certain number of properties. In the framework of the population balance theory these properties are usually referred to as coordinates and divided into two main groups (Hulburt, Katz, 1964; Ramkrishna, 2000):

- external coordinates (i.e., the spatial position of each single entity, as determined for instance by its center of mass)

- internal coordinates (quantities related to the intimate properties of the particle[1] such as size, physical and chemical composition, morphology, etc.)

Let us assume to have at time t a suspension composed by a certain number of particles. Each suspended particle can be characterized by a vector $\mathbf{x} = [x, y, z]$ indicating the spatial position of its center of mass (c.o.m) and a vector $\boldsymbol{\xi} = [\xi_1, \xi_2, ..., \xi_m]$ accommodating all its relevant internal coordinates. Therefore, denoting with Ω_ξ and Ω_x the domain of the internal variables (or phase state space) and the domain of the external variables (or physical space state), respectively, the total number of particles

---

[1]In the following, the term *particle* will be used to indicate clusters and primary particles without distinction.

in the system at time t is given by:

$$N_p\left(t\right) = \int_{\Omega_x} d\Omega_x \int_{\Omega_\xi} n\left(\mathbf{x}, \boldsymbol{\xi}, t\right) d\Omega_\xi \tag{2.1}$$

with $n\left(\mathbf{x}, \boldsymbol{\xi}, t\right)$ being the number density function (NDF) and $d\Omega_x$ and $d\Omega_\xi$, the infinitesimal volumes in the external and internal coordinate space, respectively. Therefore, by tracking the evolution of the NDF it is possible to precisely follow the dynamics of the dispersed phase, as the NDF enables us to characterize the entire population of dispersed particles at any time t and at any position in both the physical space and phase space.

In general terms, the change in the NDF can occur as a consequence of two kinds of events, namely continuous and discrete (or discontinuous) events. This distinction between the two has to be based on time/length scales comparisons. A typical example of continuous event is the growth of solid crystals; during this process, the size of the crystal grows due to the surface deposition of single molecules which occurs on a time and length scale much smaller than the scales associated to the change in size of the crystal. Conversely, when two particle collide and aggregate, the length scale of this process is of the same order of magnitude of the particle size, thus aggregation processes cause a discontinuous jump in the internal variable space. A similar argument holds for breakage processes as well.

Therefore, omitting, for the sake of conciseness, the dependence on time and space, a balance equation for the NDF $n\left(\mathbf{x}, \boldsymbol{\xi}, t\right)$ may be written as follows:

$$\frac{\partial}{\partial t}\left(\int_{\Omega_x} d\Omega_x \int_{\Omega_\xi} n d\Omega_\xi\right) = -\int_{\Omega_\xi} d\Omega_\xi \int_{\partial\Omega_x} \left(n\dot{\mathbf{x}}\right) \cdot dA_x - \int_{\Omega_x} d\Omega_x \int_{\partial\Omega_\xi} \left(n\dot{\boldsymbol{\xi}}\right) \cdot dA_\xi +$$
$$+ \int_{\Omega_x} d\Omega_x \int_{\Omega_\xi} h_\xi d\Omega_\xi \tag{2.2}$$

where $\dot{\mathbf{x}}$ and $\dot{\boldsymbol{\xi}}$ represent the continuous rates of change in the external and internal coordinate space; dA_r and dA_x are local, infinitesimal area vectors pointing out of the surfaces $\partial\Omega_x$ and $\partial\Omega_\xi$ of the physical and phase space, respectively. Finally, h_ξ represents the discontinuous rate of change of the NDF per unit volume of both phase state and physical space occurring as a consequence of discrete processes not accounted for by the other terms. Assuming the function $n\left(\mathbf{x}, \boldsymbol{\xi}, t\right)$ to be continuous, by using the divergence theorem, Eq. (2.2) may be rewritten as:

$$\frac{\partial}{\partial t}\left(\int_{\Omega_x} d\Omega_x \int_{\Omega_\xi} n d\Omega_\xi\right) = -\int_{\Omega_\xi} d\Omega_\xi \int_{\Omega_x} \boldsymbol{\nabla}_x \cdot \left(n\dot{\mathbf{x}}\right) d\Omega_x - \int_{\Omega_x} d\Omega_x \int_{\Omega_\xi} \boldsymbol{\nabla}_\xi \cdot \left(n\dot{\boldsymbol{\xi}}\right) d\Omega_\xi +$$
$$+ \int_{\Omega_x} d\Omega_x \int_{\Omega_\xi} h_\xi d\Omega_\xi \tag{2.3}$$

where $\boldsymbol{\nabla}_x$ and $\boldsymbol{\nabla}_\xi$ are the divergence operators in the physical and phase space. The arbitrariness of the domain of integration and the continuity of the integrand function

allow us to write the previous equation as:

$$\frac{\partial n}{\partial t} = -\boldsymbol{\nabla}_x \cdot (n\dot{\mathbf{x}}) - \boldsymbol{\nabla}_\xi \cdot \left(n\dot{\boldsymbol{\xi}}\right) + h_\xi \tag{2.4}$$

generally referred to as Population Balance Equation.

However, Eq. (2.4) can be simplified under some circumstances. In a well-mixed colloidal suspension, spatial heterogeneities may be neglected and therefore the dependence of the number density function on the physical space variable disregarded. Furthermore, for insoluble solids, such as silica or polymeric particles in water, the distribution of the particle size is affected solely by discontinuous phenomena, such as aggregation and breakage. Therefore the first two terms on the r.h.s. can be dropped out leading to the following simpler formulation:

$$\frac{\partial n\left(\boldsymbol{\xi}, t\right)}{\partial t} = h_\xi\left(\boldsymbol{\xi}, t\right) \tag{2.5}$$

where finally the dependence on time and phase space variables has been reintroduced.

2.1.1 Birth and death function

As already pointed out, the aggregation and breakage processes occurring in colloidal suspension have to be considered as discontinuous phenomena having an abrupt effect on the NDF. Commonly the modelling of such phenomena is carried out resorting to birth and death functions and, as a consequence, the term h_ξ of Eq. (2.5) is generally split as:

$$h_\xi = h_\xi^+ + h_\xi^- \tag{2.6}$$

where the terms h_ξ^+ and h_ξ^- represent the rate of appearance and the rate of loss of particles per unit volume due to such discontinuous events.

Birth and death functions for aggregation phenomena

When a suspension is sufficiently dilute i.e., characterized by a low solid content, aggregation can be reasonably considered as a binary event, that is an event which involves two particles at a time. In rigorous terms, if the population number density is small, the probability that during a time interval dt more than two particles aggregate simultaneously is only of order $\mathcal{O}\left(dt^2\right)$, whereas that of two particles is $\mathcal{O}\left(dt\right)$ (Ramkrishna, 2000).

Let us assume that the population of particles is distributed solely according to one internal variable ξ, made coincident with the mass. The source (or birth) term due to aggregation to be included in the PBE can be derived by simply imposing the conservation of mass in each aggregation event; this means that particles of mass ξ are generated as the result of the aggregation of particles of mass $(\xi - \xi')$ with

particles of mass ξ'. Therefore the birth rate h^+ for particles of mass ξ is given by:

$$h^+ (\xi, t) = \frac{1}{2} \int_0^\xi k^a \left(\xi', \xi - \xi'\right) n \left(\xi', t\right) n \left(\xi - \xi', t\right) d\xi' \qquad (2.7)$$

where the function k^a represents the aggregation rate constant. The prefactor $1/2$ is included to avoid the redundancy that would arise with the adopted interval of integration: both ξ' and $\xi - \xi'$ vary in fact in the range $[0, \xi]$, thus to avoid pair double counting a correction is needed.

The sink or death term instead reads as:

$$h^- (\xi, t) = n (\xi, t) \int_0^\infty k^a \left(\xi, \xi'\right) n \left(\xi', t\right) d\xi' \qquad (2.8)$$

and states that the disappearance of particles of mass ξ is due to the aggregation of such particles with all the other suspended particles.

Birth and death functions for breakage phenomena

The breakage of colloidal aggregates is generally considered as a first-order process, i.e., a process involving one aggregate at once and determined by its interaction with the dispersing medium. It is a complex phenomenon governed by a balance between the disruptive force exerted by the viscous stress on the aggregate structure and the internal cohesive force of the aggregate itself. Limiting again the discussion to a mono-variate case, in which the only considered internal coordinate is the cluster mass ξ and assuming the fluid properties to be evenly distributed in the system, the aggregate breakage can be described resorting to the term:

$$k^b (\xi, t) \, dt \qquad (2.9)$$

which expresses the probability that an aggregate characterized by its mass ξ undergoes a breakage event in a time interval dt. Therefore, based on this definition, it is possible to state that the number of particles disappearing per unit time and unit volume as a consequence of breakage is given by:

$$h^- (\xi, t) = k^b (\xi, t) \, n (\xi) \qquad (2.10)$$

Upon breakage a certain number of fragments (or daughter particles) characterized by their own mass are generated. Therefore, a birth function is also needed to fully describe the breakage event; the birth function has to count for:

- the number of generated fragments ν_f

- the distribution of the mass over the generated fragments

The first quantity is obviously a scalar and can assume in principle any value larger or equal to 2; the second quantity is generally modelled with a conditional probability density function $\Gamma (\xi | \xi', t)$, which represents the distribution of the particle masses of

the fragments produced upon breakage of a parent particle of mass ξ'. As such, this function has to satisfy:

$$\int_0^\xi \Gamma\left(\xi|\xi',t\right) d\xi = 1 \tag{2.11}$$

which simply states that the sum of all probabilities of producing the daughter particles of state ξ from the parent particle ξ' is unity. Moreover the conservation of mass must hold, therefore

$$\Gamma\left(\xi|\xi',t\right) = 0 \text{ for } \xi > \xi' \qquad \xi' = \nu_f\left(\xi'\right) \int_0^{\xi'} \xi\Gamma\left(\xi|\xi',t\right) d\xi \tag{2.12}$$

with the first equation stating that no daughter particle with a mass larger than the parent aggregate can be formed; whereas the second equation states that the sum of the masses of all the daughter particles equals the mass of the parent one.

The birth function reads as:

$$h^+\left(\xi,t\right) = \int_\xi^\infty \nu_f\left(\xi'\right) k^b\left(\xi',t\right) \Gamma\left(\xi|\xi',t\right) n\left(\xi',t\right) d\xi' \tag{2.13}$$

and finally the mono-variate PBE for a colloidal suspension undergoing both aggregation and breakage event can be written as:

$$\begin{aligned}
\frac{\partial n\left(\xi,t\right)}{\partial t} =& \frac{1}{2} \int_0^\xi k^a\left(\xi',\xi-\xi'\right) n\left(\xi',t\right) n\left(\xi-\xi',t\right) d\xi' \\
& - n\left(\xi,t\right) \int_0^\infty k^a\left(\xi,\xi'\right) n\left(\xi',t\right) d\xi' \\
& -k^b\left(\xi,t\right) n\left(\xi\right) + \int_\xi^\infty \nu_f\left(\xi'\right) k^b\left(\xi',t\right) \Gamma\left(\xi|\xi',t\right) n\left(\xi',t\right) d\xi'
\end{aligned} \tag{2.14}$$

In the following a review of the aggregation and breakage rate functions for some typical processes will be presented. Regarding aggregation, the discussion will be limited to the case of spherical particles characterized by only one internal coordinate. This coordinate will be assumed to be the particle radius a; this is clearly an oversimplification of what happens in colloidal suspensions, where primary particles aggregate maintaining their identities and forming clusters, which frequently show a porous internal structure and an overall shape far from the spherical symmetry. However this approximation will be adopted for the time being and relaxed at later stage.

The current understanding of breakage phenomena is still poor compared to aggregation due to a lack of knowledge of the underlying physics and to the inherent difficulties of direct observation. Nevertheless, the relevant literature about cluster breakage will be briefly revisited. For the sake of simplicity, the discussion is restricted to systems in stationary laminar conditions. Although the physical mechanism of aggregation and breakup are practically the same in laminar and turbulent flows, the interplay of such a mechanism with the dynamics of turbulence makes the description of these phenomena considerably more complex in turbulent fluids.

Aggregation rate

Each aggregation event can be assumed to be determined by two subsequent steps: the approach between the two particles and the actual aggregation. During the first step the particles are brought in close proximity. This may be due to one or more of the following mechanism:

  i) gradient of the flow field

  ii) brownian motion

  iii) differential settling

In the first case the approaching of the particles is favoured by the velocity gradient of the continuous phase which causes the particles to move with different relative velocities, thereby leading to their encounter. This mechanism is generally referred to as orthokinetic aggregation. In the second case, the encounter is promoted by the random thermal motion of the particles, in a mechanism called perikinetic aggregation. In the last case the encounter is caused by the different settling velocity of the particles, possibly due to their different densities and/or sizes. Generally speaking, the first mechanism is predominant in stirred suspensions, whereas the last two may have a significant role in the case of quiescent continuous phase.

The second step of the aggregation consists in the formation of a mechanical contact between the particles. This step is affected by the nature of the inter-particle interaction: hydrodynamic interaction (in particular lubrication) and colloidal interaction come into play during this phase and their interplay has a strong effect on the particle fate. While hydrodynamic interactions generally act impeding aggregation, the colloidal interaction may or not favour the aggregation depending on the physio-chemical nature of the particles and the solvent.

The first rigorous modelling of the aggregation rate for such processes dates back to the work of Smoluchowski (1917). In his seminal work, even if a number of approximations were adopted, Smoluchowski drawn a series of expressions that still represent the reference framework for colloidal suspension studies. He assumed that suspended particles are perfectly smooth spheres not interacting with each other by means of hydrodynamic interaction and sticking irreversibly upon contact. In these circumstances every encounter between particles leads to a permanent aggregation.

Aggregation kernel for laminar shear   Let us assume that the flow field in a moving fluid can approximated at least locally as a simple laminar shear flow $\dot{\gamma}$ (Fig. 2.1). A single spherical particle i is conveniently located in the center of the reference system and, as a consequence of the velocity gradient, it will be approached by other suspended particles j. The interaction between the particles is neglected and particles are assumed to be carried passively by the flow field, thereby following linear trajectories.

If we assume that the particles coagulate irreversibly upon contact, a collision sphere of radius $a_{ij} = a_i + a_j$ and centred in the center of particle i can be identified.
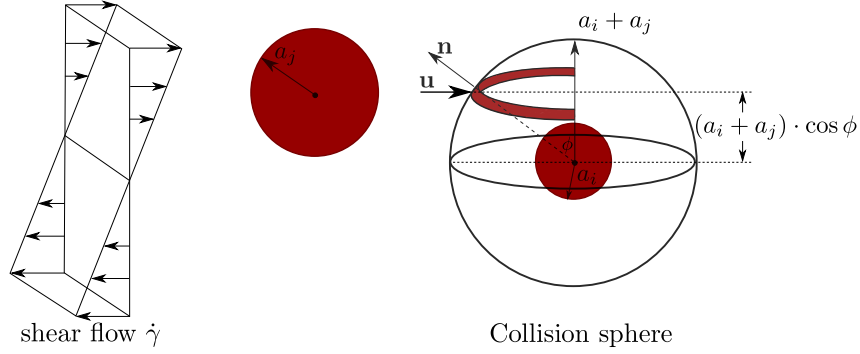
Figure 2.1: Simplified model of particle collision in shear flow. Particle i is fixed in the origin of the reference system; particle j is carried passively by the shear flow field.

Therefore, the mass transfer rate (m.t.r.) of j particles towards particle i can be written as

$$\text{m.t.r.} = \int_A n_j \left(\mathbf{n} \cdot \mathbf{u}\right) dS \qquad (2.15)$$

where $\left(\mathbf{n} \cdot \mathbf{u}\right)$ represents the component of the velocity field orthogonal to the infinitesimal surface element dS of the collision sphere and where n_j is the number concentration of j particles. By considering that $|\mathbf{u}| = \dot{\gamma}\left(a_i + a_j\right)\cos\phi$ and $dS = 2\left[\left(a_i + a_j\right)\sin\phi\right] \cdot \left[\left(a_i + a_j\right) d\phi\right]$, the integration of Eq. (2.15) leads to:

$$\text{m.t.r.} = \frac{4}{3}\dot{\gamma}\left(a_i + a_j\right)^3 n_j \qquad (2.16)$$

If the concentration of i particles is n_i, then the number of aggregation events per unit volume and unit time is given by:

$$f_{ij}^a = \frac{4}{3}\dot{\gamma}\left(a_i + a_j\right)^3 n_i n_j \qquad (2.17)$$

and therefore the aggregation rate constant can be finally written as:

$$k_{ij}^a = \frac{4}{3}\dot{\gamma}\left(a_i + a_j\right)^3 \qquad (2.18)$$

which represents the well-known orthokinetic aggregation kernel for laminar shear, which, as apparent, has a strong dependency on the particle size.

Aggregation kernel for Brownian motion Let us assume that the suspension is constituted by a certain number of isolated spherical particles uniformly distributed in the system, with each particle describing a random Brownian motion independent of all the other particles. Furthermore, let us assume that a particle i with radius a_i is fixed in the origin of the reference system, acting as a collector for all the other suspended particles j, which have a radius equal to a_j. At the steady state, by using the Fick diffusion equation it is possible to state that, in spherical coordinates, the

mass transfer rate of particles j towards the particle i is given by:

$$\text{m.t.r.} = 4\pi r^2 D \frac{\partial n_j}{\partial r} \tag{2.19}$$

where D represents the particle diffusivity and r the radial coordinate. Imposing that at the central particle surface the concentration n_j vanishes, so that the surface of the central particle acts as a perfect sink ($r = a_i + a_j$, $n_j = 0$) and that at sufficiently large distance from it, the concentration is n_j (for $r = \infty$, $n = n_j$) the m.t.r. reads as:

$$\text{m.t.r.} = 4\pi D \left(a_i + a_j\right) n_j \tag{2.20}$$

If the central particle is in Brownian motion too, the diffusion constant in Eq. (2.20) must take into account the relative motion of the particles; by using the Einstein equation for the diffusion coefficient ($D_{ij} = D_i + D_j$), the aggregation rate constant finally reads as (Friedlander, 1977):

$$k_{ij}^a = 4\pi \left(D_i + D_j\right)\left(a_i + a_j\right) \tag{2.21}$$

Furthermore, when the Stokes-Einstein relation for diffusion holds, Eq. (2.21) can be rewritten as:

$$k_{ij}^a = \frac{2k_B T}{3\mu}\left(\frac{1}{a_i} + \frac{1}{a_j}\right)\left(a_i + a_j\right) \tag{2.22}$$

where μ is the medium viscosity. The aggregation rate of Eq. (2.22) is the widely used Brownian (or perikinetic) aggregation kernel, first derived by Smoluchowski (1917).

Aggregation kernel in differential settling   Another relevant aggregation mechanism arises when heavy particles with different density and/or size settle from a suspension. Heavier particles settle more rapidly than lighter ones and, therefore, during their fall, they may encounter and aggregate the latter ones. Assuming again the spherical symmetry of the particles and employing the Stokes' law for drag force, the collision frequency for particle of equal density and different size can be straightforwardly drawn as (Elimelech et al., 1995):

$$k_{ij}^a = \left(\frac{2\pi g}{9\mu}\right)\left(\rho_s - \rho_l\right)\left(a_i + a_j\right)^3\left(a_i - a_j\right) \tag{2.23}$$

where ρ_s and ρ_l are the density of the suspended particles and of the liquid phase, respectively. Clearly this aggregation rate will be more important as the difference in density of the two phases increases. Furthermore as the size of the particles increases as a result of aggregation, as predictable from Eq. (2.23) a substantial increase of the aggregation rate is expected.

Comparison of aggregation rate constants   In order to compare the relative importance of the three different aggregation regimes presented above, Fig. 2.2 reports the respective rate constants for varying particle radius; in Fig. 2.2a, for the sake of
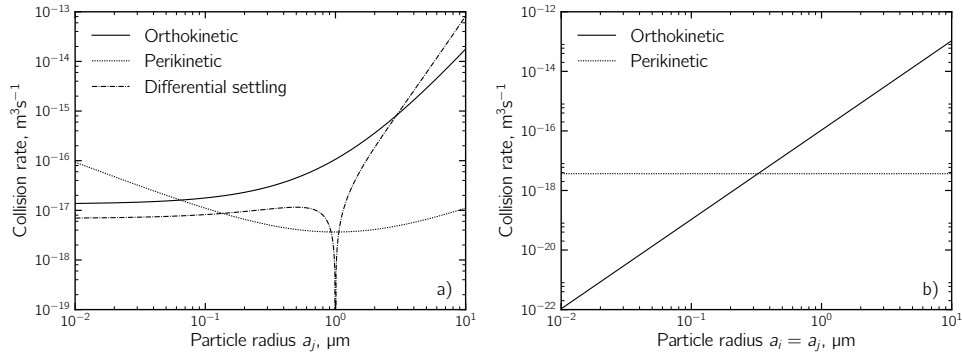
Figure 2.2: a) Comparison of the collision rate constants for three different regimes (Eqs. (2.18),(2.22),(2.23)). For all regimes particle i is taken to have a radius equal to $1\,\mu$m; particle j radius ranges from $0.01\,\mu$m to $10\,\mu$m. For differential settling the solid density ρ_s is set equal to $2\,\mathrm{g\,cm^{-3}}$. b) Collision rate constant for orthokinetic and perikinetic aggregation as a function of the common particle radius. In both plots, the continuous phase properties are referred to water at room temperature and, for orthokinetic aggregation, $\dot{\gamma} = 10\,\mathrm{s^{-1}}$.

simplicity, one particle radius is kept fixed and equal to $1\,\mu$m, the second one has been varied between $0.01\,\mu$m and $10\,\mu$m. It is apparent that perikinetic aggregation gives relatively high aggregation rates for small particle diameter a_j (as a consequence of the large particle diffusivity), it passes through a minimum for equally sized particles and increase again for increasing a_j. This is due to the fact that when increasing the particle size, even if a reduction of the diffusivity occurs, the aggregation rate grows as a consequence of the increased capture section of the particle. However, for large particles, perikinetic aggregation is generally negligible if compared to differential settling and orthokinetic aggregation. As noticeable in Eqs. (2.18) and (2.23) the aggregation rates of these two mechanisms present a strong dependence on particle size and therefore they prevail for large particle size. Clearly the differential settling rate approaches zero as the involved particles become comparable in size. In this case particle present the same settling velocity and capture phenomena no longer take place. In Fig. 2.2b the particles have been assumed to have the same size. It is evident that for common particle radius larger than 300 nm, the orthokinetic aggregation rate is prevailing over the perikinetic one, which becomes practically negligible.

However, it is worth to mention that the rates plotted in Fig. 2.2 are highly sensitive to the particular set of parameters adopted. Therefore, even if the general trend is essentially captured by the plotted curves, in real situations a proper characterization of the investigated system has to be carried out.

Aggregation efficiency As already pointed out in the previous paragraphs, the derivation of the aggregation rates for the three analysed mechanisms was possible because a number of approximations were adopted. However, several works have shown that these approximations are not always appropriate. For Brownian aggregation, for instance, the assumption of constant diffusion coefficients has been demonstrated

to break down when particle are close to each other (Alam, 1987; Kerminen, 1994; Spielman, 1970): as a consequence of lubrication interaction, approaching particles experience an increased resistance to aggregation, thereby a lower collision rate than the theoretical one should be expected. In laminar shear and differential settling, the assumption of rectilinear trajectories of the particles is also an oversimplification of the real situation (Arp, Mason, 1976; Van de Ven, Mason, 1976; Vanni, Baldi, 2002); the hydrodynamic interaction between particles causes the deflection of the particle trajectories which has been extensively proven to have profound implications on the aggregation rate. Furthermore the theoretical aggregation rates do not take into account the interparticle interaction: colloidal interactions can have in fact a substantial effect in either increasing or decreasing the aggregation rates.

In order to take into account such phenomena, two approaches have been developed and widely used, namely the stability ratio and the aggregation efficiency approach. Even if they are substantially equivalent, they are traditionally applied to different situations; for perikinetic studies it is conventional to adopt the stability ratio; it simply expresses the ratio between the theoretical rate constant and the one found when colloidal interactions hold. When particles are subject to mutual interaction forces, Eq. (2.19) need to be modified in order to count for the additional diffusion flux of j particles due to such interactions. Therefore the mass transfer rate reads as:

$$\text{m.t.r.} = 4\pi r^2 D \left(\frac{\partial n_j}{\partial r} + \frac{n_j}{k_B T} \frac{\partial V}{\partial r} \right) \tag{2.24}$$

where V represent the potential energy arising from the interaction of two particles. The integration of Eq. (2.24) leads to:

$$\text{m.t.r.} = \frac{4\pi D \left(a_i + a_j \right) n_j}{W} \tag{2.25}$$

where the correction factor W, known as stability ratio, is equal to:

$$W = \left(a_i + a_j \right) \int_{(a_i + a_j)}^{\infty} \frac{\exp \left[V\left(r \right) / k_B T \right]}{r^2} dr \tag{2.26}$$

where r is the center-to-center distance between two particles. The value of W is strongly dependent on the nature of the colloidal interaction acting on the particles: when an attractive interaction between the particles holds, the stability ratio is less than unity, leading to an increase of the collision rate, compared to a purely diffusion mechanism. Conversely, when the interaction is repulsive, W can assume values much larger than unity, thus substantially reducing the collision rate, possibly up to the point of completely hindering the aggregation process.

In orthokinetic aggregation, rather than the stability ratio, the most common choice is to resort to the aggregation efficiency; as already mentioned, the interparticle interaction can substantially alter the particle trajectories, thus modifying the extension of the aggregation cross section, which, in the idealized case, has radius $a_i + a_j$. The aggregation efficiency is simply defined as the ratio between the flow rate of j particles towards the collector i through the actual collision cross section and the

flow rate through the symmetric circular cross section hypothesized by Smoluchowski. Therefore, for a shear flow $\dot{\gamma} y \mathbf{e}_z$ (with $\mathbf{e}_z$ being the unit vector aligned with the flow direction and y being the velocity gradient direction) the aggregation efficiency reads as:

$$\alpha_{ij} = \frac{n_j \int_{S_{\text{act}}} \dot{\gamma} y dS}{n_j \int_{S_{\text{Smol}}} \dot{\gamma} y dS} \tag{2.27}$$

The first attempt in this direction was made by Curtis, Hocking (1970). They took into account Van der Waals and hydrodynamic interactions to track the relative motion of a pair of equal spherical particles and evaluated aggregation cross sections and aggregation efficiencies. They pointed out the importance of including inter-particle interactions and demonstrated the limit of the linear trajectory analysis of Smoluchowki, but their definition of aggregation efficiency was later seen to be incorrect. Later Van de Ven and Mason extended the approach of Curtis and Hocking, founding an approximate formula for the aggregation efficiency when no electrostatic repulsive force exists (Van de Ven, Mason, 1977):

$$\alpha_{ij} = c_1 \left(\frac{A_H}{36\pi\mu\dot{\gamma}a^3} \right)^{0.18} \tag{2.28}$$

where A_H is the Hamaker constant of the system, μ the medium viscosity and a is the common primary particle radius, whereas c_1 is a parameter of the order of the unity, slightly dependent on the particle radius. On the basis of Eq. (2.28), it is possible to state that the dependence of the aggregation rate on the shear rate $\dot{\gamma}$ is slightly non linear, differently from the prediction of Smoluchowski; multiplying, in fact, the theoretical aggregation rate (Eq. (2.18)) by the aggregation efficiency of Eq. (2.28), it follows that the aggregation rate is proportional to $\dot{\gamma}^{0.82}$. Adler further expanded the work of Van de Ven and Mason to the case of heterocoagulation (Adler, 1981a; Adler, 1981b), that is the coagulation of particles with different properties, focusing his investigation on the effect of the particle size ratio.

The works just mentioned focused solely on the aggregation efficiency of solid spherical particles; however, upon aggregation, clusters of primary particles are produced, frequently characterized by porous and rather irregular structures; in order to take into account the porous structure of clusters, Kusters et al. (1997) have developed a core shell-like model, which assumes clusters to be composed by a solid impermeable core and by a completely permeable shell, leading to a good agreement with experimental data. Similarly, Bäbler (2008) adopted the Brinkman equation to model the fluid flow inside the porous structure of the aggregates, observing that collision between similar aggregates are more favoured compared to the collisions between aggregates displaying large mass disproportion. However, at the present day, no expression useful to model the aggregation efficiency of porous clusters is available; the wide variability observed in the clusters shape and internal structure makes indeed this task extremely challenging.

Breakage frequency and daughter size distribution

Compared to aggregation, the modelling of the rate of breakage is more complicated because of the scarce understanding of the underlying physics of the process. Each breakup event is determined in fact by an intricate interplay between cluster morphology, external shear and interactions between particles, including both hydrodynamic and colloidal interactions; in addition, in shear flow, the intertwining between rotation and deformation of the clusters further increases the complexity of the problem.

Generally speaking, in laminar flows breakup occurs when the fluid flow is violent enough to give rise to a hydrodynamic stress that exceeds the cluster strength. Therefore, it is common to identify a critical shear rate $\dot{\gamma}_{cr}$ upon which breakup occurs almost instantaneously. Such a critical value is generally related to the size of the aggregate by means of a power-law of the following kind:

$$\dot{\gamma}_{cr} \propto R^{-q} \tag{2.29}$$

with R indicating the size of the aggregate and q being a breakup exponent dependent on the cluster morphology. As demonstrated numerically by Harada et al. (2006), the aggregate fractal dimension has profound implications on the breakage behaviour: the breakage of open clusters was seen to occur as a consequence of the detachment of single branches, which are then restructured, attaining a compact shape. Differently, compact clusters were seen to be less prone to breakage; they progressively deform during rotation and possibly break into a number of fragments. These different behaviours are a consequence of the different structural features of open and dense clusters such as connectivity and space filling properties. In fact, to observe fragmentation in open clusters a fewer number of bonds need to be broken; in addition, for the same mass, open clusters present a larger size, thus the total hydrodynamic force acting on them is larger compared to dense clusters. (Harshe, Lattuada, 2011). Furthermore, in open clusters shielding effects are negligible and, as pointed out in different works, the viscous stress can propagate along the filaments and eventually accumulate in some critical locations where the failure of one or more bonds can occur (Gastaldi, Vanni, 2011; Vanni, Gastaldi, 2011). Therefore, given the intrinsic complexity of the process, a mathematical expression of general validity which correlates $\dot{\gamma}_{cr}$ to the morphology, to the interparticle interactions and properties of the fluid is still missing.

Upon breakage a number of fragments (or daughter particles) are generated. Therefore, for a complete description of the breakup event a model for the distribution of mass over the newly generated particles is also needed. The mass of the individual fragments depends primarily on the stress distribution in the aggregate structure. A frequent assumption is that upon breakage two fragments are generated with a mass ratio that can vary in a broad range, spanning from a symmetric splitting (implying that two equally sized fragments are generated) to an erosion-like mechanism upon which single monomers or, more in general, small fragments are detached from the aggregate surface.

.

2.2 Overview of solution methods

The solution of PBE is generally a complicated task; as shown in the previous section, even when a mono variate population is considered, a complex integro-differential equation is obtained, whose analytical solution is possible only in a few idealized cases in which substantial simplifying assumptions are made. For this reason, a variety of methods has been developed in order to solve PBE in situations of practical interest. These methods can be classified on the basis of the adopted solution strategy: in Sectional Methods (SM) the internal coordinate is discretized into classes, whose number and size can vary according to the particular problem studied (Hounslow et al., 1988; Kumar, Ramkrishna, 1996a; Vanni, 2000). The Methods of Moments (MOM), first developed by Hulburt, Katz (1964), tackle the solution of PBE by solving the transport equation only for some moments of the number density functions, thereby reducing substantially the computational cost; however, the information they provide is generally limited to some integral properties of the suspension. Furthermore, their accuracy has to be assessed with other detailed solution methods (Buffo et al., 2013; Zucca et al., 2007). Finally, Monte Carlo methods are based on an *artificial realization* of the system behaviour that tracks the evolution of a certain number of particles, assumed to be statistically representative of the whole population (Liffman, 1992; Shah et al., 1977; Zhao et al., 2007). In the following, both the discrete approach of SM methods and the stochastic approach of MC are introduced.

2.2.1 Discrete formulation of PBE

The discretization approach is useful to approximate derivatives and integrals which typically appear in population balance and has been proven to be notably successful in a variety of applications. Restricting again the discussion to a mono variate aggregation-breakage process, the PBE can be written as (Ramkrishna, 2000):

$$\frac{\partial n\left(\xi,t\right)}{\partial t} = H\left[n,\xi,t\right] \tag{2.30}$$

where H is an operator counting for the source and sink terms of both aggregation and breakage processes:

$$
\begin{aligned}
H\left[n,\xi,t\right] = &\frac{1}{2}\int_0^\xi k^a\left(\xi',\xi-\xi'\right)n\left(\xi',t\right)n\left(\xi-\xi',t\right)d\xi' + \\
&- n\left(\xi,t\right)\int_0^\infty k^a\left(\xi,\xi'\right)n\left(\xi',t\right)d\xi' + \\
&+ \int_\xi^\infty \nu_f\left(\xi'\right)k^b\left(\xi',t\right)\Gamma\left(\xi|\xi',t\right)n\left(\xi',t\right)d\xi' + \\
&- k^b\left(\xi,t\right)n\left(\xi,t\right)
\end{aligned}
\tag{2.31}
$$

After discretization of the internal variable space in a number Q of intervals $I_i = [\xi_i, \xi_{i+1}[$, whose length can vary according to any scheme, the integration of Eq. (2.30)

over I_i leads to the equation:

$$\frac{d}{dt} \int_{\xi_i}^{\xi_{i+1}} n\left(\xi, t\right) d\xi = \int_{\xi_i}^{\xi_{i+1}} H\left[n, \xi, t\right] d\xi \qquad i = 0, 1, 2, ...Q \qquad (2.32)$$

which, indicating by $N_i\left(t\right) = \int_{\xi_i}^{\xi_{i+1}} n\left(\xi, t\right) d\xi$ the number concentration of particles of class i and restoring the full expression of the H operator, can be rewritten as:

$$\frac{dN_i}{dt} = \int_{\xi_i}^{\xi_{i+1}} d\xi \left[\frac{1}{2} \sum_{j=0}^{i-1} \int_{\xi_j}^{\xi_{j+1}} k^a\left(\xi - \xi', \xi'\right) n\left(\xi - \xi', t\right) n\left(\xi', t\right) d\xi' + \right.$$

$$- n\left(\xi, t\right) \sum_{j=0}^{Q} \int_{\xi_j}^{\xi_{j+1}} k^a\left(\xi - \xi', \xi'\right) n\left(\xi', t\right) d\xi' - k^b\left(\xi\right) n\left(\xi, t\right) + \qquad (2.33)$$

$$\left. + \sum_{j=1}^{Q} \int_{\xi_j}^{\xi_{j+1}} \nu_f\left(\xi'\right) k^b\left(\xi'\right) \Gamma\left(\xi|\xi'\right) n\left(\xi', t\right) d\xi' \right]$$

In Eq. (2.33) the integrals with respect to ξ' are expressed as the sum of $Q + 1$ integrals over subintervals. However, the resulting $Q + 1$ equations are unclosed in the variables N_i. Therefore, provided that the discretization is fine enough, in order to rewrite the above equations solely in terms of N_i, the mean value theorem can be used:

$$\int_{\xi_i}^{\xi_{i+1}} d\xi\left(\xi, \xi'\right) \int_{\xi_j}^{\xi_{j+1}} k^a d\xi' n\left(\xi'\right) n\left(\xi\right) \approx k^a\left(\xi_i, \xi_j\right) \int_{\xi_i}^{\xi_{i+1}} d\xi \int_{\xi_j}^{\xi_{j+1}} d\xi' n\left(\xi'\right) n\left(\xi\right)$$

$$= k^a\left(\xi_i, \xi_j\right) N_i N_j$$

$$(2.34)$$

Finally, by using the identity of Eq. (2.34) and adopting a fine linear grid ($x_i = ih$, with constant h), Eq. (2.33) transforms into:

$$\frac{dN_i}{dt} = \frac{1}{2} \sum_{j=0}^{i-1} N_j N_{i-j} k^a_{j, i-j} - N_i \sum_{j=0}^{Q} N_j k^a_{i,j} + \sum_{j=i}^{Q} \nu_j k^b_j \Gamma_{i|j} N_j - k^b_i N_i \qquad (2.35)$$

where for the sake of conciseness:

$$k^a_{i,j} = k^a\left(\xi_i, \xi_j\right), \quad \nu_j = \nu_f\left(\xi_j\right), \quad k^b_j = k^b\left(\xi_j\right), \quad \Gamma_{i|j} = \Gamma\left(\xi_i|\xi_j\right) \qquad (2.36)$$

Equation (2.35) is the well-known discrete population balance equation for an aggregation-breakage process. However, if the discretization is carried out adopting a very fine grid, for instance with the values N_i (with $i = 1, 2, 3, ...Q$) being the number concentrations of the aggregates made by a number i of monomers, the solution of Eq. (2.35) can be a demanding task in terms of computational resources. Let us consider for example the aggregation process that leads to the formation of a $10\,\mu m$ particle starting from $1\,\mu m$ sized primary particles; assuming the size of the aggregates $R \propto i^3$, a $10\,\mu m$ aggregate will be formed by 1000 monomers, meaning that a number

$Q = 1000$ of equations must be solved simultaneously in order to properly track the aggregation dynamics. This represents the main drawback of the discretized PBE. Therefore, approximate approaches have been developed such as geometric grid, in which the size spectrum is divided in intervals whose size increase according to a geometric progression (Batterham et al., 1981; Hill, Ng, 1995; Hounslow et al., 1988), arbitrarily divided grids (Vanni, 1999) or mixed grids where a combination of uniform, nonuniform and geometric partitions is used (Kumar, Ramkrishna, 1996a; Kumar, Ramkrishna, 1996b).

2.2.2 Monte Carlo method

Monte Carlo (MC) simulations reside in the realm of stochastic methods; they are used to obtain an *artificial realization* of the system behaviour. This is done by observing the individual behaviour of the particles in a reservoir as it develops in time. Clearly the number of particles in a real colloidal suspension can be extremely large and it is not feasible to observe each individual particle; therefore, a small sample of test particles is generally adopted and it is assumed that its behaviour is indicative of the behaviour of the system as a whole (Liffman, 1992).

The mathematical basis of MC rests on two basic informations:

- the initial condition of the system, in terms of number and properties of the particles,

- the probabilities or frequencies for each of the transformation taking place in the system, namely disappearance of existing particles and appearance of new particles for a colloidal suspension.

Therefore, on the basis of these information, a sample path of the process can be created by artificially generating random variables that satisfy the specified probability laws of change (Ramkrishna, 2000). By generating and averaging a number of such sample paths, the expected or mean behaviour of the system can be inferred.

The main advantage of MC methods is that the discretization of the internal space variable is not required. This results into a significantly reduced programming effort compared to deterministic methods and allows the inclusion of multiple mechanisms (aggregation, breakup, ...) in a straightforward manner. Furthermore MC methods represent practically the only feasible way to deal with complex multivariate PBE.

Monte Carlo methods classification   Broadly speaking, MC methods can be distinguished in two classes according to the approach used for the discretization of time (or more in general of the evolutionary coordinate). In time-driven simulations, an arbitrary time step is chosen and the simulation implements all possible events within that time interval. However its length can be varied throughout the simulation according to any law (Liffman, 1992). In event-driven simulations, first the time is advanced by an appropriate time-step, randomly sampled according to a probability distribution, and then one event is implemented. The main advantage of this latter technique is that the length of the time-step adjusts itself to the rates of the various

processes and no consistency checks are needed to verify the results of the simulation (Garcia et al., 1987; Shah et al., 1977). In this context, the time interval elapsing between two subsequent events is often referred to as *interval of quiescence*, *IQ* (Kendall, 1950).

Monte Carlo methods can be further classified according to the strategy used to adjust the number of simulated particles during the calculation (Zhao et al., 2007). In fact, if the simulation is started with N_p particles, after $N_p - 1$ aggregation events, all the particles will be included in one single aggregate. The most serious consequence of this phenomenon is the loss of accuracy, in that the reduced number of simulated particles undermines the statistical robustness of the obtained results. On the other hand, if, as a consequence of breakage phenomena, a proliferation of particles takes place in the simulated volume, the simulation has to be stopped if the storing capacity of the array containing the particle information is reached. To circumvent such problems two different approaches have been developed: in a constant-number MC simulation (Smith, Matsoukas, 1998), whenever a position in the particle array is vacated as a consequence of an aggregation event, an existing particle is randomly chosen and a copy of it is used to fill the vacancy. Conversely, when a breakage event takes place, a number of randomly chosen array positions are overwritten to accommodate the information relative to the newly generated fragments. Since all particles have the same probability to be chosen to fill the vacancy or to be overwritten, these operations on average leave the size distribution unaltered. Another approach consists in adjusting the number of particles periodically (Liffman, 1992): when the number of simulated particles falls below a threshold value large enough to prevent statistical fatigue, an exact copy of the simulated subsystem is added to itself preserving both solid fraction and particle size distribution. On the contrary, when breakage prevails over aggregation, the population is halved.

In Chapter 4, a detailed description of the Monte Carlo algorithm adopted for the present work is provided and tested against the Discrete PBE for a simple purely aggregating system.

References

Adler, P. M. 1981a. "Heterocoagulation in shear flow". *Journal of Colloid and Interface Science* 83. 106–115.

— 1981b. "Interaction of unequal spheres: I. Hydrodynamic interaction: Colloidal forces". *Journal of Colloid and Interface Science* 84. 461–473.

Alam, M. K. 1987. "The effect of van der Waals and viscous forces on aerosol coagulation". *Aerosol Science and Technology* 6. 41–52.

Arp, P. A., Mason, S. G. 1976. "Orthokinetic collisions of hard spheres in simple shear flow". *Canadian Journal of Chemistry* 54. 3769–3774.

Bäbler, M. U. 2008. "A collision efficiency model for flow-induced coagulation of fractal aggregates". *AIChE journal* 54. 1748–1760.

Batterham, R. J., Hall, J. S., Barton, G. (1981). "Pelletizing kinetics and simulation of full scale balling circuits". *Proceedings of the 3rd International Symposium on Agglomeration.* Vol. 136. Nurnberg W. Germany.

Buffo, A., Vanni, M., Marchisio, D., Fox, R. O. 2013. "Multivariate quadrature-based moments methods for turbulent polydisperse gas–liquid systems". *International Journal of Multiphase Flow* 50. 41–57.

Curtis, A. S. G., Hocking, L. M. 1970. "Collision efficiency of equal spherical particles in a shear flow. The influence of London-van der Waals forces". *Transactions of the Faraday Society* 66 1381–1390.

Elimelech, M., Gregory, J., Jia, X., Williams, R. A. (1995). *Particle deposition and aggregation: measurement, modelling and simulation.* 1st edition. Butterworth-Heinemann, Oxford (UK).

Friedlander, S. K. (1977). *Smoke, dust and haze: Fundamentals of aerosol behavior.* 1st edition. Wiley-Interscience, New York (NY).

Garcia, A. L., Van Den Broeck, C., Aertsens, M., Serneels, R. 1987. "A Monte Carlo simulation of coagulation". *Physica A: Statistical Mechanics and its Applications* 143. 535–546.

Gastaldi, A., Vanni, M. 2011. "The distribution of stresses in rigid fractal-like aggregates in a uniform flow field". *Journal of Colloid and Interface Science* 357. 18–30.

Harada, S., Tanaka, R., Nogami, H., Sawada, M. 2006. "Dependence of fragmentation behavior of colloidal aggregates on their fractal structure". *Journal of Colloid and Interface Science* 301. 123–129.

Harshe, Y. M., Lattuada, M. 2011. "Breakage rate of colloidal aggregates in shear flow through Stokesian dynamics". *Langmuir* 28. 283–292.

Hill, P. J., Ng, K. M. 1995. "New discretization procedure for the breakage equation". *AIChE Journal* 41. 1204–1216.

Hounslow, M., Ryall, R., Marshall, V. 1988. "A discretized population balance for nucleation, growth and aggregation". *AIChE Journal* 34. 1821–1832.

Hulburt, H. M., Katz, S. 1964. "Some problems in particle technology: A statistical mechanical formulation". *Chemical Engineering Science* 19. 555–574.

Kendall, D. G. 1950. "An artificial realization of a simple "birth-and-death" process". *Journal of the Royal Statistical Society. Series B* 12. 116–119.

Kerminen, V. M. 1994. "Simulation of Brownian coagulation in the presence of van der Waals forces and viscous interactions". *Aerosol Science and Technology* 20. 207–214.

Kumar, S., Ramkrishna, D. 1996a. "On the solution of population balance equations by discretization—I. A fixed pivot technique". *Chemical Engineering Science* 51. 1311–1332.

Kumar, S., Ramkrishna, D. 1996b. "On the solution of population balance equations by discretization—II. A moving pivot technique". *Chemical Engineering Science* 51. 1333–1342.

Kusters, K. A., Wijers, J. G., Thoenes, D. 1997. "Aggregation kinetics of small particles in agitated vessels". *Chemical Engineering Science* 52. 107–121.

Liffman, K. 1992. "A direct simulation Monte-Carlo method for cluster coagulation". *Journal of Computational Physics* 100. 116–127.

Ramkrishna, D. (2000). *Population balances: Theory and applications to particulate systems in engineering.* 1st edition. Academic press, San Diego (CA).

Shah, B., Ramkrishna, D., Borwanker, J. 1977. "Simulation of particulate systems using the concept of the interval of quiescence". *AIChE Journal* 23. 897–904.

Smith, M., Matsoukas, T. 1998. "Constant-number Monte Carlo simulation of population balances". *Chemical Engineering Science* 53. 1777–1786.

Smoluchowski, M. V. 1917. "Versuch einer mathematischen Theorie der Koagulationskinetik kolloider Lösungen". *Zeitschrift für physikalische Chemie* 92. 129–168.

Spielman, L. A. 1970. "Viscous interactions in Brownian coagulation". *Journal of Colloid and Interface Science* 33. 562–571.

Van de Ven, T. G. M., Mason, S. G. 1976. "The microrheology of colloidal dispersions: IV. Pairs of interacting spheres in shear flow". *Journal of Colloid and Interface Science* 57. 505–516.

— 1977. "The microrheology of colloidal dispersions VII. Orthokinetic doublet formation of spheres". *Colloid & Polymer Science* 255. 468–479.

Vanni, M. 1999. "Discretization procedure for the breakage equation". *AIChE journal* 45. 916–919.

— 2000. "Approximate population balance equations for aggregation–breakage processes". *Journal of Colloid and Interface Science* 221. 143–160.

Vanni, M., Baldi, G. 2002. "Coagulation efficiency of colloidal particles in shear flow". *Advances in Colloid and Interface Science* 97. 151–177.

Vanni, M., Gastaldi, A. 2011. "Hydrodynamic forces and critical stresses in low-density aggregates under shear flow". *Langmuir* 27. 12822–12833.

Zhao, H., Maisels, A., Matsoukas, T., Zheng, C. 2007. "Analysis of four Monte Carlo methods for the solution of population balances in dispersed systems". *Powder Technology* 173. 38–50.

Zucca, A., Marchisio, D. L., Vanni, M., Barresi, A. A. 2007. "Validation of bivariate DQMOM for nanoparticle processes simulation". *AIChE Journal* 53. 918–931.

Chapter 3

Discrete Element Method

A Discrete Element Method (DEM) is a numerical method able to investigate dynamically the behaviour of a sample of particles. By modelling all the relevant forces acting on them, a DEM is able to track the motion of each particle giving profound insights into the system dynamics.

In the case of colloidal suspensions, a DEM has to model both hydrodynamic and colloidal interactions between particles; since colloidal particles, because of their small size, have negligible inertia, these interactions balance each other exactly at any time so that for each particle a simple force/torque balance of the following kind can be written:

$$\begin{cases} \mathbf{F}^H = -\mathbf{F}^{coll} \\ \mathbf{T}^H = -\mathbf{T}^{coll} \end{cases} \tag{3.1}$$

where the superscripts H and *coll* indicate hydrodynamic and colloidal interactions, respectively. To model hydrodynamic forces and torques one needs in principle to solve the Navier-Stokes equation, imposing the proper boundary conditions at the surface of every particle. However, for most of the cases of interest, the particle Reynolds number is generally very small, so that the Stokes equation can be used instead. Even though by such an assumption the complexity of the problem reduces significantly, a huge amount of computational resources is still needed especially when a dynamic simulation is performed. This inconvenience restricts the applicability of this approach to very small samples of particles (Schlauch et al., 2013).

To circumvent this problem, a number of works employed the so-called *free draining approximation*, FDA. Without explicitly solving the Stokes equation, the FDA simply assumes that each suspended particle experiences the hydrodynamic stresses as if it is isolated and not interacting with the nearby elements (Becker et al., 2009; Eggersdorfer et al., 2010). However, this assumption breaks down and surely overestimates drag forces when considering dense suspensions or, more in general, when particles come in close proximity or aggregate. Therefore, alternative approaches were developed to take into account such screening phenomena; Higashitani, Iimura (1998), for instance, by simple geometric considerations, succeeded in computing the

actual portion of the particle surface directly exposed to the flow and in evaluating accordingly the hydrodynamic stresses acting on the particles.

A more rigorous approach named Stokesian Dynamics (SD) was developed by Brady, Bossis ([1988](#)), using a truncated multipole expansion of the rigorous solution of the Stokes equation for the far-field interactions and results from the lubrication theory for the near-contact forces. This approach is capable of modelling accurately hydrodynamic interactions at a reasonable computational cost. For this reason, it has been adopted in this work and coupled with models for colloidal interactions.

Colloidal interactions among particles can be distinguished in pre-contact interactions and post-contact interactions. The former are generally introduced in DEM simulations according to the DLVO theory, taking into account both Van der Waals and electrical double layer interactions.

The post-contact interactions are generally introduced on the basis of the theory of contact mechanics. The most accepted framework in this context is the JKR theory by Johnson, Kendall and Roberts, which allows to model the post-contact response accounting for both adhesion and elastic properties of the particle (Johnson et al., [1971](#)). However, recently it has been shown by Pantina, Furst ([2005](#)) that primary particles upon contact interact also by means of tangential interaction i.e., forces that provide a resistance to the relative displacement along the contact plane, resulting in a certain sliding, rolling and twisting resistance. These effects have been included in the developed DEM by implementing the spring-like force model proposed by Becker, Briesen ([2008](#)).

In this chapter an overall description of the developed Discrete Element Method is provided. A great deal of attention will be given to the modelling of the hydrodynamic interactions between particles as well as to the modelling of colloidal interactions. Regarding the former point, the discussion will start from the analysis of the equations governing the Stokes flow regime, to move afterwards to the behaviour of a single particle suspended in a Stokes flow. Finally, the multi-particle hydrodynamics, particularly relevant for the modelling of colloidal suspensions, will be revisited in great detail with a special focus on the adopted Stokesian Dynamics technique, which represents the core of the developed DEM. The modelling of the colloidal interactions between particles will include both the pre-contact and the post-contact interactions; the DLVO theory and a model to count for tangential interactions will be analysed and their coupling with SD thoroughly explained.

3.1 Hydrodynamic interaction

The momentum transport in a fluid is described by the well-known Navier-Stokes equations which, for an incompressible fluid, reads in the dimensionless form as:

$$\nabla^* \cdot \mathbf{u}^* = 0$$
$$Re \left(\frac{\partial \mathbf{u}^*}{\partial t^*} + \mathbf{u}^* \cdot \nabla^* \mathbf{u}^* \right) = -\nabla^* p^* + \nabla^{*2} \mathbf{u}^* \tag{3.2}$$

where

$$\nabla^* = L\nabla, \quad \mathbf{u}^* = \frac{\mathbf{u}}{U}, \quad p^* = \frac{pL}{\mu U}, \quad t^* = \frac{t}{L/U}, \quad Re = \frac{\rho_l U L}{\mu} \tag{3.3}$$

and where L and U represent respectively a characteristic length and velocity of the flow field, whereas μ and ρ_l are the dynamic viscosity and density of the fluid. It is clear from the analysis of Eq. (3.2) that the Reynolds number Re can be regarded as a measure of the relative importance of the viscous effects compared to the inertial effects. If we suppose that a spherical particle with radius a moves with a velocity U in a fluid, then the Reynolds number at the particle scale is:

$$Re = \frac{\rho_l U a}{\mu} \tag{3.4}$$

Recalling that in colloidal suspension, particle radii are in the micrometer scale and that, as a result of the smallness of particles, the velocity scale is generally small as well, the Reynolds number assumes values well below 1 in most of the application of practical interest. As a consequence, the l.h.s. term in Eq. (3.2) can be safely neglected. Doing so, the Stokes equation is obtained, which in dimensional form, reads as:

$$\nabla \cdot \mathbf{u} = 0 \tag{3.5}$$
$$0 = -\nabla p + \mu \nabla^2 \mathbf{u} \tag{3.6}$$

Equations (3.5) and (3.6) are the equations governing the so-called Stokes flow regime.

3.1.1 Stokes flow

The Stokes equations present some interesting properties worth to analyse, since they are useful to simplify substantially the study of suspension dynamics, allowing to derive results about a flow without solving it fully.

1. Linearity

By looking at Eq. (3.6) it is apparent that both the nonlinear convective term and the time dependent term have been dropped out from the full Navier Stokes equation. This implies that the Stokes equation is linear in the velocity $\mathbf{u}$. An important direct mathematical consequence of the linearity is that the principle of superposition of solutions can be applied; this means that adding different solutions of the Stokes equations, a solution of the Stokes equations is still obtained; for instance, considering the case of a particle sedimenting and, at the same time, rotating about its center of mass, the flow field in the surrounding medium can be obtained determining the flow field caused by settling (without rotation) and adding to this the flow due to the rotation (without settling).

2. Reversibility

Another consequence of the linearity is that the Stokes equations are reversible. In mathematical terms this means that if $\{\mathbf{u}, p\}$ is a solution of the equation, $\{-\mathbf{u}, -p\}$

will be a solution as well. This implies that a time-reversed Stokes flow solves the same equations as the original Stokes flow.

3. Instantaneity

As apparent the Stokes equations lack of an explicit dependence on time; therefore, there is no history dependence of the fluid motion and, as a consequence, the flow is determined exclusively by the actual configuration imposed by the boundary conditions, due for example to the suspended particles. This means that the information coming from the boundary conditions are propagated instantaneously to the entire fluid and the solution will depend on time only if the boundary conditions change in time.

For other properties of the Stokes equation, interested readers are referred to the specialized literature. (Guazzelli, Morris, 2011; Kim, Karrila, 1991)

3.1.2 Single particle hydrodynamics

The study of colloidal suspensions is a multi-particle problem in that it has to deal with the interaction of a large number of particles. However, before addressing the hydrodynamics of a multitude of particles, it is useful to start from the analysis of the behaviour of a single, isolated particle in some simple flow configurations. In particular we are concerned here with the disturbance in the flow field induced by a particle and with the hydrodynamic stresses acting on it. However, before discussing on these cases, some preliminary considerations are worthwhile to be presented here since they will ease the solution of the Stokes equation in some relevant cases; by taking the divergence of both terms of Eq. (3.6) and imposing the continuity condition of Eq. (3.5) one obtains:

$$\nabla \cdot (\nabla p) = \nabla \cdot \left(\mu \nabla^2 \mathbf{u} \right) = \mu \nabla^2 \left(\nabla \cdot \mathbf{u} \right) \rightarrow \nabla^2 p = 0 \tag{3.7}$$

meaning that the pressure field in the liquid is independent of the velocity field and can be calculated autonomously once that the boundary conditions are known. Furthermore, taking the Laplacian of both sides of Eq. (3.6) and using the result of Eq. (3.7) one obtains:

$$\nabla^2 \left(\nabla p \right) = \nabla^2 \left(\mu \nabla^2 \mathbf{u} \right) \rightarrow \nabla \cdot \left(\nabla^2 p \right) = \mu \nabla^4 \mathbf{u} \rightarrow \nabla^4 \mathbf{u} = 0 \tag{3.8}$$

which means that the velocity field is in turn independent of the pressure field.

The flow field in any position identified by the position vector $\mathbf{x}$ can be described by a Taylor expansion, centred in a generic point $\mathbf{x}_0$, as $\mathbf{u}^\infty \left(\mathbf{x} \right) = \mathbf{u}^\infty \left(\mathbf{x}_0 \right) + \nabla \mathbf{u}^\infty \left(\mathbf{x}_0 \right) \cdot \left(\mathbf{x} - \mathbf{x}_0 \right) + ...$. Therefore, neglecting the higher order terms and provided that $\left(\mathbf{x} - \mathbf{x}_0 \right)$ is appropriately small, the velocity field can be seen in any point as the superposition of a uniform translation and a linearly varying velocity. If we assume the reference system to be centred in $\mathbf{x}_0$ and $\mathbf{u}^\infty \left(\mathbf{x}_0 \right) = \mathbf{u}^\infty$, the velocity field may be further decomposed as:

$$\mathbf{u}_\infty \left(\mathbf{x} \right) = \mathbf{u}^\infty + \boldsymbol{\Omega}^\infty \cdot \mathbf{x} + \boldsymbol{E}^\infty \cdot \mathbf{x} \tag{3.9}$$
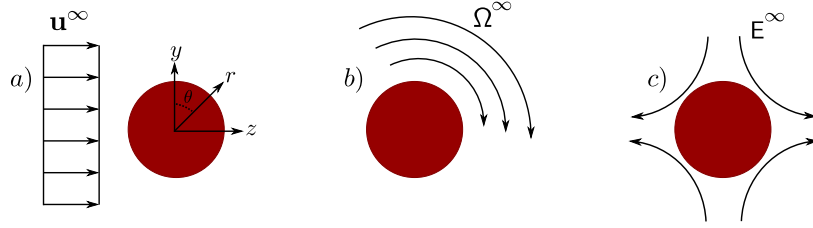
Figure 3.1: a) Particle immersed in a uniform flow field moving with velocity $\mathbf{u}_\infty$. b) Particle in a pure rotating flow field with a rate-of-rotation $\boldsymbol{\Omega}_\infty$. c) Particle in a pure straining flow field with a rate-of-strain $\boldsymbol{E}_\infty$.

where $\boldsymbol{\Omega}^\infty$ and $\boldsymbol{E}^\infty$ are the rate-of-rotation and the rate-of-strain tensors, respectively, whose components in index notation are equal to:

$$\Omega_{ij}^\infty = \frac{1}{2}\left[\frac{\partial u_i}{\partial x_j} - \frac{\partial u_j}{\partial x_i}\right], \qquad E_{ij}^\infty = \frac{1}{2}\left[\frac{\partial u_i}{\partial x_j} + \frac{\partial u_j}{\partial x_i}\right] \tag{3.10}$$

where, for the sake of conciseness, the ∞ superscript has been omitted in the component definition. The rate-of-rotation tensor $\boldsymbol{\Omega}^\infty$ is antisymmetric; therefore its three independent components may be used to form the angular velocity pseudo-vector $\boldsymbol{\omega}^\infty$ related to $\boldsymbol{\Omega}^\infty$ according to:

$$\omega_i = -\frac{1}{2}\epsilon_{ijk}\Omega_{jk} \tag{3.11}$$

where ϵ_{ijk} is the Levi-Civita tensor.

The rate-of-strain tensor is traceless (as a consequence of continuity) and symmetric, thus it can be conveniently reduced to a 5-elements vector $\mathbf{e}^\infty$. As it will be clear later, the proper way of selecting the elements is the following one:

$$\mathbf{e}^\infty = (E_{xx} - E_{zz}, 2E_{xy}, 2E_{xz}, 2E_{yz}, E_{yy} - E_{zz}) \tag{3.12}$$

Due to the linearity of the Stokes equations, the response of a spherical particle to the general fluid flow given by Eq. (3.9) can be obtained by the superposition of the responses to a uniform flow ($\mathbf{u}^\infty$), rotational flow ($\boldsymbol{\Omega}^\infty \cdot \mathbf{x}$) and straining flow ($\boldsymbol{E}^\infty \cdot \mathbf{x}$). Therefore, in the following, each of these single flows will be examined in more detail.

Spherical particle in a uniform flow field

Let us consider a fixed spherical particle of radius a held fixed in a uniform flow field moving with velocity $\mathbf{u}^\infty$ (Fig. 3.1a). In a 3D spherical reference system (r, θ, ϕ), after imposing that the no-slip velocity boundary condition holds at the particle surface and that at sufficiently large distance from the particle, the velocity field and the pressure field recover the velocity $\mathbf{u}^\infty$ and the pressure p^∞ respectively, the

velocity and pressure field are given by (Bird et al., 2002):

$$u_r = u^\infty \left(1 - \frac{3}{2}\frac{a}{r} + \frac{1}{2}\frac{a^3}{r^3} \right) \cos\theta, \tag{3.13}$$

$$u_\theta = u^\infty \left(-1 + \frac{3}{4}\frac{a}{r} + \frac{1}{4}\frac{a^3}{r^3} \right) \sin\theta, \tag{3.14}$$

$$p = p^\infty - \frac{3\mu u^\infty}{2a}\frac{a^2}{r^2}\cos\theta. \tag{3.15}$$

equivalent in index notation to:

$$u_i = -\frac{3}{4}au_j^\infty \left(\frac{\delta_{ij}}{r} + \frac{x_i x_j}{r^3} \right) - \frac{3}{4}a^3 u_j^\infty \left(\frac{\delta_{ij}}{3r^3} - \frac{x_i x_j}{r^5} \right) \tag{3.16}$$

$$p = p_\infty = -\frac{3\mu a}{2}\frac{u_j^\infty x_j}{r^3} \tag{3.17}$$

where $r = |\mathbf{x}|$ and δ_{ij} is the Kronecker delta function. It is apparent that the disturbance induced by the particle decays very slowly: as r^{-1} for the dominant part of velocity field and as r^{-2} for the pressure field. This result is of paramount importance when studying the hydrodynamics of a multitude of particles, meaning that the flow field experienced by each particle is affected by the presence of other particles even when relatively far apart.

To conclude the discussion it is worthwhile to compute the hydrodynamic force acting on the particle; it can be evaluated by integrating the stress tensor $\boldsymbol{\sigma}$ over the particle surface as:

$$\mathbf{F}^H = \int_{S_\alpha} (\boldsymbol{\sigma} \cdot \mathbf{n}) \, dS \tag{3.18}$$

where the stress tensor is $\boldsymbol{\sigma} = -p\boldsymbol{\delta} + \mu \left(\nabla\mathbf{u} + \nabla\mathbf{u}^T \right)$. A simple interpretation of Eq. (3.18) is that the hydrodynamic force is a sum of infinitesimal forces $(\boldsymbol{\sigma} \cdot \mathbf{n}) \, dS$, where $\boldsymbol{\sigma} \cdot \mathbf{n}$ is the traction vector. The integral of Eq. (3.18) leads to the well-known Stokes drag force:

$$\mathbf{F}^H = 6\pi\mu a \mathbf{u}^\infty \tag{3.19}$$

The Stokes drag force is given by the sum of two distinct contributes, comparable in magnitude: the first is due solely to the pressure component of the stress and equals $2\pi\mu a\mathbf{u}^\infty$ (*form drag*), whereas the second is due to the viscous tangential stress acting on the particle surface (*friction drag*) and is equal to $4\pi\mu a\mathbf{u}^\infty$. The result of Eq. (3.19) can be easily extended to the case of a particle translating with velocity $\mathbf{u}^\alpha$ in a fluid moving with uniform velocity $\mathbf{u}^\infty$. It suffices to solve the problem in a reference frame moving with the particle and then bring back the solution to a fixed reference frame. The Stokes drag in this case would be given by:

$$\mathbf{F}^H = 6\pi\mu a \left(\mathbf{u}^\infty - \mathbf{u}^\alpha \right) \tag{3.20}$$

and, as apparent, it scales linearly with the relative velocity between particle and fluid. It is worth to point out that this procedure is made possible by the lack of inertia of Stokes flow, that allows to change the system reference frame without giving rise to any additional fictitious force.

Spherical particle in rotating flow field

Let us assume to have a spherical particle of radius a fixed in the center of the reference system and immersed in fluid flow rotating with velocity $\boldsymbol{\omega}_\infty$ (Fig. 3.1b). After imposing that:

$$
\begin{cases}
\mathbf{u} = 0 & \text{for} \quad r = |\mathbf{x}| = a \\
\mathbf{u} = \boldsymbol{\omega}^\infty \times \mathbf{x} = \mathbf{u}^\infty & \text{for} \quad r = |\mathbf{x}| \to \infty \\
p = p^\infty & \text{for} \quad r = |\mathbf{x}| \to \infty
\end{cases}
\tag{3.21}
$$

the solution of the Stokes equation for the velocity and pressure field reads as (Guazzelli, Morris, 2011):

$$
\begin{cases}
\mathbf{u}\left(\mathbf{x}\right) = \boldsymbol{\omega}^\infty \times \mathbf{x} \left[1 - \left(\dfrac{a}{r}\right)^3\right] \\
p\left(\mathbf{x}\right) = p^\infty
\end{cases}
\tag{3.22}
$$

where $\boldsymbol{\omega}^\infty$ and p^∞ are the undisturbed angular velocity and pressure. It can be noticed that the pressure field is not affected by the presence of the particle, while the disturbance on the velocity field decays as r^{-2}. As done in the previous case, it is possible to calculate the stress acting on the particle. Given the symmetry of the problem, it can be reasonably expected that the net force is zero. On the contrary, a net torque acts on the particle:

$$
\mathbf{T}^H = \int_{S_\alpha} \mathbf{x} \times \left(\boldsymbol{\sigma} \cdot \mathbf{n}\right) dS.
\tag{3.23}
$$

Equation (3.23) can be seen as the sum of the infinitesimal torques $\mathbf{x} \times \left(\boldsymbol{\sigma} \cdot \mathbf{n}\right) dS$, where $\mathbf{x}$ is the local level arm (of length a) relative to the infinitesimal force element $\left(\boldsymbol{\sigma} \cdot \mathbf{n}\right) dS$. The integration of Eq. (3.23) leads to:

$$
\mathbf{T}^H = 8\pi\mu a^3 \boldsymbol{\omega}^\infty.
\tag{3.24}
$$

As done before, if the particle rotates with velocity $\boldsymbol{\omega}^\alpha$ in a flow field rotating with angular velocity $\boldsymbol{\omega}^\infty$ the torque reads as:

$$
\mathbf{T}^H = 8\pi\mu a^3 \left(\boldsymbol{\omega}^\infty - \boldsymbol{\omega}^\alpha\right)
\tag{3.25}
$$

again linearly proportional to the relative angular velocity between particle and fluid.

Spherical particle in straining flow

The third basic case is that of a particle held fixed in a pure straining flow (Fig. 3.1c). Imposing the following boundary conditions:

$$
\begin{cases}
\mathbf{u} = 0 & \text{for} \quad r = |\mathbf{x}| = a \\
\mathbf{u} = \mathbf{E}^\infty \cdot \mathbf{x} = \mathbf{u}^\infty & \text{for} \quad \mathbf{x} \to \infty \\
p = p^\infty & \text{for} \quad \mathbf{x} \to \infty
\end{cases}
\tag{3.26}
$$

the velocity and pressure fields in index notation are given by (Guazzelli, Morris, 2011):

$$
\begin{cases}
u_i\left(\mathbf{x}\right) = u_i^\infty\left(\mathbf{x}\right) - \dfrac{5a^3}{2}\dfrac{x_i\left(x_j E_{jk}^\infty x_k\right)}{r^5} - \dfrac{a^5}{2}E_{jk}^\infty\left[\dfrac{\delta_{ij}x_k + \delta_{ik}x_j}{r^5} - \dfrac{5x_i x_j x_k}{r^7}\right] \\
p\left(\mathbf{x}\right) = p^\infty\left(\mathbf{x}\right) - 5\mu a^3\dfrac{x_i E_{ij}^\infty x_j}{r^5}
\end{cases}
\tag{3.27}
$$

In a straining flow field neither a net torque nor a net force acts on the particle; however, hydrodynamic stresses will act on its surface. In this regard, it is useful to define the stresslet S_{ij}. The stresslet is a symmetric traceless tensor of size 3×3 which corresponds to the symmetric portion of the first moment of the hydrodynamic force and, as such, is intimately related to the hydrodynamic torque. In fact, the first moment M_{ij} can be computed as:

$$
M_{ij} = \int_S x_i \sigma_{jk} n_k dS = \int_S \frac{1}{2}\left(x_j \sigma_{ik} + x_i \sigma_{jk}\right)n_k dS + \int_S \frac{1}{2}\left(x_i \sigma_{jk} - x_j \sigma_{ik}\right)n_k dS
\tag{3.28}
$$

and split as:

$$
\begin{cases}
S_{ij} = \frac{1}{2}\int_S \left(x_j \sigma_{ik} + x_i \sigma_{jk}\right)n_k dS \\[2mm]
A_{ij} = \frac{1}{2}\int_S \left(x_i \sigma_{jk} - x_j \sigma_{ik}\right)n_k dS
\end{cases}
\tag{3.29}
$$

where the tensor A_{ij} is the antisymmetric part of M_{ij} and contains the same information of the hydrodynamic torque $\mathbf{T}^H$, to which is related as $A_{ij} = -\frac{1}{2}\epsilon_{ijk}T_k$, whereas the symmetric component S_{ij} is the stresslet tensor. By integrating Eq. (3.29) over the particle surface one obtains:

$$
S_{ij} = \frac{20}{3}\pi\mu a^3 E_{ij}^\infty
\tag{3.30}
$$

As E_{ij}^∞, the stresslet tensor is symmetric and traceless. Therefore it can be reduced to a 5-elements vector:

$$
\mathbf{s} = \left(S_{xx}, S_{xy}, S_{xz}, S_{yz}, S_{yy}\right)
\tag{3.31}
$$

The stresslet has an important role in studying colloidal suspension rheology: physically it can be interpreted as the result of the resistance of the rigid particles to the straining components of the flow and as such it provides a measure of the additional
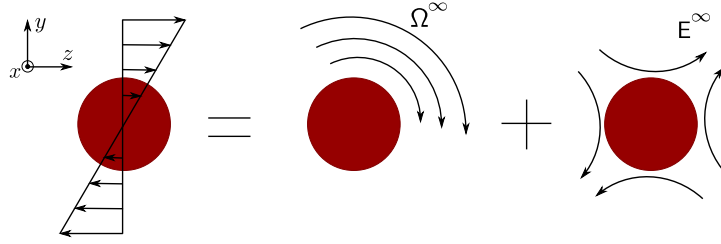
Figure 3.2: Decomposition of a shear flow field as the sum of a pure rotating and pure straining flow field.

stress associated with the presence of the suspended particles. This implies that an increase in the rate of viscous dissipation of mechanical energy should be expected when dispersing particles in a medium, meaning ultimately that a suspension of rigid particles has an effective viscosity larger than that of the pure medium.

Freely moving particle in shear flow

To conclude the discussion about the single particle hydrodynamics it is worthwhile to analyse the case of a freely moving particle in a linearly varying flow field. This case can be considered to be the most representative for a stirred colloidal suspension, where suspended particles are moved by the imposed flow field. In particular we are concerned here with a spherical particle in a shear flow field of the form $\mathbf{u}^\infty = (0, 0, \dot{\gamma} y)$ as represented in Fig. 3.2. In order to make use of the previous results, it is useful to decompose the shear flow field as the superposition of a pure rotating and a pure straining motion according to:

$$\mathbf{u}^\infty(\mathbf{x}) = \boldsymbol{\Omega}^\infty \cdot \mathbf{x} + \boldsymbol{E}^\infty \cdot \mathbf{x} \tag{3.32}$$

where $\boldsymbol{\Omega}^\infty$ and $\boldsymbol{E}^\infty$, for the particular case of Fig. 3.2, are equal to:

$$\boldsymbol{\Omega}^\infty = \frac{1}{2} \begin{bmatrix} 0 & 0 & 0 \\ 0 & 0 & -\dot{\gamma} \\ 0 & \dot{\gamma} & 0 \end{bmatrix} \qquad \boldsymbol{E}^\infty = \frac{1}{2} \begin{bmatrix} 0 & 0 & 0 \\ 0 & 0 & \dot{\gamma} \\ 0 & \dot{\gamma} & 0 \end{bmatrix} \tag{3.33}$$

The particle, in such conditions, undergoes a rigid body motion that matches the ambient velocity and vorticity in its center of mass, so that, as can be deduced from Eq. (3.20) and Eq. (3.25), $\mathbf{F}^H = 0$ and $\mathbf{T}^H = 0$. However, given its rigidity, the particle is not able to relieve the local straining motion in the fluid; thus the particle will produce a disturbance on the imposed flow field which is again given by Eq. (3.27).

Matrix formulation of the mobility problem

Many physical problems in suspension dynamics, rather than the disturbed flow field, require the knowledge of the motion of the suspended particle in response to an applied external force or torque in a known imposed flow field. Such problems are generally referred to as *mobility* problems; since inertia plays a negligible role on the microscale of colloidal particles, the hydrodynamic force/torque balances the applied forces/torque, so that it is possible to write:

$$\begin{cases} \mathbf{F}^H = -\mathbf{F}^{ext} \\ \mathbf{T}^H = -\mathbf{T}^{ext} \end{cases} \tag{3.34}$$

Furthermore, given that $\mathbf{F}^H$ and $\mathbf{T}^H$ scale linearly with the relative particle velocity with regard to the surrounding flow field, it follows that the problem of determining translational and angular velocity of the particle can be conveniently formulated in terms of a system of linear equations of the following kind:

$$\begin{bmatrix}
a' & 0 & 0 & 0 & 0 & 0 & 0 & 0 & 0 & 0 & 0 \\
0 & a' & 0 & 0 & 0 & 0 & 0 & 0 & 0 & 0 & 0 \\
0 & 0 & a' & 0 & 0 & 0 & 0 & 0 & 0 & 0 & 0 \\
0 & 0 & 0 & b' & 0 & 0 & 0 & 0 & 0 & 0 & 0 \\
0 & 0 & 0 & 0 & b' & 0 & 0 & 0 & 0 & 0 & 0 \\
0 & 0 & 0 & 0 & 0 & b' & 0 & 0 & 0 & 0 & 0 \\
0 & 0 & 0 & 0 & 0 & 0 & 2c' & 0 & 0 & 0 & c' \\
0 & 0 & 0 & 0 & 0 & 0 & 0 & 2c' & 0 & 0 & 0 \\
0 & 0 & 0 & 0 & 0 & 0 & 0 & 0 & 2c' & 0 & 0 \\
0 & 0 & 0 & 0 & 0 & 0 & 0 & 0 & 0 & 2c' & 0 \\
0 & 0 & 0 & 0 & 0 & 0 & c' & 0 & 0 & 0 & 2c'
\end{bmatrix}
\begin{Bmatrix}
F_x^{ext} \\ F_y^{ext} \\ F_z^{ext} \\ T_x^{ext} \\ T_y^{ext} \\ T_z^{ext} \\ S_{xx} \\ S_{xy} \\ S_{xz} \\ S_{yz} \\ S_{yy}
\end{Bmatrix}
=
\begin{Bmatrix}
u^\infty(x^\alpha) - u_x^\alpha \\
u^\infty(y^\alpha) - u_y^\alpha \\
u^\infty(z^\alpha) - u_z^\alpha \\
\omega_x^\infty - \omega_x^\alpha \\
\omega_y^\infty - \omega_y^\alpha \\
\omega_z^\infty - \omega_z^\alpha \\
E_{xx}^\infty - E_{zz}^\infty \\
2E_{xy}^\infty \\
2E_{xz}^\infty \\
2E_{yz}^\infty \\
E_{yy}^\infty - E_{zz}^\infty
\end{Bmatrix}
\tag{3.35}$$

where

$$a' = \frac{1}{6\pi\mu a}, \quad b' = \frac{1}{8\pi\mu a^3}, \quad c' = \frac{3}{20\pi\mu a^3}$$

In Eq. (3.35) the ambient linear velocity $\mathbf{u}^\infty$ is evaluated in the position occupied by the particle α, whereas the angular velocity is constant and independent of the position. Furthermore it is worth to point out that both the tensors $\boldsymbol{S}$ and $\boldsymbol{E}$, taking advantage of their symmetry, have been reduced to 5-elements vector. As a result the coefficient matrix, referred to as *mobility* matrix has dimension 11×11. This method can be straightforwardly extended to the case of a number n_p of spherical particles, leading to a system of $11n_p$ independent equations. This approach, commonly defined as *free draining approximation*, implicitly assumes that the n_p particles do not interact hydrodynamically with each other; this is clearly a major simplification of the problem in that, as it has been shown, the leading portion of the hydrodynamic interaction decays quite slow with the distance (as r^{-1}), therefore care must be taken when applying this approach even to very dilute suspensions.

3.1.3 Multi-particle hydrodynamics - Stokesian Dynamics

When considering colloidal suspensions many-body hydrodynamic interactions become important. The expression of the force, torque and stresslet reported previously are correct for the case of a single, isolated particle, but they lose their validity when other particles are present in the suspension. In such a case, in fact, the flow field that each particle experiences is different from the imposed one in that it is affected by the presence of the other particles. Therefore, for a rigorous evaluation of hydrodynamic interactions it is necessary to quantify this mutual disturbance. In this context, Stokesian Dynamics (SD) is the most well-established technique, since it is able to properly count for both the long-ranged and short-ranged hydrodynamic interactions for any configuration of a finite number of spherical particles.

Defining the flow field disturbance as $u_i'(\mathbf{x}) = u_i(\mathbf{x}) - u_i^\infty(\mathbf{x})$, i.e., as the difference between the disturbed flow field $u_i(\mathbf{x})$ and the one we would have if no particle is suspended $u_i^\infty(\mathbf{x})$, it is possible to use to the Faxén laws to evaluate force, torque and stresslet acting on each suspended particle α of radius a as (Batchelor, Green, 1972):

$$F_i^\alpha = 6\pi\mu a \left[- \left(1 + \frac{a^2}{6}\nabla^2 \right) u_i'\left(\mathbf{x}^\alpha\right) + \left(u_i^\alpha - u_i^\infty(\mathbf{x}^\alpha) \right) \right]$$

$$T_i^\alpha = 8\pi\mu a^3 \left[-\frac{1}{2}\epsilon_{ijk}\nabla_j u_k'(\mathbf{x}^\alpha) + \left(\omega_i^\alpha - \omega_i^\infty(\mathbf{x}^\alpha) \right) \right] \tag{3.36}$$

$$S_{ij}^\alpha = \frac{20}{3}\pi\mu a^3 \left[- \left(1 + \frac{a^2}{10}\nabla^2 \right) E_{ij}'(\mathbf{x}^\alpha) + \left(-E_{ij}^\infty \right) \right]$$

It is apparent that the Faxén laws are similar to the expression drawn for the force, torque and stresslet acting on a single particle, except for an additional term counting for the disturbance; the term $u_i'(\mathbf{x}_\alpha)$ represents in fact the disturbance induced by all the particles other than α in the position occupied by the α particle itself. Similarly $E_{ij}'(\mathbf{x}^\alpha)$ is the disturbed rate-of-strain evaluated in $\mathbf{x}_\alpha$.

However, the equations reported in Eq. (3.36) are not closed; a model for the disturbed flow field is still needed. The fundamental object for such a task is the point-force solution of the Stokes equation, frequently referred to as *Stokeslet*. It is possible to obtain the Stokeslet in a rather simple way by using the velocity field solution for the case of a particle fixed in a uniform flow field (Eq. 3.16) and by expressing it in terms of the drag force of Eq. (3.19). Doing so the flow field reads as:

$$u_i = \left(\frac{\delta_{ij}}{r} + \frac{x_i x_j}{r^3} \right) \cdot \frac{F_i^H}{8\pi\mu} + \left(\frac{\delta_{ij}}{3r^2} - \frac{x_i x_j}{r^5} \right) \cdot \frac{a^2 F_i^H}{8\pi\mu} \tag{3.37}$$

which, keeping fixed the magnitude of the drag force, in the limit of vanishing particle radius $a \to 0$, allows to get the point force solution (or stokeslet) of the Stokes flow:

$$u_i^{PF} = \left(\frac{\delta_{ij}}{r} + \frac{x_i x_j}{r^3} \right) \cdot \frac{F_i^H}{8\pi\mu} = J_{ij} \cdot \frac{F_i^H}{8\pi\mu} \tag{3.38}$$

where the second-rank tensor J_{ij}, also known as stokeslet propagator or Oseen tensor, has been used to get a more compact notation. In a similar fashion, it is also possible to obtain the solution for a point-torque and point-stresslet:

$$u_i^{PT} = \frac{1}{8\pi\mu}\frac{\epsilon_{ijk}T_j^H r_k}{r^3} = R_{ij}\frac{T_j^H}{8\pi\mu} \qquad u_i^{PS} = -\frac{3x_i x_j x_k}{r^5}\frac{S_{jk}}{8\pi\mu} = K_{ijk}\frac{S_{jk}}{8\pi\mu} \qquad (3.39)$$

These expressions are useful to construct the solution of the Stokes flow for a certain distribution of forces as a superposition of the flow fields generated independently by each of the forces. Let us assume to have n_p suspended particles and a distribution of forces acting on the fluid and due to such particles equal to $f_j = \sigma_{jk}n_k$, where σ_{jk} is the stress tensor and n_k a vector locally normal to the surface of the particle and pointing into the fluid; the flow field in any point of the suspension may therefore be expressed as (Kim, Karrila, 1991):

$$u_i(\mathbf{x}) = u_i^\infty(\mathbf{x}) - \frac{1}{8\pi\mu}\sum_{\alpha=1}^{n_p}\int_{S_\alpha} J_{ij}(\mathbf{x}-\mathbf{y})f_j(\mathbf{y})dS_y, \qquad (3.40)$$

where u_i^∞ is the undisturbed flow field, $\mathbf{x}$ is a generic position in the fluid-particle continuum and $\mathbf{y}$ is the position vector identifying the point of application of each differential force. Stokesian Dynamics, rather than solving Eq. (3.40), uses a multipole expansion of the flow field about the centre $\mathbf{x}_\alpha$ of each particle, which reads as:

$$\begin{aligned}
u_i(\mathbf{x}) =& u_i^\infty(\mathbf{x}) - \frac{1}{8\pi\mu}\sum_{\alpha=1}^{n_p}\int_{S_\alpha} J_{ij}(\mathbf{x}-\mathbf{y})\,|_{\mathbf{y}=\mathbf{x}^\alpha}f_j(\mathbf{y})dS_y+ \\
&+\int_{S_\alpha}\frac{\partial}{\partial x_k}J_{ij}(\mathbf{x}-\mathbf{y})\,|_{\mathbf{y}=\mathbf{x}^\alpha}(y_k-x_k^\alpha)f_j(\mathbf{y})dS_y + ...
\end{aligned} \qquad (3.41)$$

where the n-th multipole moment is given by:

$$Q_n^\alpha = -\int_{S_\alpha}(y_i-x_i^\alpha)^n f_j(\mathbf{y})dS_y \qquad (3.42)$$

The zero-moment is the total force F_j^α exerted by the particle on the fluid. The first moment has instead two components: an antisymmetric component corresponding to the torque T_j^α and a symmetric component corresponding to the stresslet S_{jk}^α. Equation (3.41) can be therefore rewritten as (Durlofsky et al., 1987):

$$u_i'(\mathbf{x}) = u_i(\mathbf{x})-u_i^\infty(\mathbf{x}) = \frac{1}{8\pi\mu}\sum_{\alpha=1}^{n_p}(1+\frac{1}{6}a^2\nabla^2)J_{ij}F_j^\alpha + R_{ij}T_j^\alpha + (1+\frac{1}{10}a^2\nabla^2)K_{ijk}S_{jk}^\alpha, \qquad (3.43)$$

where J_{ij}, R_{ij} and K_{ijk} represent the propagator function for the force, torque and stresslet as defined in (3.38) and (3.39). Therefore, inserting Eq. (3.43) in the Faxén laws of Eq. (3.36), the problem is finally closed; a linear system of equations relating the particle velocities ($\mathbf{u}^\alpha$, $\boldsymbol{\omega}^\alpha$) and the fluid rate-of-strain $\mathbf{e}^\infty$ to the hydrodynamic

forces, torques and stresslet ($\mathbf{F}^\alpha$, $\mathbf{T}^\alpha$, $\mathbf{S}^\alpha$) is finally obtained:

$$
\left\{
\begin{array}{c}
\mathbf{u}^1 - \mathbf{u}^\infty\left(\mathbf{x}^1\right) \\
\vdots \\
\mathbf{u}^\alpha - \mathbf{u}^\infty\left(\mathbf{x}^\alpha\right) \\
\vdots \\
\mathbf{u}^{np} - \mathbf{u}^\infty\left(\mathbf{x}^{np}\right) \\
\boldsymbol{\omega}^1 - \boldsymbol{\omega}^\infty \\
\vdots \\
\boldsymbol{\omega}^\alpha - \boldsymbol{\omega}^\infty \\
\vdots \\
\boldsymbol{\omega}^{np} - \boldsymbol{\omega}^\infty \\
-\mathbf{e}^\infty \\
\vdots \\
-\mathbf{e}^\infty \\
\vdots \\
-\mathbf{e}^\infty
\end{array}
\right\}
= -\mathcal{M}^\infty \cdot
\left\{
\begin{array}{c}
\mathbf{F}^1 \\
\vdots \\
\mathbf{F}^\alpha \\
\vdots \\
\mathbf{F}^{np} \\
\mathbf{T}^1 \\
\vdots \\
\mathbf{T}^\alpha \\
\vdots \\
\mathbf{T}^{np} \\
\mathbf{s}^1 \\
\vdots \\
\mathbf{s}^\alpha \\
\vdots \\
\mathbf{s}^{np}
\end{array}
\right\}
\tag{3.44}
$$

The system has size $11n_p \times 11n_p$ and the matrix $\mathcal{M}^\infty$ is referred to as far-field mobility matrix. This denomination comes from the fact that it still includes only the long-ranged part of the hydrodynamic interactions. The mobility matrix is symmetric and positive definite [1] and may be conveniently divided in submatrices as:

$$
\mathcal{M}^\infty =
\begin{pmatrix}
M_{UF}^\infty & M_{UT}^\infty & M_{US}^\infty \\
M_{\Omega F}^\infty & M_{\Omega T}^\infty & M_{\Omega S}^\infty \\
M_{EF}^\infty & M_{ET}^\infty & M_{ES}^\infty
\end{pmatrix}
\tag{3.45}
$$

where the subscripts indicate the coupling of the various components. Appendix A reports the expressions of the terms of the mobility matrix of Eq. (3.45).

The procedure followed to obtain the linear system of Eq. (3.44) has been based on a multipole expansion of the rigorous velocity field. The expansion has been truncated at the level of the first moment, including, as a consequence, particle force, torque and stresslet; this formulation of Stokesian Dynamics is referred to as FTS formulation. However, lower order formulations are also possible, although at the cost of a reduced accuracy: for instance, if the multipole expansion is truncated at the level of the zero-th moment, to include only the particle force, the F version of SD is obtained: in this case the mobility matrix would be given solely by M_{UF}^∞ and the method would not allow to track the particle angular motion; a more accurate

---

[1] The matrix $\mathcal{M}^\infty$ is symmetric and positive definite in the full form in which all the 9 components of E_{ij}^∞ and S_{ij} are included; this would result into a matrix of size $15n_p \times 15n_p$. However these features can be preserved in the more compact form of size $11n_p \times 11n_p$ with a proper choice of the 5 independent components of E_{ij}^∞ and S_{ij}. It can be shown that a proper choice is given by Eq. (3.12) and Eq. (3.31)

version can be obtained if hydrodynamic torques are included; the FT version of SD is then obtained.

The mobility matrix of Eq. (3.45) still lacks of the lubrication effects, which play a predominant role when particles come in close proximity, giving rise to very large and highly localized interaction. The main feature of SD is indeed the introduction of such interactions. The main assumption is that, because of their short-ranged nature, lubrication forces are essentially two-body interactions and as such they can be introduced in a pair-wise additivity manner. Thus, SD prescribes to compute the overall resistance matrix $\mathcal{R}$, by inverting the far-field mobility matrix $\mathcal{M}^\infty$ and correcting it by using the exact two-body resistance functions $\mathcal{R}_{2B}$, thus (Brady, Bossis, 1988):

$$\mathcal{R} = (\mathcal{M}^\infty)^{-1} + \mathcal{R}_{2B} - \mathcal{R}_{2B}^\infty \qquad (3.46)$$

where the matrix $\mathcal{R}_{2B}^\infty$, corresponding to the far-field two-body resistance function, is used in order to not count twice for the far-field interactions, that are already counted for upon inversion of $\mathcal{M}^\infty$. The expressions for the coefficients of $\mathcal{R}_{2B}^\infty$ as a function of particle distance are reported by Kim, Karrila (1991). The resistance matrix $\mathcal{R}$ is finally obtained and the linear system of Eq. (3.44) can be rewritten as:

$$\begin{bmatrix} R^{UF} & R^{\Omega F} & R^{EF} \\ R^{UT} & R^{\Omega T} & R^{ET} \\ R^{US} & R^{\Omega S} & R^{ES} \end{bmatrix} \begin{Bmatrix} \mathbf{u}^\alpha - \mathbf{u}^\infty \\ \boldsymbol{\omega}^\alpha - \boldsymbol{\omega}^\infty \\ -\mathbf{e}^\infty \end{Bmatrix} = - \begin{Bmatrix} \mathbf{F}^H \\ \mathbf{T}^H \\ \mathbf{S}^H \end{Bmatrix} \qquad (3.47)$$

where a more compact notation has been used. The matrix $\mathcal{R}$ counts now for the complete spectrum of the hydrodynamic interaction, from the far-field to the near-field part.

However, because of lubrication, the resistance matrix $\mathcal{R}$ has leading terms diverging as $1/h$ and $\log(1/h)$, which give infinitely large lubrication forces that, in turn, prevent the possibility of a real contact upon collision between particles. However, this would hold true only for perfectly smooth spherical particles and cannot be representative of a colloidal suspension where particles frequently present a finite surface roughness, where medium immobilization phenomena may limit lubrication effects. In order to try to mimic this reality, we made use of a *cut-off length scale* $\tilde{h}_{co}$ to regularize the singularities (Seto et al., 2013): as the dimensionless gap h/a between two approaching particles become lower than $\tilde{h}_{co}$, the pair lubrication correction is no longer updated, but kept evaluated at $h = \tilde{h}_{co}a$. In the simulations a value $\tilde{h}_{co} = 2 \cdot 10^{-4}$ was adopted.

3.2 Particle–particle colloidal interaction

The stability of colloidal suspensions is governed by the colloidal interaction between the particles. If a strong enough repulsion holds, the suspension is stable. On the contrary, if the repulsion is mild or even replaced by an attractive interaction, the stability is lost and particles aggregate.

Traditionally the interaction between colloidal particles is thought to be the result of two different components: one repulsive component arising from the interaction of the electrical double layer surrounding the particles and an attractive interaction due to the London-Van der Waals forces (Israelachvili, 2011). These two contributes together form the basis of the well-known DLVO theory, developed independently by Derjaguin and Landau and Verwey and Overbeek. The DLVO theory still represents the standard framework in colloidal suspension studies. However, more recently, other kind of interactions have been recognized to have a strong influence on the aggregation behaviour of colloidal particles; post-contact interactions are in fact more and more frequently taken into account, since they play a key role in the aggregate morphology and strength.

In this section both the DLVO theory and the model adopted for the post-contact interactions will be described, with a particular attention to their implementation in the DEM simulations.

3.2.1 Pre-contact interaction

Van der Waals attraction

The London-Van der Waals interaction between macroscopic bodies, as colloidal particles are, results from the interaction between the constituent molecules. Therefore, in order to understand how these interactions between particles act it is useful to start from the analysis of the interaction at a molecular level.

Most of the molecules have a zero electric charge, but often the electric charge is not evenly distributed; therefore, molecules frequently have a more negative side and a more positive side. To a first approximation, the electric properties of such molecules can be described with a dipole moment $\vec{\eta}$ i.e, a vector pointing from the negative side to the positive side of the molecule, whose length gives a measure of the molecule overall polarity. When two dipoles are close and allowed to rotate freely two effects come into play: the attraction between the dipoles tend to align them with their oppositely charges facing each other; the thermal fluctuations tend to enforce a random orientation drifting the two dipoles away from the minimum energy configuration. However, on average, the balance between these two opposing effects results in a net preferential orientation. To calculate the net interaction, it is necessary to integrate over all the possible orientations; doing so, a thermally averaged dipole–dipole free energy is obtained (Kappl, 2009):

$$V = -\frac{\eta_1^2 \eta_2^2}{3\left(4\pi\varepsilon_0\right)^2 k_B T} \cdot \frac{1}{h^6} = -\frac{C_{Keesom}}{h^6} \tag{3.48}$$

where η_1, η_2 are the intensity of dipoles, ε_0 is the vacuum permittivity, h is the distance separating them and $k_B T$ the average kinetic energy. This free energy of interaction is often referred to as Keesom energy.

An interaction energy holds also for the case of a static dipole and a non-polar molecule i.e., a molecule with no electrical dipole. This interaction arises from a

charge shift in the non-polar molecule induced by the charge of the static dipole. In such a system the energy of interaction, also known as Debye interaction, is given by (Kappl, 2009):

$$V = -\frac{\eta^2 \alpha_m}{(4\pi\varepsilon_0)} \cdot \frac{1}{h^6} = -\frac{C_{Debye}}{h^6} \tag{3.49}$$

where η is the static dipole moment of the charged molecule and α_m is the polarizability of the non polar molecule.

The energies of interaction of Eq. (3.49) and Eq. (3.48) are derived using classical physics concepts. However, they are not able to explain the attraction that is observed between two non-polar molecules; the so-called London or dispersion force is responsible for such interactions. The explanation for the London forces has to be looked for in the quantum mechanical theory. Briefly speaking, it is well known that in an atom electrons orbit around a positive nucleus with a frequency ν_e typically in the order of 10^{15}-10^{16} Hz. Therefore, instantaneously the atom is polar and the direction of the dipole changes approximately according to the electron rotation frequency. When two such atoms are in close proximity, they start to influence each other and, on average, this leads to an attractive energy of interaction equal to (Kappl, 2009):

$$V = -\frac{3}{2}\frac{I_1 I_2}{I_1 + I_2}\frac{\alpha_{m,1}\alpha_{m,2}}{h^6} = -\frac{C_{London}}{h^6}. \tag{3.50}$$

where I_1 e I_2 are the first ionization energies of the interacting atoms or molecules and where $\alpha_{m,1}$ and $\alpha_{m,2}$ are their polarizability.

The combination of the Keesom, Debye and London forces contribute all together to the Van der Waals interaction between molecules. Since they all scale as h^{-6} it is possible to write:

$$V^{VdW} = -\frac{C_{VdW}}{h^6} \qquad C_{VdW} = C_{Keesom} + C_{Debye} + C_{London} \tag{3.51}$$

with the London interaction that generally prevails over the others.

However, when the separation between two interacting molecule is large, a steeper decrease of the interaction energy holds for the London dispersion forces; this can be easily explained by considering that the electric field generated by a dipole moment expands with the the speed of light, reaching and polarizing the second molecule, that in turn generates an electric field expanding with the speed of light. The characteristic time of this exchange can be estimated to be h/c, with c being the speed of light. The characteristic time for the change of the dipole moment is $1/\nu_e$. Therefore if:

$$\frac{1}{\nu_e} < \frac{h}{c} \tag{3.52}$$

the energy of interaction would be weaken. This effect is referred to as retardation effect and for distances in the order of tens of nanometres it leads to a steeper decrease of the energy of interaction between molecules as h^{-7}. As it will be explained soon, this effect is also relevant when considering macroscopic bodies.
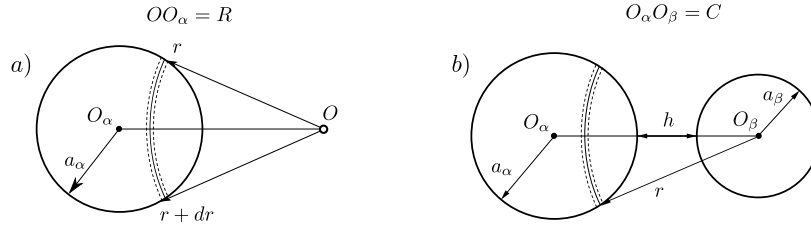
Figure 3.3: a) Interaction between an atom O and a macroscopic spherical particle α. b) Interaction between two macroscopic spheres α and β.

The computation of the energy of interaction between macroscopic bodies can be obtained with a pairwise summation of the interactions between all molecules in the two bodies. This approach, developed by Hamaker (1937), implicitly assumes that the interaction between a pair of molecules is not affected by the presence of a third molecule. Even if this assumption cannot be expected to hold true in a solid body, the results obtained have been shown to be of general validity and have represented the most robust framework in the understanding of the behaviour of colloidal particles. Adopting the pair-additivity principle, the Van der Waals interaction between two generic macroscopic bodies α, β with atomic densities q_α e q_β, in vacuum can be computed as:

$$V_{\alpha\beta}^{VdW} = - \int_{V_\alpha} dV_\alpha \int_{V_\beta} \frac{q_\alpha q_\beta \lambda^{VdW}}{r^6} dV_\beta, \qquad (3.53)$$

where V_α e V_β are the volumes of the bodies and r represents the distance between two infinitesimal volumes dV_α e dV_β. λ^{VdW} is instead the London-Van der Waals constant. The application of the Hamaker integration method to several geometries can be found elsewhere (*Dispersion forces*). Here we are interested in computing the interaction between a pair of spherical particles; for such a purpose, it is useful to first consider the interaction between an atom or molecule O placed at a distance R from a macroscopic sphere (Fig. 3.3a). By using Eq. (3.53) the energy of interaction for such a system is given by:

$$V_{\alpha O}^{VdW} = - \int_{R-a_\alpha}^{R+a_\alpha} \frac{\lambda^{VdW} q_\alpha}{r^6} \pi \frac{r}{R} \left[a_\alpha^2 - (R-r)^2 \right] dr, \qquad (3.54)$$

where $\pi \dfrac{r}{R} \left[a_\alpha^2 - (R-r)^2 \right)] dr$ is the particle infinitesimal volume between the two spheres centred in O with radius r e $r+dr$, respectively. By using Eq. (3.54), the interaction potential between two macroscopic spheres of radius a_α and a_β whose centres are separated by a distance C (Fig. 3.3b) can be computed as:

$$V_{\alpha\beta}^{VdW} = - \int_{C-a_\alpha}^{C+a_\alpha} V_{\alpha O}^{VdW} q_\beta \pi \frac{R}{C} \left[a_\beta^2 - \left(C - R^2 \right) \right] dr. \qquad (3.55)$$

and by solving the integral one obtains:

$$V_{\alpha\beta}^{VdW} = -\frac{A_H}{12}\left[\frac{y}{x^2+xy+x}+\frac{y}{x^2+xy+x+y}+2\ln\frac{x^2+xy+x}{x^2+xy+x+y}\right] \quad (3.56)$$

$$\text{with}\qquad x=\frac{h}{2a_\alpha}\qquad y=\frac{a_\beta}{a_\alpha}\qquad A_H=\pi^2 q_\alpha q_\beta \lambda^{VdW}$$

where h is the minimum distance between the surface of the particles and A_H is the Hamaker constant of the system under consideration. Under the assumption of identical spheres ($a_\alpha = a_\beta = a$), separated by a distance $h \ll 2a$, Eq. (3.56) becomes more compact and equal to:

$$V_{\alpha\beta}^{VdW} = -\frac{A_H \cdot a}{12 \cdot h} \quad (3.57)$$

This expression only applies at close approach and can be inaccurate at separations greater than about 10% of the particle radius. However, in most cases the interaction energy is negligible at these distances so that Eq. (3.57) is safely applicable. In principle, the attraction should become very strong at short distances and infinite on contact; however, other effects such as the short-ranged repulsion and the molecular roughness of the particle surface come into play at close approach and keep the attraction finite. It is common therefore to introduce a minimum approach distance z_0 in order to count for these phenomena and shift the energy minimum at a distance of the order of the Angstrom. Under these circumstances the Van der Waals potential reads as:

$$V_{\alpha\beta}^{VdW} = -\frac{A_H \cdot a}{12 \cdot (h+z_0)} \quad (3.58)$$

This latter expression is also best suited to be used in DEM simulations since the potential energy remains large but finite, thus avoiding the numerical problems that could arise from the singularity of Eq. (3.57). However, in DEM simulations, rather than the interaction potential, the interaction force is needed. This can be easily obtained as the minus derivative of the potential with respect to the distance h. The attractive force acting on a pair of interacting particle α, β is thus given by:

$$F_{\alpha\beta}^{VdW} = -\frac{dV_{\alpha\beta}^{VdW}}{dh} = \frac{A_H a}{12\,(h+z_0)^2} \quad (3.59)$$

Clearly the force acts equally on the pair of particles such that $|F_{\alpha,\beta}^{VdW}| = |F_{\beta,\alpha}^{VdW}|$.

As already mentioned, the microscopic approach by Hamaker of pairwise additivity of the individual intermolecular interactions can be questionable since it ignores the influence of neighbouring molecules. This issue was addressed in the Lifshitz theory (Israelachvili, 2011) in which the molecular structure is neglected and the bodies are treated as continuous media characterized by their bulk properties, such as dielectric constant and refractive index. However, the higher accuracy of the Lifshitz theory is paid with a larger number of parameters to be taken into account; for this reason the older Hamaker approach is still widely used thanks to its computational convenience and to the fact that the results for most of the cases of interest are correct as long
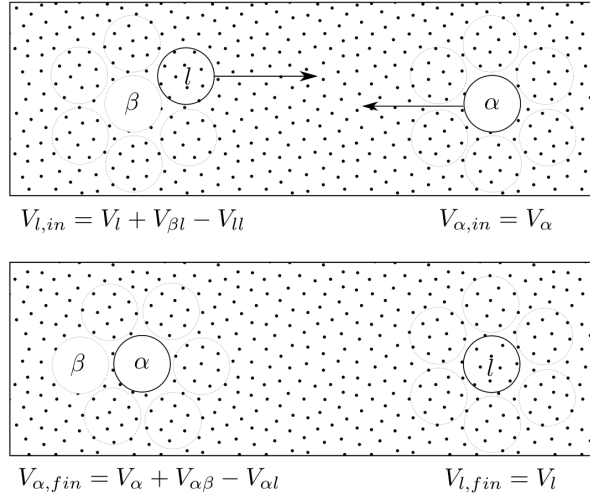
Figure 3.4: Interaction between two colloidal particles α and β dispersed in a medium l

as a proper value for the Hamaker constant is employed and retardation effects are taken into account (Bowen, Jenner, 1995).

The effect of retardation is generally taken into account with a function $f(h)$ that goes from 1 (for $h = 0$) to 0 (for $h \to \infty$); for a sphere-sphere system the following definition for the function $f(h)$ has been proposed to correct the expression of the force of Eq. (3.59) (Schenkel, Kitchener, 1960; Wiese, Healy, 1970):

$$f(h) = \begin{cases} \dfrac{1 + 3.54p}{(1 + 1.77p)^2}, & p < p_0 \\[3mm] \dfrac{0.98}{p} - \dfrac{0.434}{p^2} + \dfrac{0.067429}{p^3}, & p > p_0 \end{cases} \tag{3.60}$$

$$p = \frac{2\pi h}{\lambda_l} \quad p_0 = 0.5709 \tag{3.61}$$

where λ_l is the London wavelength (typically assumed equal to 100 nm), corresponding to the intrinsic electronic oscillations of the atoms.

Finally, the estimation of the interaction forces reduces to the determination of the Hamaker constant A_H. In colloidal suspensions the interaction between particles does not occur in vacuum but in a liquid dispersing medium. It can be shown, however, that the obtained expressions for the interaction potential are still valid, provided that a modified value for the Hamaker constant is adopted to include the effect of the medium (Berg, 2010). With regard to Fig. 3.4 the effective Hamaker constant A_H measuring the energy of interaction between two colloidal particles α and β dispersed in a medium l can be estimated by computing the energy variation between the initial state in which the particles are far apart from each other and the final state in which the particles are in contact. By defining the following energies of interaction:

- V_α, the energy of the particle α when far from particle β

- V_l, the energy of an isolated blob of liquid

- $V_{\alpha l}$, the energy of interaction between particle α and a blob of liquid l

- $V_{\alpha\beta}$, the energy of interaction between particle α and particle β

- $V_{\beta l}$, the energy of interaction between particle β and a blob of liquid l

- V_{ll}, the energy of interaction between two blobs of liquid l

the variation in free energy of the system between the initial state and the final state can be computed as the sum of two contributes: one given by the energy required to move the particle α close to particle β and one given by the energy required to move away a blob of liquid l from its original position close to particle β to an infinite distance. Therefore, the total energy variation is given by:

$$\Delta V = [(V_\alpha + V_{\alpha\beta} - V_{\alpha l}) - (V_\alpha)] + [(V_l) - (V_l + V_{\beta l} - V_{ll})] \\ = V_{\alpha\beta} - V_{\alpha l} - V_{\beta S} + V_{ll} \tag{3.62}$$

From which it follows that the Hamaker constant for the system formed by two particles immersed in a dispersing medium is:

$$A_{H,\alpha l \beta} = \pi^2 \left\{ q_\alpha q_\beta \lambda_{\alpha\beta}^{VdW} - q_\alpha q_l \lambda_{\alpha l}^{VdW} - q_\beta q_l \lambda_{\beta l}^{VdW} + q_l q_l \lambda_{ll}^{VdW} \right\} \\ = A_{H,\alpha\beta} - A_{H,l\beta} - A_{H,\alpha l} + A_{H,ll} \tag{3.63}$$

where the generic $A_{H,ij}$ denotes the Hamaker constant for materials i and j interacting across vacuum.

Another similar relation is given by:

$$A_{H,\alpha l \beta} \approx \sqrt{A_{H,\alpha l \alpha} A_{H,\beta l \beta}} \tag{3.64}$$

and it implies that from the knowledge of the single Hamaker constant for particle α and β interacting across the medium l with themselves, it is possible to estimate the Hamaker constant for the interaction between particle α and particle β across the medium l with a simple geometric mean.

Finally, the Hamaker constant for the interaction of two solid particles of the same material $A_{H,\alpha\alpha}$ can be related to the surface tension γ_s of the solid by a thought experiment[2]; let us imagine to break the solid in two parts and to bring them at an infinite distance. The work required is then given by $A_{H,\alpha\alpha}/12\pi z_0^2$ with z_0 being the initial separation between two atoms of the fragments. Upon breakage two new surfaces are created; the work required per unit area to create such surfaces is $2\gamma_s$.

---

[2]The method is rigorous for Van de Waals solids. In the other cases one obtains the component of γ_s due to Van der Waals forces.

Therefore, equating the two results the surface tension of the solid is given by:

$$\gamma_s = \frac{A_{H,\alpha\alpha}}{24\pi z_0^2} \tag{3.65}$$

In many cases good estimations of the surface energy are obtained when an interatomic distance of 1.65 Å is used (Kappl, 2009). If the experiment was performed in a liquid medium, rather than in vacuum, the same relationship would relate the effective Hamaker constant $A_{H,\alpha l\alpha}$ and the solid-liquid interfacial tension γ_{sl}.

Electrical double layer interaction

Frequently colloidal particles in a dispersing medium present a surface charge. Water, for instance, because of its high dielectric constant, is a good solvent for ions and therefore most surfaces in water are charged. Three main mechanisms can lead to the charging of a surface:

- specific adsorption of ions

- selective dissolution

- ionization of superficial groups

With regard to the first mechanism, ions in specific conditions can adsorb on a solid surface via chemisorption (by chemical bonds) or via physisorption (by van der Waals interaction), thus charging the surface. The selective dissolution is responsible for the charging of silver iodide particles, among others, because of the different solubility in water of silver and iodide ions. The ionization of superficial groups occurs for instance in metal oxides which can easily present a surface charge, either positive or negative, depending on the value of the pH of the medium. However other mechanisms can be responsible for surface charging such as ion sputtering, application of an electric field, synthesis of polymeric particles with charged superficial groups, etc.

Whatever the origin of surface charge is, it must be balanced by an equal and opposite charge in the medium. This balancing is obtained by an excess number of oppositely charged ions (or counterions) and by a deficit of similarly charged ions (or coions) in the solution close to the charged surface. In its entirety this system is called electrical double layer (EDL).

Different models have been proposed for the electrical double layer, varying mainly in the assumptions made (Hunter, 1981): the simplest model is the one proposed by Helmhotz which assumes that counterions approach the charged surface and stick to it at a distance equal to the radius of the counterion plus a a single solvation layer. The result is that a linear potential drop holds in this thin region spanning from the solid surface to the so-called outer Helmholtz Plane. This situation corresponds exactly to the case of an electrical capacitor with two plates of charge separated by a short distance. An improvement to this model came from the work of Gouy and Chapman, even if a number of simplifications is still adopted:

- the solvent is a uniform medium with a permittivity independent of the distance from the surface

- ions behave as point-like charges free to approach the solid surface up to any distance, thus neglecting solvation phenomena

- the surface charge is uniformly distributed over the solid surface

However, by taking into account the thermal motion of the ions, which tend to drive them away from the surface, they obtained the more realistic picture of a diffuse layer of ions extending from the charged surface to the bulk of the medium. Further refinements of this model have been proposed by Stern, who combined the Helmhotz model with the Gouy and Chapman model of diffuse layer. He argued that a layer of immobilized hydrated counterions is adsorbed onto the solid surface and a linear potential drop occurs across the layer comprised between the solid surface and the plane along which the counterion centres are aligned. The value of the potential on the outer boundary of this layer is frequently indicated as Stern potential.

Other more sophisticated model have been proposed, however for the scope of this work, in the following, the discussion will be limited to the diffuse layer model of Gouy and Chapman because of its simplicity and relevance in the modelling of EDL interaction between colloidal particles.

In order to compute the interaction between charged colloidal particles it is useful to start from the simple case of a single planar surface with a constant homogeneously distributed surface charge. For such a system the relation between the electrical potential Ψ and the charge density ϱ in the medium is given by the Poisson equation as:

$$\nabla^2 \Psi = -\frac{\varrho}{\varepsilon_r \varepsilon_0} \tag{3.66}$$

where ε_r is the relative permittivity of the medium and ε_0 the vacuum permittivity. However, before applying Eq. (3.66), the distribution of charge in the medium is needed. This information can be obtained resorting to a Boltzmann statistics:

$$c^+ = c_0^+ \cdot \mathrm{e}^{\left(-q^+ e\Psi / k_B T\right)}, \qquad c^- = c_0^- \cdot \mathrm{e}^{\left(q^- e\Psi / k_B T\right)} \tag{3.67}$$

where c^+ and c^- represent the number concentration of coions and counterions (of valence q^+ and q^-) at the point in the solution where the potential is Ψ. c_0^+ and c_0^- represent instead their concentration in the bulk of the medium. Equation (3.67) implies that if a ion has a charge opposite to the sign of the potential, then its local concentration will be higher than the bulk value and vice versa. Therefore, when the potential has a negative sign, there will be a local excess of cations and a deficit of anions. If, for the sake of simplicity, a symmetric monovalent electrolyte is dissolved in the medium, then the Poisson equation, in the monodimensional case, reads as:

$$\frac{d^2 \Psi}{dx^2} = \frac{c_0 e}{\varepsilon_r \varepsilon_0} \cdot \left(\exp\left(\frac{e\Psi(x)}{k_B T}\right) - \exp\left(-\frac{e\Psi(x)}{k_B T}\right) \right) \tag{3.68}$$

where e is the elementary charge and c_0 the salt bulk concentration expressed as molecules per unit volume. Equation (3.68) is often referred to as Poisson-Boltzmann equation. For low potentials, generally below 50 mV, the Debye-Hückel (DH) approximation is often used; the DH approximation expands the exponential term into a series and retains only the linear term. Under this approximation and imposing that $\Psi(x=0) = \Psi_0$ and $\Psi = 0$ for $x \to \infty$, the solution of Eq. (3.68) can be easily obtained:

$$\Psi = \Psi_0 \cdot \mathrm{e}^{-\kappa x} \tag{3.69}$$

with the parameter κ governing the potential decay given by:

$$\kappa = \left(\frac{2c_0 e^2}{\varepsilon_r \varepsilon_0 k_b T} \right)^{1/2} \tag{3.70}$$

The reciprocal of κ is commonly indicated as Debye length λ_d and it determines the thickness of the diffuse layer; at a distance λ_d from the charged surface in fact the value of the potential has fallen to a value $1/\mathrm{e}$ ($=1/2.72$) of the surface potential. As noticeable, the extension of the electrical double layer depends on the bulk concentration of the solution. The higher it is, the thinner is the diffuse layer. Typical values of λ_d ranges between 1 nm and 100 nm.

When dealing with spherical particles, if the radius of the particle is much larger than the Debye length, the planar approach just outlined is still feasible. Furthermore, since in general fairly low potentials characterize colloidal particles, the linear approximation of the exponential terms does not pose any problem. All this considered, the exponential potential distribution of Eq. (3.69) remain a fair model for colloidal particles as well.

However, when two charged surfaces approach each other, their electric double layers overlap, giving rise to an interaction. The precise way in which the double layers respond to each other depends on a number of factors. One distinction is between interaction at constant surface potential or constant surface charge. The former case corresponds to the maintenance of the surface-bulk chemical equilibrium during approach. Constant-charge interaction might be expected instead when the approach is so fast that the particles do not vary their surface charge. It should be pointed out that neither the constant potential nor the constant charge assumption are completely correct. However, the presence of Stern layers and the uncertainty over the liquid-surface charge transfer rate make it difficult to develop more reliable models for the EDL interactions. Adopting the constant surface potential Hogg et al. (1966) succeeded in deriving a general expression to describe the potential energy of interaction between dissimilar spherical colloidal particles with surface potential $\Psi_{0,\alpha}$ and $\Psi_{0,\beta}$:

$$V_{\alpha\beta}^{EDL} = \frac{4\pi\varepsilon_r\varepsilon_0 a_\alpha a_\beta \left(\Psi_{0,\alpha}^2 + \Psi_{0,\beta}^2\right)}{4\left(a_\alpha + a_\beta\right)} \left[\frac{2\Psi_{0,\alpha}\Psi_{0,\beta}}{\left(\Psi_{0,\alpha}^2 + \Psi_{0,\beta}^2\right)} \ln\left(\frac{1 + \exp\left(-\kappa h\right)}{1 - \exp\left(-\kappa h\right)}\right) + \ln\left(1 - \exp\left(-2\kappa h\right)\right) \right] \tag{3.71}$$
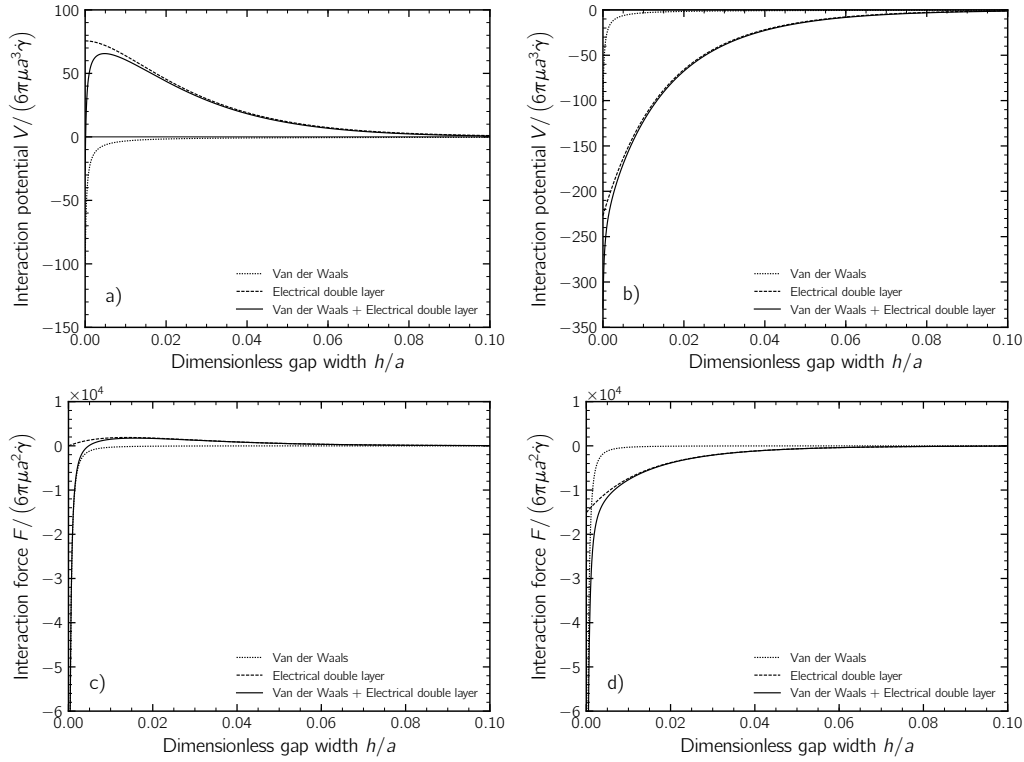
Figure 3.5: Total interaction for a pair of polystyrene spherical particles of radius $a = 500$ nm dispersed in water. The Hamaker constant for such a system is $0.95 \cdot 10^{-20}$ J (Kappl, 2009). In plot a) and b), the Van der Waals interaction is modeled according to Eq. (3.58) and the electrical double layer interaction according to Eq. (3.72). The total interaction potential have been made dimensionless by using the shear convective energy, where $\dot{\gamma} = 10$ s^{-1} and $\mu = 10^{-3}$ Pa s. Plot a) refers to the interaction of a pair of like particles with surface potential equal to $\Psi_0 = +40$ mV. Plot b) refers to the interaction of a pair of unlike particles with surface potentials equal to $\Psi_{0,\alpha} = +40$ mV and $\Psi_{0,\beta} = -40$ mV. In both cases a Debye length $\lambda_d = 10$ nm was used. c) and d) plots report the same information in terms of force of interaction. Note that for the case of like particles a strong repulsive force holds at small separation, but it is concealed by the even stronger Van der Waals attraction at contact.

This formula was derived using the linear approximation of the Poisson-Boltzmann equation in conjunction with the Derjaguin approximation, thus its use is restricted to the case of spheres with small surface potentials (up to 50 mV) and when the surface-to-surface distance is much smaller than the particle size. Attempts have been made to extend this approach to cover the constant charge case, but the resulting expressions have been shown to be very inaccurate; for constant charge interaction in fact the surface potentials of the particles can reach very high values and the linear approximation of the Poisson-Boltzmann equation can no longer be applied. A more recent expression has been provided by Ohshima (1994) by solving the linearised spherical Poisson-Boltzmann equation for constant surface potentials without the use of the Derjaguin approximation:

$$V_{\alpha\beta}^{EDL} = 4\pi\epsilon_r\epsilon_0 \frac{a_\alpha a_\beta}{a_\alpha + a_\beta} \left[\Psi_{0,\alpha}\Psi_{0,\beta}e^{-\kappa h} - \frac{1}{4}\left(\Psi_{0,\alpha}^2 + \Psi_{0,\beta}^2\right)e^{-2\kappa h} \right] \qquad (3.72)$$

In this work Eq. (3.72) has been used as it should give more accurate estimations of the interaction potential for any particle-particle separation distance.

In Fig. 3.5 the total interaction potential (obtained as a superposition of Van der Waals and electrical double layer interaction) is plotted for a pair of particles of radius $a = 500$ nm as a function of the surface-to-surface distance h. Both the case of like particles (with the same surface potential) and the case of unlike particles (with opposite surface potential) is addressed. A Debye length λ_d equal to 10 nm was used, corresponding approximately to a medium with a 1 mM concentration of monovalent salt. As apparent, when particles present a surface potential of the same sign, an energy barrier arises opposing their aggregation. The surface-to-surface distance at which such a barrier appears coincides approximately with λ_d. When considering oppositely charged particles such a barrier does not exist and an attractive interaction holds, promoting the aggregation of the particles. From the trend of the interaction potential it is also clear that Van der Waals and electrical double layer interaction have different range of action, with the former being substantially more short-ranged.

3.2.2 Post-contact interaction

When two particles come in mechanical contact, attractive forces cause the adhesion between their surfaces and the deformation of the particle profile.

In this context the most established theory is the JKR theory named after Johnson, Kendall and Roberts (Johnson et al., 1971), who extended the classical Hertz theory of contact mechanics to count for the adhesive interaction between contacting bodies. The JKR theory argues that if adhesion forces act on contacting particles, then the contact area is considerably larger than that predicted by the Hertzian theory (Fig. 3.6). Furthermore, differently from the Hertzian theory that states that the deformed particle profile is tangent to the contact plane, the JKR theory assumes the perpendicularity between the particle profile and the contact plane.

However, before discussing on the JKR theory and its implementation in the DEM model, it is useful to extend the definition of the quantity h, used so far to
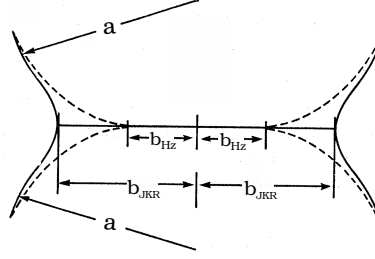
Figure 3.6: Comparison of the extension of the contact area between the JKR theory and the Hertz theory; a is the radius of the particles, b the radius of the circular contacting region.

indicate the surface-to-surface distance between two particles; h can be computed as:

$$h = r - 2a \tag{3.73}$$

with r being the distance between the centres of two particles of radius a. Clearly h is larger than zero for non-touching particles and equal to zero for a one-point contact. However, in the framework of contact mechanics, the same definition of h of Eq. (3.73) is also used in the case of deformed contacting particles. In such a situation h takes on negative values and, in this context, it is often referred to as indentation.

According to the JKR theory the relation between the indentation h and the contact radius b is given by:

$$h\left(b\right) = \frac{2}{3}\frac{b_0^2}{a}\left[-3\left(\frac{b}{b_0}\right)^2 + 2\sqrt{\frac{b}{b_0}}\right] \tag{3.74}$$

where b_0 represents the zero-load contact radius, i.e., the radius of the contact area when no external load acts on the particles. The value of b_0 is solely determined by the adhesive interactions and reads as:

$$b_0 = \left(\frac{9\pi\gamma_s a^2 \left(1 - \nu^2\right)}{2E}\right)^{1/3} \tag{3.75}$$

where γ_s is the surface energy of the solid, E is the elastic modulus of the particles and ν the Poisson ratio. If an external load F acts on the particles the contact radius b would change according to:

$$b\left(F\right) = \frac{b_0}{2^{2/3}}\left(1 + \sqrt{1 + \frac{F}{|F_{adh}|}}\right)^{2/3} \qquad |F_{adh}| = \frac{3}{2}\pi\gamma_s a. \tag{3.76}$$

Therefore, when an external tensile force $F = |F_{adh}|$ is applied on the contacting particles, the detachment of the surface will occur. This will happen at a positive distance h, referred to as pull-off distance. Combining Eq. (3.76) and Eq. (3.74) this
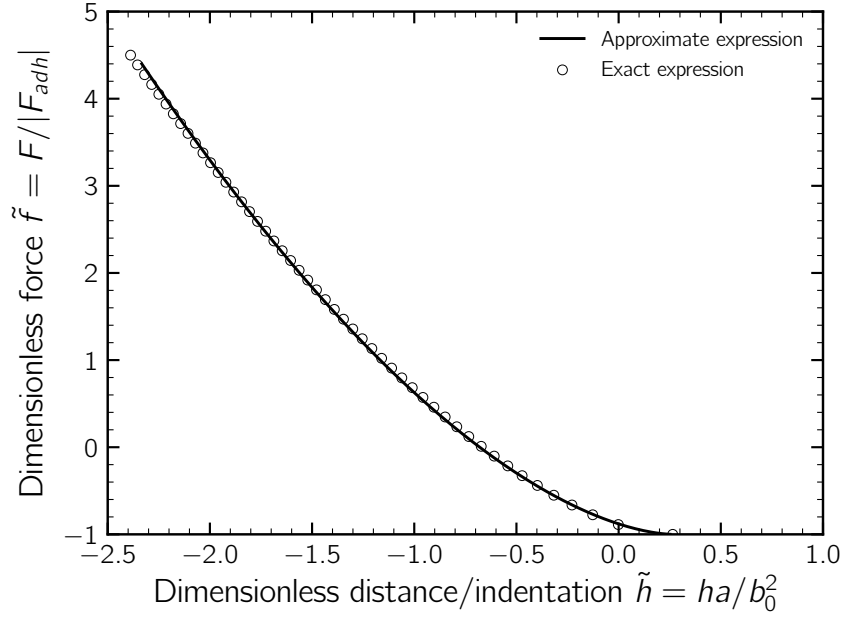
Figure 3.7: Comparison between the exact (Eq. (3.78)) and the approximate (Eq. (3.80)) relation between force and distance.

distance is given by:

$$h_{po} = \frac{b_0^2}{2^{1/3}3a} \qquad (3.77)$$

In physical terms it means that, while particles are moving far apart, a small neck of material would be present at the contact, acting to prevent complete detachment, as long as its length is smaller than h_{po}. Finally replacing Eq. (3.76) in Eq. (3.74) the following expression relating the distance h to the force is obtained:

$$\tilde{h} = \left(\frac{1 + \sqrt{1 + \tilde{f}}}{2}\right)^{1/3} \cdot \frac{1 - 3\sqrt{1 + \tilde{f}}}{3}. \qquad (3.78)$$

$$\tilde{h} = ha/b_0^2$$
$$\tilde{f} = F/|F_{adh}| \qquad (3.79)$$

which can be approximated as:

$$\tilde{f} = -1 + 1.1 \cdot \left(\tilde{h}_{po} - \tilde{h}\right)^{5/3} \qquad (3.80)$$

This last equation is best suited to be used in DEM simulations, in that it provides straightforwardly the force acting on the particles as function of the surface-to-surface distance (or indentation) with no need to perform time-consuming numerical inversion of Eq. (3.78). In Fig 3.7 both expressions are plotted, showing that a fairly good agreement holds.

53
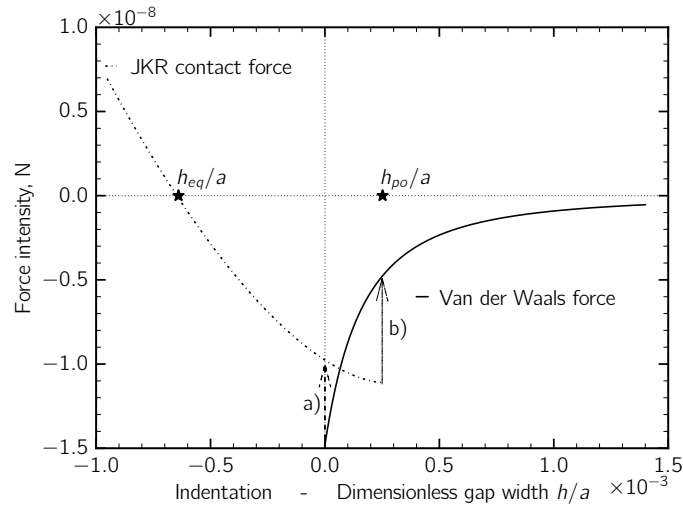
Figure 3.8: Model for the contact-detachment hysteresis. Positive values of the force mean a repulsive interaction, negative values an attractive interaction.

One point of the theory deserves particular comment; when two particles get in contact or detach only intermolecular forces contribute to the cohesive strength, whereas chemical bonds are not involved. For instance, the adhesion of two particles of silica is due to the Van der Waals attractive force and not to the formation of the covalent bonds that instead characterize the interior of silica. This fact implies that the term γ_s of Eq. (3.75) and Eq. (3.76) is only the contribution of intermolecular forces to the total surface energy and, as such, it can be estimated from the Hamaker constant by Eq. (3.65).

Figure 3.8 shows the total model for the interactions between a pair of particles for which EDL interactions are completely screened. Both the Van der Waals attraction force and the JKR contact force are plotted. As can be noticed, two discontinuities are present: one at contact ($h/a = 0$) and one at detachment ($h/a = h_{po}/a$). These discontinuities can be explained as follows: when two particles approach each other the Van der Waals attraction favour their contact which occurs for $h/a = 0$. Once in mechanical contact, the strong attraction between their surface cause them to further approach; the force acting on the particles exhibits its first discontinuity (indicated by the arrow a in the plot) and promotes the deformation of the particles, until the equilibrium configuration (h_{eq}) is reached. From this configuration if an external compressive load act on the doublet, trying to further deform the particles, a repulsive interaction arises; on the contrary, if a tensile load is applied, an attractive force arises counteracting the external load. However, if the applied tensile load is strong enough (equal to the adhesion force keeping the particle in contact) the bond is broken and the detachment of the surfaces occurs at $h/a = h_{po}/a$. Once the particles are separated, the force acting on them is again given by the Van der Waals interaction (discontinuity b).

At this stage it is worth to mention that the additional adhesion force due to the EDL interactions has no substantial effect in the contact-detachment model just
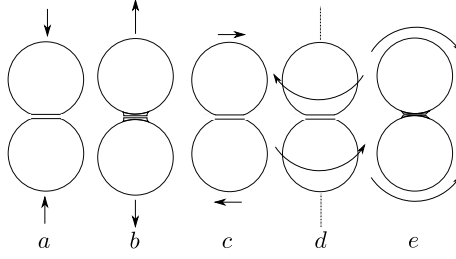
Figure 3.9: Schematic representation of the degrees of freedom associated to a pair of contacting particles.

outlined. The adhesion force due to such interactions is in fact negligibly small compared to Van der Waals adhesion force (Fig. 3.5d).

Tangential interaction model

The implementation of the JKR theory of contact mechanics provides the bond between primary particles with a resistance to tensile and compression stress (Fig. 3.9a,b), thus when in contact the motion of the particles along the center-to-center direction is hindered by adhesion. However, as shown by Pantina, Furst (2005), the large adhesion force between two bonded colloidal particles is able to also hinder the relative displacement along the contact surface. Several methods were proposed to model such interactions and to provide to contacting particles a resistance to sliding, twisting and rolling (Fig. 3.9 c,d,e). Inci et al. (2014) modelled these non-central interactions between contacting particles via a 3-body angular potential using an approach typical of Molecular Dynamics. Marshall (2009) extended the traditional spring-dashpot-slider model of Cundall, Strack (1979) by introducing three different models to hinder each of the possible relative motion modes along the contact plane. In this work the more compact model proposed by Becker, Briesen (2008) is adopted (Fig. 3.10); this spring-like model is able to couple the rolling and sliding resistance by introducing a simple rod-spring system, whose parameters are derived from the experimental observation by Pantina and Furst. The basic idea behind this model is that, after the contact between a pair of particles is established, a thought system composed by two rods and two springs is initialized; more precisely, each rod is rigidly connected to one particle center and reaches the center of the other particle, to which is connected by means of an elastic spring (Fig. 3.10a). Each spring length grows proportionally to the relative tangential velocity between the rod end point and the particle center. Therefore, indicating by α and β the two contacting particles, the elongation evolution of the spring with length $\zeta_{\alpha\beta}$, rigidly connected to particle α, is given by:

$$\dot{\boldsymbol{\zeta}}_{\alpha\beta} = (\mathbf{u}_\beta - \mathbf{u}_\alpha)_t - (\boldsymbol{\omega}_\alpha \times \mathbf{n}_{\alpha\beta}) \cdot 2a \tag{3.81}$$

And similarly for the spring connected to particle β:

$$\dot{\boldsymbol{\zeta}}_{\beta\alpha} = (\mathbf{u}_\alpha - \mathbf{u}_\beta)_t - (\boldsymbol{\omega}_\beta \times \mathbf{n}_{\alpha\beta}) \cdot 2a \tag{3.82}$$
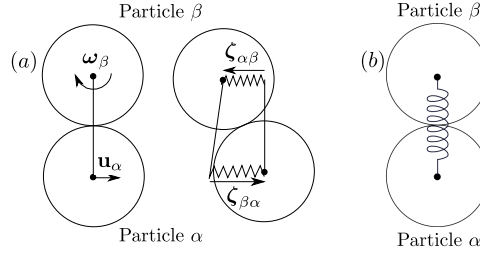
Figure 3.10: Schematic representation of tangential interaction model by Becker, Briesen (2008)

where $\mathbf{n}_{\alpha\beta}$ indicates the unit vector connecting the particle centers and pointing to particle β; the subscript t indicates that only the projection of the particle relative linear velocity on the plane orthogonal to $\mathbf{n}_{\alpha\beta}$ contributes to the spring elongation. Similarly, the second term on the r.h.s. of Eq. (3.81) and (3.82) computes only the contribution to the spring elongation due to the rolling motion. It is easy to deduce that in case of pure twisting motion this contribution would be zero. At every time the instantaneous elongation of the springs follows from a simple Euler integration scheme as:

$$\begin{aligned}
\boldsymbol{\zeta}_{\alpha\beta}|_{t+\Delta t} &= \boldsymbol{\zeta}_{\alpha\beta}|_t + \dot{\boldsymbol{\zeta}}_{\alpha\beta} \cdot \Delta t \\
\boldsymbol{\zeta}_{\beta\alpha}|_{t+\Delta t} &= \boldsymbol{\zeta}_{\beta\alpha}|_t + \dot{\boldsymbol{\zeta}}_{\beta\alpha} \cdot \Delta t
\end{aligned} \tag{3.83}$$

where the integration is started at the time of contact and is carried out as long as the particle are in contact. It is worth to point out that the springs must be continuously mapped to the plane perpendicular to $\mathbf{n}_{\alpha\beta}$. Finally the restoring forces and torques are given by:

$$\begin{aligned}
\mathbf{F}_\alpha &= k_\zeta \cdot \boldsymbol{\zeta}_{\alpha\beta} - k_\zeta \cdot \boldsymbol{\zeta}_{\beta\alpha} \\
\mathbf{F}_\beta &= k_\zeta \cdot \boldsymbol{\zeta}_{\beta\alpha} - k_\zeta \cdot \boldsymbol{\zeta}_{\alpha\beta}
\end{aligned} \tag{3.84}$$

$$\begin{aligned}
\mathbf{T}_\alpha &= 2ak_\zeta \cdot \left(\mathbf{n}_{\alpha\beta} \times \boldsymbol{\zeta}_{\alpha\beta}\right) \\
\mathbf{T}_\beta &= -2ak_\zeta \cdot \left(\mathbf{n}_{\alpha\beta} \times \boldsymbol{\zeta}_{\beta\alpha}\right)
\end{aligned} \tag{3.85}$$

where k_ζ is the stiffness of the springs. In order to allow restructuring effect, each spring stops extending if its elongation exceeds a maximum value ζ_{max}.

In a similar way, a torsional spring can also be introduced when two particles get in contact in order to confer a resistance to the twisting motion to the bond (Fig. 3.10d). Denoting by $\vartheta_{\alpha,\beta}$ the twisting angle of the spring, its derivative can be computed as:

$$\dot{\vartheta}_{\alpha\beta} = (\boldsymbol{\omega}_\beta - \boldsymbol{\omega}_\alpha) \cdot \mathbf{n}_{\alpha\beta}. \tag{3.86}$$

where the dot product allows us to isolate the component of relative angular velocity which contributes to the twisting motion. As done for the tangential springs, by following the evolution of the torsion angle, at any time, the restoring torque is given

by:

$$\mathbf{T}_\alpha = -\mathbf{T}_\beta = k_\vartheta \vartheta_{\alpha,\beta} \mathbf{n}_{\alpha,\beta} \tag{3.87}$$

where k_ϑ represents the stiffness of the torsional spring. A value of maximum torsional angle ϑ_{max} has to be identified as well, in order to allow restructuring effects. In Appendix B the procedure proposed by Becker, Briesen (2008) for the estimation of the 4 parameters (k_ζ, ζ_{max}, k_ϑ, ϑ_{max}) of the model is illustrated.

3.2.3 Viscous dissipation

In DEM simulation it is common practice to add a viscous damping at the inter-particle contacts; the strong variability of the interaction which, as shown in Fig. 3.8, change quite abruptly from an attraction to a repulsion interaction around the equilibrium position h_{eq}, induces substantial oscillations of the particle position, posing severe numerical problems. In order to circumvent this inconvenience, a dissipative force proportional to the particle relative velocity along the center-to-center direction was introduced. Indicating by α and β a pair of contacting particles and with $\mathbf{n}_{\alpha\beta} = (\mathbf{x}_\beta - \mathbf{x}_\alpha)/|\mathbf{x}_\beta - \mathbf{x}_\alpha|$ the unit vector connecting their center, the viscous force can be computed as:

$$\mathbf{F}_\beta^{diss} = -k_v \left[(\mathbf{u}_\beta - \mathbf{u}_\alpha) \cdot \mathbf{n}_{\alpha\beta} \right] \mathbf{n}_{\alpha\beta} \qquad \mathbf{F}_\beta^{diss} = -\mathbf{F}_\alpha^{diss} \tag{3.88}$$

with k_v being the viscous damping constant. It is possible to recast Eq. (3.88) in the following matrix form, which is best suited to be combined with Stokesian Dynamics:

$$\begin{Bmatrix} \mathbf{F}_{diss}^1 \\ \mathbf{F}_{diss}^2 \\ \vdots \\ \mathbf{F}_{diss}^{n_p} \end{Bmatrix} = [\mathcal{K}] \begin{Bmatrix} \mathbf{u}^1 - \mathbf{u}^\infty \left(\mathbf{x}^1\right) \\ \mathbf{u}^2 - \mathbf{u}^\infty \left(\mathbf{x}^2\right) \\ \vdots \\ \mathbf{u}^{n_p} - \mathbf{u}^\infty \left(\mathbf{x}^{n_p}\right) \end{Bmatrix} + \begin{Bmatrix} \mathbf{J}^1 \\ \mathbf{J}^2 \\ \vdots \\ \mathbf{J}^{n_p} \end{Bmatrix} \tag{3.89}$$

or in a more compact notation as:

$$\mathbf{F}^{diss} = \mathcal{K} \cdot \boldsymbol{\Delta}\mathbf{u} + \mathbf{J}. \tag{3.90}$$

The details of the derivation of Eq. (3.89) are reported in Appendix C.

3.2.4 Coupling of SD and interparticle interaction

The coupling of Stokesian Dynamics with the model presented for the colloidal interactions can be achieved by simply imposing a force/torque balance of the following kind:

$$\begin{cases} \mathbf{F}^H = -\mathbf{F}^{coll} \\ \mathbf{T}^H = -\mathbf{T}^{coll} \end{cases} \tag{3.91}$$

where the acceleration term has been neglected given the negligible inertia of the particle and where the terms $\mathbf{F}^{coll}$ and $\mathbf{T}^{coll}$ account for all the forces and torques

arising from the inter-particle interactions evaluated in a pair-additivity manner among all the primary particles. Therefore the linear system of Eq. (3.47) can be rewritten as:

$$\begin{bmatrix} R^{UF} & R^{\Omega F} \\ R^{UT} & R^{\Omega T} \end{bmatrix} \begin{Bmatrix} \mathbf{u}^\alpha - \mathbf{u}^\infty \\ \boldsymbol{\omega}^\alpha - \boldsymbol{\omega}^\infty \end{Bmatrix} = \begin{Bmatrix} \mathbf{F}^{coll} \\ \mathbf{T}^{coll} \end{Bmatrix} - \begin{Bmatrix} R^{EF} \cdot \mathbf{e}^\infty \\ R^{ET} \cdot \mathbf{e}^\infty \end{Bmatrix} \tag{3.92}$$

After introducing the viscous dissipative force of Eq. (3.90) the system reads as:

$$\begin{bmatrix} R^{UF} & R^{\Omega F} \\ R^{UT} & R^{\Omega T} \end{bmatrix} \begin{Bmatrix} \mathbf{u}^\alpha - \mathbf{u}^\infty \\ \boldsymbol{\omega}^\alpha - \boldsymbol{\omega}^\infty \end{Bmatrix} = \begin{Bmatrix} \mathbf{F}^{coll} - \mathcal{K}\left(\mathbf{u}^\alpha - \mathbf{u}^\infty\right) + \mathbf{J} \\ \mathbf{T}^{coll} \end{Bmatrix} - \begin{Bmatrix} R^{EF} \cdot \mathbf{e}^\infty \\ R^{ET} \cdot \mathbf{e}^\infty \end{Bmatrix} \tag{3.93}$$

and after rearranging the terms:

$$\begin{bmatrix} R^{UF} + \mathcal{K} & R^{\Omega F} \\ R^{UT} & R^{\Omega T} \end{bmatrix} \begin{Bmatrix} \mathbf{u}^\alpha - \mathbf{u}^\infty \\ \boldsymbol{\omega}^\alpha - \boldsymbol{\omega}^\infty \end{Bmatrix} = \begin{Bmatrix} \mathbf{F}^{coll} + \mathbf{J} \\ \mathbf{T}^{coll} \end{Bmatrix} - \begin{Bmatrix} R^{EF} \cdot \mathbf{e}^\infty \\ R^{ET} \cdot \mathbf{e}^\infty \end{Bmatrix} \tag{3.94}$$

Therefore, from the solution of Eq. (3.94) the particle linear and angular velocity $\mathbf{u}^\alpha$ and $\boldsymbol{\omega}^\alpha$ are obtained.

Both the inversion of the mobility matrix, performed to apply the lubrication correction, and the solution of the linear system of Eq. (3.94) represent the bottleneck of the entire simulation, since they need to be performed at each time step. The typical computational cost scales with the number of simulated primary particles as $\mathcal{O}\left(n_p^3\right)$ (Ichiki, 2002). Since the time-step is required to be small enough to properly account for the steep variation of the inter-particle interaction, in order to reduce the computational cost, the following approach was adopted (Seto et al., 2012): since the resistance matrix $\mathcal{R}$ and its inverse depend only on the relative distance between the primary particles, both can be safely reused for a certain number of iterations, provided that the variation of the relative distances is limited. Doing so, it is possible to avoid to perform the inversion of the far field mobility matrix $\mathcal{M}^\infty$ at each time step by storing and reusing its inverse $\mathcal{R}^\infty$. The time interval between two subsequent updates was adjusted as $\Delta t_{update} = \frac{0.1 \cdot a}{\max_\alpha |\mathbf{u}^\infty(\mathbf{x}_\alpha)|}$. However, because of its rapidly varying behaviour, the lubrication correction, applied to the far-field resistance matrix, has been updated constantly prior to the solution of Eq. (3.94).

Integration procedure Once their velocities are determined, the trajectories of the particles can be computed by a simple explicit Euler integration scheme:

$$\begin{cases} x|_{t+\Delta t} = x|_t + u_x|_t \cdot \Delta t, \\ y|_{t+\Delta t} = y|_t + u_y|_t \cdot \Delta t, \\ z|_{t+\Delta t} = z|_t + u_z|_t \cdot \Delta t. \end{cases} \tag{3.95}$$

To follow the angular motion a reference system fixed in the particle center has to be created (ϕ, θ, ψ) at the beginning of the simulation. The rate of variation of its

angular position relative to a fixed reference system (x,y,z) can be obtained as:

$$\begin{Bmatrix} \dot{\phi} \\ \dot{\theta} \\ \dot{\psi} \end{Bmatrix} = \mathcal{T} \cdot \begin{Bmatrix} \omega_x \\ \omega_y \\ \omega_z \end{Bmatrix}, \qquad \mathcal{T} = \begin{bmatrix} 1 & \sin\phi\tan\theta & -\cos\phi\tan\theta \\ 0 & \cos\phi & \sin\phi \\ 0 & -\sin\phi/\cos\theta & \cos\phi/\cos\theta \end{bmatrix}. \tag{3.96}$$

where the matrix $\mathcal{T}$ is used to transform the angular velocity components of the particles $(\omega_x, \omega_y, \omega_z)$ with respect to the reference system x,y,z in the rate of variation of the angles ϕ, θ, ζ. At every time t the angular position of the monomers follows from:

$$\begin{cases} \phi|_{t+\Delta t} = \phi|_t + \dot{\phi}|_t \cdot \Delta t, \\ \theta|_{t+\Delta t} = \theta|_t + \dot{\theta}|_t \cdot \Delta t, \\ \psi|_{t+\Delta t} = \psi|_t + \dot{\psi}|_t \cdot \Delta t. \end{cases} \tag{3.97}$$

The length of the time step Δt is a critical choice in DEM simulations. This is due to the steep variation of the forces acting on close monomers. Therefore, care must be taken to properly simulate both the lubrication effects and the colloidal interaction. In this work, in order to avoid interpenetration and, more in general, non-physical behaviour, an adaptive scheme for the choice of the integration step was used: at every iteration, the most critical pairs of close but non-contacting monomers was identified, by looking at their relative distance. After looping over all these pairs, the timestep was set as $\Delta t = \min(\Delta t_b, \Delta t_{opt})$, in which Δt_b is a basis value chosen at the beginning of the simulation and Δt_{opt} is the minimum of the optimal values estimated for all the critical pairs α,β as

$$\Delta t_{opt}^{\alpha,\beta} = \begin{cases} \dfrac{0.02 z_0}{|\mathbf{u}_\alpha - \mathbf{u}_\beta|} & \text{if} \quad h < 10 z_0 \\ \dfrac{0.5 z_0}{|\mathbf{u}_\alpha - \mathbf{u}_\beta|} & \text{if} \quad h < 100 z_0 \\ \dfrac{5 z_0}{|\mathbf{u}_\alpha - \mathbf{u}_\beta|} & \text{otherwise} \end{cases} \tag{3.98}$$

with h being the surface-to-surface distance and z_0 the minimum approach distance. In this way it was possible to capture all the near-contact effects when particles are close to each other and adopt a longer timestep when particles are far apart, thus reducing the computational cost of the simulation. Typically the length of the time-step ranged from 10^{-7} to 10^{-10} s.

3.3 Quality of the simulations and computational performance

In this section, in order to validate the developed DEM, the results of some static and dynamic simulations are shown. When possible a comparison with previously reported data is shown.
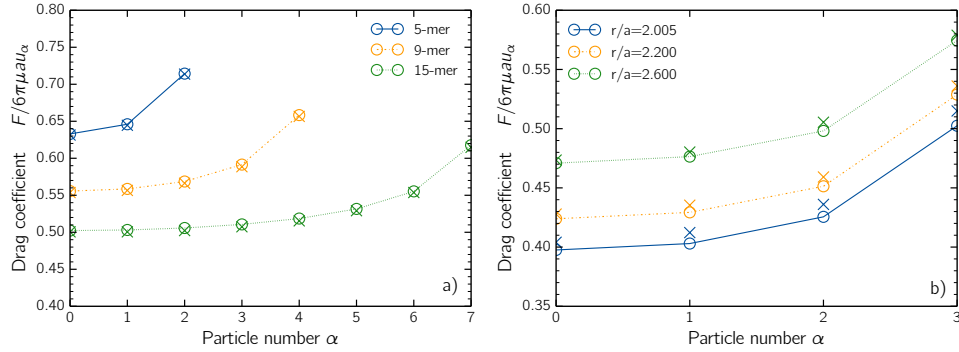
Figure 3.11: Drag coefficient $\lambda = F/6\pi\mu au_\alpha$ for horizontal chains of non-touching particles. Comparison between the values computed by the developed DEM method (circles) and the results by Ganatos et al. (1978) (x marks). Given the symmetry of the system, only the drag coefficient of one half of the chain is reported. a) Drag coefficient of 5,9,15-particles chains. Particle spacing is fixed and equal to 4 radii. b) Drag coefficient for a 7-particle chain for 3 different values of the dimensionless particle spacing r/a.

3.3.1 Drag coefficient for sedimenting chains

The first considered case is the one of horizontal chains of non-touching particles, sedimenting in a quiescent fluid along the direction perpendicular to the line connecting their centers. The results are compared with those obtained by Ganatos et al. (1978) via a collocation technique. Figure 3.11a reports the drag coefficient of each particle computed as $\lambda = F/6\pi\mu au_\alpha$, where F is the applied force and u_α is the sedimenting velocity. The figure reports the data relative to 5,9,15-particles chains. As apparent an excellent agreement with the results by Ganatos et al. (1978) was obtained. The data show that as length of the chain is increased, the particles experience a reduced drag and, as a consequence, they sediment faster. Regardless of the chain length, the central particle always show the larger sedimenting velocity and, for the particular case of the 15-particles chain, this velocity is approximately twice the sedimenting velocity of an isolated particle.

Figure 3.11b shows the drag coefficient of a 7-particles sedimenting chain for 3 different values of the particle spacing r/a. The agreement with the results provided by Ganatos et al. (1978) is still fairly good; the maximum discrepancy between the two set of data is about 2.4%. From the data it is possible to infer that the settling velocity of the chain increases as the gap between the particle is reduced, thus showing the role of particle crowding on the sedimentation behaviour. However it is worth to mention that, since the particle configuration changes dynamically during sedimentation, the results are referred to the initial configuration. Both cases provide evidence that the developed DEM addresses properly the modelling of hydrodynamic interactions.
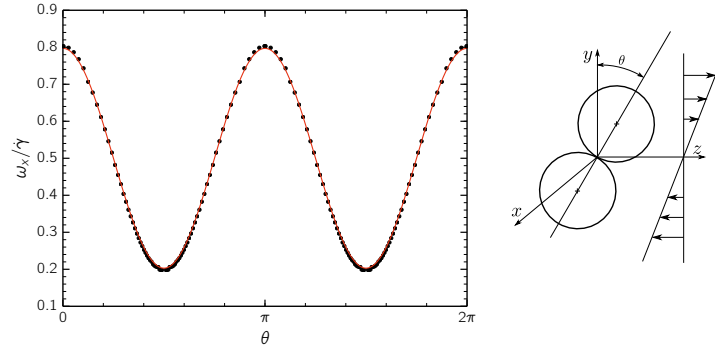
Figure 3.12: Angular velocity of a dimer in shear flow as a function of the orientation. The red curve is the analytical solution of Eq. (3.99); the black dots represent the simulation data.

3.3.2 Dimer in shear flow

The second considered case is the motion of a doublet of touching particles in a uniform shear flow with a velocity gradient $\dot{\gamma} = du_z^\infty/dy$. If the doublet axis lies on the $y-z$ plane, in creeping flow conditions, the doublet rotation can be described analytically as (Nir, Acrivos, 1973):

$$\omega_x = -\frac{1}{2}\dot{\gamma}\left[1 + 0.594\cos\left(2\theta\right)\right], \quad \omega_y = \omega_x = 0 \tag{3.99}$$

where θ is the angle between the doublet axis and the velocity gradient direction y. As apparent from Fig. 3.12 a very good agreement between the analytical solution and the simulation data is achieved; the angular velocity of the doubled exhibits a sinusoidal trend, with the angular velocity oscillating periodically between a maximum and minimum value. The maximum value corresponds to the maximum alignment of the doublet axis with the velocity gradient direction, whereas the minimum occurs when the doublet axis is aligned with the flow direction.

3.3.3 Aggregation and breakup of clusters

Finally, to show qualitatively the capability of the DEM in simulating aggregation and breakup events, two sequences of snapshots are reported. In Fig. 3.13 an aggregation event between two clusters composed by 61 and 57 primary particles, respectively, is shown. The clusters are suspended in a uniform shear flow $\dot{\gamma} = du_z^\infty/dy$. As apparent both the translational and angular motion of each primary particle is tracked. The event can be ideally divided in three subsequent steps: the approaching stage, during which the clusters move towards each other, while rotating about their center of mass; the formation of a new bond between two of their constituent primary particles; the restructuring step (not shown in the figure) during which the newly generated aggregate is restructured by the viscous stress of the flow field. During this phase other bonds in the aggregate structure may be formed.
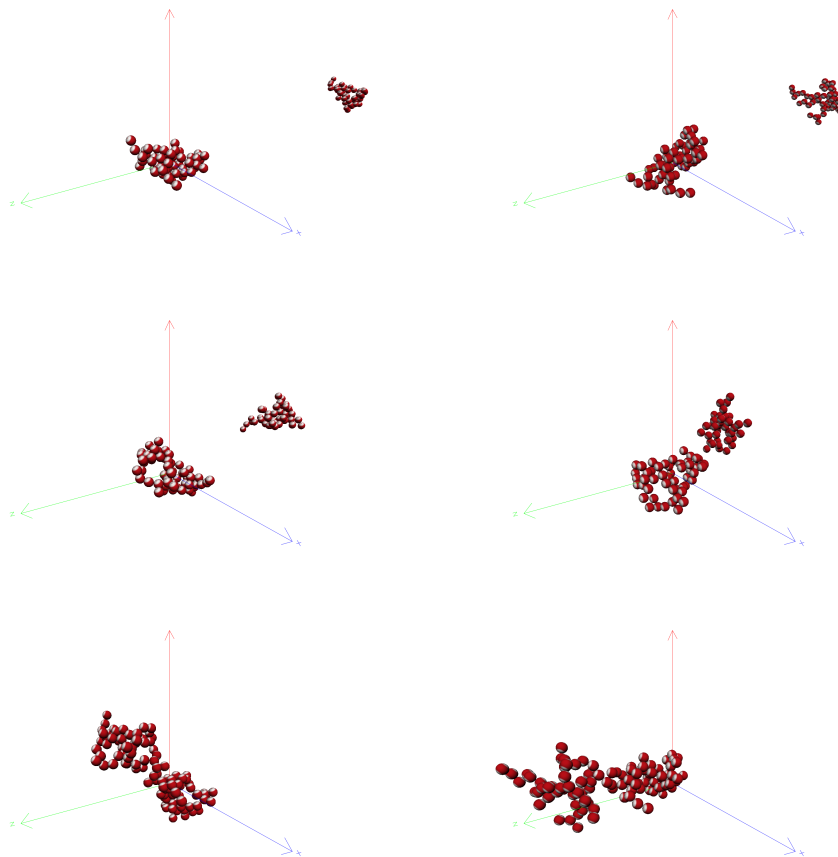
Figure 3.13: Snapshots of an aggregation event in simple shear flow ($\mu\dot{\gamma} = 0.01$ Pa). Primary particle radius is 500 nm. The total simulated time is 2.2 s.
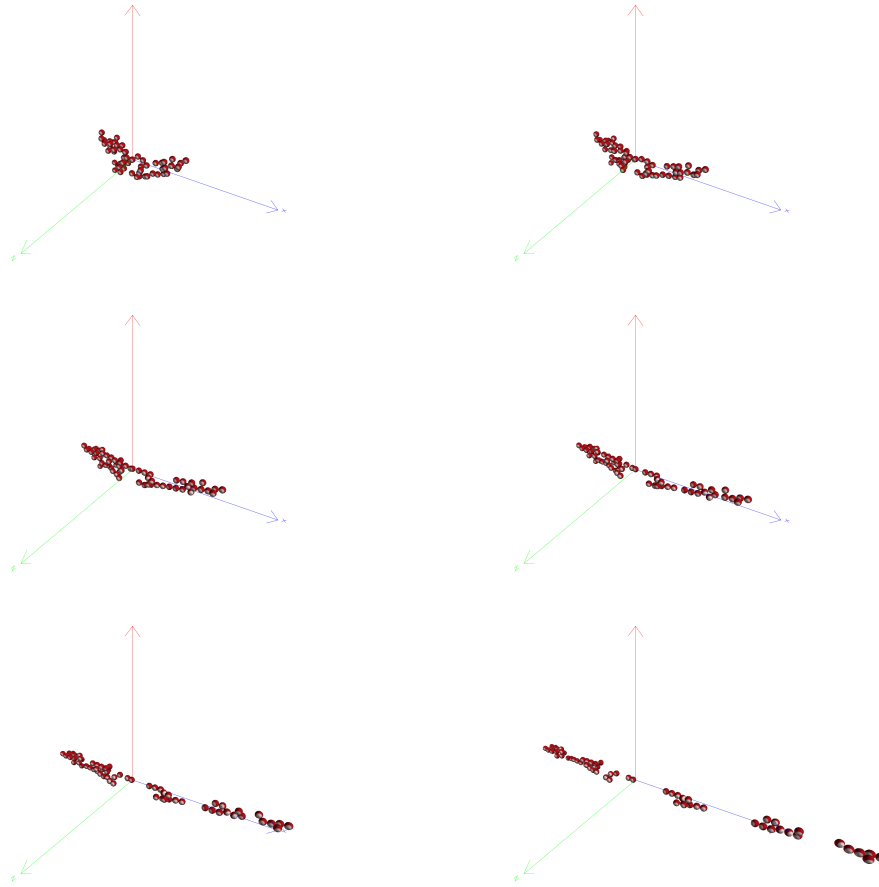
Figure 3.14: Snapshots of a breakup event in elongational flow ($\mu\dot{\gamma} = 1000$ Pa). The cluster is composed by 64 primary particle of radius 100 nm. The total simulated time is 0.016 s.

A breakup event may occur when the hydrodynamic force exceeds the cluster strength. In this condition, the cluster fails in the most stressed locations, giving birth to a number of smaller fragments. Figure 3.14 shows a sequence of snapshots of such an event: the center of mass of a 64-particle cluster is placed in the stagnation point of a uni-axial extensional flow of constant intensity $\mu\dot{\gamma} = 1000$ Pa. As apparent, the aggregate is first stretched along the flow direction and, at a later stage, it fails. The first bond to fail is approximately located in the center of mass of the cluster. However, after this first event, a cascade of bond failure events occurs leading, in this particular case, to the generation of 7 fragments, each of which is composed by a number of primary particles ranging from 2 to 14. It is interesting to note that the smaller fragments are generated around the stagnation point of the flow, where the propagation and accumulation of stresses causes the rupture of a larger number of bonds.
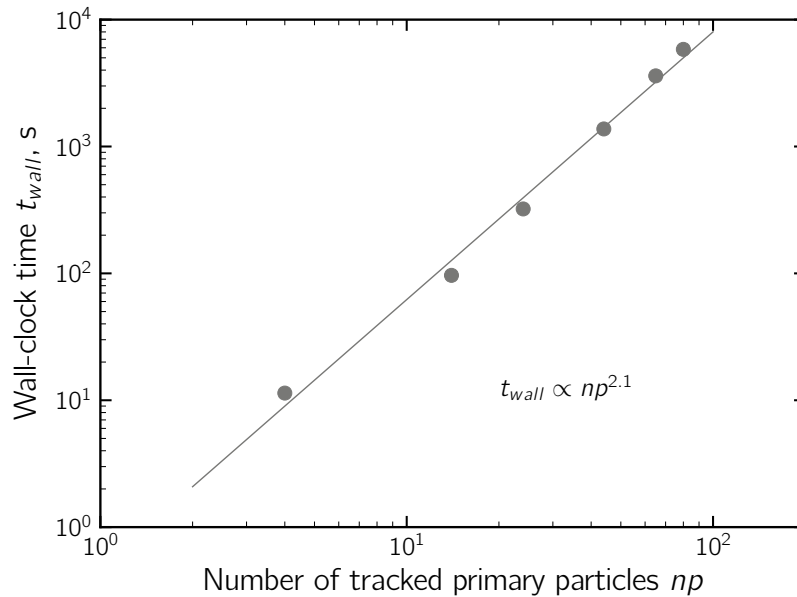
Figure 3.15: Wall-clock time as a function of the number of tracked primary particles. The data were obtained from the simulations of the shear-induced rotation of clusters of different sizes. For all data, the simulated time is 0.06 s.

3.3.4 Computational performance

To conclude this chapter it is finally worth to analyse the computational performance of the developed DEM. To this purpose, different DEM simulations of the shear-induced rotation of clusters of different sizes were performed. The data are reported in Fig. 3.15, where the wall-clock time needed to perform the DEM simulation is plotted against the number of tracked primary particles. It is apparent that the simulation time quickly increases as the n_p grows. Therefore, one can easily conclude that the simulation of even few seconds of the aggregation process of a statistically significant sample of particles would be extremely demanding.

References

Batchelor, G. K., Green, J. T. 1972. "The hydrodynamic interaction of two small freely-moving spheres in a linear flow field". *Journal of Fluid Mechanics* 56. 375–400.

Becker, V., Briesen, H. 2008. "Tangential-force model for interactions between bonded colloidal particles". *Physical Review E* 78. 061404.

Becker, V., Schlauch, E., Behr, M., Briesen, H. 2009. "Restructuring of colloidal aggregates in shear flows and limitations of the free-draining approximation". *Journal of Colloid and Interface Science* 339. 362–372.

Berg, J. C. (2010). *An introduction to interfaces & colloids: the bridge to nanoscience.* 1st edition. World Scientific.

Bird, R. B., Stewart, W. E., Lightfoot, E. N. (2002). *Transport phenomena*. John Wiley & Sons, New York (NY).

Bowen, W. R., Jenner, F. 1995. "The calculation of dispersion forces for engineering applications". *Advances in colloid and interface science* 56 201–243.

Brady, J. F., Bossis, G. 1988. "Stokesian dynamics". *Annual Review of Fluid Mechanics* 20. 111–157.

Cundall, P. A., Strack, O. D. 1979. "A discrete numerical model for granular assemblies". *Geotechnique* 29. 47–65.

Durlofsky, L., Brady, J. F., Bossis, G. 1987. "Dynamic simulation of hydrodynamically interacting particles". *Journal of Fluid Mechanics* 180 21–49.

Eggersdorfer, M., Kadau, D, Herrmann, H., Pratsinis, S. 2010. "Fragmentation and restructuring of soft-agglomerates under shear". *Journal of Colloid and Interface Science* 342. 261–268.

Ganatos, P., Pfeffer, R., Weinbaum, S. 1978. "A numerical-solution technique for three-dimensional Stokes flows, with application to the motion of strongly interacting spheres in a plane". *Journal of Fluid Mechanics* 84. 79–111.

Guazzelli, E., Morris, J. F. (2011). *A physical introduction to suspension dynamics*. 1st edition. Cambridge University Press.

Hamaker, H. C. 1937. "The London—Van der Waals attraction between spherical particles". *Physica* 4. 1058–1072.

Higashitani, K., Iimura, K. 1998. "Two-dimensional simulation of the breakup process of aggregates in shear and elongational flows". *Journal of Colloid and Interface Science* 204. 320–327.

Hogg, R., Healy, T. W., Fuerstenau, D. 1966. "Mutual coagulation of colloidal dispersions". *Transactions of the Faraday Society* 62. 1638–1651.

Hunter, R. J. (1981). *Zeta potential in colloid science: principles and applications*. 1st edition. Vol. 2. Academic press, San Diego (CA).

Ichiki, K. 2002. "Improvement of the Stokesian dynamics method for systems with a finite number of particles". *Journal of Fluid Mechanics* 452. 231–262.

Inci, G., Arnold, A., Kronenburg, A., Weeber, R. 2014. "Modeling nanoparticle agglomeration using local interactions". *Aerosol Science and Technology* 48. 842–852.

Israelachvili, J. N. (2011). *Intermolecular and surface forces*. 3rd edition. Academic press.

Johnson, K., Kendall, K, Roberts, A. (1971). "Surface energy and the contact of elastic solids". *Proceedings of the Royal Society of London A: Mathematical, Physical and Engineering Sciences*. Vol. 324 301–313.

Kappl, M. et al. (2009). *Surface and interfacial forces*. John Wiley & Sons.

Kim, S., Karrila, S. J. (1991). *Microhydrodynamics: principles and selected applications*. Butterworth-Heinemann.

Mahanty, J, Ninham, B. W. *Dispersion forces*. 1st edition. Academic press, London (UK).

Marshall, J. 2009. "Discrete-element modeling of particulate aerosol flows". *Journal of Computational Physics* 228. 1541–1561.

Nir, A., Acrivos, A. 1973. "On the creeping motion of two arbitrary-sized touching spheres in a linear shear field". *Journal of Fluid Mechanics* 59. 209–223.

Ohshima, H. 1994. "Electrostatic interaction between two dissimilar spheres: an explicit analytic expression". *Journal of Colloid and Interface Science* 162. 487–495.

Pantina, J. P., Furst, E. M. 2005. "Elasticity and critical bending moment of model colloidal aggregates". *Physical Review Letters* 94. 138301.

Schenkel, J., Kitchener, J. 1960. "A test of the Derjaguin-Verwey-Overbeek theory with a colloidal suspension". *Transactions of the Faraday Society* 56. 161–173.

Schlauch, E., Ernst, M., Seto, R., Briesen, H., Sommerfeld, M., Behr, M. 2013. "Comparison of three simulation methods for colloidal aggregates in Stokes flow: Finite elements, lattice Boltzmann and Stokesian dynamics". *Computers & Fluids* 86. 199–209.

Seto, R, Botet, R, Auernhammer, G., Briesen, H. 2012. "Restructuring of colloidal aggregates in shear flow: coupling interparticle contact models with Stokesian dynamics." *The European physical Journal E, Soft Matter* 35. 9805.

Seto, R., Mari, R., Morris, J. F., Denn, M. M. 2013. "Discontinuous shear thickening of frictional hard-sphere suspensions". *Physical Review Letters* 111. 218301.

Wiese, G., Healy, T. 1970. "Effect of particle size on colloid stability". *Transactions of the Faraday Society* 66. 490–499.

Chapter 4

MC–DEM coupling

In a stirred colloidal suspension different phenomena take place simultaneously such as aggregation, breakage and restructuring of the aggregates. However, in the context of PBE, the rigorous modelling of such phenomena is still a challenging task. As discussed in Chapter 2, the rectilinear approach by Smoluchowski (1917) does not take into account the interaction between approaching particles, thus it needs to be integrated with proper models for the aggregation efficiency. However, while the aggregation efficiency of spherical particles has been widely investigated, a model for the aggregation efficiency of clusters is still missing.

Similarly, a problem arises when modelling breakage phenomena: the breakup of an aggregate in a uniform shear flow occurs almost instantaneously once its size has grown over a certain critical value. This makes indeed the modelling in PBE of such a behaviour extremely difficult. In addition, the lack of reliable models for the fragment mass distribution further complicates this task.

Recently, the importance of restructuring phenomena has been recognized for the dynamics of aggregation-breakup processes; the reason is twofold: firstly, the compaction of the aggregate structure induced by the viscous stresses is responsible for reducing the aggregate capture section and therefore for lowering the pair aggregation rate. Secondly, the breakage behaviour of the aggregates is strongly dependent on the morphology and to its intricate evolution under the action of viscous stress (Becker, Briesen, 2010; Harada et al., 2006; Horii et al., 2015). For these reasons, it is necessary in principle to use multivariate population balance equation in which the fractal dimension, the surface area (or any other relevant quantity related to the morphology of the aggregate) is employed alongside the aggregate size. Particle surface area as a second internal variable was introduced for instance by Koch, Friedlander (1990) and Tandon, Rosner (1999) to take into account particle coalescence, but the evolving aggregate morphology was assumed to have no influence on the aggregation rate, considered to be only a function of particle volume. A bivariate population balance formalism which accounts for the joint evolution of aggregate size and fractal dimension was developed by Kostoglou, Konstandopoulos (2001) and applied to model aggregate compaction by including a restructuring rate in the PBE. However, several arbitrary choices have to be made to model such a term.
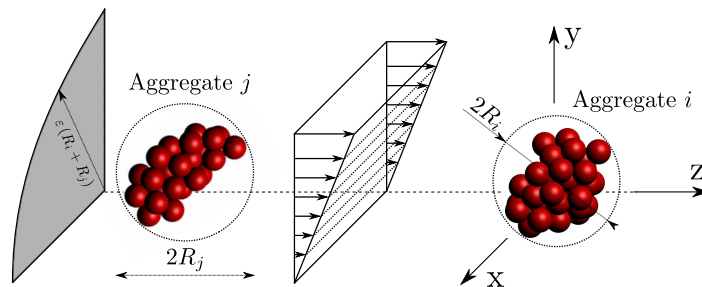
Figure 4.1: Schematic of an encounter between aggregates i and j in a reference frame moving with particle i. The gray area represents a quarter of the encounter cross-section for the process: if aggregate j flows through such section, a close encounter between the two particles is expected.

Discrete Element Method simulations are better suited to follow the dynamical behavior of a dispersed system. As explained in Chapter 3, a DEM is able to track the trajectory of each primary particle (isolated or bond to others to form a cluster), thus allowing to gain profound insight both in the suspension dynamics and in the cluster morphology (Camejo et al., 2014; Isella, Drossinos, 2010; Marshall, 2009). However, the high computational cost of DEM simulations has restricted so far their application to small populations or even to the investigation of the behaviour of single aggregates (Seto et al., 2012; Seto et al., 2011; Vanni, Gastaldi, 2011).

In this work, a mixed stochastic-deterministic method has been developed and applied to study the dynamics of a dilute and well-mixed colloidal suspension under the effect of a shear flow. In order to circumvent the high computational cost typically associated to pure DEM simulations, the method is built on a combination of the mean-field approach of PBE (solved in a stochastic way by means of a Monte Carlo algorithm) with detailed DEM simulations. The basic idea behind such a combination is that if a suspension is sufficiently dilute its dynamics can be described by a sequence of binary encounter events between the suspended particles, each of which can result into an aggregation, a breakage, a restructuring of the aggregates or into any combination of these phenomena. Therefore, the MC is used to sample a statistically expected sequence of such events and the DEM is used to accurately simulate them. Hence, through this coupling, the DEM method is used to track the motion of just two clusters at a time, thereby reducing significantly the computational cost of the method.

The only event taken into account by the MC is the near-encounter between pairs of particles. Each near-encounter can result into three main outcomes, that are recognized on the basis of the number of particles detected at the end of the DEM simulation; the first possibility is the missed aggregation: the aggregates pass close to each other without colliding. Therefore the DEM simulation returns two aggregates composed by the same number of primary particles they had before their encounter. The second possibility is the aggregation: the involved aggregates come into mechanical contact, sticking to each other and generating a new single aggregate. The last possibility consists in the breakup: the two approaching aggregates collide and

form a new aggregate whose dimension is larger than the critical one. In such a case the aggregate undergoes an almost instantaneous breakup soon after its generation, giving birth to a number of smaller fragments. As already explained in Chapter 2, this breakup dynamics is a characteristic of spatially uniform shear flows for which breakup occurs when aggregates grow over a dimension R such that $\dot{\gamma}_{cr}(R) < \dot{\gamma}$ or, equivalently, for fixed aggregate size, when the shear rate is increased over the critical value bearable by the aggregate.

In order to setup the Monte Carlo algorithm, a model is needed to evaluate the frequency of a near encounter i.e., the probability for a certain pair of aggregates to meet each other in the suspension, collide and possibly undergo breakage. In this regard, Fig. 4.1 shows two aggregates, i and j, approaching each other in a shear flow field in a reference frame moving with aggregate i. The size of an aggregate is characterized by its external radius, which is the maximum distance between the surface of a primary particle and the center of mass of the aggregate: $R = \max_k(|\mathbf{x}_k - \mathbf{x}_{cm}|) + a$, where $|\mathbf{x}_k - \mathbf{x}_{cm}|$ is the distance of the k-th primary particle, with radius a, from the center of mass of the aggregate. If the aggregates were two solid spheres of radii R_i and R_j and no colloidal or lubrication interaction acted between them (as in the original approach by Smoluchowski for shear coagulation (Smoluchowski, 1917)), particle j would eventually collide with particle i if its center of mass crosses the circular collision cross section of radius $(R_i + R_j)$, located on a $z = $ constant plane far upstream of particle i. As shown in Chapter 2, the expected frequency for this type of collision in a volume ΔV is:

$$f_{ij} = \frac{4}{3}\dot{\gamma}(R_i + R_j)^3 n_i n_j \Delta V \tag{4.1}$$

where n_i and n_j are the expected number concentrations of particles i and j, both equal to $1/\Delta V$, because only one i-particle and one j-particle are present in the subvolume. However, the irregular shape of the particles and the presence of hydrodynamic interactions changes the probability of contact. Hence, passing through the cross-section does not necessarily lead to a an aggregation. This is why the rate given by Eq. (4.1) has been regarded as the frequency at which a close encounter is expected between i and j, with the actual outcome of the encounter being ascertained a posteriori with the detailed DEM simulation. Finally, to gain even more generality, it is convenient to define the encounter cross section for the couple of particles i and j as the circular section of radius $\varepsilon(R_i + R_j)$, where ε is a parameter of order unity, chosen in such a way to capture all collision events. Typically, ε is slightly smaller than the unity for the interaction of primary particles at low shear rates and can be reduced considerably for the encounter of large and less compact aggregates under intense shear rates. Therefore, in the end, the encounter frequency between i and j particles reads as:

$$f_{ij}^e = \frac{4}{3}\dot{\gamma}\frac{\varepsilon^3 (R_i + R_j)^3}{\Delta V} \tag{4.2}$$

However, at the risk of being redundant, it is worth to emphasize that, differently from Smoluchowski analysis, this information has been used to model solely the encounter
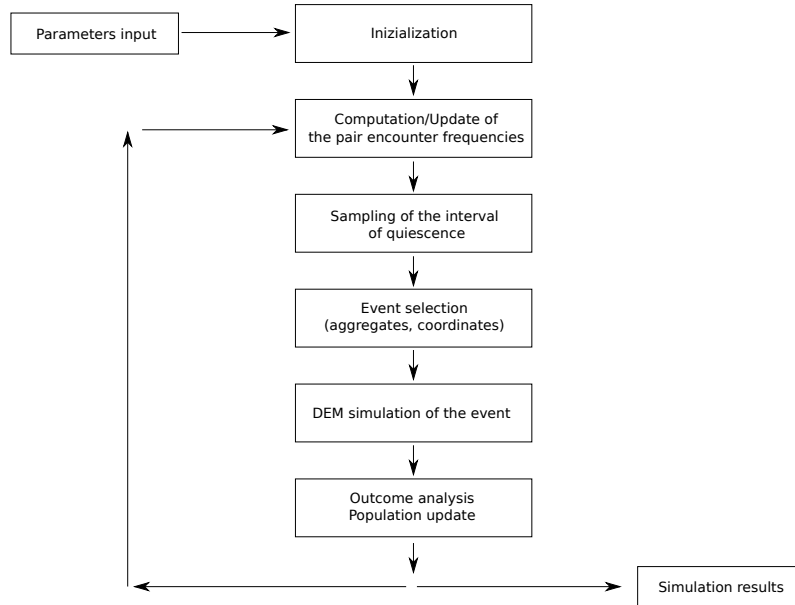
Figure 4.2: Flowchart of the MC-DEM simulation technique.

frequency between pairs of clusters with the actual outcome being evaluated with a DEM simulation.

In the following a detailed description of the overall method is presented.

4.1 Summary of the simulation procedure

The MC method adopted is an event-driven, rejection-free algorithm and can be divided in a sequence of 6 steps. Figure 4.2 reports the flowchart of the method. The initial two steps are the initialization of the particle population and the computation of the encounter frequencies, which are followed by a repeating loop of 4 subsequent steps:

1. *Initialization of the simulation*

At the beginning of the simulation a value for the solid fraction of the suspension and an initial distribution for the size and the morphologies of the aggregates of the population are chosen; the main informations regarding the aggregates are stored in two arrays P and R, whose elements P_i and R_i contain respectively the number of primary particles forming the i-th aggregate and its outer radius. Furthermore, the geometry of each aggregate is also stored, reporting the spatial coordinates of all the constituent monomers expressed in a reference system centred in the center of mass of the aggregate they belong to. No assumption has been made on the spatial distribution of the aggregates in the sample, since this information is not crucial for a dilute and well-mixed suspension.
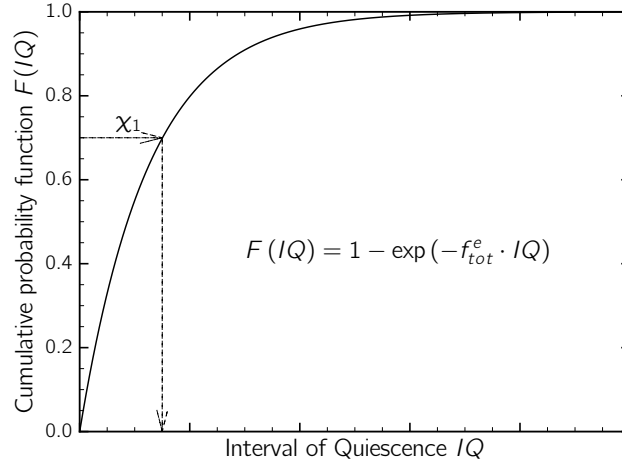
Figure 4.3: Representation of the procedure adopted to sample stochastically the interval of quiescence. χ_1 is a random number drawn from a uniform distribution between 0 and 1.

2. *Computation of the pair near-encounter frequencies*

The frequencies of near-encounters between each pair of aggregates i,j are computed, according to Eq. (4.2), and stored in a matrix of dimension $N_p \times N_p$, with N_p being the number of particles in the simulated volume; since the expression of the frequency is symmetric ($f_{ij}^e = f_{ji}^e$), the resulting matrix is symmetric as well.

3. *Sampling of the interval of quiescence*

At any time t, in the presence of N_p suspended particles, the total encounter frequency is given by:

$$f_{tot}^e\left(t\right) = \sum_{i=1}^{N_p} \sum_{j=i+1}^{N_p} f_{i,j}^e\left(t\right) \tag{4.3}$$

From this piece of information an interval of quiescence IQ separating two subsequent encounter events can be inferred (Shah et al., 1977). Since the encounters are stochastic in nature, the time elapsing between two encounters can be estimated resorting to a probability distribution. As prescribed by Shah et al. (1977), a cumulative probability distribution function of the following kind has been used:

$$F\left(IQ\right) = 1 - \exp\left(-f_{tot}^e \cdot IQ\right) \tag{4.4}$$

Therefore the IQ can be estimated by sampling a random number χ_1, drawn from a uniform distribution between 0 and 1, and resorting to the cumulative distribution function of Eq. (4.4). In Fig. 4.3 a schematic representation of the technique is depicted. This approach is generally referred to as event-driven and it has been preferred over the time-driven approach because it allows to sample a time interval between two subsequent events in a completely self-regulated way: the IQ in fact adapts itself to the total encounter frequency, with no need of a predetermined
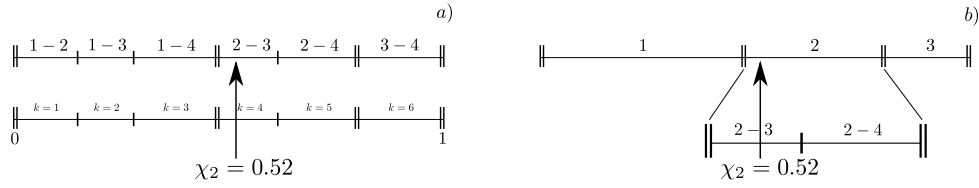
Figure 4.4: Representation of two procedures to sample the aggregating pair for a small population composed by 4 particles. a) Inversion method. b) Modified inversion method.

discretization of time. In Appendix D the argument that leads to the exponential distribution of Eq. (4.4) is illustrated.

4. *Event selection*

Once determined the time at which a new encounter occurs, the Monte Carlo method is used to sample the aggregates involved. The probability of each event k involving a pair i,j can be computed as:

$$Pr_k = \frac{f^e_{ij|k}}{f^e_{tot}} \tag{4.5}$$

Therefore, after properly ordering the list of possible events (Fig. 4.4a), by picking a random number χ_2 from a uniform distribution between 0 and 1, the chosen event is the one with index q that satisfies the following relationship:

$$\sum_{k=1}^{q-1} f_{ij|k} < f^e_{tot} \cdot \chi_2 < \sum_{k=1}^{q} f_{ij|k} \tag{4.6}$$

where q can assume any value from 1 to $N_p(N_p - 1)/2$. This procedure is known as *inversion method* and it can be used for any probability distribution with a discrete set of states. However, it can become prohibitive when N_p is large, in that it requires to perform time-consuming summations. Therefore, a variant of the *inversion method* has been used (Kruis et al., 2000). In this case only the sum of all the possible encounter rates for each particle i is computed as $S_i = \sum_{j \neq i}^{N_p} f^e_{ij}$. Therefore, the condition of Eq. (4.6) can be rewritten as a sequence of two steps (Kruis et al., 2000):

$$S_{i-1} \leq f^e_{tot} \cdot \chi_2 \leq S_i$$
$$S_{i-1} + \sum_{j=i+1}^{j-1} f^e_{ij} \leq f^e_{tot} \cdot \chi_2 \leq S_{i-1} + \sum_{j=i+1}^{j} f^e_{ij} \tag{4.7}$$

This modified version of the inversion method, intuitively depicted in Fig. 4.4b, has been adopted for the present work and preferred over the also frequently used acceptance-rejection method; by this method a pair i,j is selected completely at
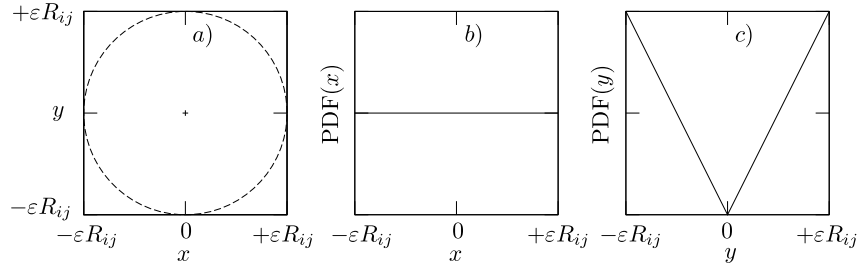
Figure 4.5: Encounter cross section on a $x - y$ plane (graph a) and distribution of the probability that aggregate j crosses the plane at given x (graph b) and y (graph c) coordinates.

random, independently of its encounter probability, and it is accepted if:

$$\chi_2 < \frac{f_{ij}^e}{\max\left(f_{ij}^e\right)} \tag{4.8}$$

where χ_2 is again a number sampled from a uniform distribution between 0 and 1. If the pair is rejected a new number χ_2 is selected and the procedure repeated until the condition of Eq. (4.8) is met. This method requires the computation of one encounter frequency at time and it does not require neither to store data nor to compute the long summations of Eq. (4.6). However, as pointed out by Kruis et al. (2000), this technique has two relevant drawbacks: first, it may introduce a substantial error in the computation; second, it can considerably slow down the computation in some specific situations: in fact when the range of particle sizes increases, the ratio of the collision rate and the maximum collision rate becomes very small and a large number of rejections should be expected. For these reasons it was disregarded in favour of the modified inversion method.

Before launching the DEM simulation of the event, the MC is also used to select the initial coordinates of the aggregates. At the beginning of each encounter the center of mass of aggregate i is placed in the origin of the reference system (Fig. 4.1); aggregate j is instead located far upstream from aggregate i and inside the encounter cross section. Its exact position has to be determined on the basis of statistical considerations. Far from aggregate i the translational velocity of aggregate j equals the undisturbed fluid velocity, $\dot{\gamma} y \mathbf{e}_z$, which is linearly increasing with y and independent from x. The probability for particle j to cross the encounter cross section should reproduce such a distribution. If we examine the square of size $\varepsilon(R_i + R_j)$ enclosing the encounter cross section, as shown in graph a) of Fig. 4.5, the initial coordinates (x_j^0, y_j^0) for aggregate j can be found by picking up a pair of random numbers from a uniform probability distribution for x (graph b) and a linear probability distribution for y (graph c), respectively. The sampling is repeated until the relation $\sqrt{x_j^{0^2} + y_j^{0^2}} \leq \varepsilon(R_i + R_j)$ is satisfied, in order to place the center of mass of the aggregate j inside the encounter cross section. The z_j^0-coordinate is set equal to $\pm 5(R_i + R_j)$ (with the $\pm$ sign decided according to the sign of the y coordinate):

at this distance the long-ranged hydrodynamic interactions acting between the two approaching aggregates are very small and we can reasonably assume that, in this initial configuration, the particles have a negligible effect on each other, thus they both have the same velocity as the undisturbed fluid flow.

5. *DEM simulation*

The next step consists in the simulation by means of the DEM of the encounter event between the two sampled aggregates. Each encounter has to be simulated for a time long enough to allow the aggregates to approach from their initial position, collide and either reach a stable configuration through the rearrangement of the monomers or undergo breakup. In non-dimensional terms, the time needed by the DEM simulation was estimated as:

$$\dot{\gamma}t_s = \frac{|z_j^0| - (R_i + R_j)}{y_j^0} + 4\pi N_{rot} \qquad (4.9)$$

where the first term approximates the time required for contact (z_j^0 and y_j^0 are the initial coordinates of the aggregate j, while aggregate i is initially in the origin of the reference system); N_{rot} is the approximate number of rotations the aggregate generated upon collision undergoes before the DEM simulation is stopped, assuming an angular velocity of $\dot{\gamma}/2$; a value of $N_{rot} = 8$ has been used based on what recently reported by Ren et al. (2015), who showed that 8 rotations are enough to allow the aggregates to rearrange their internal structure or to allow the aggregates to undergo breakup. However, it should be pointed out that the assumption of a period of rotation equal to $\dot{\gamma}/2$ is a simplification of the reality: only perfectly round-shaped particles exhibit such period of rotation, whereas elongated aggregates generally present a longer one (Frappier et al., 2010). However, test simulations showed that the time of Eq. (4.9) is large enough to assure a certain relaxation of the aggregates either formed upon aggregation or upon breakage.

On the basis of the outcome of the encounter simulated by the DEM, the information relative to the population are updated. In the case of a missed aggregation the two aggregates pass close to each other without colliding and with no change in the number of constituent primary particles. Therefore no update of the array P is needed:

$$\begin{cases} P_i^{new} = P_i^{old} \\ P_j^{new} = P_j^{old} \end{cases} \qquad (4.10)$$

In Eq. (4.10) the superscript *old* and *new* are referred to the elements of the vector P before and after the DEM simulation. On the contrary the outer radii are updated according to the detected final geometries of the aggregates.

$$\begin{cases} R_i^{new} = \text{computed from new geometry} \\ R_j^{new} = \text{computed from new geometry} \end{cases} \qquad (4.11)$$
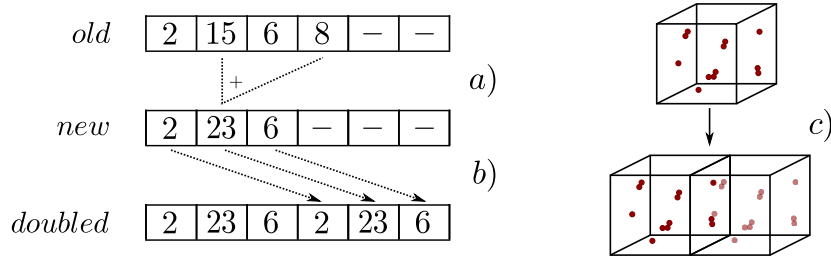
Figure 4.6: a) Representation of the procedure to update the particle array after an aggregation event for a small population. The numbers in the array indicate the number of constituent primary particles. b), c) Representation of the *topping-up* approach (Liffman, 1992).

Even if no collision occurred in fact, the fluid stresses exerted by the fluid and the hydrodynamic interaction between the aggregates may have rearranged the positions of the primary particles, deforming the overall morphology of the aggregates.

In the case of an aggregation, the aggregate collided, leading to the generation of a new larger aggregate, with the consequent net loss of an aggregate from the population. In such a case both the vector P and R need to be updated. Regarding the vector P the update is performed as:

$$\begin{cases} P_i^{new} = P_i^{old} + P_j^{old} \\ P_j^{new} = P_{N_p}^{old} \\ P_{N_p}^{new} = 0 \end{cases} \tag{4.12}$$

where the old i-th element of the P array is replaced by the sum of the number of primary particles composing the two initial clusters; the last element of the array is instead moved, replacing the disappeared j-th cluster. The technique is illustrated in Fig. 4.6a. Furthermore the R array is updated, as well as the morphologies of the aggregates.

The third possibility consists in the generation of three or more aggregates as outcome of the DEM simulation. This phenomenon can be explained by the breakup, in three or more fragments of the newly generated aggregate. Therefore, when a number of fragments $\nu_f > 2$, each composed by $P_1, P_2, ...P_m$ primary particles, is generated:

$$\begin{cases} P_i^{new} = P_1 \\ P_j^{new} = P_2 \\ \overline{P_{N_p+(m-2)}^{new} = P_m \quad m = 3, ...\nu_f} \end{cases} \tag{4.13}$$

In a similar way also the R array and the geometries are updated. Finally it is worth to point out that the eventuality of a binary breakage after a collision, with or without an exchange of primary particles between the two initial aggregates, can be easily managed in a way similar to the case of a missed collision.
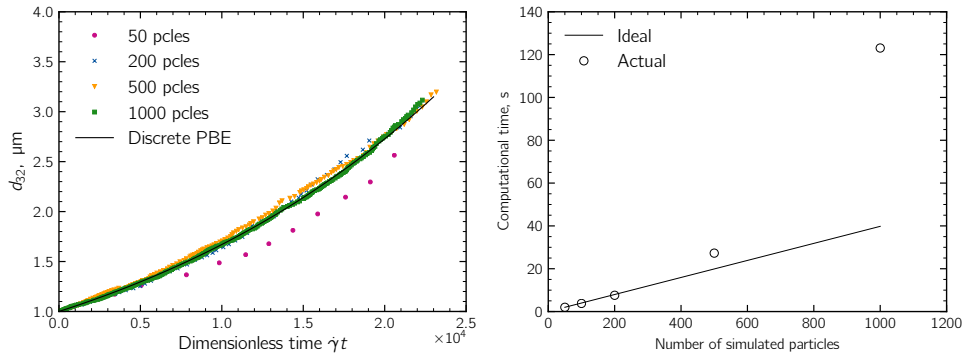
Figure 4.7: Comparison of the temporal trend of the Sauter diamater d_{32} as obtained from the discrete PBE and the MC simulation for different values of the number of simulated particles (left plot). Wall clock time of the MC simulations as a function of the number of simulated particles (right plot).

If aggregation prevails on breakup, the reduction of the number of simulated aggregates does not allow to get statistically reliable result. Several approach have been used to circumvent this problem (Liffman, 1992; Smith, Matsoukas, 1998). In this work the procedure by Liffman (1992) was adopted: whether the number of simulated aggregates falls below a critical value, the volume of the subsystem is doubled and every aggregate present is cloned; this approach, referred to as *topping-up*, is equivalent to adding an exact copy of the subsystem to itself and allows to preserve the particle size distribution as well as the suspension solid fraction. The critical value as been set equal to $N_{a,min} = 3/4 N_{a,0}$. In Fig. 4.6b),c) the technique is intuitively described. In the opposite case of prevailing breakup, no particular action has been adopted; during simulations, the breakage events never led to such a proliferation of particles to ask for a halving strategy.

6. *Frequency update* Due to the changes in geometry, the birth of new aggregates and the death of old ones originated by the aforementioned events, the encounter frequencies involving any of the aggregates returning from the DEM simulation are updated or calculated ex-novo, updating the frequency matrix. Different approaches may be used to carry out such a task, minimizing the number of operation to be performed. However, given that the bottleneck of the whole technique is represented by the DEM simulations, no particular strategy has been adopted.

When all the information relative to the population have been updated, the step from 3 to 6 are covered again until the desired number of events has been simulated.

4.1.1 Test case - Purely aggregating suspension

In order to validate the MC technique a simple test case was run. A purely aggregating suspension subject to a uniform shear flow of intensity $\dot{\gamma} = 10$ s^{-1} was simulated by using both the discrete formulation of PBE and the event-driven MC algorithm developed; the simulations were started from monomeric conditions i.e, the suspension was initially composed by isolated primary particles. The particles have radius 500
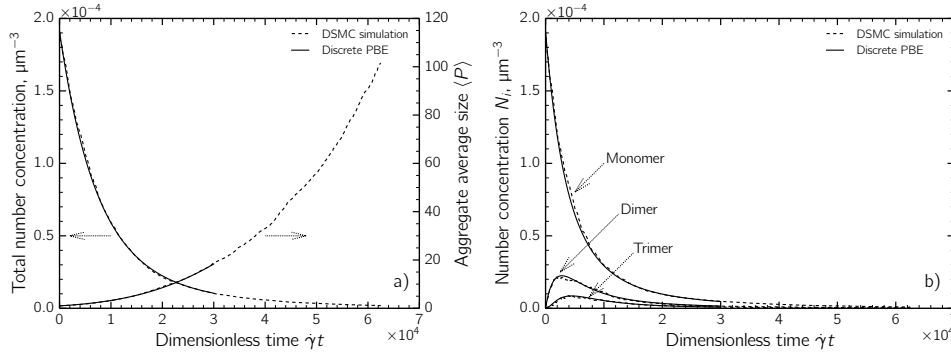
Figure 4.8: Comparison of the results for the discrete PBE and the MC simulation, as obtained by averaging three different realizations. a) Temporal trend of the total aggregate concentration and aggregate average size. b) Temporal trend of the number concentration of a sample of small aggregates.

nm and are dispersed in a dilute suspension with a volume solid fraction equal to 10^{-4}. The aggregation frequency of Eq. (2.18) has been used to setup both methods. A unity aggregation efficiency was imposed, thus the MC was used as stand-alone with no DEM simulations performed. To choose the number of simulated particles, different MC simulations were run and the results were compared with the solution of the discrete PBE formulation:

$$\frac{dN_i}{dt} = \frac{1}{2} \sum_{j=0}^{i-1} N_j N_{i-j} k_{j,i-j}^a - N_i \sum_{j=0}^{Q} N_j k_{i,j}^a \qquad i = 1, 2, ...Q \qquad (4.14)$$

where N_i indicates the number concentration of the i-fold particle. A number of equations $Q{=}4000$ were solved. The results of the comparison are reported in the left plot of Fig. 4.7, where the temporal trend of the mean Sauter diameter of the population is shown. It is apparent that the accuracy of the results increases as the number of particles grows. However, as a drawback, the computational time needed to run the simulation increases as well, as shown in the right plot of Fig. 4.7. In the plot two sets of data are reported: the circles correspond to the actual computational time measured at the end of the simulation, whereas the line represents the theoretical increasing law. Theoretically in fact, the number of events to simulate (and as consequence the computational time) should scale linearly with the number of simulated particles. However, this is not the case, because as the number of simulated particles increases, the number of operations performed by the MC algorithm to sample the aggregating pair and update frequencies increases as well, thus determining a more than linear increase of the computational time. Therefore, as a trade off between accuracy and computational cost, a sample composed by 200 particles was selected for the simulations.

Some additional results of the comparison are shown in Fig. 4.8 for 200 simulated particles. Figure 4.8a reports the temporal trend of the total number concentration of particles and the particle average size, whereas Fig. 4.8b reports the temporal

trend of the number concentration of a sample of small cluster. As apparent, the results obtained with the two methods compare perfectly well, thus validating the MC approach developed and the choice of the number of particles to be simulated.

Finally, it is worth to mention that the relatively small number of equations solved with the discrete PBE limited the simulation to about $3 \cdot 10^4$ time units. This is due to the fact that the discretization used cannot deal with aggregates composed by a number of monomers larger than Q; therefore when such aggregates appear in the suspension, the simulation has to be stopped. This problem do not affect the MC technique.

References

Becker, V., Briesen, H. 2010. "A master curve for the onset of shear induced restructuring of fractal colloidal aggregates". *Journal of Colloid and Interface Science* 346. 32–36.

Camejo, M., Espeso, D., Bonilla, L. 2014. "Influence of primary-particle density in the morphology of agglomerates". *Physical Review E* 90. 012306.

Frappier, G, Lartiges, B., Skali-Lami, S. 2010. "Floc cohesive force in reversible aggregation: a Couette laminar flow investigation". *Langmuir* 26. 10475–10488.

Harada, S., Tanaka, R., Nogami, H., Sawada, M. 2006. "Dependence of fragmentation behavior of colloidal aggregates on their fractal structure". *Journal of Colloid and Interface Science* 301. 123–129.

Horii, K., Yamada, R., Harada, S. 2015. "Strength deterioration of nonfractal particle aggregates in simple shear flow". *Langmuir* 31. 7909–7918.

Isella, L., Drossinos, Y. 2010. "Langevin agglomeration of nanoparticles interacting via a central potential". *Physical Review E* 82. 011404.1–15.

Koch, W, Friedlander, S. 1990. "The effect of particle coalescence on the surface area of a coagulating aerosol". *Journal of Colloid and Interface Science* 140. 419–427.

Kostoglou, M., Konstandopoulos, A. G. 2001. "Evolution of aggregate size and fractal dimension during Brownian coagulation". *Journal of Aerosol Science* 32. 1399–1420.

Kruis, F. E., Maisels, A., Fissan, H. 2000. "Direct simulation Monte Carlo method for particle coagulation and aggregation". *AIChE Journal* 46. 1735–1742.

Liffman, K. 1992. "A direct simulation Monte-Carlo method for cluster coagulation". *Journal of Computational Physics* 100. 116–127.

Marshall, J. 2009. "Discrete-element modeling of particulate aerosol flows". *Journal of Computational Physics* 228. 1541–1561.

Ren, Z., Harshe, Y. M., Lattuada, M. 2015. "Influence of the potential well on the breakage rate of colloidal aggregates in simple shear and uniaxial extensional flows". *Langmuir* 31. 5712–5721.

Seto, R, Botet, R, Auernhammer, G., Briesen, H. 2012. "Restructuring of colloidal aggregates in shear flow: coupling interparticle contact models with Stokesian dynamics." *The European physical Journal E, Soft Matter* 35. 9805.

Seto, R., Botet, R., Briesen, H. 2011. "Hydrodynamic stress on small colloidal aggregates in shear flow using Stokesian dynamics". *Physical Review E* 84. 041405.

Shah, B., Ramkrishna, D., Borwanker, J. 1977. "Simulation of particulate systems using the concept of the interval of quiescence". *AIChE Journal* 23. 897–904.

Smith, M., Matsoukas, T. 1998. "Constant-number Monte Carlo simulation of population balances". *Chemical Engineering Science* 53. 1777–1786.

Smoluchowski, M. V. 1917. "Versuch einer mathematischen Theorie der Koagulationskinetik kolloider Lösungen". *Zeitschrift für physikalische Chemie* 92. 129–168.

Tandon, P., Rosner, D. E. 1999. "Monte Carlo simulation of particle aggregation and simultaneous restructuring". *Journal of Colloid and Interface Science* 213. 273–286.

Vanni, M., Gastaldi, A. 2011. "Hydrodynamic forces and critical stresses in low-density aggregates under shear flow". *Langmuir* 27. 12822–12833.

Chapter 5

Comparison between two modelling approaches to colloidal interactions

The MC-DEM method described in Chapter 4 is here applied to study the shear-induced aggregation of dilute colloidal suspensions. The primary aim is to investigate the effect of tangential interactions on the aggregation behaviour; it was shown in fact that bonds between particles are capable of withstanding, to a certain extent, tangential stresses and bending moments (Pantina, Furst, 2005). On the basis of this observation, Becker, Briesen (2008) developed a spring-like model that, by introducing elastic restoring forces and torques, was seen to properly describe the stiffness of the aggregates and the transition from the rotational regime to the restructuring regime. Small aggregates in a mild shear rate rotate as rigid bodies since the shear stresses on the aggregate structure are not sufficient to overcome the bending and torsional resistance of the bonds. When aggregates grow in size, the effect of the propagation and accumulation of stress over the aggregate structure are more intense and determine the single bond resistance to be overcome, thus causing the restructuring of the aggregate. For even larger aggregates breakup finally may occur (Becker, Briesen, 2010; Becker et al., 2009). A similar transition takes place when, keeping fixed the size of the aggregates, the applied shear stresses are increased (Vanni, Gastaldi, 2011).

While the role of tangential interactions on the restructuring behaviour has been adequately investigated, its role on the aggregation dynamics and on the morphologies of the aggregates produced upon shear aggregation is still unknown. For this reason simulations were performed to ascertain the effect of tangential interaction on the aggregation process. [1]

---

[1]Part of the work described in this chapter has been previously published in "Shear-induced aggregation of colloidal particles: A comparison between two different approaches to the modelling of colloidal interactions" by Frungieri, Vanni (2017)

81

Table 5.1: Physical properties of the simulated system

Parameter	Symbol	Value
Hamaker constant	A_H	$0.97 \cdot 10^{-20}$ J
Surface energy	γ_s	$4.7 \cdot 10^{-3}$ J m^{-2}
Minimum approach distance	z_0	0.165 nm
Monomer radius	a	500 nm
Medium viscosity	μ	10^{-3} Pa s
Medium density	ρ_l	1000 kg m^{-3}
Particle density	ρ_p	1000 kg m^{-3}
Shear rate	$\dot{\gamma}$	10 s^{-1}
Encounter cross section parameter	ε	1
Elastic modulus	E	3.4 GPa
Poisson ratio	ν	0.5

Table 5.2: Physical properties of the spring-like model

Parameter	Symbol	Value
Tangential spring stiffness	k_ξ	$1.85 \cdot 10^{-5}$ N m^{-1}
Torsional spring stiffness	k_ϑ	$9.2 \cdot 10^{-18}$ N m rad^{-1}
Maximal spring elongation	ξ_{max}	50 nm
Maximal spring torsion	ϑ_{max}	0.10 rad

5.1   Setup of the simulations

Simulations were carried out starting from a mono-disperse population composed by 200 polystyrene primary particles with radius $a = 500$ nm. The suspension has a volume solid fraction equal to 10^{-4} m^3/m^3. The particles are dispersed in water at room temperature and exposed to a spatially uniform shear flow with a rate $\dot{\gamma}$ equal to 10 s^{-1}. The values of the physical variables of the simulations are reported in Table 5.1. The elastic properties of the solid (elastic modulus and Poisson ratio) are typical of relatively compliant polymeric materials, such as polystyrene. Similarly, the value of Hamaker constant is typical of polymeric particles dispersed in water. The set of parameters used leads to a Péclet number (Pe $= 6\pi\mu a^3\dot{\gamma}/k_B T$) equal approximately to 6 for isolated monomers and to much larger values for clusters; in these conditions thermal motion can be safely neglected and the aggregation can be assumed to be driven uniquely by the gradient of the flow field, regardless of the actual size of the involved particles.

In order to clarify the effect of tangential interactions, two populations of particles were simulated:

- Population A is composed by primary particles interacting only by means of central forces, namely the ones due to Van der Waals interactions and the ones arising from the contact mechanics.
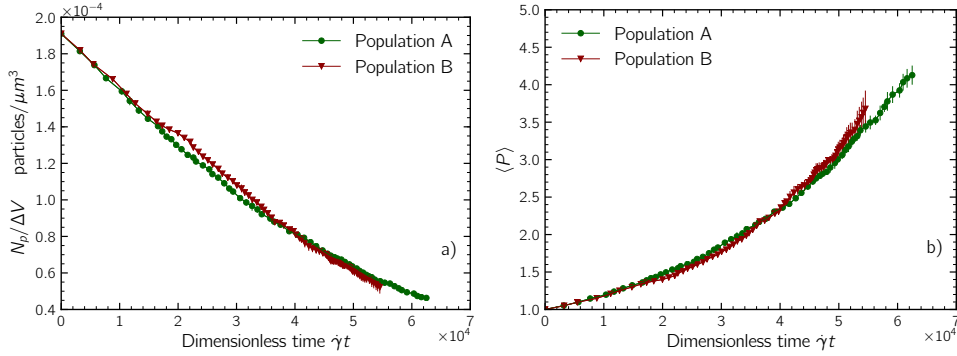
Figure 5.1: Integral properties of the two analyzed suspensions: a) time evolution of the suspension concentration in terms of number of particles per volume. b) Time evolution of the average size of the suspended aggregates, expressed in terms of number of primary particles per cluster. Each curve was obtained by averaging the data relative to three different realizations. The error bars indicate the standard deviation of the data.

- Population B is composed by primary particles interacting by means of both central and tangential interactions, with the latter ones modelled by the spring-like force model by Becker, Briesen (2008), whose parameters are reported in Table 5.2.

In both populations electrical double layer interactions were assumed to be completely screened; thus particles are subject solely to attractive interactions. Although the code developed is intrinsically capable of simulating breakup, the simulations were stopped well before clusters attained large enough sizes to be vulnerable to breakup; according to the criterion by Vanni, Gastaldi (2011), with the adopted set of parameter, clusters more than 100 times bigger than the maximum size reached here are required for breakup.

5.2 Suspension dynamics

The most apparent consequence of aggregation is the reduction of the number of suspended particles and, consequently, the increase of the particle average size. In this regard Fig. 5.1a reports the temporal trend of the suspension total concentration, whereas Fig. 5.1b shows the average size of the suspended particles; the size of each particle i is expressed in terms of number of constituent primary particles P_i and the average size $\langle P \rangle$ was obtained by averaging P_i over the whole population. In both plots the dimensionless time $\dot{\gamma}t$ was used as evolutionary coordinate. Ten encounter events elapsed between two subsequent points of the curves; the encounters which turned into aggregations determined the loss of aggregates from the population and increased the average size; on the contrary, the encounters which turned into missed aggregations left the population unaffected. As apparent, in the simulated time interval, the suspensions show an almost linear decrease of the total concentration, with no particular difference among the two populations. Similarly, $\langle P \rangle$ shows a monotonic increasing trend, with a rate of size growth (i.e., the slope of the curve)
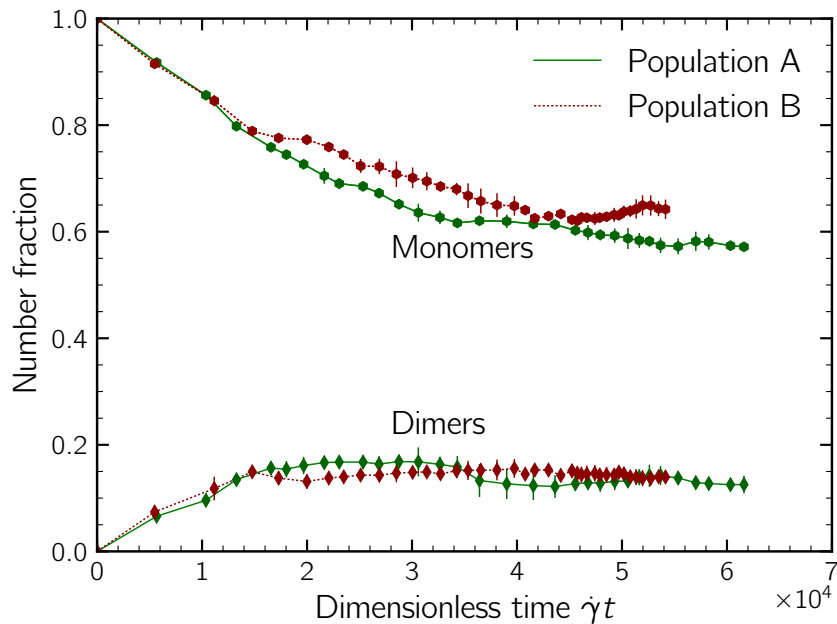
Figure 5.2: Time evolution of the number fractions of monomers and dimers.

increasing continuously throughout the aggregation process. This effect was already reported in the literature and explained as a consequence of the enhancement of the average aggregation rate caused by the formation of larger aggregates which show larger capture sections (Kusters et al., 1997; Wang et al., 2005): the aggregation frequency scales in fact as the cube of the external radius of the aggregates, thus the increase of the average cluster size determines a substantial speed-up of the growth rate which prevails over the reduction one would expect from the decrease of the overall suspension concentration. Furthermore, it is apparent that the two populations show a rather similar growth behaviour; in the simulated time interval the two curves are almost perfectly overlapped.

The reason for this similarity has to be looked for in the particle size distribution of the two suspensions; in this regard, Fig. 5.2 shows the temporal evolution of the number fraction of monomers and dimers for the two analysed populations. It is evident that these small particles represent approximately 80% of the populations. Hence, they affect substantially all the statistical variables based on the number distribution. Clearly, the geometry of monomers and dimers is fixed and is not influenced by the presence of tangential interactions. This explains why the average size based on the number distribution $\langle P \rangle$ does not show relevant differences between the two populations.

Significant differences emerge instead when looking at the evolution of statistical variables that are more sensitive to the biggest aggregates of the population, such as the average outer radius. Figure 5.3 illustrates the evolution of the Sauter diameter
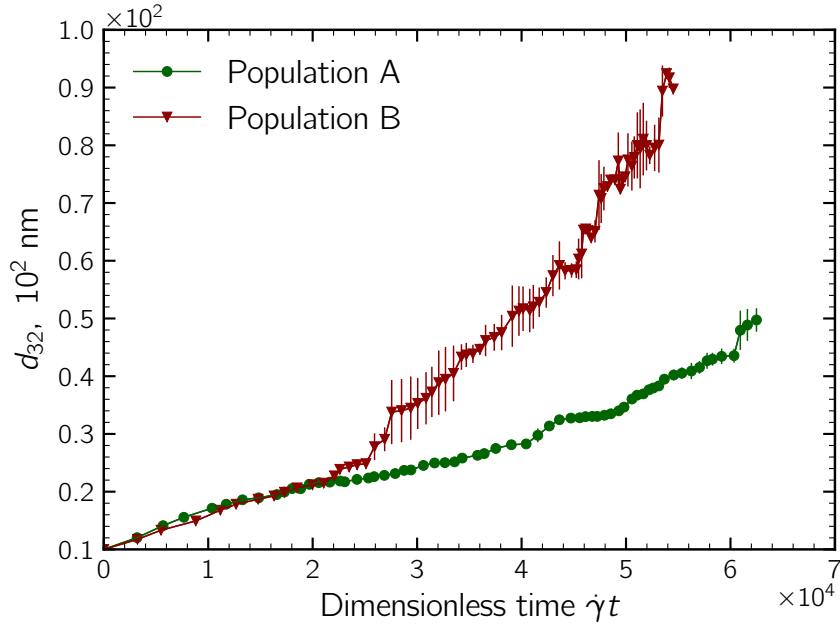
Figure 5.3: Evolution of the average size of the suspended aggregates in terms of Sauter diameter, Eq. (5.1). The error bars show the standard deviation of the data as estimated from three different realizations.

d_{32} computed on the basis of the outer radius of the aggregates as:

$$d_{32} = 2 \cdot \frac{\sum_{i=1}^{N_p} R_i^3}{\sum_{i=1}^{N_p} R_i^2} \ , \tag{5.1}$$

with N_p being the number of suspended aggregates; this average size characterizes the volume to surface ratio of the populations. Differently from $\langle P \rangle$, the Sauter diameters of the two populations coincide only in the initial part of the aggregation process. After about 25000 time units, the curve relative to Population B exhibits a steep increase, reaching significantly larger values compared to Population A. This suggests that the larger aggregates of the two populations differ somehow in the characteristic morphology, although they are on average composed by the same number of primary particles. From Fig. 5.3 it is also apparent that Population A shows a monotonic and steady increase of d_{32}, whereas Population B exhibits also occasional reductions of this variable. These reductions have not to be related to breakup events, but rather to the restructuring phenomena which involve clusters; even if an encounter did not turn into an aggregation, the DEM simulations frequently returned aggregates with slightly different morphology characterized by a more compact structure; this is due to the hydrodynamic interactions between approaching aggregates which may determine a compaction of the clusters. This feature is not present in Population A, in which compaction phenomena are much faster and take place soon after a new aggregate is generated. Population B also shows a noticeably larger scatter of data among the

Population A

Population B

$P = 18$
$R = 24.8$
$\langle n_c \rangle = 5.33$
$A.R. = 1.75$

$P = 18$
$R = 44.9$
$\langle n_c \rangle = 2.00$
$A.R. = 3.18$

$P = 80$
$R = 47.7$
$\langle n_c \rangle = 5.85$
$A.R. = 1.45$

$P = 66$
$R = 60.7$
$\langle n_c \rangle = 2.64$
$A.R. = 1.80$

$P = 109$
$R = 55.4$
$\langle n_c \rangle = 5.89$
$A.R. = 1.35$

$P = 125$
$R = 83.7$
$\langle n_c \rangle = 2.66$
$A.R. = 2.18$
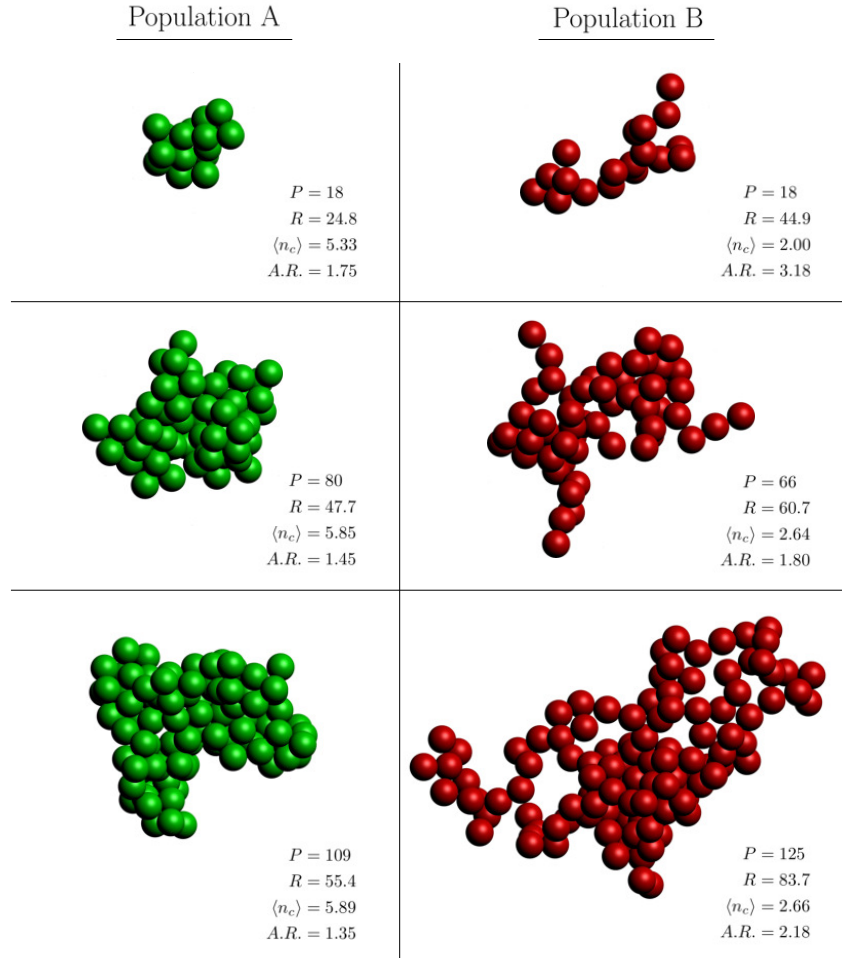
Figure 5.4: A small sample of the two populations of clusters.

different realizations, meaning that a wider variety of structures are produced upon aggregation.

5.3 Cluster characterization

From the analysis of the Sauter diameters, it is clear that the clusters of the two populations are significantly different in their morphological properties. In order to give a visual overview of these different features, Fig. 5.4 reports the geometry of a small sample of the populations of clusters. Each line of the figure compares two clusters with similar number of primary particles P. It is immediately apparent that the clusters from Population A are more compact than those from Population B. They also show smaller outer radius R and a larger number of contacts per primary particle $\langle n_c \rangle$. Conversely, the aggregates of Population B have more elongated shape with larger aspect ratio ($A.R.$) and exhibit branches extending from a rather compact central core. In the next section, these considerations will be elaborated in a more
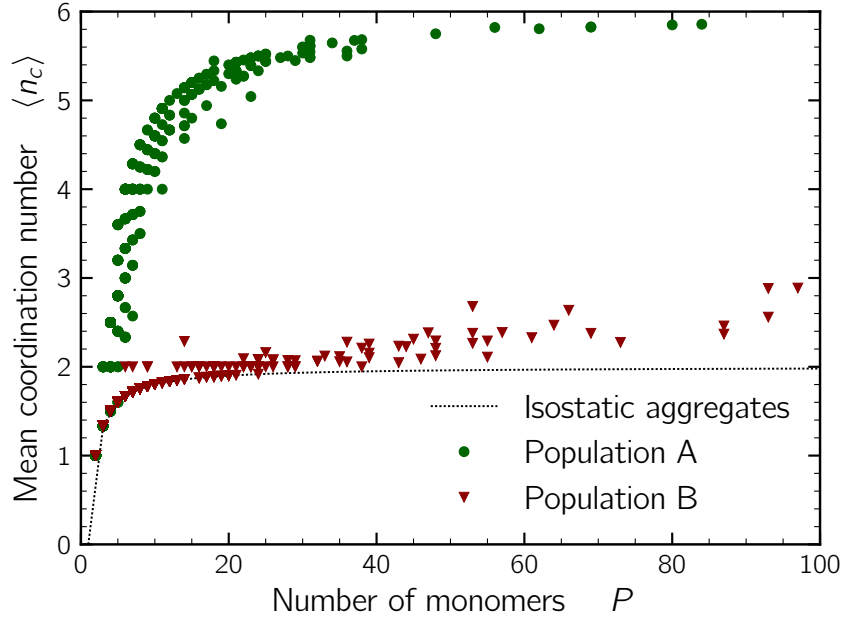
Figure 5.5: Mean coordination number for the two populations of clusters as a function of the cluster size.

quantitative way, by characterizing statistically the structure of the formed aggregates at both local and global level.

5.3.1 Local structure - Coordination number and trimer angle

A relevant piece of information on the structure of colloidal aggregates is given by the number of monomer-monomer bonds; this number provides a measure of the compactness of the cluster structure. Figure 5.5 illustrates the relationship between the number of primary particles P composing the clusters and the average coordination number $\langle n_c \rangle = 2n_b/P$, with n_b being the number of bonds detected in the aggregate.

For both populations the average coordination number $\langle n_c \rangle$ increases with the size of the cluster: obviously, in small clusters most of the particles are located on the outer region of the aggregate, exposed to the dispersing medium and thus involved in a small number of contacts; on the contrary, in large clusters, the fraction of primary particles in the internal region of the structure is much bigger. Such particles are responsible for the increase of $\langle n_c \rangle$ as they are involved in a larger number of bonds, being fully surrounded by other primary particles.

Apart from this similarity, a striking difference in the value of $\langle n_c \rangle$ for the two populations stands out. The primary particles of Population A, interacting only via central interactions, form aggregates characterized by closely packed structures with average coordination numbers close to 6 for the biggest clusters; in these aggregates the primary particles are free to slide and roll over each other, thereby making clusters
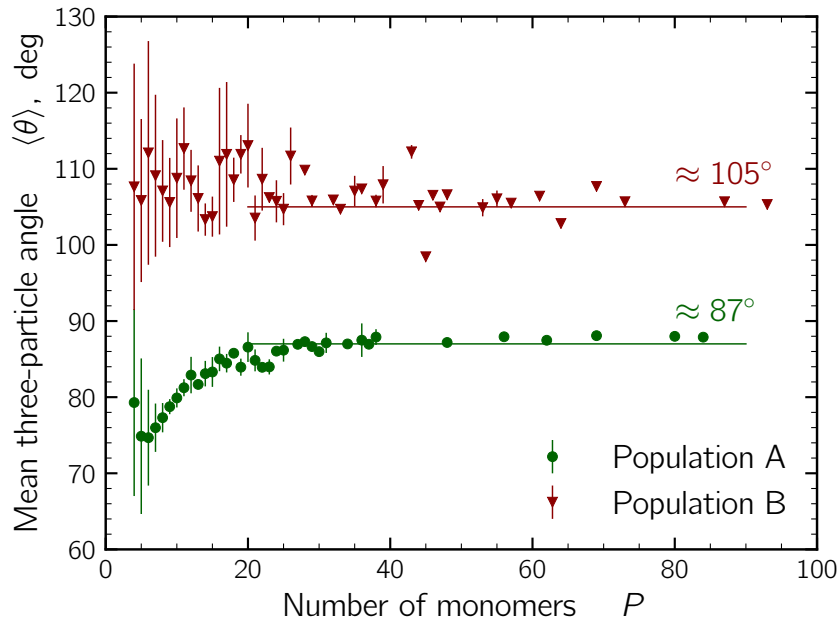
Figure 5.6: Average three particle angle as a function of the number of constituent primary particles P

to soon reach a compact structure under the effect of the viscous shear stresses. On the contrary, the presence of tangential interactions in Population B prevents the generation of a compact arrangement and indeed the clusters of this population are highly porous. From a structural point of view, the smallest aggregates of Population B can be classified as isostatic; their coordination number equals in fact $2(P-1)/P$, the coordination number inferred by Gastaldi, Vanni (2011) for isostatic cluster. Isostatic cluster are obtained when each aggregation event leads to the generation of a single new interparticle bond between the two involved aggregates, with the structure of the newly generated aggregate being frozen after generation. With Population B such a situation occurs when the aggregates are relatively small, while bigger aggregates present an average coordination number slightly larger than the isostatic one. This is due to internal restructuring; the restoring forces arising from tangential interactions are not able in fact to indefinitely hinder the relative motion of adjacent particles along the contact surface; this happens because in these aggregates the stresses generated by the dispersing medium are propagated and accumulated along the filaments of the structure, causing the tangential or bending resistance of the bond to be exceeded in some locations. As a consequence, restructuring phenomena take place, leading to an increase in the number of contacts and making large clusters slightly over-constrained.

Another indicator of the cluster local structure is the mean three-particle angle $\langle \theta \rangle$, plotted as a function of P in Fig. 5.6. To compute $\langle \theta \rangle$, all the existing groups of three connected primary particles in the cluster were identified and characterized by the trimer angle $\theta_{\alpha\gamma\beta}$, formed by the two straight lines passing through the centre of

the intermediate particle γ and through the centres of the other two particles α and β; the angle $\theta_{\alpha\gamma\beta}$ was computed as:

$$\theta_{\alpha\gamma\beta} = 2 \cdot \arcsin\left(\frac{r_{\alpha\beta}}{4a}\right) \tag{5.2}$$

where $r_{\alpha\beta}$ is the centre-to-centre distance between particles α and β. For rigid particles the angle can vary from 60°, corresponding to particles arranged to form an equilateral triangle, to 180°, corresponding to particles aligned in a straight chain. However, it is worth to mention that angles slightly smaller than 60° were also observed, because of the deformation of the contact region predicted by the JKR theory.

Both classes of clusters reach an asymptotic value of $\langle\theta\rangle$ as the number of constituent primary particles increases; this plateau value is approximately equal to 87° for the aggregates of Population A and to 105° for those of Population B, confirming that the primary particles are assembled in a quite different manner in the two populations. The larger angles of Population B show that these clusters have a more open and tenuous structure compared to those of Population A. The asymptotic angle of Population B is very close to the value reported for syntethic DLCA clusters (Melas et al., 2014). This fact indicates that the morphology of rigid aggregates is influenced mainly by the condition of destabilisation (full or partial), whereas the type of aggregation (perikinetic or orthokinetic) plays a minor role. It is no coincidence that also the fractal dimension has similar values (around 1.8) in both perikinetic and orthokinetic aggregation for fully destabilised suspensions.

It is also apparent that a wider scatter of the data characterizes Population B, especially for small cluster size, indicating that a greater variety of shapes exists. On the contrary, the smaller clusters of Population A present a more recurrent pattern, due to the fact that upon contact a large-scale restructuring occurs, always ending in a compact structure.

5.3.2 Global scale structure - Aspect ratio

The response of an aggregate to the fluid flow is very similar to the response of an ellipsoid with the same inertia matrix as the aggregate (Harshe et al., 2010). For this reason, the geometric properties of an aggregate are often expressed in terms of those of the inertia-equivalent ellipsoid. In particular, the aspect ratio of a cluster can be defined as:

$$A.R. = \frac{2a_1}{a_2 + a_3}, \tag{5.3}$$

where a_1 is the major semiaxis of the equivalent ellipsoid and a_2 and a_3 are the two minor ones. Equation (5.3) returns values close to 1 for round-shaped aggregates and substantially larger values for rod-shaped ones.

In order to calculate the lengths of the semiaxis, it is useful to compute the inertia tensor of a single primary particle α with respect to its centre of mass, $\mathbf{I}_\alpha = (2/5)m_\alpha a^2\mathbf{i}$, where $\mathbf{i}$ is the identity tensor and m_α the mass of the primary particle. Subsequently, in order to obtain the inertia tensor relative to the centre of

mass of the aggregate, the parallel axis theorem in its tensorial formulation can be applied to the inertia tensor of each primary particle α as:

$$\mathbf{I}'_\alpha = \mathbf{I}_\alpha + m_\alpha \left(|(\mathbf{x}_\alpha - \mathbf{x}_{com})|^2 \, \mathbf{i} - (\mathbf{x}_\alpha - \mathbf{x}_{com})(\mathbf{x}_\alpha - \mathbf{x}_{com}) \right) \tag{5.4}$$

where $\mathbf{x}_\alpha$ is the position vector of the α monomer and $\mathbf{x}_{com}$ identifies the position of the centre of mass of the aggregate. Finally, the inertia tensor of the whole cluster can be obtained as:

$$\mathbf{I}_{\text{cluster}} = \sum_\alpha \mathbf{I}'_\alpha \tag{5.5}$$

The principal moments of inertia ($I_1 > I_2 > I_3$) of the cluster were computed by diagonalization of $\mathbf{I}_{\text{cluster}}$ and the length of the principal semi-axes ($a_1 > a_2 > a_3$) are given by the following equations (Fellay et al., 2013):

$$a_1 = \sqrt{\frac{5}{2} \frac{I_2 + I_3 - I_1}{\sum_\alpha m_\alpha}}$$
$$a_2 = \sqrt{\frac{5}{2} \frac{I_1 + I_3 - I_2}{\sum_\alpha m_\alpha}} \tag{5.6}$$
$$a_3 = \sqrt{\frac{5}{2} \frac{I_1 + I_2 - I_3}{\sum_\alpha m_\alpha}}$$

Figure 5.7 shows the distribution of the aspect ratio for the two populations of aggregates sampled after 600 encounters from the beginning of the aggregation process. The distribution of the aspect ratio for the clusters of Population A exhibits a peak at low values (around 1.5), meaning that most of the clusters have a spheroidal shape. High values of aspect ratio (i.e., larger than 2.5) are obtained only by the biggest aggregates, which are quite few in comparison to the small ones. Differently, the aggregates of Population B have a broader variety of structures; a peak of the distribution is detectable for $A.R. \approx 2$, but its height is significantly lower than the peak of Population A. Moreover a long tail extending up to values of aspect ratio larger than 5 characterizes this distribution. This is due to the fact that for this population only minor rearrangements take place and the open and elongated structure generated at the very first contact is preserved during the aggregation process, whereas the ability of the monomers of Population A to mutually slide and roll at contact generates compact structures, which are less elongated.

The aspect ratio has a strong impact on the collision rate and has to be accounted for in order to explain the similar rate of aggregation of the examined classes of particles (Fig. 5.1). Indeed, at a first sight one would expect faster aggregation for Population B, because of the larger radius of these aggregates (Fig. 5.3), which gives a much larger encounter cross section with respect to the compact aggregates of Population A. On the contrary, the aggregation rate is nearly the same for both populations, as apparent from the evolution of the mean aggregate size $\langle P \rangle$ and number concentration reported in Fig. 5.1. As shown by the aspect ratio, the
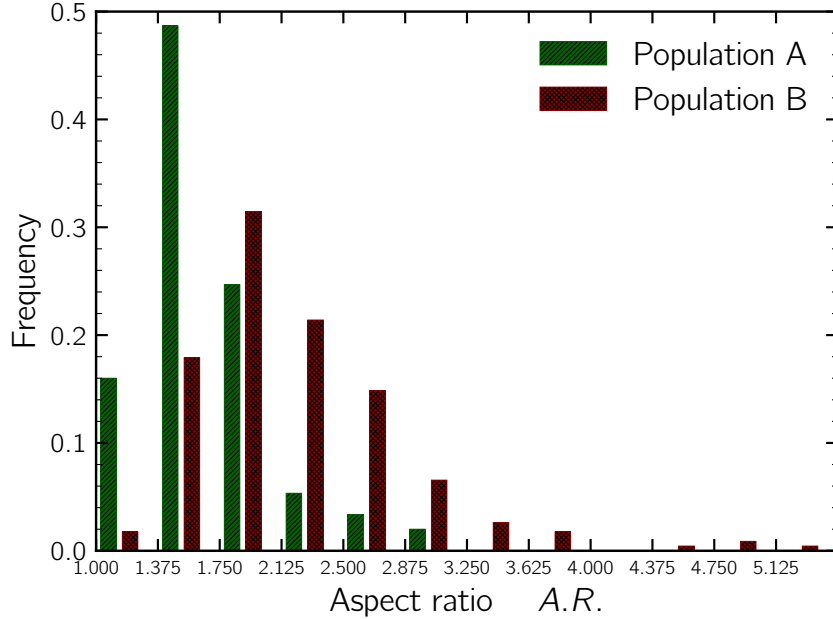
Figure 5.7: Distribution of the aspect ratio for the two populations. Only clusters composed by at least 5 primary particles were considered.

aggregates of Population B are highly elongated and thus, while rotating in the shear flow, they spend most of their time aligned or partially aligned with the fluid flow (Fellay et al., 2013; Vanni, Gastaldi, 2011), making contact more difficult during the encounter and reducing significantly the aggregation efficiency. For this reason, even if on average the clusters of Population B present larger cross section, their reduced aggregation efficiency makes the aggregation rate of Population B similar to that of Population A.

5.3.3 Mass-size scaling law

Aggregates are often characterized on the basis of their gyration radius R_g, which is defined as the root-mean-square distance of the monomers from the centre of mass of the aggregate and, for a cluster composed by P primary particles, reads as:

$$R_g = \sqrt{\frac{1}{P} \sum_\alpha |\mathbf{x}_\alpha - \mathbf{x}_{cm}|^2} \tag{5.7}$$

It is common to relate the gyration radius to the mass of the aggregates, or equivalently to the number of constituent primary particles, by means of a power-law of the following kind:

$$P = k_f \cdot (R_g/a)^{d_f} \tag{5.8}$$

where the two parameters are the pre-factor k_f and the power-law exponent d_f. Equation (5.8) was used to fit the set of data of the two populations in order to
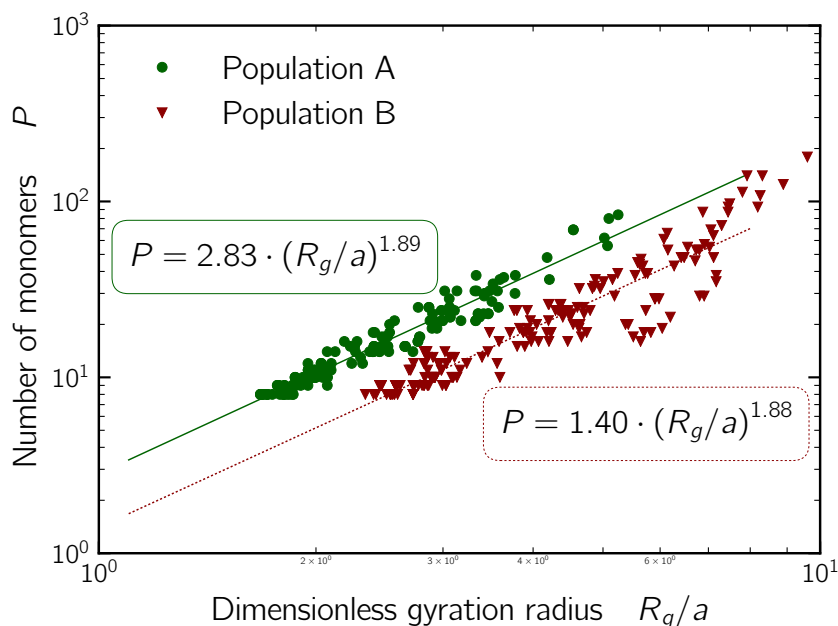
Figure 5.8: Number of monomers P versus dimensionless gyration radius R_g/a for the two populations of aggregates in a log-log plot. In the rectangles the power-law equations of the fitting lines are reported.

estimate the parameters k_f and d_f. The aggregates employed for the estimation of d_f and k_f were drawn by sampling the populations every 100 encounter events and excluding the clusters composed by less than 8 primary particles. The results are shown in Fig. 5.8. As apparent, the two populations exhibit very similar values of the power-law exponent, whereas a quite large difference exists between their prefactors, with the one relative to Population A being twice as large than that of Population B.

As well known, rigid aggregates have a fractal structure and the power-law exponent is their fractal dimension (Jullien, Botet, 1987; Meakin, 1999). Values of d_f around 1.80 and prefactors around the unity are typical of rigid aggregates produced in fully destabilized colloidal suspensions, in which all collisions between clusters lead to a permanent and rigid bond. These conditions are close to those adopted for the generation of Population B. The slightly higher values for the exponent (1.88) and prefactor (1.40) are most likely due to the presence of a level of restructuring after contact, which is witnessed by the coordination number, as discussed previously.

In spite of the similar value of power-law exponent, the aggregates of Population A have very different features. They are compact and do not exhibit the sequence of dense and void region that is typical of fractal objects with small fractal dimension. On the contrary, all the primary particles are confined in a narrow region of space, where the solid density is close to that of a randomly close-packed structure. These aggregates are not rigid and undergo different deformations in the flow field, depending on their size. The smallest clusters normally retain a spheroidal shape, while the largest aggregates can be stretched more easily and become partially elongated in

the shear flow. Indeed, it is this gradual change of shape with size that is reflected by the small value (1.89) of the power law exponent for this population and not the presence of a fractal structure.

In the plot a significant deviation of the data from the fitting lines is noticeable for both populations, although it is more intense for Population B. As pointed in a number of works this behaviour may be a consequence of the broad variety of shapes and aspect ratios exhibited by these clusters (Heinson et al., 2010; Heinson et al., 2012). This fact suggest that a complex interplay between the aspect ratio, the power-law exponent and pre-factor may exist and therefore all these parameters appear as essential ingredients for a full characterization of a population of clusters.

5.4 Conclusion

In this chapter the developed MC-DEM method was employed to study the shear-induced aggregation of a fully destabilised suspension. Simulations were carried out starting from a monodisperse population of polystyrene primary particles. The aggregation behaviour of two different populations of particles was investigated: the first population was composed by primary particles interacting only by means of central forces, arising from Van der Waals interactions and JKR contact forces; in the second population, primary particles were capable of withstanding also mutual sliding and rolling by the onset of tangential interaction upon contact; to count for such interactions the model by Becker, Briesen (2008) was implemented.

Results showed that substantial differences in the cluster morphology appear when introducing tangential interactions: when counting for such interactions, primary particles aggregate to form structures that are porous and branched, and characterized by low values of the coordination number. The absence of tangential interaction, instead, allows primary particles to slide and roll over each other, leading to the formation of dense and highly connected clusters. Tangential interaction has also an impact on the global shape of the clusters: when such interactions are taken into account, a wide variety of clusters shapes is obtained, as shown by evaluating the aspect ratio. Conversely, for particles interacting only by means of central forces, intense restructuring phenomena take place, leading to the formation of mainly spheroidal aggregates.

The mass-size power law gives similar values of the power-law exponent for the two populations of clusters. Such a value, however, reflects two very different features of the populations: a true low-density fractal structure in the presence of tangential interaction, and a size-dependent shape of the clusters when tangential interactions are absent.

References

Becker, V., Briesen, H. 2008. "Tangential-force model for interactions between bonded colloidal particles". *Physical Review E* 78. 061404.

Becker, V., Briesen, H. 2010. "A master curve for the onset of shear induced restructuring of fractal colloidal aggregates". *Journal of Colloid and Interface Science* 346. 32–36.

Becker, V., Schlauch, E., Behr, M., Briesen, H. 2009. "Restructuring of colloidal aggregates in shear flows and limitations of the free-draining approximation". *Journal of Colloid and Interface Science* 339. 362–372.

Fellay, L. S., Twist, C., Vanni, M. 2013. "Motion of rigid aggregates under different flow conditions". *Acta Mechanica* 224. 2225.

Frungieri, G., Vanni, M. 2017. "Shear-induced aggregation of colloidal particles: A comparison between two different approaches to the modelling of colloidal interactions". *The Canadian Journal of Chemical Engineering* 95. 1768–1780.

Gastaldi, A., Vanni, M. 2011. "The distribution of stresses in rigid fractal-like aggregates in a uniform flow field". *Journal of Colloid and Interface Science* 357. 18–30.

Harshe, Y. M., Ehrl, L., Lattuada, M. 2010. "Hydrodynamic properties of rigid fractal aggregates of arbitrary morphology". *Journal of Colloid and Interface Science* 352. 87–98.

Heinson, W., Sorensen, C., Chakrabarti, A 2010. "Does shape anisotropy control the fractal dimension in diffusion-limited cluster-cluster aggregation?" *Aerosol Science and Technology* 44. 1–5.

— 2012. "A three parameter description of the structure of diffusion limited cluster fractal aggregates". *Journal of Colloid and Interface Science* 375. 65–69.

Jullien, R., Botet, R. (1987). *Aggregation and Fractal Aggregates.* 1st edition. World Scientific, Singapore.

Kusters, K. A., Wijers, J. G., Thoenes, D. 1997. "Aggregation kinetics of small particles in agitated vessels". *Chemical Engineering Science* 52. 107–121.

Meakin, P. 1999. "A historical introduction to computer models for fractal aggregates". *Journal of Sol-Gel Science and Technology* 15. 97–117.

Melas, A. D., Isella, L., Konstandopoulos, A. G., Drossinos, Y. 2014. "Morphology and mobility of synthetic colloidal aggregates". *Journal of Colloid and Interface Science* 417 27–36.

Pantina, J. P., Furst, E. M. 2005. "Elasticity and critical bending moment of model colloidal aggregates". *Physical Review Letters* 94. 138301.

Vanni, M., Gastaldi, A. 2011. "Hydrodynamic forces and critical stresses in low-density aggregates under shear flow". *Langmuir* 27. 12822–12833.

Wang, L., Marchisio, D. L., Vigil, R. D., Fox, R. O. 2005. "CFD simulation of aggregation and breakage processes in laminar Taylor–Couette flow". *Journal of Colloid and Interface Science* 282. 380–396.

Chapter 6

Aggregation efficiency

As mentioned in Chapter 3, the aggregation rate of solid spherical particles has been extensively investigated since the seminal work by Smoluchowski (1917). The most notable advancement was provided by Van de Ven, Mason (1977), who evaluated the aggregation rate for pairs of non-brownian spherical particles suspended in shear flow, addressing both hydrodynamic and colloidal interactions. The former were modelled after a parametrization of the rigorous solution of the creeping motion equations in bispherical coordinates; the latter were introduced according to the DLVO theory, varying both intensity and range of action of the Van der Waals attraction and electrical double layer repulsion. Doing so, the relative trajectories of particles were obtained, showing the limitations of the rectilinear approach by Smoluchowski (1917) and the key role that inter-particle interactions have on the aggregation efficiency. Hydrodynamic interactions cause in fact a deflection of the relative particle trajectories which leads to a reduction of the aggregation efficiency. The attractive colloidal forces, on the other hand, deflect the relative particle trajectories oppositely and lead to an increase of the aggregation efficiency. Vanni, Baldi (2002) further investigated the phenomenon by introducing rigorous models for the colloidal interactions; a grid-based technique was adopted, allowing to evaluate particle trajectories and aggregation efficiencies in a completely predictive manner.

The aforementioned works are focused on pairs of spherical particles and hence the formation of doublets. However, when a suspension is unstable and particles aggregate, clusters bigger than dimers are also formed. Given their larger capture section, the dynamics of the suspension will be mainly determined by the aggregation events involving such clusters. As shown in Chapter 5, clusters, when tangential interactions are taken into account, present a porous, branched structure and a wide variability of shapes; round-shaped and rod-shaped clusters coexist in suspension. Therefore, given the diverse overall shape and the characteristic lacunarity of the structures, the results relative to the aggregation efficiency of solid spherical particles cannot be extended straightforwardly to the case of clusters.

A number of works have investigated the aggregation efficiency of porous clusters. Kusters et al. (1997), for instance, developed a model that pictures a porous cluster as consisting of an impermeable core and a completely permeable shell where the fluid

flow is able to freely penetrate. By such a model, they argued that the hydrodynamic interactions between clusters are much less pronounced compared to that of solid rigid spheres, thus resulting in an enhanced aggregation efficiency. However, the analysis is restricted to the case of spherical clusters. Veerapaneni, Wiesner (1996) studied the fluid collection efficiency of fractal clusters assuming a radially varying permeability; the aggregate structure was divided in a number of concentric shells, each of which characterized by a constant permeability. The Brinkmann equation was then solved in each shell and the Stokes equation was solved in the exterior of the aggregate. Similarly, Bäbler (2008) developed a model able to count for both hydrodynamic and colloidal interactions. The former were calculated starting from the Brinkmann equation, whereas the latter were included considering the forces between the closest pair of primary particles of the two approaching aggregates. Even if such models picture the aggregates in a more realistic way, they are still based on several arbitrary assumptions.

For these reasons, for the present work, DEM simulations were performed to evaluate the aggregation efficiency of porous and rigid clusters with realistic structures. Electric double layer interactions were assumed to be completely screened; therefore aggregate interact only by means of attractive Van der Waals interactions and hydrodynamic interactions. Differently from previous works, no symplifying assumption was made on the cluster morphology; the aggregates adopted were the ones generated upon simulation of the shear-induced aggregation reported in Chapter 5, in which tangential interactions were included; therefore the aggregate structure which determines the hydrodynamic interaction and the interparticle forces is taken explicitly into account by the DEM, without resorting to any arbitrary choice.

The aim of this chapter is to ascertain which are the main factors affecting the aggregation efficiency of clusters. After explaining the details of the grid-based technique adopted following the work by Vanni, Baldi (2002), the case of aggregation of monomers, used as a validation of the technique, and the case of the aggregation of clusters will be both addressed.

6.1 Setup of the simulations

In order to evaluate aggregation efficiencies the DEM was combined with a grid-based technique, as reported in the work by Vanni, Baldi (2002): the aggregation efficiency was evaluated in a shear flow $\mathbf{u}^{\infty}(\mathbf{x}) = \dot{\gamma} y \mathbf{e}_z$ with $\dot{\gamma} = 10 \text{ s}^{-1}$ (Fig. 6.1a). Given a pair of aggregates i,j with outer radius respectively equal to R_i and R_j, a 20×20 evenly spaced quadrilateral mesh was generated in a plane $z = -5 \cdot (R_i + R_j)$ within the quadrant $y > 0$, $x > 0$. The size of each side of the mesh was set equal to $R_i + R_j$. At the beginning of each simulation the centre of mass of the aggregate j was placed on a node of the mesh. The aggregate i was placed instead in the origin of the reference system with a random orientation. From this initial configuration the DEM was used to track the relative motion of the aggregates and to ascertain the outcome of the event; each event can result into either an aggregation or a missed aggregation. In the former case, the two aggregates collide and generate a new larger aggregate.
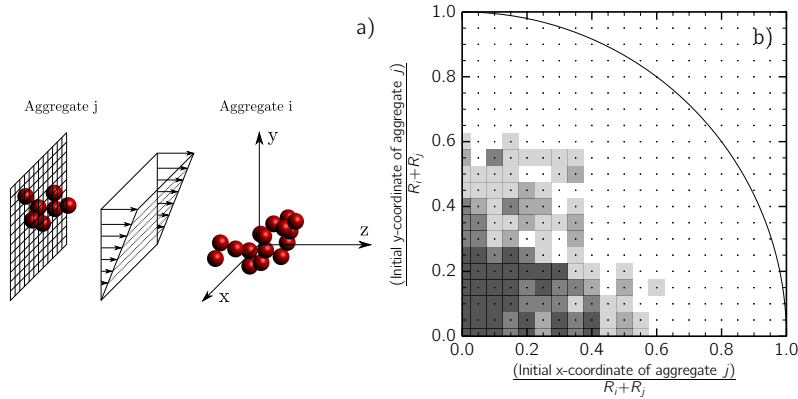
Figure 6.1: a) Qualitative illustration of the grid-based technique. From the depicted initial configuration the DEM is used to ascertain the outcome of the event. b) Example of aggregation cross section. The cell shade intensity provides a measure of the fraction of events turned into an aggregation.

In the second case, the aggregate j pass close to the aggregate i without colliding with it. In order to save computational costs, for both cases a stop criterion for the simulation was adopted: in the aggregation case, the simulation was stopped once a mechanical contact between the two involved aggregates was established; this choice is justified by the fact that, due to the intense adhesion forces, aggregates coagulate irreversibly once two of their constituent primary particles get in touch; restructuring phenomena are beyond the scope of this chapter as they are not relevant to the computation of aggregation efficiencies. For missed collisions a different criterion was adopted: once the aggregate j passed over the aggregate i, the simulation was stopped when the distance between the centres of mass of the aggregates along the z-direction exceeded a threshold value set equal to $2 \cdot (R_i + R_j)$. At this distance it is reasonable to assume that a mechanical contact between the aggregates can no longer occur. In order to infer statistical reliable informations, for each node of the mesh, every encounter event was repeated 4 times, changing each time the initial orientation of both aggregates in the flow field. The set of parameters used for the DEM simulations are the ones already reported in Table 5.1 and Table 5.2.

Following the grid-based technique just outlined, several aggregation maps were obtained. As an example, Fig. 6.1b reports the aggregation cross section obtained for the pair of clusters depicted in Fig. 6.1a. Each node of the mesh is indicated as black dot; the shaded cells are centered in the initial position of the aggregate j for which an aggregation occurred; the shade intensity provides instead a measure of the fraction of repetitions ended into a successful aggregation (ranging from 1/4 for the lighter cells to 4/4 for the darker ones).

The aggregation efficiency can be evaluated by computing the ratio between the flow rate of aggregates through the aggregation cross section and the flow rate of aggregates crossing the aggregation cross section assumed by the rectilinear approach of Smoluchowski (1917) and circumscribed by a solid curve in Fig. 6.1b. Therefore
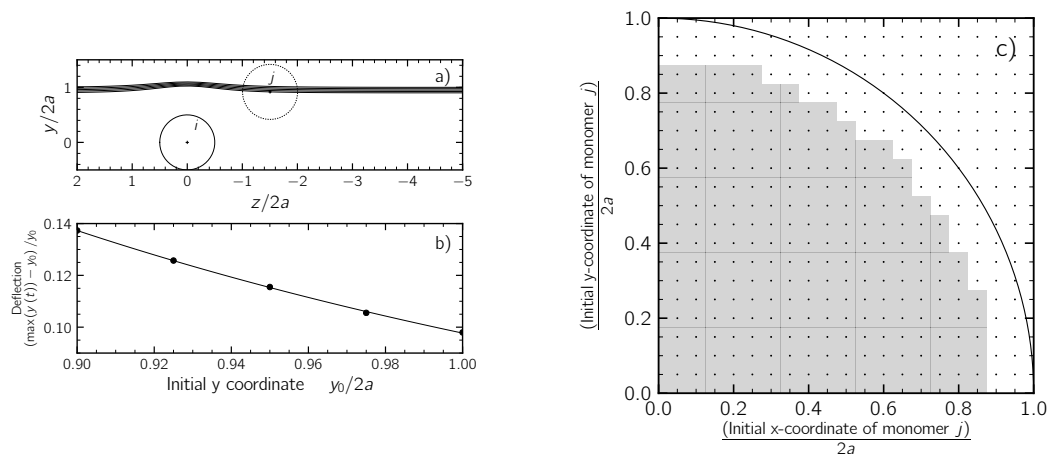
Figure 6.2: Analysis of the monomer-monomer aggregation. Both particle have radius $a = 500$ nm and are suspended in a shear flow of intensity $\dot{\gamma} = 10$ s^{-1}. a) y,z trajectories of the primary particle j in a reference system centered in the center of particle i. For all the trajectories reported, the release point is $x_0 = 0$. b) Entity of the deflection of the trajectory of the particle j as a function of the release coordinate y_0. c) Aggregation cross section.

the aggregation efficiency α_{ij} relative to a pair of aggregates i and j follows as:

$$\alpha_{ij} = \frac{\int_{S_{\text{sh}}} \dot{\gamma} y \cdot c\left(x, y\right) dS}{\int_{S_{\text{Smol}}} \dot{\gamma} y dS} \tag{6.1}$$

where the integral at the numerator is extended to the whole shaded region, whereas the one at denominator computes the flow rate through the Smoluchowski cross section. The weight function $c\left(x, y\right)$ is included in order to quantify the fraction of successful aggregation over the total number of repetitions performed for each node of the grid.

6.2 Monomer-monomer aggregation

As a validation of the developed technique, the well studied monomer-monomer aggregation was analysed first. To study this phenomenon, the grid-based approach outlined earlier was employed with the only obvious modification in the number of repetitions performed; because of the spherical symmetry of both particles, it is sufficient to execute just one repetition for each node of the mesh. Figure 6.2a reports the trajectories of the j particles which led to a missed aggregation. The trajectories are rectilinear when particles are far apart and become curvilinear as the relative distance reduces. This effect is the consequence of the hydrodynamic interactions that become more intense as the particles come close to each other. These interactions hinder the formation of a doublet and reduce the collision cross section with respect to Smoluchowski's analysis. Therefore, when a substantial offset between the initial position of the particles is present, the Van der Waals attraction is not

able to overcome the viscous resistance to contact. This is due to the fact that Van der Waals attraction are short-ranged, being appreciable when the surface-to-surface distance between the particle is in the order of 20 nm, and thus they are not able to counteract the much more long-ranged viscous resistance.

In order to quantify the entity of the deflection, the difference between the maximum y-coordinate reached during the motion, $\max(y(t))$, and the initial y-coordinate $y(t=0)$ was computed. Figure 6.2b reports this quantity as a function of the initial y-coordinate of the j primary particle. As predictable, as the initial y-coordinate increases, the disturb the particle j perceives is diminished as a result of a lower hydrodynamic interaction; the quantity used to measure the deflection was found to follow precisely a decay law of the kind $y_0^{-3.2}$. In Fig. 6.2c the aggregation cross section is depicted together with the theoretical aggregation cross section of radius $2a$; as apparent, when hydrodynamic interactions are taken into account the aggregation cross section reduces in size, becoming smaller than the theoretical one; the radius of the effective aggregation section is approximately equal to $1.7a$. According to Eq. 6.1, this results into an aggregation efficiency equal to 0.70. Despite the coarseness of the grid, this value compares perfectly well with the one reported by Van de Ven, Mason (1977) and Vanni, Baldi (2002) for same conditions, thus validating the developed technique.

6.3 Monomer-cluster aggregation

When moving to clusters, orientation becomes a crucial issue. As already mentioned, this aspect was addressed changing time by time the initial orientation of the aggregates. Despite the relatively low number of repetitions, this strategy makes it possible to uncouple the computed efficiencies from the relative orientations.

Figure 6.3a reports the collision efficiencies $\alpha_{i,1}$ relative to a primary particle and an aggregate i as a function of their mass ratio m_i/m_1. It is apparent that, as the size difference between the involved aggregates increases, a reduction in the aggregation efficiency appears. This phenomenon can be interpreted in the light of a magnified hydrodynamic force acting on the approaching primary particle, when the aggregate i grows in size. Hydrodynamic interactions are in fact additive in Stokes regime. Therefore, it is clear that the larger the number of primary particle composing the i aggregate is, the more intense is the disturb induced in the surrounding medium. As a consequence, the approaching primary particle is substantially deviated from the rectilinear trajectory, thus reducing $\alpha_{i,1}$. Figure 6.3b reports the deflection of the trajectory of the primary particle computed as the difference between the maximum y-coordinate reached during the motion $\max(y_1(t))$ and the initial y-coordinate $y_1(t=0)$, normalized by the primary particle radius a. To infer statistical reliable data, an average extended to all the events which turned into a missed collision, was performed. As apparent, the trajectory of the monomer is more substantially deviated from the rectilinear streamline of the flow field, as the size of the i aggregate increases, thereby confirming that the disturbance effect induced on the approaching primary particle increases with the mass of the cluster. It is worth to point out that
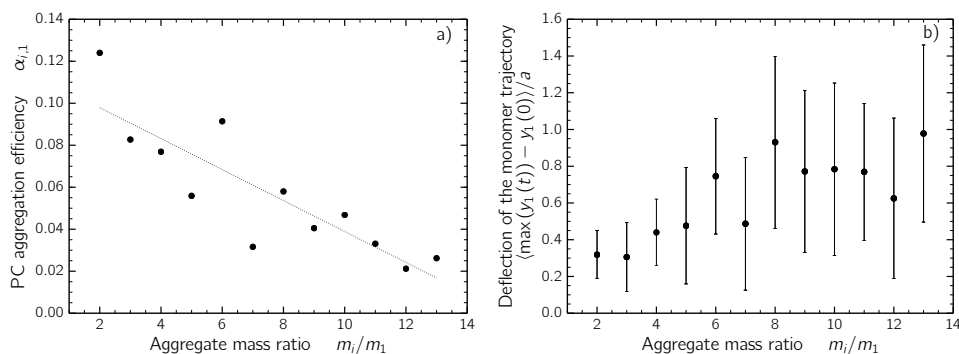
Figure 6.3: a) Primary particle-cluster (PC) aggregation efficiency as a function of the relative mass. b) Average deflection of the primary particle trajectory as a function of the aggregate mass ratio. The average is extended to all the encounter events which turned into a missed aggregation. Error bars indicate the standard deviation of the data.

the wide scatter of the data has not to be regarded as an uncertainty affecting the results, but rather as a consequence of the initial y-coordinate of the primary particle; the release point of the j particle, as witnessed by Fig. 6.2b, has in fact a strong influence on the entity of the hydrodynamic interaction and, as a consequence, on the deflection of the trajectory.

6.4   Cluster-cluster aggregation

When the aggregates involved in an encounter event are comparable in size, their morphology plays a central role; in particular, the aspect ratio appeared to affect seriously aggregation efficiencies. Figure 6.4a reports the aggregation efficiencies computed for different pairs of aggregate i,j; two aggregates with different aspect ratio $A.R.$ were used as central i aggregates, according to the set-up scheme of Fig. 6.1. Encounter simulations with several j aggregates, different in $A.R.$, were performed. As apparent, whether the $A.R.$ of the i aggregate is, a noticeable reduction in the aggregation efficiency arises as the $A.R.$ of the j aggregate grows. Furthermore all the aggregation efficiency values relative to the most spherical i aggregate ($A.R. = 1.54$) are well above the aggregation efficiencies of the most elongated one ($A.R. = 3.33$). Therefore, it can be concluded that the reduction of the aggregation efficiency is magnified when both clusters involved in an encounter event present a rod-shaped morphology.

This phenomenon has to be explained as the consequence of the different motion of round-shaped and rod-shaped aggregates in shear flow; Figure 6.4b reports the time dependence of the aggregate cross section made dimensionless with the primary particle cross section. To obtain such a plot, a single cluster was initially placed in the shear flow $\mathbf{u}^\infty (\mathbf{x}) = \dot{\gamma} y \mathbf{e}_z$ with its major inertia axis aligned with the direction y of the gradient of the velocity field. Starting from this initial configuration, the quantitative estimation of the cross section was achieved with a simple Monte Carlo mapping technique: during the motion in shear flow, the cross section of the 2D projection
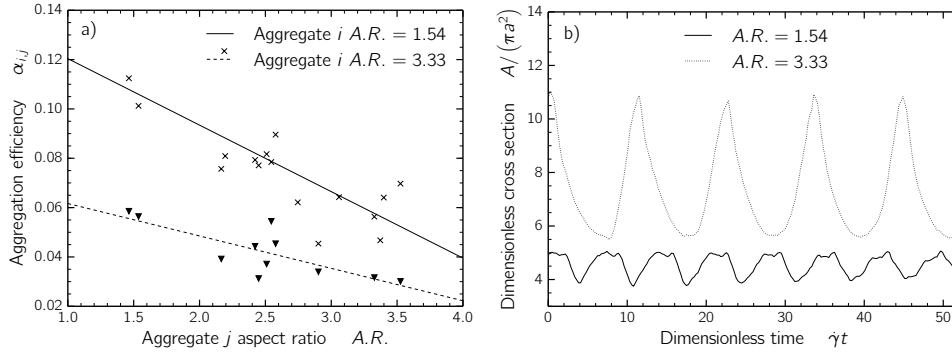
Figure 6.4: a) Cluster-cluster aggregation efficiency as a function of the aspect ratio $A.R..$ The data reported are relative to aggregates composed by a number of primary particles ranging from 3 to 20. b) Time dependence of the aggregate cross section in shear flow.

of the cluster on the plane xy was evaluated by fictitiously hitting the cluster with 10^5 darts moving along a rectilinear trajectory aligned with $\mathbf{e}_z$. The x,y coordinates of the darts were randomly chosen according to a uniform probability distribution spanning from $-R$ to $+R$, with R being the outer radius of the clusters. The cross section was finally computed as the ratio between the number of darts that crossed the cluster structure and the total number of darts that crossed the circumference of radius R. It is apparent that the most elongated aggregate shows large oscillations of the cross section; furthermore, it retains the minimum cross section configuration for a much longer period of time compared to the maximum. This means that during rotation in shear flow the aggregate spends most of its time with its major inertia axis aligned with the flow direction. This configuration corresponds to the minimum cross section. On the contrary the round-shaped aggregate shows a much more regular motion. The cross section shows rather mild oscillations around the average value. These different motions explains why as the $A.R$ increases, missed aggregation are most likely to occur, as the probability that aggregates pass close to each other with their minimum cross sections becomes bigger.

These different behaviours become even clearer when looking at the aggregate angular motion. Figures 6.5 and 6.6 report the time dependence of the x-component of the angular velocity of the two i aggregates used to obtain the plots of Fig. 6.4. For both aggregates the angular velocity shows a fluctuation around the average value ($\omega_x = \dot{\gamma}/2$), but the amplitude of the fluctuations differs substantially in the two cases. For the rod-shaped aggregate the velocity stays at its minimum value for a quite long time, during which the rotation is slow. The long duration of this phase has to be related to the reduced magnitude of the overall hydrodynamic torque acting on the aggregate. As apparent in Fig. 6.5b, this stage corresponds to the maximum alignment of the principal inertia axis with the flow direction (the z-direction in this particular case). Quite suddenly ω_x steeply increases to reach its maximum value. This peak occurs when the aggregate is orthogonal to zero-shear plane (Fig. 6.5c). In this situation the torque acting on the aggregate is at its maximum value and make the aggregate to rapidly rotate till it aligns again with the fluid velocity. In the plots
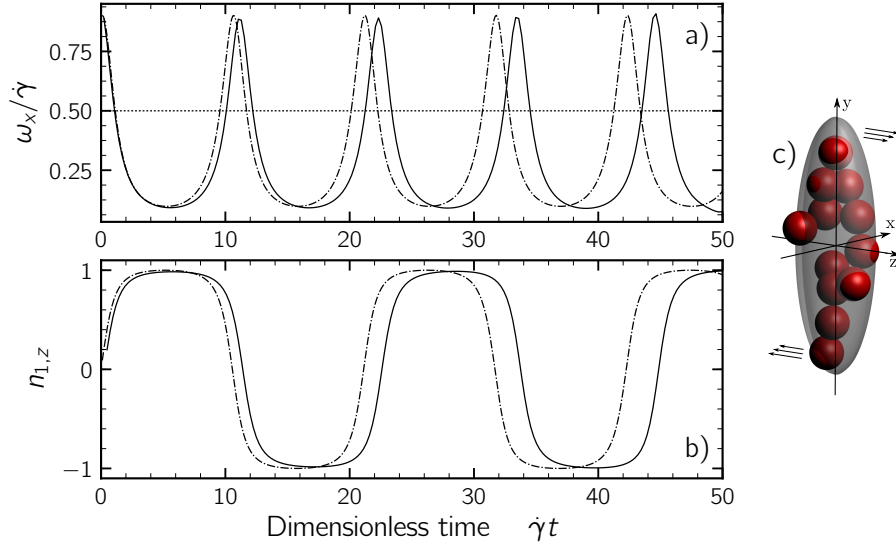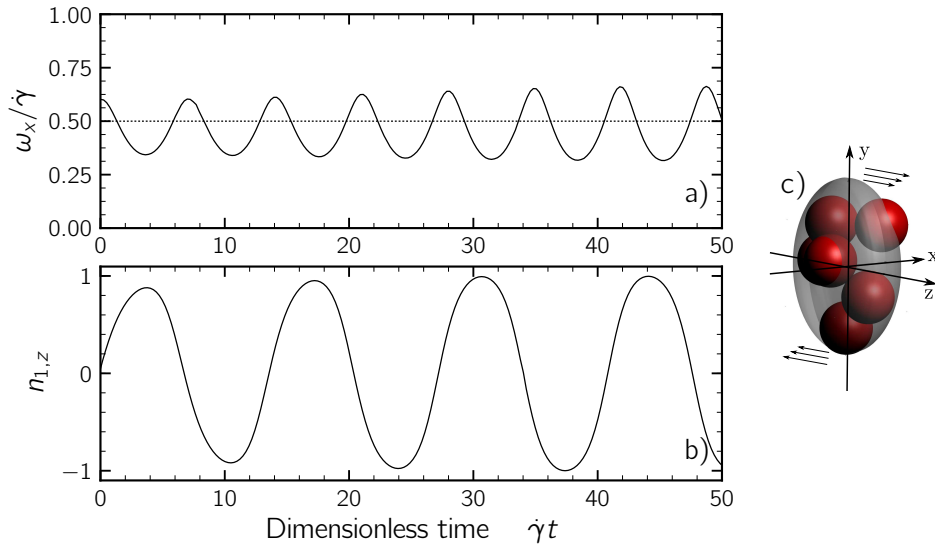
Figure 6.5: Motion of a rod-shaped aggregate ($A.R.$=3.33) composed by 12 primary particles suspended in a shear flow $\mathbf{u}^\infty(\mathbf{x}) = \dot{\gamma}y\mathbf{e}_z$. The dashed lines are relative to the motion of the inertia equivalent ellipsoid computed according to Jeffery (1922). a) Time dependence of the x-component of the angular velocity (solid curve). The dotted line represents the angular velocity of a perfectly spherical particle. b) Time dependence of the z-component of the principal inertia axis unit vector, $n_{1,z}$. c) Representation of the aggregate structure and of the inertia-equivalent ellipsoid.

Figure 6.6: Motion of a round-shaped aggregate ($A.R.$=1.54) composed by 6 primary particles suspended in a shear flow $\mathbf{u}^\infty(\mathbf{x}) = \dot{\gamma}y\mathbf{e}_z$. a) Time dependence of the x-component of the angular velocity (solid curve). The dotted line represents the angular velocity of a perfectly spherical particle. b) Time dependence of the z-component of the principal inertia axis unit vector, $n_{1,z}$. c) Representation of the aggregate structure and of the inertia-equivalent ellipsoid.

of Fig. 6.5a,b the Jeffery solution of the motion of the inertia equivalent ellipsoid of the cluster are also shown (Jeffery, 1922). A good agreement between the cluster and the ellipsoid motion holds, in spite of the irregular shape of the cluster.

The round-shaped aggregate (Fig. 6.6) exhibits a more regular behaviour: the angular velocity oscillates about the average value ($\omega_x = \dot{\gamma}/2$) as well, but oscillations are much smoother and characterized by a smaller amplitude.

From the plots of Fig 6.5 and 6.6 it is also possible to draw the period of rotation as the time interval elapsing between two subsequent peaks of $n_{1,z}$. For the rod-shaped aggregate this period is approximately $22\dot{\gamma}t$, while for the round-shaped one is $\approx 12.5\dot{\gamma}t$. Both value compares quite well with the period of rotation of an ellipsoid with the same aspect ratio, which can be estimated as (Frappier et al., 2010):

$$T_{rot}\dot{\gamma} = 2\pi \left(A.R. + A.R.^{-1} \right) \tag{6.2}$$

which leads to 22.8 and and 13.7 for $A.R. = 3.33$ and $A.R. = 1.54$, respectively. The small discrepancy between the values estimated from Eq. (6.2) and the ones obtained from the DEM simulations of the aggregate motion has to be reasonably ascribed to the irregular structure of the clusters, which gives rise to two minor components of angular velocity, ω_y and ω_z. These minor components oscillate with a much smaller magnitude around the null value and are most likely responsible for such a discrepancy. Given their small magnitude these components are not reported in Figs. 6.5, 6.6.

Finally, it is worth to mention that the angular motion is strongly related to the initial orientation of the aggregate in shear flow. In the plots of Fig. 6.4b, 6.5, 6.6, in order to highlight the different behaviours of the clusters, depending on their aspect ratio, the DEM simulations were started with the major axis of the aggregate aligned with the direction of the gradient of the flow field. However, the qualitative behaviour remain the same when a different initial orientation is adopted. Furthermore, as already mentioned, the aggregation efficiency was calculated by enforcing a random orientation of the aggregates before launching the DEM simulations, thus results should be considered of general validity.

6.5 Conclusion

The aggregation efficiency of rigid aggregates with complex and realistic morphology suspended in a uniform shear flow was investigated. The aggregates adopted were generated by means of the MC-DEM algorithm adopted in Chapter 5 to reproduce a particular realization of a shear-induced aggregation process. The aggregates, composed by equally sized spherical primary particles interacting via both central and tangential interactions, covered a quite broad range of masses and aspect ratios. To quantify collision efficiencies in shear flow a grid-based technique was employed together with the DEM model.

First, the case of solid spherical particles was addressed, leading to a good agreement with previous works. Simulations involving clusters highlighted that two main factors determine collision probabilities: for particle-cluster aggregation events,

size disproportion appeared to strongly affect aggregation. Large aggregates appeared able in fact to substantially disturb the flow field and, as a consequence, to significantly deflect the primary particle trajectory, thus preventing aggregation. Differently, in cluster-cluster encounters, the aspect ratio *A.R.* turned up to be the main factor affecting collision efficiencies. Large *A.R.* has been linked, in fact, to a significant reduction of the time-averaged collision cross section of the aggregates. A fairly good agreement was found with the Jeffery trajectories of ellipsoid suspended in laminar shear.

Results indicate this methodology as a valid approach for the determination of the aggregation efficiencies of irregular clusters of colloidal particles. However, further work may be necessary to expand the library of analysed clusters in order to state if the validity of these findings can be directly extended to larger aggregates. In perspective, such a study may lead to a precise correlation between morphologies and aggregation efficiency to be used to fine-tune Population Balance Equations.

References

Bäbler, M. U. 2008. "A collision efficiency model for flow-induced coagulation of fractal aggregates". *AIChE journal* 54. 1748–1760.

Frappier, G, Lartiges, B., Skali-Lami, S. 2010. "Floc cohesive force in reversible aggregation: a Couette laminar flow investigation". *Langmuir* 26. 10475–10488.

Jeffery, G. B. (1922). "The motion of ellipsoidal particles immersed in a viscous fluid". *Proceedings of the royal society of London A: Mathematical, physical and engineering sciences*. Vol. 102. 715. The Royal Society 161–179.

Kusters, K. A., Wijers, J. G., Thoenes, D. 1997. "Aggregation kinetics of small particles in agitated vessels". *Chemical Engineering Science* 52. 107–121.

Smoluchowski, M. V. 1917. "Versuch einer mathematischen Theorie der Koagulationskinetik kolloider Lösungen". *Zeitschrift für physikalische Chemie* 92. 129–168.

Van de Ven, T. G. M., Mason, S. G. 1977. "The microrheology of colloidal dispersions VII. Orthokinetic doublet formation of spheres". *Colloid & Polymer Science* 255. 468–479.

Vanni, M., Baldi, G. 2002. "Coagulation efficiency of colloidal particles in shear flow". *Advances in Colloid and Interface Science* 97. 151–177.

Veerapaneni, S., Wiesner, M. R. 1996. "Hydrodynamics of fractal aggregates with radially varying permeability". *Journal of Colloid and Interface Science* 177. 45–57.

Chapter 7

Aggregation-breakage equilibrium

The dynamics of a colloidal suspension subject to a shear flow initially proceeds through the aggregation of the primary particles of the disperse phase. Subsequently, when the size of the aggregates becomes so large that the hydrodynamic stress acting on them exceeds their cohesive strength, the bigger clusters start breaking up and, in the end, a dynamic steady state condition may be reached, in which the properties of the suspension do not change any longer and the effects of aggregation and breakup balance each other. The evolution toward this dynamic steady state situation is typical of the colloidal processes conducted under intense stirring and was evidenced experimentally and numerically both under simple laminar flow configurations (Frappier et al., 2010; Oles, 1992; Serra et al., 1997; Wang et al., 2005) and in complex turbulent flow fields (Flesch et al., 1999; Marchisio et al., 2006; Soos et al., 2008).

In this chapter the dynamics of a suspension subject to both aggregation and breakage phenomena is simulated. The MC-DEM method is applied to investigate the evolution of the suspension under the effect of severe viscous stresses. The discussion will be focused in particular on the aggregation and breakage dynamics and on the aggregate structure.

7.1   Setup of the simulations

Simulations were conducted starting from a monodisperse population composed by 200 polystyrene primary particles with a radius equal to 500 nm. The sample volume of the suspension has a volume fraction of solid $\varphi = 10^{-4}$. Particles are assumed to interact only by central forces. As seen in Chapter 5, this should lead to the generation of close-packed soft clusters. The viscosity of the dispersing medium was varied in the range 75-112.5 cP, which combined with an imposed shear flow $\mathbf{u}^{\infty}(\mathbf{x}) = \dot{\gamma} y \mathbf{e}_z$ with constant and spatially uniform rate $\dot{\gamma} = 10^4$ s^{-1}, corresponds to viscous stress ranging from 750 to 1125 Pa. At room temperature these conditions give Péclet numbers of the order of 10^5, making the effects of Brownian motion negligible and the dynamics of the suspension to be determined solely by shear. The physical properties of the particles do not differ from those adopted in Chapter 5 and reported in Table 5.1.
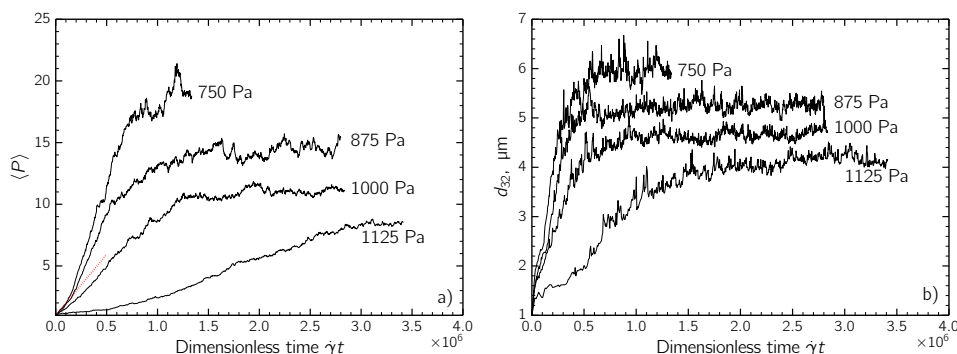
Figure 7.1: Time evolution of the average size of the clusters $\langle P \rangle$ (a) and of the mean Sauter diameter of the population d_{32} (b) for suspensions at shear stresses of $\mu\dot{\gamma} = 750, 875, 1000, 1125$ Pa. The small dashed line in plot a) represents the expected initial growth rate for 750 Pa computed according to Eq. (7.1).

7.2 Dynamics of the population and size evolution

The consequence of the phenomena of aggregation and breakage is the variation of the size of the clusters dispersed in the suspension. In this regard, the plot of Fig. 7.1a shows the temporal evolution of the mean size of the aggregates for four different values of the shear stress $\mu\dot{\gamma}$. The size of aggregate i, in this case, is the number of its primary particles, P_i, and the mean size $\langle P \rangle$ is the arithmetic average of P_i over the whole population. The behaviour at the two lower stresses (750 and 875 Pa) is similar to the one exhibited by suspensions stirred under moderate shear rate; at the initial stages of the process the role of breakup is negligible and the evolution of the suspension is determined solely by aggregation. The initial slope of the curve, when aggregation occurs exclusively between primary particles can be estimated as:

$$\frac{\mathrm{d}\langle P \rangle}{\mathrm{d}t}\bigg|_{t=0} = \frac{4}{\pi}\alpha_{11}\varphi\dot{\gamma} \tag{7.1}$$

where the aggregation efficiency of monomers α_{11} can be predicted quantitatively by using the expression by Van de Ven, Mason (1976):

$$\alpha_{11} = f\left(\frac{A_H}{36\pi\mu\dot{\gamma}a^3}\right)^{0.18}, \tag{7.2}$$

where f is around 0.95 for polymeric particles of 500 nm. The aggregation efficiency is small for such high shear stress (Eq. (7.2) gives 0.077 for 750 Pa), making the process quite slow. Such small values of aggregation efficiency have to be related to the intense hydrodynamic interactions between approaching particles which induce a significant deflection of the particle trajectories, thereby preventing the aggregation and slowing down the aggregation process. This phenomenon was already observed in a number of works and usually referred to as *viscous retardation* (Alam, 1987). As
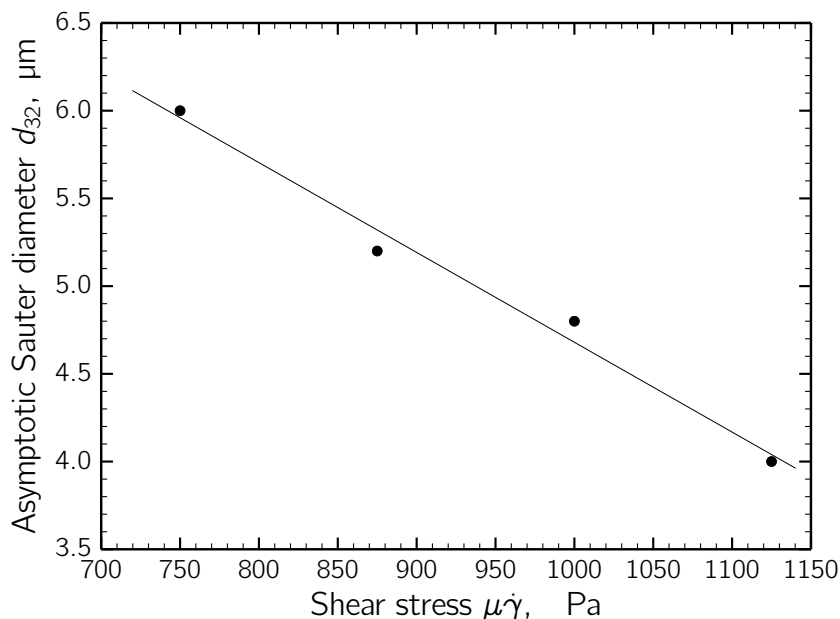
Figure 7.2: Asymptotic Sauter diameter as a function of the shear stress. Circles represent the simulation data as inferred from Fig. 7.1b, the solid line a linear fitting of the data.

apparent in Fig 7.1a, a good agreement was obtained between the theoretical value of the growth rate, estimated by means of Eq. (7.1) and the simulation data.

Since the collision rate is proportional to the cube of the particle size, the generation of the first aggregates leads to an increase of the rate of size enlargement, as clearly visible in the very first part of the curve at 750 Pa. It is also apparent that this condition of self-accelerated aggregation is soon dampened by the breakup of the largest aggregates: initially, still in the growth region, some fluctuations of the average size can be observed and explained as the consequence of occasional breakup events. Subsequently, the role of breakup becomes more and more important and eventually aggregation and breakage balance each other, leading to an asymptotic value of the average particle size. As a consequence of the combination of self-accelerated growth and breakup phenomena the curve relative to the suspension at 750 Pa shows a peculiar S-shape, already observed by various researchers (Oles, 1992; Wang et al., 2005). When the viscous stress is increased breakup affects in a more substantial way the suspension and cluster failures appear starting from the very beginning of the process. This explains why, for the shear stresses of 1000 and 1125 Pa, the initial slope of the growth curve is much smaller than the prediction of Eq. 7.1 (not shown in the plot) and explains the qualitatively different shape of the curves. An additional and more apparent feature of Fig 7.1a is the decrease of the asymptotic size at higher viscous stress. This result is consistent with the expectation that breakup becomes more significant as viscous stresses grow.
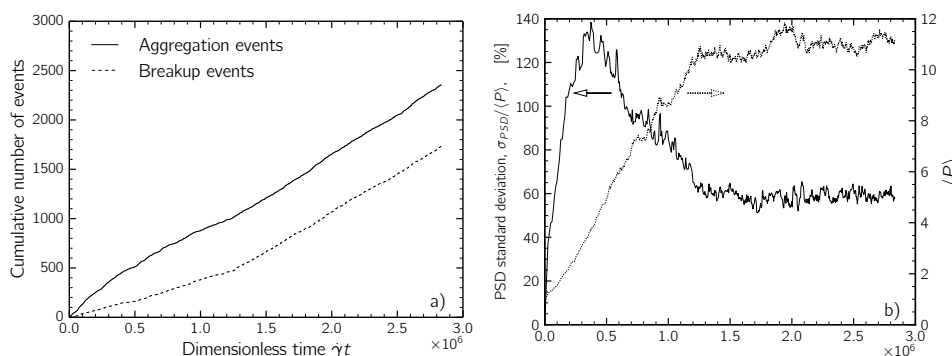
Figure 7.3: a) Cumulative number of aggregation and breakup events as a function of time. b) Time evolution of the average size $\langle P \rangle$ and of the standard deviation of the size distribution, σ_{PSD}. Both plots refer to the suspension $\mu\dot{\gamma}$=1000 Pa.

The graph of Fig. 7.1b reports the average size of the aggregates in terms of average Sauter diameter, computed for the four populations as:

$$d_{32} = 2 \cdot \frac{\sum_{i=1}^{N_a} R_i^3}{\sum_{i=1}^{N_a} R_i^2}. \tag{7.3}$$

with R_i being the outer radius of each aggregate. Differently from $\langle P \rangle$, the Sauter diameter exhibits quite large fluctuations during its temporal evolution. This is partly due to the higher sensitivity of d_{32} to the larger aggregates of the distribution, whose concentration is relatively small and oscillates significantly in time, but it is also a consequence of the periodic deformation experienced by clusters during their motion; in fact, at the end of the DEM simulation, even if a missed collision occurred, the aggregates frequently showed a different morphology, and consequently a different outer radius R_i, compared to their initial structure; this is the consequence of the partial rearrangement of the monomers positions occurring during encounters, as a result of the hydrodynamic interactions they experience while approaching. The asymptotic values of Fig. 7.1b are reported in Fig. 7.2 as a function of the shear stress, making more apparent the reduction of the steady state average dimension when increasing $\mu\dot{\gamma}$. As clear from the plot the asymptotic size follows fairly well a linear decreasing trend. A similar scaling was observed by Oles (1992); however, it should be pointed out that this linear relationship holds true only in the range of viscous stress investigated herein, as it leads to vanishing aggregate size for sufficiently large stress.

Figure 7.3a shows the cumulative number of aggregation and breakage events as a function of time for $\mu\dot{\gamma} = 1000$ Pa. The plot confirms that the equilibrium size of the suspended clusters is the result of a balance between aggregation and breakage events: after an initial transient state during which aggregation prevails over breakage, eventually aggregation and breakage events occur with the same frequency, as inferable from the slopes of the two curves, which are virtually identical after approximately $1.3 \cdot 10^6$ time units. A similar pattern holds also for the other
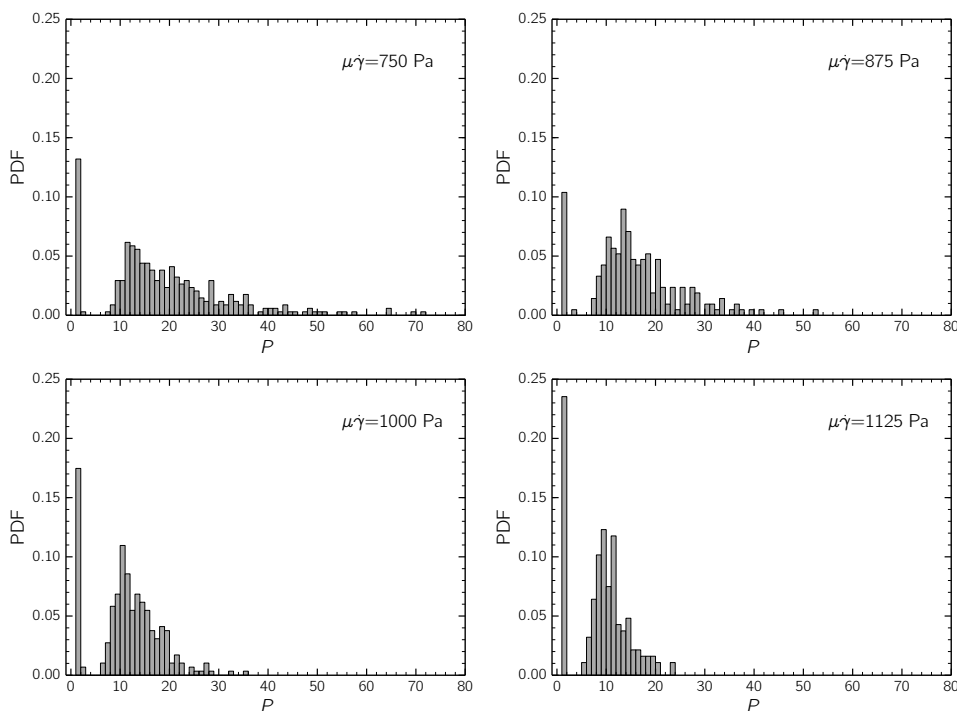
Figure 7.4: Equilibrium particle size distribution for the four analyzed suspensions. The bins corresponds to the number of constituent primary particles; the y axis reports the number fraction.

suspensions, even if breakup phenomena start affecting the system at different times, depending on the viscous stress intensity.

The equilibrium that sets in the suspensions regards also the particle size distribution. Figure 7.3b reports both the time evolution of the standard deviation of the particle size distribution and the average particle size $\langle P \rangle$ for $\mu\dot{\gamma} = 1000$ Pa. At the beginning of the process σ_{PSD} is very small, since the population is made mostly of equally sized monomers. As aggregation proceeds and larger particles are formed, σ_{PSD} increases, passes through a maximum, and eventually reaches a stationary value at around 60% of the average particle size, meaning that the PSD does not change any longer in time. As clear from the plot, the steady state is attained quite simultaneously both in the average size and in the standard deviation of the size distribution.

The full particle size distribution for the four asymptotic populations (i.e., after the steady state condition has been reached) is shown in Figure 7.4. The x-axis reports the size of the aggregates in terms of number of constituent primary particles P, whereas the y-axis reports the probability density function expressed in terms of number fraction. All the suspensions exhibit a bimodal distribution, with a first peak of the distribution for $P = 1$, corresponding to isolated primary particles, and a second peak centred at $P \approx 10 - 13$, regardless of the applied shear stress. The reason for the large fraction of monomers still present at the steady state has to

be looked for in the particular aggregation dynamics occurring in shear flow; the aggregation rate in such a flow configuration is a strong function of the particle size, in that it scales with the cube of the radius of the particle. This implies that when large clusters appear in the suspension, the growth dynamics is mainly governed by the aggregation of such clusters, at the expenses of the smaller ones, including monomers. It can also be observed that the height of the peak is particularly large for the two suspensions subject to the larger stress (1000 and 1125 Pa); as it will be addressed later on, this is due to the fact that larger viscous stresses lead to the breakup of smaller clusters, which frequently give birth to primary particles in an erosion-like breakage mechanism. Furthermore, it was observed that breakage often occurs with the generation of a number of satellite primary particles at the location where bond failure occurs.

The remaining part of the distribution (i.e., the part of the distribution related to the aggregates) resembles a log-normal curve, with a tail whose extension depends strongly on the applied shear stress: it is relatively long for $\mu\dot{\gamma} = 750$ Pa and it progressively reduces as $\mu\dot{\gamma}$ is increased. This can be easily explained if one considers that larger viscous stresses promote on average the breakage of smaller clusters; as a result the asymptotic PSD becomes narrower and present a shorter tail as $\mu\dot{\gamma}$ increases.

7.3 Cluster characterization

In this section the characteristic morphology of the clusters is investigated in terms of mass-size relationship, aspect ratio and mean coordination number. In order to give a direct visual impression of the features of the aggregates, Table 7.1 reports the geometry of a small sample of the population of clusters in the dynamic steady state, together with some of the quantities used to characterize them. While all aggregates are similar in terms of compactness and bond density, their shapes differ significantly in the population, ranging from nearly spherical entities to highly elongated ones.

7.3.1 Local structure - Coordination number

The local structure of the clusters was characterized on the basis of the average coordination number. Figure 7.5a illustrates the relationship between the number of primary particles P and the average coordination number $\langle n_c \rangle = 2n_b/P$, with n_b being the number of bonds detected in the aggregate. The data are relative to the population $\mu\dot{\gamma} = 1000$ Pa; however no significant differences were observed when varying the intensity of the viscous stress, at least in the particular range investigated in this chapter. In the plot the coordination number of isostatic aggregates is reported as well with a dotted line to allow comparison. It is apparent that most clusters, with the only exception of the very small ones, have an over-constrained structure, with an average coordination number well above the one relative to isostatic aggregates. This is a consequence of the particular model adopted for the colloidal interactions. As demonstrated in Chapter 5 when tangential interactions are not included, primary

Table 7.1: Geometries and main characteristics of a sample of clusters of the suspension with $\mu\dot{\gamma} = 750$ Pa at the dynamic steady state. P: number of primary particles; R_g gyration radius; R: outer radius; A.R.: aspect ratio; $\langle n_c \rangle$: mean coordination number

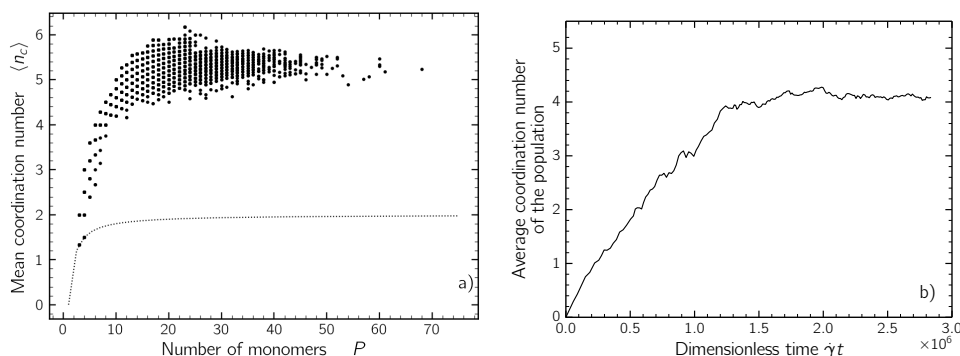| Geometry	P	R_g/a	R/a	A.R.	$\langle n_c \rangle$
	21	2.76	5.08	2.25	5.43
	54	4.10	8.42	1.69	5.33
	27	3.56	7.20	2.90	5.41
	15	2.18	4.20	1.43	5.20
	15	2.28	4.16	1.38	5.20
	18	2.88	5.82	2.90	5.33
	22	2.68	4.84	1.74	5.46
	30	3.24	6.48	1.49	5.68
	29	3.34	6.84	2.44	5.59
	19	3.20	6.38	3.64	5.37

Figure 7.5: a) Average coordination number as a function of the cluster size P. Data were obtained by regularly sampling the population, with a sampling frequency equal to 300 encounters. The dotted line represents the coordination number of isostatic aggregates. b) Average coordination number of the entire population as a function of time. Both plots are relative to the suspension $\mu\dot{\gamma} = 1000$ Pa.

particles are free to slide and roll over each other upon contact, leading to the generation of closely packed structures. In addition, it is apparent that $\langle n_c \rangle$ increases with the size of the cluster, reaching an asymptotic value approximately equal to 5: this behaviour was already reported in Chapter 5 and explained as a consequence of the reduced surface to volume ratio of the larger clusters.

Figure 7.5b reports the temporal trend of the average coordination number of the whole suspension; it was computed averaging the mean coordination number of each cluster over all the population. At $\dot{\gamma}t = 0$, the population average coordination number is equal to zero, since the population is composed by isolated primary particles; this is followed by an almost linearly increasing trend and finally a constant value is reached equal approximately to 4. This asymptotic value is obviously affected by the distribution of the particle size; at the steady state, the asymptotic population is composed by a notable fraction of isolated primary particles and other small clusters which are responsible for the reduced average coordination number of the population.

7.3.2 Global structure - Aspect ratio

As apparent in Table 7.1 the population of aggregates at equilibrium shows a wide variety of shapes, with the coexistence of sphere-like and rod-like aggregates. In order to quantify the aspect ratio of the clusters their structure was translated into their inertia equivalent ellipsoid (see Chapter 5 for the adopted methodology). After evaluating their principal axis of inertia ($a_1 > a_2 > a_3$), the aspect ratio $A.R.$ was computed as:

$$A.R. = \frac{2a_1}{a_2 + a_3} \geq 1 \tag{7.4}$$

where $A.R.$ values close to 1 indicate clusters with a sphere-like structure, whereas larger values are relative to rod-like clusters. The distribution of the $A.R.$ relative to the asymptotic population for $\mu\dot{\gamma} = 1000$ Pa is shown in Fig. 7.6a; as clearly
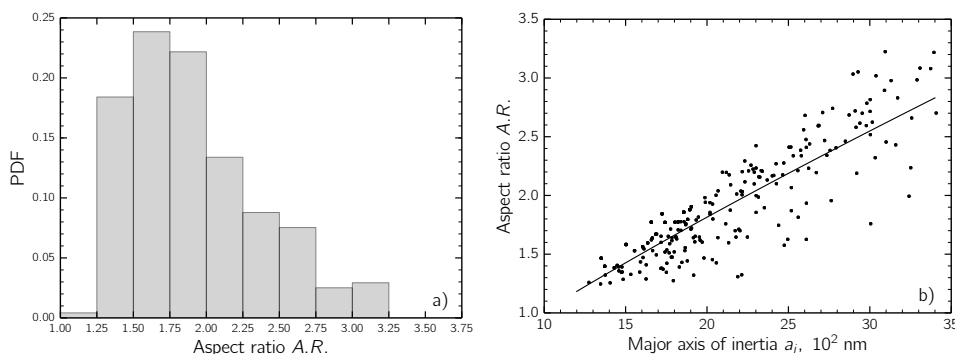
Figure 7.6: a) Distribution of the aspect ratio $A.R.$ over the population of clusters of the population $\mu\dot{\gamma} = 1000$ Pa sampled after the steady state was attained. Only cluster composed at least by 5 primary particles were considered. b) Relationship between cluster size, expressed in terms of length of the major inertia axis a_1, and aspect ratio.

visible, most of the clusters present a slightly elongated structure ($1.25 < A.R. < 2.00$), whereas only a small amount of them shows a well-defined tubular structure ($A.R. > 2.50$). A similar pattern was observed for all the suspensions analysed herein, regardless of the viscous stress imposed. This means that viscous stresses have little effect on the $A.R.$ of the clusters, which is primarily influenced by the model adopted for the colloidal interactions. The distribution of Fig. 7.6a compares in fact fairly well with the one presented in Chapter 5 for the population of particles interacting only by means of central forces, even if much lower viscous stresses were applied.

A relationship between the cluster dimension and the aspect ratio was seen to hold. In this regard Fig. 7.6b reports the values of $A.R.$ as a function of the cluster major inertia axis a_1. As apparent, most of the larger clusters present elongated structures, whereas the smaller ones present a more spheroidal shape. As it will be addressed, this feature can be explained as the consequence of breakage phenomena: the clusters that more frequently undergo breakup generally present an elongated structure and, upon fragmentation, they generate a number of fragments with a more spheroidal structure.

7.3.3 Mass-size scaling

The relationship between mass and size of the clusters is shown in Fig. 7.7. The data are relative to the steady state population $\mu\dot{\gamma} = 1000$ Pa. The fitting of the data points (P, R_g) with a law of the following kind:

$$P = k_f \cdot (R_g/a)^{d_f} \tag{7.5}$$

led to a pre-factor k_f equal to 3.41 and a power-law exponent d_f equal to 1.67. Both values lie in the range of values reported in previous works (Brasil et al., 2000) but are significantly different from the ones obtained in Chapter 5 ($k_f = 2.83$ and $d_f = 1.89$) for the particles interacting solely by central forces, even if they have similar morphologies. Such a discrepancy should be reasonably ascribed to the
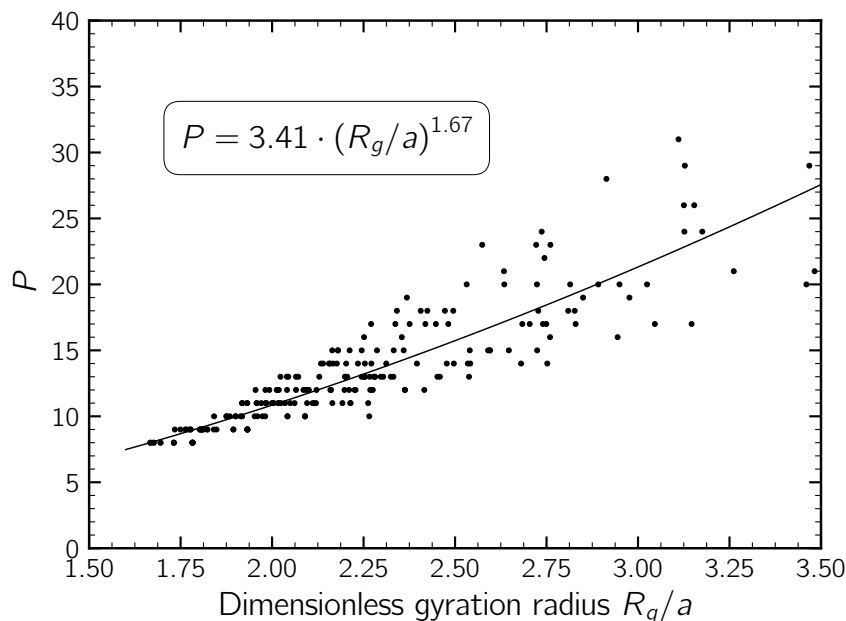
Figure 7.7: Mass-size scaling law for the asymptotic population $\mu\dot\gamma = 1000$ Pa; mass is expressed in terms of number of primary particles P, the size in terms of gyration radius. In the square the equation relating these two quantities is reported.

high sensitivity of the fitting procedure to the particle size distribution; the cluster generated herein are in fact substantially smaller, as a consequence of the breakage phenomena, although virtually identical in terms of compactness and overall shape to those obtained in Chapter 5. Furthermore it is apparent that there is a substantial deviation of the data points from the scaling law especially for large clusters.

7.4 Mechanism of breakup

As discussed earlier, all the suspensions attained a dynamic balance between aggregation and breakup, which caused the suspension to reach a plateau value in the average particle size and the PSD to exhibit a steady state. It is well known that the breakage of a cluster in a moving fluid occurs when the disruptive forces due to the viscous stresses exceed the cohesion force that keeps the particle in contact. The cluster breakage can be due to two distinct mechanisms: first, it may be due to flow heterogeneities; therefore, when a cluster, generated in a region of low shear stress, ends in a region where larger shear stresses act, it can undergo breakage if the local stresses exceed its cohesive strength. A second mechanism is instead more intimately related to the cluster size and morphology; in a spatially uniform shear flow of intensity $\dot\gamma$, if the cluster grows over a certain critical dimension R, it rapidly undergoes fragmentation if $\dot\gamma > \dot\gamma_{cr}(R)$. However, besides the dimension, in this breakup mechanism the cluster shape plays a key role as well: viscous stress acting on the cluster propagate across its structure and accumulate in some critical locations,
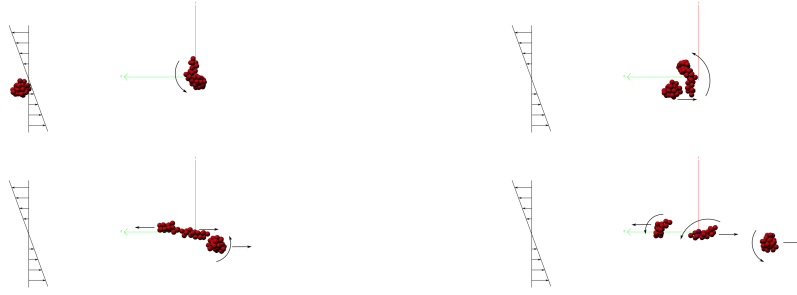
Figure 7.8: Snapshots of an encounter event in simple shear flow ($\mu\dot{\gamma} = 750$ Pa) leading to the breakup of one of the aggregate involved due to the hydrodynamic interaction.
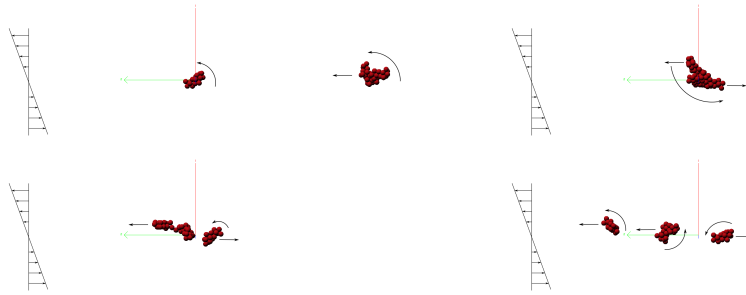

Figure 7.9: Snapshots of an encounter event in simple shear flow ($\mu\dot{\gamma} = 750$ Pa) leading to the breakup of the newly generated aggregate.

where the failure eventually occurs (Vanni, Gastaldi, 2011). Thus, it can be expected that this propagation and accumulation phenomena is much more effective when cluster have an elongated structure.

In the laminar flow configuration investigated herein both mechanisms were observed. Regarding the former one, even if the imposed flow configuration is spatially uniform, breakage events were seen to occur as a consequence of the hydrodynamic interaction between clusters; clusters, while approaching, mutually disturb the flow field that each one experiences, thus locally inducing flow heterogeneities. Figure 7.8 depicts a typical breakup event occurred by this mechanism: the round-shaped aggregate induces a substantial disturb on the flow field, and without an actual collision, it causes the breakage of the central elongated aggregate in two fragments with similar dimension. It is also apparent, that such fragments show a less elongated structure than the parent one, thus justifying the trend shown in Fig. 7.6b.

The breakage of clusters, whose dimension exceeds a certain threshold value, was seen to occur more frequently. As an example, Fig. 7.9 reports the snapshots of a breakup event occurring by such a mechanism: the two involved aggregates collide, form a temporary mechanical contact and finally the resulting aggregate break generating three almost equally sized fragments.

Regardless of the mechanism by which breakage occurred, a dependence between the size of the cluster undergoing breakage and the imposed viscous stress was seen to
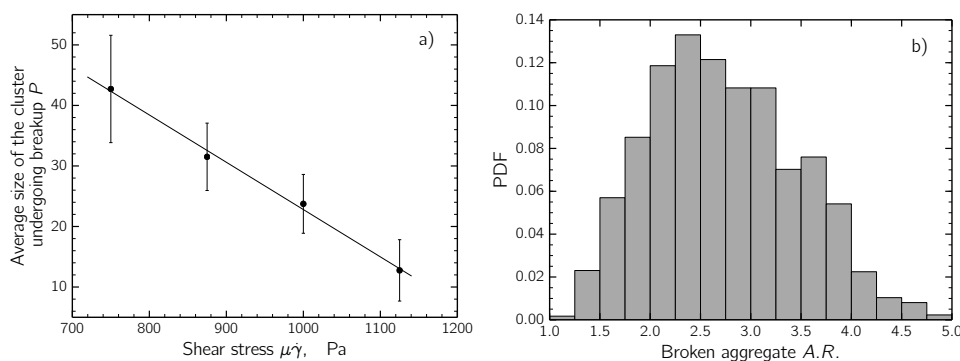
Figure 7.10: a) Size of the cluster undergoing breakage as a function of the applied viscous stress. The circles indicate the dimension in terms of number of primary particles composing the aggregate, as obtained by averaging over all the breakage events. The error bars represent the standard deviation of the data. b) Probability density function of the aspect ratio of the cluster undergoing breakage. Data are referred to the suspension $\mu\dot{\gamma} = 1000$ Pa.

hold. In this regard, Fig. 7.10a reports the dependence between these two quantities, where the cluster dimension is expressed in terms of number of constituent primary particles. As apparent the data are fitted fairly well by a linear relationship, with the average size of the broken cluster decreasing as $\mu\dot{\gamma}$ grows. This result is consistent with the growth behaviour of Fig. 7.1 and confirms that the more severe the viscous stresses are, the earlier breakup starts to affect the suspension dynamics. However, it is worth to emphasize that the linear relationship of Fig. 7.10a holds true for the set of parameters adopted herein; thus it cannot be straightforwardly extended to predict the breakup behaviour outside the range of viscous stress investigated in this work.

As already mentioned, the cluster shape plays a central role in the breakup behaviour. In particular the aspect ratio $A.R.$ appeared as the most influential factor, alongside the cluster dimension. Figure 7.10b reports the probability density function for the $A.R.$ of the aggregate undergoing breakage. The distribution covers a broad range of aspect ratio and it exhibits a peak for $A.R. = 2.25 - 2.50$. However, it should be pointed out that these data are affected by the distribution of the $A.R.$ over the whole population. As shown in Fig. 7.6a, highly elongated and almost spherical aggregates have a rather low concentration in the suspension, thereby the data of Fig. 7.10b cannot be considered as a real breakage frequency. Furthermore, it is possible to note that the distribution of Fig. 7.10b reaches value of $A.R.$ not represented in the plot of Fig. 7.6; this discrepancy is simply due to the different approach used to obtain the data of the two plots: Figure 7.6a reports the data relative to the population sampled at a certain time after the steady state was attained; the data reported in Fig. 7.10b are instead cumulative, meaning that they accounts for all the breakage events occurred during the whole simulated interval of time. Nevertheless, the appearance of a peak in the distribution of the broken aggregates for a value of $A.R. = 2.25 - 2.50$, much larger that the peak $A.R. = 1.50 - 1.75$ appearing in Fig. 7.6a, proves that elongated aggregates are more prone to breakage compared to the round-shaped ones.
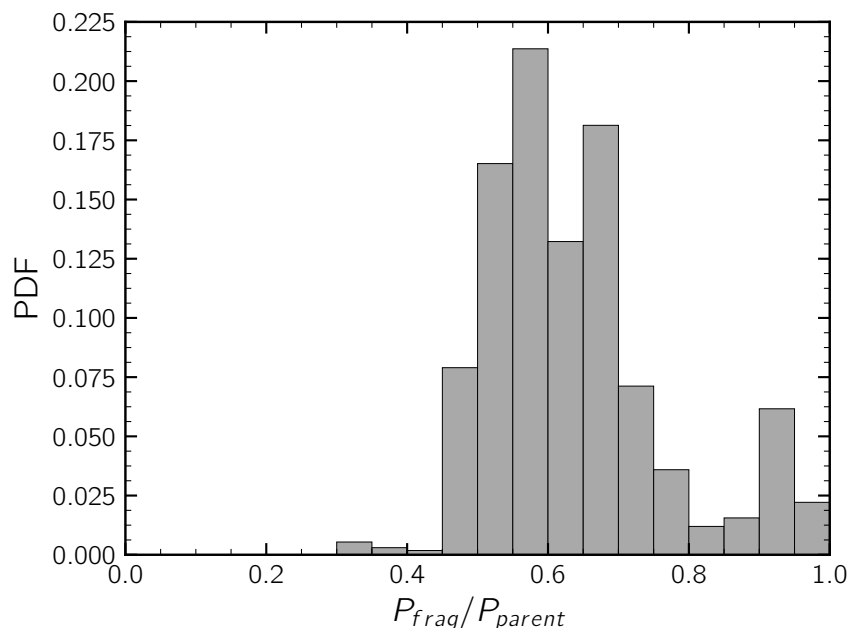
Figure 7.11: Distribution of the mass of the fragments generated upon breakage. Data were obtained averaging over all the breakup events occurred in the suspension $\mu\dot{\gamma} = 1000$ Pa.

Finally, the distribution of the mass of the fragments was investigated. Figure 7.11 reports such an information for the suspension $\mu\dot{\gamma} = 1000$ Pa. The plot reports solely the mass of the larger fragment generated upon breakage. As it can be noticed, the distribution extends from 0.30 to 1.0. Obviously, such a value of the lower limit implies that a number of fragments larger than two may be produced upon breakage. If this were not the case, the distribution would start from values of P_{frag}/P_{parent} strictly higher than 0.50. The PDF of the fragment mass provides some significant insight into the breakup behaviour: first it is apparent that in most cases the larger fragment generated upon breakage has a mass between 50% and 70% of the mass of the parent aggregate. This suggests that breakage frequently occurs by the generation of fragments of comparable size (fragmentation), as already demonstrated by the snapshots of Fig. 7.8. Conversely some events generate fragments with a $P_{frag}/P_{parent} > 0.90$; this implies that also an erosion-like breakup mechanism takes place in the suspension, giving birth to small clusters or even to single monomers, as also witnessed by the PSD of Fig. 7.4.

7.5 Conclusion

In this chapter the dynamics of suspensions subject to severe viscous stresses was investigated. Simulations were conducted starting from a monodisperse population of colloidal particles under fully destabilized conditions.

For low viscous stress the initial growth behavior was seen to compare fairly well with the theoretical expressions reported in literature. Clusters grew, reaching rather

large dimension, but soon their growth was hindered by breakup events. For larger viscous stresses, the breakup started to affect the suspension at a rather early stage. In the analysed range of viscous stress all the suspensions attained a dynamic balance between aggregation and breakage process, which was made apparent by the analysis of the temporal trend of the particle average size and by the particle size distribution.

The breakup phenomena were studied and emerged to occur by two different mechanisms: the first consists in the instantaneous breakup of the clusters that grew over a certain critical dimension; the second occurring as a consequence of the hydrodynamic interaction between approaching aggregates, which, mutually disturbing each other, introduce flow heterogeneities in the imposed flow field. Finally, the effect of the cluster aspect ratio on the breakup and the fragment size distributions were analysed.

References

Alam, M. K. 1987. "The effect of van der Waals and viscous forces on aerosol coagulation". *Aerosol Science and Technology* 6. 41–52.

Brasil, A., Farias, T., Carvalho, M. 2000. "Evaluation of the Fractal Properties of Cluster–Cluster Aggregates". *Aerosol Science & Technology* 33. 440–454.

Flesch, J. C., Spicer, P. T., Pratsinis, S. E. 1999. "Laminar and turbulent shear-induced flocculation of fractal aggregates". *AIChE journal* 45. 1114–1124.

Frappier, G, Lartiges, B., Skali-Lami, S. 2010. "Floc cohesive force in reversible aggregation: a Couette laminar flow investigation". *Langmuir* 26. 10475–10488.

Marchisio, D. L., Soos, M., Sefcik, J., Morbidelli, M. 2006. "Role of turbulent shear rate distribution in aggregation and breakage processes". *AIChE journal* 52. 158–173.

Oles, V. 1992. "Shear-induced aggregation and breakup of polystyrene latex particles". *Journal of Colloid and Interface Science* 154. 351–358.

Serra, T., Colomer, J., Casamitjana, X. 1997. "Aggregation and breakup of particles in a shear flow". *Journal of Colloid and Interface Science* 187. 466–473.

Soos, M., Moussa, A. S., Ehrl, L., Sefcik, J., Wu, H., Morbidelli, M. 2008. "Effect of shear rate on aggregate size and morphology investigated under turbulent conditions in stirred tank". *Journal of Colloid and Interface Science* 319. 577–589.

Van de Ven, T. G. M., Mason, S. G. 1976. "The microrheology of colloidal dispersions: IV. Pairs of interacting spheres in shear flow". *Journal of Colloid and Interface Science* 57. 505–516.

Vanni, M., Gastaldi, A. 2011. "Hydrodynamic forces and critical stresses in low-density aggregates under shear flow". *Langmuir* 27. 12822–12833.

Wang, L., Marchisio, D. L., Vigil, R. D., Fox, R. O. 2005. "CFD simulation of aggregation and breakage processes in laminar Taylor–Couette flow". *Journal of Colloid and Interface Science* 282. 380–396.

Chapter 8

Heteroaggregation of oppositely charged particles

Frequently colloidal particles have a surface charge which provides an energy barrier against aggregation; therefore, in order to induce the aggregation of the particle, the suspension must be destabilized. There exists a number of different methods useful to trigger the aggregation of charged particles (Yates et al., 2008): high molecular weight polymers can be used to promote the formation of bridges between particles (Biggs et al., 2000; Zhou, Franks, 2006); the increase of the ionic strength of the dispersing medium can be exploited to compress the electrical double layer and screen the repulsion between the particles; finally, the concentration of the potential determining ions can be adjusted to neutralize the particle surface charge (Jiang et al., 2009; Liu et al., 2013). When the increase of the solid content is of no importance for the outcome of the operation, the addition of particles bearing an opposite charge can be an alternative option to the aforementioned methods. The resulting aggregation process is often referred to as *heteroaggregation* in contrast to the *homoaggregation* i.e., the aggregation of monocomponent colloidal suspensions (Kim, Berg, 2000; Kim et al., 2003).

Although various studies addressing the heteroaggregation of oppositely charged particles have appeared in the literature, (AlSunaidi et al., 2000; Hogg et al., 1966; Kim et al., 2003; López-López et al., 2005; Yates et al., 2008) a full understanding of the heteroaggregation kinetics and aggregate structure is still missing. A number of parameters affects in fact the phenomenon, namely nature of solvent and particles, electrical double layer thickness, relative concentration of anionic and cationic particles, surface potentials, Péclet number, thus making the complete study of the problem extremely challenging.

Kim et al. (2003), for instance, investigated the Brownian aggregation of mixed population of oppositely charged particles with small screening parameter, revealing that, when interactions between particles are long-ranged, chain-like structure with the particle charge alternating down the chain are produced. López-López et al. (2005) performed diffusion-limited cluster-cluster aggregation simulations varying the relative amount of cationic and anionic particles. After imposing that only aggregation
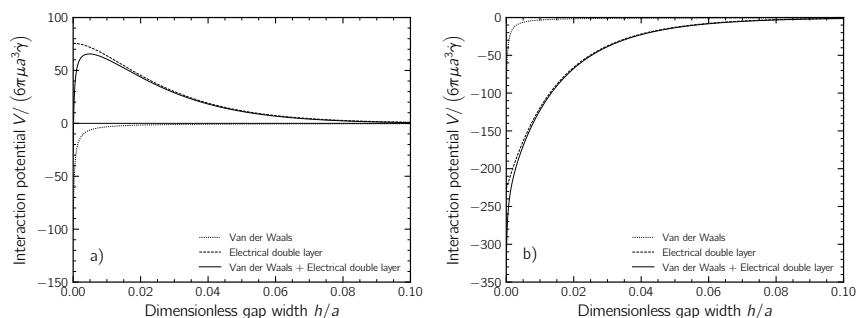
Figure 8.1: Interaction potential for a pair of primary particles with (a) same surface potential ($\Psi_\alpha = \Psi_\beta$=40 mV) and (b) opposite surface potentials ($\Psi_\alpha = -\Psi_\beta = 40$ mV). For both cases a dimensionless Debye screening parameter κa=50, with $a = 500$ nm, was adopted; the viscous stress is equal to $\mu\dot\gamma = 10^{-3}$ Pa. The Hamaker constant is $0.95\cdot10^{-20}$ J.

events between unlike particles can occur, they found out that a critical concentration separating two different aggregation regimes exists: when the suspension is formed by a fraction of particles of one kind falling in the range 0.825–0.875, they demonstrated that stable aggregates are produced; these aggregates are composed by a few minority particles placed in the inner region and are highly covered by the majority ones on the surface, thus providing a stabilization against further growth; on the contrary, for suspensions with a composition smaller than this critical concentration, they argue that such stable aggregates are never formed and the aggregation proceeds indefinitely. In similar conditions, AlSunaidi et al. (2000), performing Brownian diffusion simulations, observed the same behavior but they found a slightly lower value for this critical concentration; however, this may be due to the geometric constraints imposed by the on-lattice approach used.

All these previous works were focused on perikinetic aggregation. In a stirred suspension, due to the different aggregation dynamics and to the restructuring phenomena, such size stabilization may not occur or however the value of such a critical concentration may be different. For this reason, the developed MC-DEM method was employed to study the shear-aggregation of suspensions characterized by the coexistence of cationic and anionic colloidal particles in different relative amount, in order to ascertain if size stabilization should be expected.

8.1 Aggregation efficiency

The aim of this chapter is to study the aggregation occurring in suspensions in which particles with +40 mV and −40 mV surface potentials are dispersed in various relative amounts. However, before discussing on the population aggregation dynamics, it is useful to investigate how primary particles aggregate depending on their surface potentials; the complex interplay between hydrodynamic and colloidal interactions determines in fact the aggregation efficiency of colloidal particles, which, especially when starting from monomeric conditions, has serious implications on the early stage of the aggregation phenomenon.
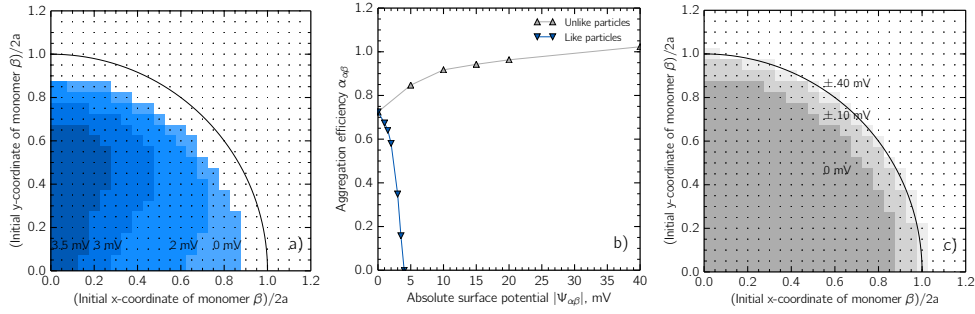
Figure 8.2: a) Aggregation cross sections for a pair of like particles with surface potential ranging from $0\,\mathrm{mV}$ to $3.5\,\mathrm{mV}$. b) Aggregation efficiency as a function of the surface potentials of the particles. c) Aggregation cross sections for a pair of unlike particles with opposite surface potentials.

In Fig. 8.1 the total interaction potential is plotted for the case of like and unlike particles, normalized with the convective energy provided by the shear flow field. As apparent, for like particles (Fig. 8.1a) a rather high energy barrier appears at small separation distance, opposing aggregation. However, the height of this barrier depends on the surface potential of the particles. On the contrary, for unlike particles, such an energy barrier does not exist and a purely attractive and long-ranged interaction holds.

In order to evaluate the joint effect of hydrodynamic and colloidal interactions, in particular when varying the surface potential of the particles, the grid-based technique, already used in Chapter 6, was employed with some slight modifications: given a pair of primary particles α, β with a common radius a equal to 500 nm and a shear flow field $\mathbf{u}_\infty = \dot{\gamma} y \mathbf{e}_z$ with $\dot{\gamma} = 10\ \mathrm{s}^{-1}$, a 25×25 evenly spaced quadrilateral mesh was generated in a plane $z = -10 \cdot a$ within the quadrant $y > 0$, $x > 0$. The size of each side of the mesh was set equal to $\varepsilon(a + a)$, with $\varepsilon = 1.2$. At the beginning of each DEM simulation the center of mass of the primary particle β was placed on a node of the mesh, whereas particle α was placed in the origin of the reference system. From this initial configuration the DEM was used to track the motion of both particles and to verify the occurrence of aggregation. Different values of the surface potential were considered; the obtained aggregation cross sections for the case of like and unlike particles are depicted in Figs. 8.2a and c, respectively. In both cases $|\Psi_\alpha| = |\Psi_\beta|$. For the aggregation of like particles, since the expression of Eq. (3.72) is symmetric with respect to the sign of the surface potential, only the case in which particles bear a positive surface charge was considered.

With regard to the aggregation of like particles (Fig. 8.2a), as apparent, the shape and the size of the collision cross sections are strongly dependent on the value of the common particle surface potential. When $\Psi = 0$ mV, a net short-ranged Van der Waals attraction holds, but the aggregation cross section extension is smaller than the one hypothesized by Smoluchowski (solid curve in the plot). This is mainly due to the hydrodynamic interactions between the particles which prevent them to get at a distance where the intensity of the Van der Waals attraction is significant. However,

similarly to the Smoluchowski cross section, the obtained one exhibit a symmetric circular shape.

When particles present a common surface potential $\Psi > 0$ mV the cross sections become smaller in size and lose their symmetrical shape. This behaviour has to be related to an interplay between colloidal and lubrication interactions and to the different range of action of electrical double layer and Van der Waals interactions, with the latter being significantly more short-ranged; for the small values of Ψ used herein, the total interaction is of an attractive nature at very short distances only and slightly repulsive at larger distances. To have a better insight, it is useful to focus, for instance, on the cross section obtained for a common surface potential $\Psi = 2$ mV. In this case it can be seen that for sufficiently large initial x coordinate, the dimer formation probability changes according to the value of the initial y-coordinate of particle β. For low values of the initial y-coordinate, the relative approaching velocity between the particles is small and, as a consequence, the convective energy is not able to overcome the resistance to contact arising from both lubrication and electrical double layer repulsion. As the initial y-coordinate is increased, particles approach each other faster and the convective energy succeeds in bringing the particles up to a distance in which attraction become important, prevailing over both lubrication and repulsive electrical double layer interactions and thus leading to the aggregation of the particles. For even larger y-coordinate, the offset of the initial particle coordinates is large and particles do not aggregate anymore. These arguments still hold when increasing the particle surface potentials; however, for larger Ψ the aggregation cross sections become significantly smaller as a consequence of the increased intensity of the repulsive interaction and eventually aggregation no longer occur for common surface potential $\Psi > 4$ mV.

On the contrary, when particles bear opposite surface charges the extension of the aggregation cross section grows as the difference between their surface potential increases (Fig. 8.2c). This behaviour can be easily explained considering that more intense and more long-ranged attraction forces act on the particles when increasing $|\Psi|$.

The values of aggregation efficiencies were calculated by computing the ratio between the flow rate of particles crossing the obtained collision section S with the flow rate crossing the collision section assumed by the model of Smoluchowski, circumscribed by a solid curve in Figs. 8.2a,c. Therefore, for a pair of primary particles α,β the aggregation efficiency $\alpha_{\alpha\beta}$ reads as:

$$\alpha_{\alpha\beta} = \frac{\int_S \dot{\gamma}ydS}{\int_{S_{Smol}} \dot{\gamma}ydS} \tag{8.1}$$

Figure 8.2b reports the values of aggregation efficiencies computed according to Eq. (8.1). As noticeable, for the case of like particles the aggregation efficiency goes rapidly to zero as the surface potentials increase over 4 mV. As already stated, this behaviour is the consequence of the joint action of lubrication resistance and electrical double layer repulsion, which both act preventing particles to aggregate. Conversely, for unlike particles, the aggregation efficiency shows a monotonic increasing trend

Table 8.1: Physical properties of the simulated suspensions

Parameter	Symbol	Value
Volume fraction of solid	φ	10^{-4}
Hamaker constant	A_H	$0.97 \cdot 10^{-20}$ J
Particle surface potential	Ψ	$\pm$ 40 mV
Reciprocal Debye length	κ	10^8 m^{-1}
Vacuum permittivity	ε_0	$8.854 \cdot 10^{-12}$ F m^{-1}
Water relative permittivity	ε_r	80.1
Minimum approach distance	z_0	0.165 nm
Monomer radius	a	500 nm
Medium viscosity	μ	10^{-3} Pa s
Medium density	ρ_l	1000 kg m^{-3}
Particle density	ρ_p	1000 kg m^{-3}
Shear rate	$\dot{\gamma}$	10 s^{-1}
Population composition	x_A	0.50–0.85

as the difference between the surface potentials of the particle grows and assumes values slightly larger than 1 for $\Psi = \pm 40$ mV.

Despite the coarseness of the grid used, on the basis of the computed aggregation efficiencies, it is possible to reasonably conclude that, with the adopted set of parameters, for mixed populations of cationic and anionic particles with absolute surface potentials larger than 4 mV only heteroaggregation events can occur.

8.2 Population dynamics

8.3 Setup of the simulations

In order to study the population dynamics, different simulations were performed starting from a monodisperse population of polystyrene colloidal particles with radius a=500 nm; particles bearing opposite surface charges with low surfaces potential ($\Psi = \pm$ 40 mV) and surrounded by a thin electrical double layer were considered; a dimensionless Debye screening parameter κa=50, with κ being the reciprocal of the Debye length, was adopted. No tangential interactions were included. A relatively mild shear rate was assumed to act on the suspension ($\dot{\gamma}$=10 s^{-1}). The relevant parameters of the simulations are listed in Table 8.1.

The only parameter which was varied in the simulations is the initial population composition; denoting with A and B the cationic and anionic primary particle, respectively, it is possible to define the composition x_A as:

$$x_A = \frac{n_{A,0}}{n_{A,0} + n_{B,0}} \tag{8.2}$$

where $n_{A,0}$ and $n_{B,0}$ indicate the initial number concentration of primary particle A and B dispersed in the suspension. Because of the symmetry of the system, in which
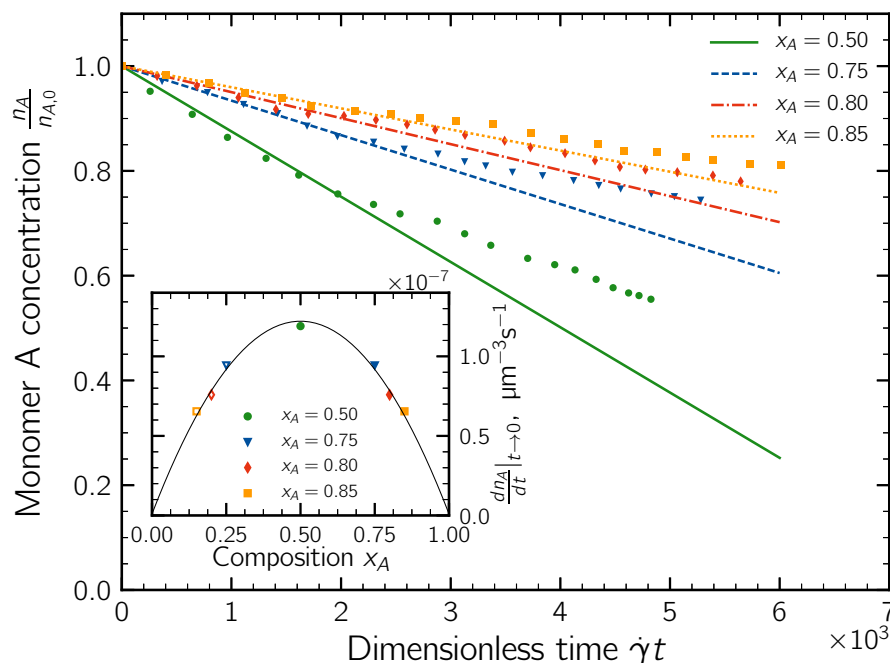
Figure 8.3: Temporal trend of the monomer A numeric concentration for the 4 suspensions analyzed. The symbols represent the simulation data as obtained averaging over 5 different realizations of the MC-DEM method. In the inset the initial dimer formation rates are plotted as a function of the initial composition x_A; only simulations with $x_A \geq 0.5$ were actually performed.

particles present the same absolute surface potentials, only suspensions in which $x_A \geq 0.5$ were simulated. Therefore in the following A and B particles will also be referred to as majority and minority particles, respectively.

It is worth to point out that the simulations are limited to the investigation of the initial stage of the process, when only aggregation events take place; therefore, aggregates never reached dimension large enough to be vulnerable to breakage.

Early stage kinetics

The early stage kinetics of an aggregation process carried out starting from a population of isolated particles is determined almost exclusively by monomer-monomer aggregation; as demonstrated in the previous section, with the adopted set of parameters only heteroaggregation events involving oppositely charged particles can occur; therefore, the rate of disappearance of monomer A, and equivalently of monomer B, can be described as:

$$\frac{dn_A}{dt}\big|_{t\to 0} = -k^a n_{A,0} n_{B,0} = -k^a n_{tot,0}^2 x_A \left(1 - x_A\right) \tag{8.3}$$

where k^a represents the monomer aggregation rate, or equivalently the dimer formation rate, given by the product of the Smoluchowski encounter rate with the aggregation

efficiency α_{AB} computed by the grid-based technique, and where $n_{tot,0}$ is the initial total number concentration including both monomer A and monomer B.

In the plot of Fig. 8.3 the simulation data $n_A/n_{A,0}$, obtained averaging the results over 5 different realizations of the MC-DEM method are reported; the straight lines were obtained with a least square fitting of the first 8 data points (corresponding to the first 80 encounters). As apparent, regardless of the value of x_A, initially the monomer A concentration follows fairly well a linearly decreasing trend. Deviations from the fitting lines appear only for larger times; this is mainly due to the fact that as soon as dimers, trimers and other larger clusters are produced, monomer-monomer encounters are no longer dominating the aggregation process; clusters, because of their larger cross section compared to the one of monomers, are more likely to be involved in aggregation events, thus lowering the rate of primary particle disappearance.

The values of the slopes of the straight lines are plotted in the inset of Fig. 8.3 as a function of the composition x_A together with Eq. (8.3). As can be noticed, the computed values follow remarkably well the parabolic function of x_A of Eq. (8.3), with the larger dimer formation rate observed in the symmetric system ($x_A = 0.50$). This can be easily explained considering that, when anionic and cationic particle are present in the suspension in the same amount, the probability for any pair of unlike particles to encounter each other in the suspension is maximum, but it sharply decreases as the suspension is enriched in one of the two classes of particles. This behaviour confirms what predicted by the HHF theory by Hogg et al. (1966) and what observed by López-López et al. (2005) performing off-lattice Brownian Dynamics simulations.

Late stage kinetics

During the early stage only aggregation events between monomers take place. This allowed us to compute a dimer formation rate constant by monitoring the temporal trend of the monomer concentration. On the contrary, in the subsequent stages of the process, a set of different encounters can occur, including both monomer-cluster and cluster-cluster. Similarly to the case of primary particles, such encounters between clusters do not necessarily result into an aggregation; the aggregation efficiency is strongly dependent upon the cluster morphology and surface composition, which may prevent or favour the aggregation. If the closest pairs of primary particles composing the two approaching clusters have an opposite surface potential, an aggregation event is the most likely to occur. On the contrary, if the aggregates approach each other with equally charged particles, once in close proximity, they may repel each other, significantly deviating their trajectories.

To better understand how these phenomena affect the aggregation dynamics, it is useful to analyse the growth behaviour of the suspensions. Figure 8.4 reports the temporal evolution of the cluster average size expressed in terms of number of constituent primary particles $\langle P \rangle$ for the 4 different initial compositions x_A. All curves start from $\langle P \rangle = 1$, corresponding to a mono-disperse population of primary particles, but soon their behaviours start to differ significantly: as discussed in the previous section, the initial growth rate is strongly related to the composition of
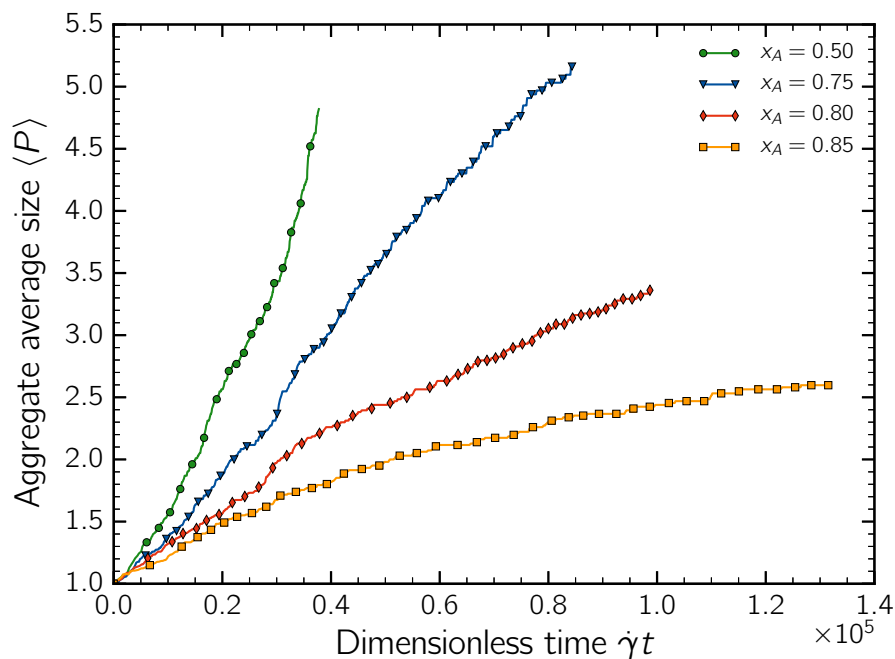
Figure 8.4: Temporal trend of the average size of the suspended clusters expressed in terms of number of primary particles per aggregate.

the population: it is faster for the symmetric system ($x_A = 0.50$) i.e., the system composed by an equal amount of cationic and anionic particles, and sharply slows down as the the suspension is enriched in one of the two classes of particles. This phenomenon is still clearly visible in the plot of Fig. 8.4. However, for longer times a qualitatively different behaviour emerges: for $x_A = 0.50$ the growth rate of the cluster average size increases throughout the aggregation process and the suspension reaches large values of $\langle P \rangle$ in a relatively short time. This behaviour can be explained as the result of the distinct phenomena: firstly, during the initial stages only one half of the monomer-monomer encounter can lead to a dimer formation. At a later stage larger clusters, composed by a comparable amount of anionic and cationic primary particles, appear in this suspension. Therefore, during a binary encounter, even if clusters approach each other with a pair of like particles, the repulsive interaction may deviate their relative trajectories and a contact can still occur involving a different pair of primary particles. Secondly, the increased average cross section of the suspended clusters determines a speed-up of the growth process, with aggregation events that take place with an increased frequency.

Looking at the curve relative to the suspension with initial composition $x_A = 0.75$, this self-accelerated growth dynamics is absent; as it will be addressed in the next section, in this suspension the clusters present a surface composition rather similar to the initial composition x_A; for this reason, the probability for two unlike particles composing the approaching clusters to touch each other is smaller compared to the symmetric system, thus the cluster-cluster aggregation efficiency reduces substantially.
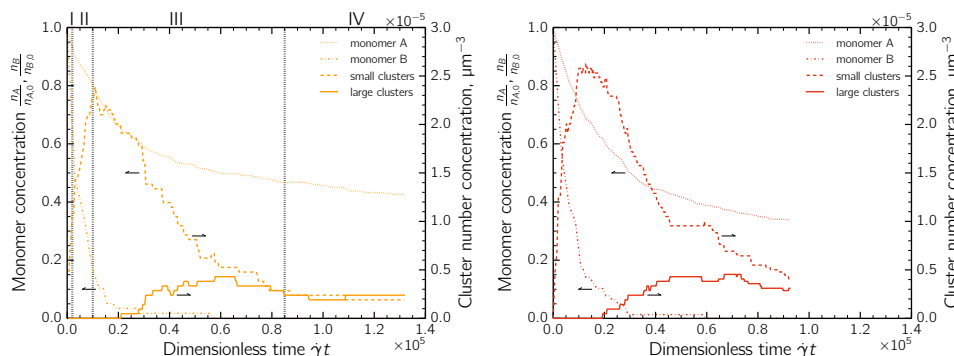
Figure 8.5: PSDs for the suspensions $x_A = 0.85$ (left plot) and $x_A = 0.80$ (right plot). Please note the different scales on the left and right y-axis.

This reduction is able to partially neutralize the speed-up we would expect as a result of the increased average cluster cross section, thus finally determining an almost linearly increasing average dimension $\langle P \rangle$. A rather similar picture emerges from the suspension with composition $x_A = 0.80$.

The growth behaviour of the suspension $x_A = 0.85$ is substantially different: the cluster growth rate progressively slows down and for large times a plateau value of $\langle P \rangle$ is attained, meaning that the clusters stopped aggregating; a size stabilization takes place in this suspension. These different trends suggest, as already pointed out by AlSunaidi et al. (2000) and López-López et al. (2005) that a critical initial composition $x_{A,c}$ should exist, discriminating between the unlimited growth behavior and the size stabilization phenomenon. Based on the growth kinetics we can reasonably state that this concentration should fall in the range 0.80–0.85.

However, it is important to bear in mind that the $\langle P \rangle$ values are highly sensitive to the cluster size distribution; the average cluster size in all the systems analysed is in fact strongly affected by the presence of a significant amount of isolated monomers which, in the particular case of the $x_A = 0.85$ suspension, represents about the 90% of the total number of suspended particles even for large times. To better clarify this aspect, Fig. 8.5 reports the variation in time of the concentration of the two classes of monomers and the one of large and small clusters, discriminated on the basis of the number of constituent monomers; clusters composed by $P \geq 10$ monomers are regarded as large ones, clusters with $2 \leq P < 10$ are considered small. Focusing on the plot relative to the suspension $x_A = 0.85$ (left plot in Fig. 8.5), it is possible to divide the aggregation dynamics in 4 subsequent steps:

I) the aggregation is dominated by monomer-monomer aggregation between unlike particles. As discussed in the previous section, this stage has a rather short duration;

II) dimers and other small clusters appear in the suspension acting as growth seeds; they aggregate with themselves and with the monomers of both classes, that are still present in a significant amount in the suspension. The end of this phase coincides approximately with the peak in the small cluster concentration.
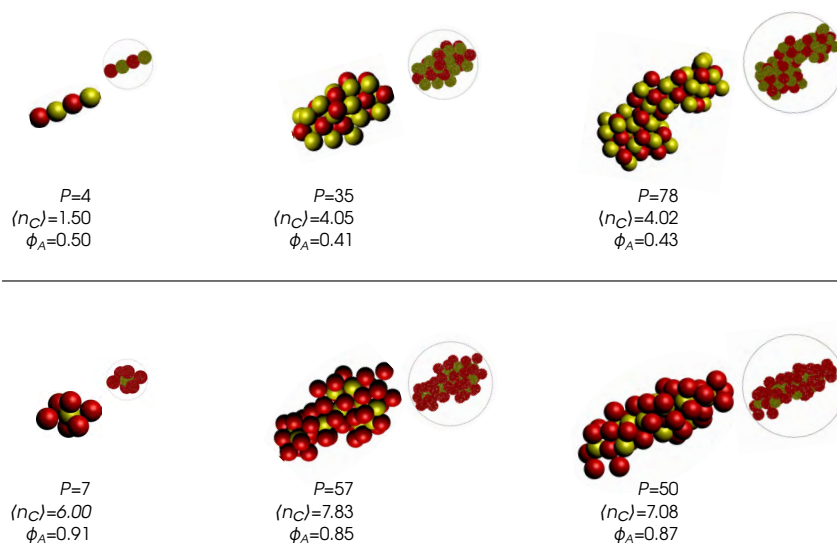
Figure 8.6: Representation of a sample of clusters from the population $x_A = 0.50$ (top) and $x_A = 0.85$ (bottom) with some of the parameters used for their characterization: P is the number of constituent primary particles, $\langle n_c \rangle$ is the minority particle average coordination number and ϕ_A, a measure of the surface composition.

III) minority particles B are totally consumed, but a significant amount of majority monomers A is still present. The aggregation is now dominated by monomer A-cluster and cluster-cluster aggregation. During this phase clusters are progressively covered by majority monomers.

IV) all superficial binding sites of the growing clusters are now saturated; clusters become stable, being fully covered by majority particles, and aggregation stops. The particle size distribution no longer changes in time and an equilibrium state sets in the suspension.

In the suspension $x_A = 0.80$ (right plot in Fig. 8.5) the initial behaviour is rather similar but the size stabilization effect does not take place; the concentration of small and large clusters keep reducing in time without reaching a constant value. This different trend suggests that no size stabilization will be reached even for large times.

Finally it is worth to point out that the growth of clusters will be in any case limited by breakage phenomena. Once clusters attain large enough size, they become more vulnerable to breakage events as a consequence of the viscous stress exerted by the flow field. Therefore, in all the suspensions in which a size stabilization effect did not occur, a plateau value of $\langle P \rangle$ is expected to be reached at a later stage, as a consequence of an equilibrium between aggregation and breakage phenomena.

8.4 Cluster characterization

The long-time behaviour of the suspensions can be better understood after characterizing the cluster structures produced upon aggregation. The aim of this characterization
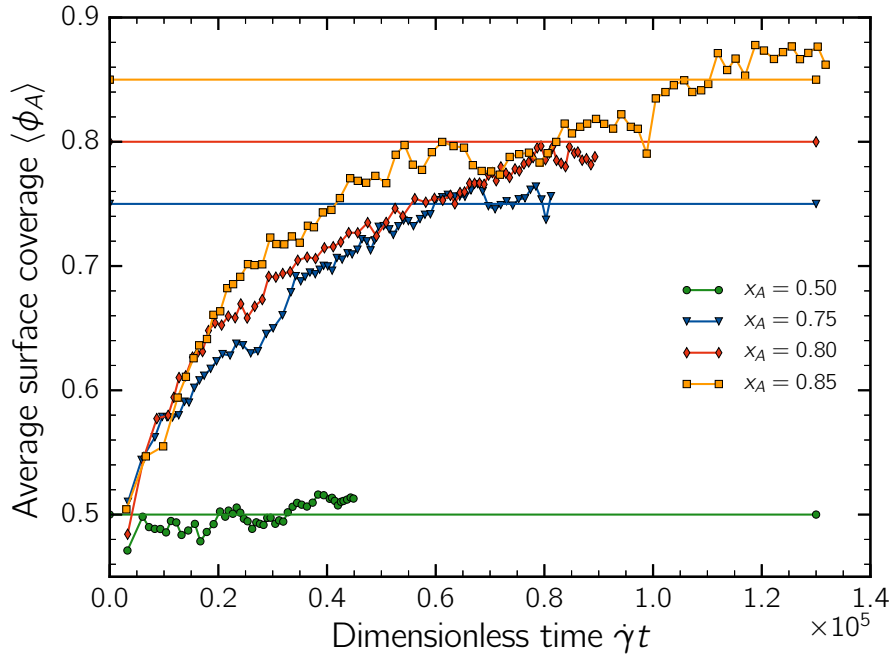
Figure 8.7: Average surface coverage of the populations of clusters as a function of time. Monomers were excluded from the calculation.

is to investigate how monomers organize in clusters depending on the composition x_A of the population. In order to gain a deeper insight into the cluster morphology, the clusters produced in all the 4 different suspensions were characterized by analysing:

- the cluster surface composition,

- the average coordination number,

- the average three-particle angle.

Figure 8.6 shows a small sample of clusters together with some of the quantities used for the characterization.

Surface composition

The size stabilization effect has to be related to the surface composition of the clusters produced upon aggregation. In order to quantitatively estimate it, a simple Monte Carlo mapping technique was developed: averaging over 100 randomly chosen different orientations, the surface composition of the 2D projection of the clusters was evaluated by fictitiously hitting the clusters with 10^5 darts whose coordinates were randomly sampled according to a uniform probability distribution spanning from $-R$ to $+R$, with R being the radius of the smaller circumference encompassing the 2D projection of the cluster. The surface composition ϕ_A was finally computed by calculating the ratio between the number of darts that hit the monomer A with the total number of

darts that hit the cluster projected area. The so obtained berry-like representations of the clusters are reported in Fig. 8.6. Figure 8.7 reports the average surface coverage of the 4 analysed populations as a function of time. Monomers were excluded from the calculation and the computation was started after the first 100 encounters, when, excluding monomers, the population is mostly composed by dimers and to a lesser extent by trimers and other small clusters. Due to the prevailing presence of dimers, all populations have an initial $\langle \phi_A \rangle$ equal approximately to 0.5. However, after a short time the surface composition start to differ significantly among the various populations. As predictable, in the symmetric system, $\langle \phi_A \rangle$ keeps oscillating around 0.50 throughout the aggregation; on the contrary, the other systems show a different behaviour with a rapidly increasing surface coverage. The rate of this increase has a weak dependence on the composition x_A, but the most striking difference between the three systems emerges for large times, when an asymptotic value of $\langle \phi_A \rangle$ is attained: the suspensions $x_A = 0.75$ and $x_A = 0.80$ reach an asymptotic value which equals the composition x_A, whereas for the suspension $x_A = 0.85$ the average surface coverage exceeds 0.85. This result combined with the observations inferred from Fig. 8.5a demonstrates that the size stabilization effect taking place in this suspension is the result of a significant coverage of the outer surface of the clusters by majority particles.

Finally, it should be mentioned that the approach we adopted to evaluate ϕ_A, even if it allowed us to get an accurate mapping of the surface of the clusters, it fails in taking into account the hindrance effects: as can be appreciated from the comparison between the 3D and the berry-like representations of the clusters structure depicted in the bottom part of Fig. 8.6, minority particles, even when placed in the most inner region of the aggregate and completely saturated by the bonded majority ones, are still detected by the Monte Carlo procedure, thus lowering the computed value of ϕ_A. However, despite this inconvenience, based on the equilibrium state observed in the PSDs (Fig. 8.5a), all the clusters reported in the bottom part of Fig. 8.6 should be regarded as stable ones.

Local structure

It is well known that the most compact packing of spheres can be obtained in face-centered cubic (FCC) and hexagonal close-packed (HCP) arrangements in which the coordination number equals 12. If primary particles packed according to any of these two arrangements, we would expect to have all particles being included in clusters if the suspension is composed by a mixture of A and B monomers in a ratio larger or equal to 1:12, so that each particle B can be in contact with at least one particle A. This case corresponds to $x_A \leq 1 - 1/13 = 0.923$. Such a value could be regarded as a critical concentration discriminating between the unlimited growth and the size stabilization behaviour in the case of FCC or HCP arrangements. Therefore, one may think to estimate the critical concentration $x_{A,c}$ by looking at the coordination number n_c of the minority primary particles of the produced clusters. Unfortunately, this quantity emerged to vary in a quite broad range, spanning from 2 to 8 in all the suspensions analysed. Based on the upper limit value we can only conclude that the critical concentration is $x_{A,c} \leq 1 - 1/(8 + 1) \approx 0.89$; however, this value does not
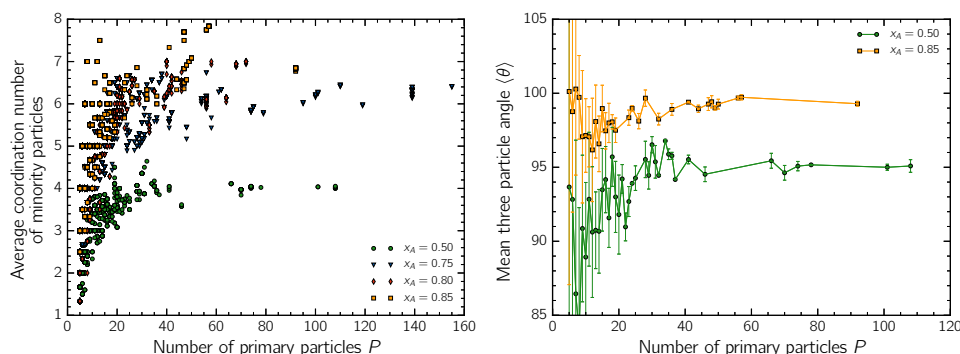
Figure 8.8: a) Average coordination number of minority particles as a function of the cluster size P. The plot reports the data relative to the populations sampled regularly at a frequency of 100 encounters. b) Mean three particle angle as a function of the cluster size. Error bars represent the standard deviation of the data.

help to restrict the range 0.80–0.85 inferred from the analysis of the growth kinetics presented in the previous sections.

A deeper understanding of the cluster morphology can be anyway gained by looking at the average coordination $\langle n_c \rangle$; this quantity was computed averaging over the values of the single coordination number of each minority particle. Figure 8.8 reports $\langle n_c \rangle$ as a function of the cluster size. It emerges that $\langle n_c \rangle$ shows a strong dependence on x_A. Focusing on the two limiting cases, it is noticeable that the average coordination number for the suspension $x_A = 0.85$ is systematically larger than the one relative to the suspension $x_A = 0.50$. This means that the packing of the clusters of these two populations are characterized by two distinct patterns. In the system $x_A = 0.85$, most of the minority particles are placed in the inner part of the cluster and are fully covered by a large number of majority ones. Conversely, in the symmetric system, as it would be expected, there is a regular alternation of minority and majority particles throughout the structure. The lower average coordination number implies that a significant fraction of minority particles is placed on the surface of the clusters, exposed to the dispersing medium and thus not fully saturated. Finally, from the high values of coordination number it is also inferable that significant restructuring effects take place after a contact establishes between a pair of unlike particles of two clusters. The monomers of the connected aggregates in fact rearrange their position in response to the shear stress, thus leading to the creation of several new bonds. In the absence of restructuring, as already observed in previous chapters, isostatic aggregates are formed, which have a coordination number close to 2.

Another useful characterization of the local cluster structure is given by the average three particle angle $\langle \theta \rangle$. To compute $\langle \theta \rangle$ all the existing groups of three connected primary particles formed by a minority particle (B) connected to two majority ones (A) were identified and characterized by the angle $\theta_{ABA'}$ formed by the two straight lines passing through the center of the intermediate particle B and through the centers of the other two particles A; finally the angle $\theta_{ABA'}$ was computed

as:

$$\theta_{ABA'} = 2 \arcsin \left(\frac{r_{AA'}}{4a} \right) \tag{8.4}$$

where $r_{AA'}$ represents the center-to-center distance between the two majority particles. This angle can vary between 60° and 180°, corresponding to an equilateral triangle and a linear chain, respectively. However, the first arrangement is hindered by the repulsive interaction between like particles A.

Figure 8.8b reports the average three-particle angle as a function of the cluster size. For the sake of clarity, only the data relative to the limiting cases are reported. As noticeable the average three-particle angles of the population $x_A = 0.85$ are systematically larger than the one relative to the population $x_A = 0.50$. This implies that when one kind of particle is present in the system in large excess the generated clusters present a quite more open structure; this is due to the large number of majority particles which arrange in such a way to avoid contact and minimize the mutual repulsion, thus conferring to clusters relatively large value of $\langle \theta \rangle$. On the contrary, in the symmetric system, as a consequence of the regular alternation between the two kind of monomers, the clusters are able to attain a more closely packed arrangement.

Furthermore it is possible to notice that small clusters present a large scatter of the data, meaning that in shear flow they experience a broad range of arrangement, ranging from linear chains to more compact structure. Conversely, as the size and the coordination number of each primary particle increase, clusters show a more recurrent pattern and the average three-particle angle relaxes to a plateau value.

8.5   Conclusion

In this chapter, the shear-induced heteroaggregation of oppositely charged particles was investigated. Simulations were performed to ascertain the effect of the relative concentration on both kinetics and cluster structure.

Similarly to what observed in perikinetic aggregation studies, the composition of the population has profound implications on both aggregation dynamics and cluster structures. Starting from monomeric conditions, the early stage kinetics appeared to be strongly affected by the relative amount of cationic and anionic particles: when they are present in an equal amount, the aggregation proceeds fast and a significant amount of dimers and other small clusters is promptly produced. On the contrary, when the suspension is enriched in one of the two class of particles, the rate of dimer formation is substantially reduced. A simple reaction model was proposed and showed to properly fit the simulation data.

Similarly, the late stage kinetics appeared to be strongly affected by the population composition. In the symmetric system the growth dynamics was seen to show a self-accelerating behaviour, with clusters that soon reached quite large sizes. In the system in which the initial population was formed by 85% of one kind of particles, the aggregation rate gradually reduced with time and, for sufficiently large times, a size stabilization took place; stable aggregates appeared in the suspension; such

aggregates were seen to be formed by a core, in which particles of the two classes were both present and by an external shell fully covered by majority particles, thus providing a shielding effect against further aggregation.

Finally, the cluster structures were characterized on the basis of their surface composition. Based on this characterization, it is possible to conclude that size stabilization effect are expected to take place in the suspension when the population is composed by a relative amount of one kind of particles in the range 80%–85%.

References

AlSunaidi, A., Lach-Hab, M., González, A. E., Blaisten-Barojas, E. 2000. "Cluster-cluster aggregation in binary mixtures". *Physical Review E* 61. 550.

Biggs, S., Habgood, M., Jameson, G. J., Yan, D. 2000. "Aggregate structures formed via a bridging flocculation mechanism". *Chemical Engineering Journal* 80. 13–22.

Hogg, R., Healy, T. W., Fuerstenau, D. 1966. "Mutual coagulation of colloidal dispersions". *Transactions of the Faraday Society* 62. 1638–1651.

Jiang, J., Oberdörster, G., Biswas, P. 2009. "Characterization of size, surface charge, and agglomeration state of nanoparticle dispersions for toxicological studies". *Journal of Nanoparticle Research* 11. 77–89.

Kim, A. Y., Berg, J. C. 2000. "Fractal heteroaggregation of oppositely charged colloids". *Journal of colloid and interface Science* 229. 607–614.

Kim, A. Y., Hauch, K. D., Berg, J. C., Martin, J. E., Anderson, R. A. 2003. "Linear chains and chain-like fractals from electrostatic heteroaggregation". *Journal of Colloid and Interface Science* 260. 149–159.

Liu, W., Sun, W., Borthwick, A. G., Ni, J. 2013. "Comparison on aggregation and sedimentation of titanium dioxide, titanate nanotubes and titanate nanotubes-TiO 2: Influence of pH, ionic strength and natural organic matter". *Colloids and Surfaces A: Physicochemical and Engineering Aspects* 434. 319–328.

López-López, J. M., Moncho-Jordá, A., Schmitt, A., Hidalgo-Álvarez, R. 2005. "Formation and structure of stable aggregates in binary diffusion-limited cluster-cluster aggregation processes". *Physical Review E* 72. 031401.

Yates, P. D., Franks, G. V., Jameson, G. J. 2008. "Orthokinetic heteroaggregation with nanoparticles: effect of particle size ratio on aggregate properties". *Colloids and Surfaces A: Physicochemical and Engineering Aspects* 326. 83–91.

Zhou, Y., Franks, G. V. 2006. "Flocculation mechanism induced by cationic polymers investigated by light scattering". *Langmuir* 22. 6775–6786.

Chapter 9

Conclusions

This thesis was devoted to the development of a novel method to study dynamically the shear-induced aggregation of dilute colloidal suspensions. The method couples the mean-field approach typical of Population Balance Equation (PBE) with the accurate predictions obtainable by Discrete Element Method (DEM) simulations: the Population Balance governing the suspension dynamics is solved stochastically by an event-driven, rejection-free Monte Carlo (MC) algorithm; the only event taken into account by the MC algorithm is the near-encounter between pair of suspended particles, whose frequency is modelled according to the Smoluchowsky two-body kinetics. However, this information is used to model solely the frequency of near-encounters, with the actual outcome of each encounter being ascertained a posteriori resorting to accurate DEM simulations. The DEM is built into the framework of Stokesian Dynamics and coupled with proper models for inter-particle interactions; as such, it is able to model accurately the hydrodynamics (both the far and near field parts) as well as the colloidal interactions between particles.

By such a combination it was possible to thoroughly follow the suspension dynamics, taking into account all the relevant phenomena occurring in the suspension, namely aggregation, restructuring and breakage of the clusters, whose modelling in the PBE framework is hampered by the lack of proper analytical expressions. Furthermore, in contrast to a pure PBE approach, where cluster properties are described by a certain number of internal properties, DEM simulations provide a full characterization of the cluster morphology where the position of each constituent monomer is explicitly considered. To the best of our knowledge, such a combination has never been used before. Finally, it is worth to mention that the combined MC-DEM has a limited computational cost compared to a pure DEM simulation of a colloidal system, in that the DEM simulations are performed to track the motion of just two aggregates at a time.

The capabilities of the MC-DEM method were exploited to investigate diverse aspects related to colloid aggregation. The first investigation focused on the effect of tangential interactions on the aggregation behaviour: traditionally, colloidal interactions between particles are modelled according to the DLVO theory and introduced in DEM simulations as central forces i.e, forces acting along the line connecting

their centers; as such, these forces confer to bonded particles a resistance solely to compressive and tensile stresses. However, an increasing attention is lately paid to the modelling of tangential interactions i.e., interactions which upon contact provide the connected particles with the capability of withstanding also bending and twisting torques. Thus, the MC-DEM method was applied to investigate the effect of these latter interactions on the aggregation behaviour. Results showed that substantial differences in the cluster morphology appear when introducing tangential interactions at contact: when counting for such interactions, primary particles aggregate forming rigid and porous cluster, characterized by low values of the coordination number and showing a wide variety of structures, ranging from spherical to more elongated ones. In the absence of tangential interaction, instead, particles are free to slide and roll over each other upon contact, leading to the formation of compact and highly connected clusters, with an overall shape characterized by a more spherical symmetry.

The MC-DEM simulations revealed that the growth kinetics is strongly affected by the morphology of the clusters. In order to evaluate this aspect on a more systematic basis, the DEM was combined with a grid-based technique to evaluate aggregation efficiencies and aggregation cross sections. First the case of monomer-monomer aggregation was analysed, leading to a good agreement with results reported in previous works. Afterwards, the cases of monomer-cluster and cluster-cluster aggregation were addressed: for monomer-cluster aggregation, large size disproportion appeared to strongly reduce aggregation efficiencies. Large aggregates were seen able to substantially disturb the flow field and, as a consequence, to significantly deflect the primary particle trajectory, thus preventing aggregation. In cluster-cluster aggregation, the aspect ratio turned up to be the main factor affecting aggregation efficiencies. Large aspect ratio has been linked, in fact, to a significant reduction of the time-averaged collision cross section of the aggregates, and consequently to a reduction of aggregation efficiency. However, this investigation leaves ample room for further activity: additional simulations may be performed to extend the library of clusters, in particular to analyse the effect of increasing size on the aggregation efficiency.

The MC-DEM was proven to be also able to capture the typical dynamical aggregation-breakage equilibrium that sets in stirred colloidal suspensions. This was made apparent by analysing the temporal trend of the particle average size and particle size distribution. Regardless of the applied viscous stress, the suspensions showed an initial aggregation-dominated phase, during which particles grew in size as a consequence of the aggregation phenomena. However, this growth did not proceed indefinitely, but it was, at a later stage, dampened by the occurrence of breakup phenomena. Breakup phenomena emerged to occur by two different mechanisms: the first consists in the instantaneous breakup of the clusters that grew over a certain critical dimension; the second, less frequent breakup mechanism occurred instead as a consequence of the hydrodynamic interaction between approaching aggregates, which, mutually disturbing each other, introduce flow heterogeneities in the imposed flow field.

Finally, the shear-induced aggregation of oppositely charged particles was studied. For the adopted values of surface potential and ionic strength, simulations showed

that only heteroaggregation events i.e, events involving oppositely charged particles, can occur. Under such conditions, the composition of the population emerged to have profound implications on both aggregation dynamics and cluster structures, which were shown to be intimately related to each other. When the population is composed by a relative amount of one kind of particles in the range 80%–85% a size stabilization was seen to take place; stable aggregates with a core-shell structure were produced. These aggregates were composed by a few minority particles placed in the inner region and were highly covered by the majority ones on the surface, thus providing a shielding effect against further growth. On the contrary, for suspensions with a composition smaller than this critical concentration, such stable aggregates did not appear and the aggregation proceeded indefinitely, although a dependence of the growth behaviour on the initial composition was observed.

In conclusion, the developed MC-DEM was proven to be a flexible and reliable tool for the study of the behaviour of dilute colloidal suspensions. However, the rather high computational cost of DEM simulations suggests to exploit the capabilities of the overall method to infer additional information about morphology of clusters, aggregation and breakup dynamics in order to fine-tune more economical techniques, such as pure PBE or MC algorithms.

References

Adler, P. M. 1981a. "Heterocoagulation in shear flow". *Journal of Colloid and Interface Science* 83. 106–115.

— 1981b. "Interaction of unequal spheres: I. Hydrodynamic interaction: Colloidal forces". *Journal of Colloid and Interface Science* 84. 461–473.

Alam, M. K. 1987. "The effect of van der Waals and viscous forces on aerosol coagulation". *Aerosol Science and Technology* 6. 41–52.

AlSunaidi, A., Lach-Hab, M., González, A. E., Blaisten-Barojas, E. 2000. "Cluster-cluster aggregation in binary mixtures". *Physical Review E* 61. 550.

Arp, P. A., Mason, S. G. 1976. "Orthokinetic collisions of hard spheres in simple shear flow". *Canadian Journal of Chemistry* 54. 3769–3774.

Bäbler, M. U. 2008. "A collision efficiency model for flow-induced coagulation of fractal aggregates". *AIChE journal* 54. 1748–1760.

Batchelor, G. K., Green, J. T. 1972. "The hydrodynamic interaction of two small freely-moving spheres in a linear flow field". *Journal of Fluid Mechanics* 56. 375–400.

Batterham, R. J., Hall, J. S., Barton, G. (1981). "Pelletizing kinetics and simulation of full scale balling circuits". *Proceedings of the 3rd International Symposium on Agglomeration*. Vol. 136. Nurnberg W. Germany.

Becker, V., Briesen, H. 2008. "Tangential-force model for interactions between bonded colloidal particles". *Physical Review E* 78. 061404.

— 2010. "A master curve for the onset of shear induced restructuring of fractal colloidal aggregates". *Journal of Colloid and Interface Science* 346. 32–36.

Becker, V., Schlauch, E., Behr, M., Briesen, H. 2009. "Restructuring of colloidal aggregates in shear flows and limitations of the free-draining approximation". *Journal of Colloid and Interface Science* 339. 362–372.

Berg, J. C. (2010). *An introduction to interfaces & colloids: the bridge to nanoscience.* 1st edition. World Scientific.

Biggs, S., Habgood, M., Jameson, G. J., Yan, D. 2000. "Aggregate structures formed via a bridging flocculation mechanism". *Chemical Engineering Journal* 80. 13–22.

Bird, R. B., Stewart, W. E., Lightfoot, E. N. (2002). *Transport phenomena.* John Wiley & Sons, New York (NY).

References

Bowen, W. R., Jenner, F. 1995. "The calculation of dispersion forces for engineering applications". *Advances in colloid and interface science* 56 201–243.

Brady, J. F., Bossis, G. 1988. "Stokesian dynamics". *Annual Review of Fluid Mechanics* 20. 111–157.

Brasil, A., Farias, T., Carvalho, M. 2000. "Evaluation of the Fractal Properties of Cluster–Cluster Aggregates". *Aerosol Science & Technology* 33. 440–454.

Buffo, A., Vanni, M., Marchisio, D., Fox, R. O. 2013. "Multivariate quadrature-based moments methods for turbulent polydisperse gas–liquid systems". *International Journal of Multiphase Flow* 50. 41–57.

Camejo, M., Espeso, D., Bonilla, L. 2014. "Influence of primary-particle density in the morphology of agglomerates". *Physical Review E* 90. 012306.

Cundall, P. A., Strack, O. D. 1979. "A discrete numerical model for granular assemblies". *Geotechnique* 29. 47–65.

Curtis, A. S. G., Hocking, L. M. 1970. "Collision efficiency of equal spherical particles in a shear flow. The influence of London-van der Waals forces". *Transactions of the Faraday Society* 66 1381–1390.

Durlofsky, L., Brady, J. F., Bossis, G. 1987. "Dynamic simulation of hydrodynamically interacting particles". *Journal of Fluid Mechanics* 180 21–49.

Eggersdorfer, M., Kadau, D, Herrmann, H., Pratsinis, S. 2010. "Fragmentation and restructuring of soft-agglomerates under shear". *Journal of Colloid and Interface Science* 342. 261–268.

Elimelech, M., Gregory, J., Jia, X., Williams, R. A. (1995). *Particle deposition and aggregation: measurement, modelling and simulation.* 1st edition. Butterworth-Heinemann, Oxford (UK).

Fellay, L. S., Twist, C., Vanni, M. 2013. "Motion of rigid aggregates under different flow conditions". *Acta Mechanica* 224. 2225.

Flesch, J. C., Spicer, P. T., Pratsinis, S. E. 1999. "Laminar and turbulent shear-induced flocculation of fractal aggregates". *AIChE journal* 45. 1114–1124.

Frappier, G, Lartiges, B., Skali-Lami, S. 2010. "Floc cohesive force in reversible aggregation: a Couette laminar flow investigation". *Langmuir* 26. 10475–10488.

Friedlander, S. K. (1977). *Smoke, dust and haze: Fundamentals of aerosol behavior.* 1st edition. Wiley-Interscience, New York (NY).

Frungieri, G., Vanni, M. 2017. "Shear-induced aggregation of colloidal particles: A comparison between two different approaches to the modelling of colloidal interactions". *The Canadian Journal of Chemical Engineering* 95. 1768–1780.

Ganatos, P., Pfeffer, R., Weinbaum, S. 1978. "A numerical-solution technique for three-dimensional Stokes flows, with application to the motion of strongly interacting spheres in a plane". *Journal of Fluid Mechanics* 84. 79–111.

Garcia, A. L., Van Den Broeck, C., Aertsens, M., Serneels, R. 1987. "A Monte Carlo simulation of coagulation". *Physica A: Statistical Mechanics and its Applications* 143. 535–546.

Gastaldi, A., Vanni, M. 2011. "The distribution of stresses in rigid fractal-like aggregates in a uniform flow field". *Journal of Colloid and Interface Science* 357. 18–30.

Gillespie, D. T. 1975. "An exact method for numerically simulating the stochastic coalescence process in a cloud". *Journal of the Atmospheric Sciences* 32. 1977–1989.

Guazzelli, E., Morris, J. F. (2011). *A physical introduction to suspension dynamics*. 1st edition. Cambridge University Press.

Hamaker, H. C. 1937. "The London—Van der Waals attraction between spherical particles". *Physica* 4. 1058–1072.

Harada, S., Tanaka, R., Nogami, H., Sawada, M. 2006. "Dependence of fragmentation behavior of colloidal aggregates on their fractal structure". *Journal of Colloid and Interface Science* 301. 123–129.

Hardy, W. 1900. "A preliminary investigation of the conditions which determine the stability of irreversible hydrosols". *The Journal of Physical Chemistry* 4. 235–253.

Harshe, Y. M., Lattuada, M. 2011. "Breakage rate of colloidal aggregates in shear flow through Stokesian dynamics". *Langmuir* 28. 283–292.

— 2016. "Universal breakup of colloidal clusters in simple shear flow". *The Journal of Physical Chemistry B* 120. 7244–7252.

Harshe, Y. M., Ehrl, L., Lattuada, M. 2010. "Hydrodynamic properties of rigid fractal aggregates of arbitrary morphology". *Journal of Colloid and Interface Science* 352. 87–98.

Heinson, W., Sorensen, C., Chakrabarti, A 2010. "Does shape anisotropy control the fractal dimension in diffusion-limited cluster-cluster aggregation?" *Aerosol Science and Technology* 44. 1–5.

— 2012. "A three parameter description of the structure of diffusion limited cluster fractal aggregates". *Journal of Colloid and Interface Science* 375. 65–69.

Higashitani, K., Iimura, K. 1998. "Two-dimensional simulation of the breakup process of aggregates in shear and elongational flows". *Journal of Colloid and Interface Science* 204. 320–327.

Hill, P. J., Ng, K. M. 1995. "New discretization procedure for the breakage equation". *AIChE Journal* 41. 1204–1216.

Hogg, R., Healy, T. W., Fuerstenau, D. 1966. "Mutual coagulation of colloidal dispersions". *Transactions of the Faraday Society* 62. 1638–1651.

Horii, K., Yamada, R., Harada, S. 2015. "Strength deterioration of nonfractal particle aggregates in simple shear flow". *Langmuir* 31. 7909–7918.

Hounslow, M., Ryall, R., Marshall, V. 1988. "A discretized population balance for nucleation, growth and aggregation". *AIChE Journal* 34. 1821–1832.

Hulburt, H. M., Katz, S. 1964. "Some problems in particle technology: A statistical mechanical formulation". *Chemical Engineering Science* 19. 555–574.

Hunter, R. J. (1981). *Zeta potential in colloid science: principles and applications*. 1st edition. Vol. 2. Academic press, San Diego (CA).

Ichiki, K. 2002. "Improvement of the Stokesian dynamics method for systems with a finite number of particles". *Journal of Fluid Mechanics* 452. 231–262.

Inci, G., Arnold, A., Kronenburg, A., Weeber, R. 2014. "Modeling nanoparticle agglomeration using local interactions". *Aerosol Science and Technology* 48. 842–852.

Isella, L., Drossinos, Y. 2010. "Langevin agglomeration of nanoparticles interacting via a central potential". *Physical Review E* 82. 011404.1–15.

Israelachvili, J. N. (2011). *Intermolecular and surface forces.* 3rd edition. Academic press.

Jeffery, G. B. (1922). "The motion of ellipsoidal particles immersed in a viscous fluid". *Proceedings of the royal society of London A: Mathematical, physical and engineering sciences.* Vol. 102. 715. The Royal Society 161–179.

Jiang, J., Oberdörster, G., Biswas, P. 2009. "Characterization of size, surface charge, and agglomeration state of nanoparticle dispersions for toxicological studies". *Journal of Nanoparticle Research* 11. 77–89.

Jing, L. 2003. "A review of techniques, advances and outstanding issues in numerical modelling for rock mechanics and rock engineering". *International Journal of Rock Mechanics and Mining Sciences* 40. 283–353.

Johnson, K., Kendall, K, Roberts, A. (1971). "Surface energy and the contact of elastic solids". *Proceedings of the Royal Society of London A: Mathematical, Physical and Engineering Sciences.* Vol. 324 301–313.

Jullien, R., Botet, R. (1987). *Aggregation and Fractal Aggregates.* 1st edition. World Scientific, Singapore.

Kappl, M. et al. (2009). *Surface and interfacial forces.* John Wiley & Sons.

Kendall, D. G. 1950. "An artificial realization of a simple "birth-and-death" process". *Journal of the Royal Statistical Society. Series B* 12. 116–119.

Kerminen, V. M. 1994. "Simulation of Brownian coagulation in the presence of van der Waals forces and viscous interactions". *Aerosol Science and Technology* 20. 207–214.

Kim, A. Y., Berg, J. C. 2000. "Fractal heteroaggregation of oppositely charged colloids". *Journal of colloid and interface Science* 229. 607–614.

Kim, A. Y., Hauch, K. D., Berg, J. C., Martin, J. E., Anderson, R. A. 2003. "Linear chains and chain-like fractals from electrostatic heteroaggregation". *Journal of Colloid and Interface Science* 260. 149–159.

Kim, S., Karrila, S. J. (1991). *Microhydrodynamics: principles and selected applications.* Butterworth-Heinemann.

Koch, W, Friedlander, S. 1990. "The effect of particle coalescence on the surface area of a coagulating aerosol". *Journal of Colloid and Interface Science* 140. 419–427.

Kostoglou, M., Konstandopoulos, A. G. 2001. "Evolution of aggregate size and fractal dimension during Brownian coagulation". *Journal of Aerosol Science* 32. 1399–1420.

Kostoglou, M., Karabelas, A. J. 1994. "Evaluation of zero order methods for simulating particle coagulation". *Journal of Colloid and Interface science* 163. 420–431.

Köylü, Ü. Ö., Faeth, G., Farias, T. L., Carvalho, M. d. G. 1995. "Fractal and projected structure properties of soot aggregates". *Combustion and Flame* 100. 621–633.

Kruis, F. E., Maisels, A., Fissan, H. 2000. "Direct simulation Monte Carlo method for particle coagulation and aggregation". *AIChE Journal* 46. 1735–1742.

Kumar, S., Ramkrishna, D. 1996a. "On the solution of population balance equations by discretization—I. A fixed pivot technique". *Chemical Engineering Science* 51. 1311–1332.

— 1996b. "On the solution of population balance equations by discretization—II. A moving pivot technique". *Chemical Engineering Science* 51. 1333–1342.

Kusters, K. A., Wijers, J. G., Thoenes, D. 1997. "Aggregation kinetics of small particles in agitated vessels". *Chemical Engineering Science* 52. 107–121.

Kyriakidis, A. S., Yiantsios, S. G., Karabelas, A. J. 1997. "A study of colloidal particle Brownian aggregation by light scattering techniques". *Journal of Colloid and Interface Science* 195. 299–306.

Lattuada, M., Wu, H., Morbidelli, M. 2003. "A simple model for the structure of fractal aggregates". *Journal of Colloid and Interface Science* 268. 106–120.

Lee, K., Matsoukas, T. 2000. "Simultaneous coagulation and break-up using constant-N Monte Carlo". *Powder Technology* 110. 82–89.

Liffman, K. 1992. "A direct simulation Monte-Carlo method for cluster coagulation". *Journal of Computational Physics* 100. 116–127.

Lin, M., Lindsay, H., Weitz, D., Ball, R., Klein, R, Meakin, P 1989. "Universality in colloid aggregation". *Nature* 339. 360–362.

Lin, M., Lindsay, H., Weitz, D., Ball, R., Klein, R, Meakin, P. 1990. "Universal reaction-limited colloid aggregation". *Physical Review A* 41. 2005–2020.

Liu, W., Sun, W., Borthwick, A. G., Ni, J. 2013. "Comparison on aggregation and sedimentation of titanium dioxide, titanate nanotubes and titanate nanotubes-TiO 2: Influence of pH, ionic strength and natural organic matter". *Colloids and Surfaces A: Physicochemical and Engineering Aspects* 434. 319–328.

López-López, J. M., Moncho-Jordá, A., Schmitt, A., Hidalgo-Álvarez, R. 2005. "Formation and structure of stable aggregates in binary diffusion-limited cluster-cluster aggregation processes". *Physical Review E* 72. 031401.

Mahanty, J, Ninham, B. W. *Dispersion forces.* 1st edition. Academic press, London (UK).

Maisels, A., Kruis, F. E., Fissan, H. 2004. "Direct simulation Monte Carlo for simultaneous nucleation, coagulation, and surface growth in dispersed systems". *Chemical Engineering Science* 59. 2231–2239.

Marchisio, D. L., Vigil, R. D., Fox, R. O. 2003. "Quadrature method of moments for aggregation–breakage processes". *Journal of Colloid and Interface Science* 258. 322–334.

Marchisio, D. L., Soos, M., Sefcik, J., Morbidelli, M. 2006. "Role of turbulent shear rate distribution in aggregation and breakage processes". *AIChE journal* 52. 158–173.

Marshall, J. 2009. "Discrete-element modeling of particulate aerosol flows". *Journal of Computational Physics* 228. 1541–1561.

Matijević, E, Babu, S. 2008. "Colloid aspects of chemical–mechanical planarization". *Journal of Colloid and Interface Science* 320. 219–237.

Matsoukas, T., Friedlander, S. K. 1991. "Dynamics of aerosol agglomerate formation". *Journal of Colloid and Interface Science* 146. 495–506.

McGraw, R. 1997. "Description of aerosol dynamics by the quadrature method of moments". *Aerosol Science and Technology* 27. 255–265.

Meakin, P. 1984. "Diffusion-limited aggregation in three dimensions: results from a new cluster-cluster aggregation model". *Journal of Colloid and Interface Science* 102. 491–504.

— 1999. "A historical introduction to computer models for fractal aggregates". *Journal of Sol-Gel Science and Technology* 15. 97–117.

Melas, A. D., Isella, L., Konstandopoulos, A. G., Drossinos, Y. 2014. "Morphology and mobility of synthetic colloidal aggregates". *Journal of Colloid and Interface Science* 417 27–36.

Mezzenga, R., Schurtenberger, P., Burbidge, A., Michel, M. 2005. "Understanding foods as soft materials". *Nature Materials* 4. 729–740.

Nir, A., Acrivos, A. 1973. "On the creeping motion of two arbitrary-sized touching spheres in a linear shear field". *Journal of Fluid Mechanics* 59. 209–223.

Ohshima, H. 1994. "Electrostatic interaction between two dissimilar spheres: an explicit analytic expression". *Journal of Colloid and Interface Science* 162. 487–495.

Oles, V. 1992. "Shear-induced aggregation and breakup of polystyrene latex particles". *Journal of Colloid and Interface Science* 154. 351–358.

Pantina, J. P., Furst, E. M. 2005. "Elasticity and critical bending moment of model colloidal aggregates". *Physical Review Letters* 94. 138301.

Ramkrishna, D. (2000). *Population balances: Theory and applications to particulate systems in engineering.* 1st edition. Academic press, San Diego (CA).

Ren, Z., Harshe, Y. M., Lattuada, M. 2015. "Influence of the potential well on the breakage rate of colloidal aggregates in simple shear and uniaxial extensional flows". *Langmuir* 31. 5712–5721.

Sánchez, D. P., Scheeres, D. J. 2012. "DEM simulation of rotation-induced reshaping and disruption of rubble-pile asteroids". *Icarus* 218. 876–894.

Schenkel, J., Kitchener, J. 1960. "A test of the Derjaguin-Verwey-Overbeek theory with a colloidal suspension". *Transactions of the Faraday Society* 56. 161–173.

Schlauch, E., Ernst, M., Seto, R., Briesen, H., Sommerfeld, M., Behr, M. 2013. "Comparison of three simulation methods for colloidal aggregates in Stokes flow: Finite elements, lattice Boltzmann and Stokesian dynamics". *Computers & Fluids* 86. 199–209.

Serra, T., Casamitjana, X. 1998. "Structure of the aggregates during the process of aggregation and breakup under a shear flow". *Journal of Colloid and Interface Science* 206. 505–511.

Serra, T., Colomer, J., Casamitjana, X. 1997. "Aggregation and breakup of particles in a shear flow". *Journal of Colloid and Interface Science* 187. 466–473.

Seto, R, Botet, R, Auernhammer, G., Briesen, H. 2012. "Restructuring of colloidal aggregates in shear flow: coupling interparticle contact models with Stokesian dynamics." *The European physical Journal E, Soft Matter* 35. 9805.

Seto, R., Botet, R., Briesen, H. 2011. "Hydrodynamic stress on small colloidal aggregates in shear flow using Stokesian dynamics". *Physical Review E* 84. 041405.

Seto, R., Mari, R., Morris, J. F., Denn, M. M. 2013. "Discontinuous shear thickening of frictional hard-sphere suspensions". *Physical Review Letters* 111. 218301.

Shah, B., Ramkrishna, D., Borwanker, J. 1977. "Simulation of particulate systems using the concept of the interval of quiescence". *AIChE Journal* 23. 897–904.

Smith, M., Matsoukas, T. 1998. "Constant-number Monte Carlo simulation of population balances". *Chemical Engineering Science* 53. 1777–1786.

Smoluchowski, M. V. 1917. "Versuch einer mathematischen Theorie der Koagulationskinetik kolloider Lösungen". *Zeitschrift für physikalische Chemie* 92. 129–168.

Soos, M., Moussa, A. S., Ehrl, L., Sefcik, J., Wu, H., Morbidelli, M. 2008. "Effect of shear rate on aggregate size and morphology investigated under turbulent conditions in stirred tank". *Journal of Colloid and Interface Science* 319. 577–589.

Spielman, L. A. 1970. "Viscous interactions in Brownian coagulation". *Journal of Colloid and Interface Science* 33. 562–571.

Tandon, P., Rosner, D. E. 1999. "Monte Carlo simulation of particle aggregation and simultaneous restructuring". *Journal of Colloid and Interface Science* 213. 273–286.

Tsuji, T., Yabumoto, K., Tanaka, T. 2008. "Spontaneous structures in three-dimensional bubbling gas-fluidized bed by parallel DEM–CFD coupling simulation". *Powder Technology* 184. 132–140.

Van de Ven, T. G. M., Mason, S. G. 1976. "The microrheology of colloidal dispersions: IV. Pairs of interacting spheres in shear flow". *Journal of Colloid and Interface Science* 57. 505–516.

— 1977. "The microrheology of colloidal dispersions VII. Orthokinetic doublet formation of spheres". *Colloid & Polymer Science* 255. 468–479.

Van Peborgh Gooch, J. R., Hounslow, M. J. 1996. "Monte Carlo simulation of size-enlargement mechanisms in crystallization". *AIChE Journal* 42. 1864–1874.

Vanni, M. 1999. "Discretization procedure for the breakage equation". *AIChE journal* 45. 916–919.

— 2000. "Approximate population balance equations for aggregation–breakage processes". *Journal of Colloid and Interface Science* 221. 143–160.

Vanni, M., Baldi, G. 2002. "Coagulation efficiency of colloidal particles in shear flow". *Advances in Colloid and Interface Science* 97. 151–177.

Vanni, M., Gastaldi, A. 2011. "Hydrodynamic forces and critical stresses in low-density aggregates under shear flow". *Langmuir* 27. 12822–12833.

Veerapaneni, S., Wiesner, M. R. 1996. "Hydrodynamics of fractal aggregates with radially varying permeability". *Journal of Colloid and Interface Science* 177. 45–57.

Wang, L., Marchisio, D. L., Vigil, R. D., Fox, R. O. 2005. "CFD simulation of aggregation and breakage processes in laminar Taylor–Couette flow". *Journal of Colloid and Interface Science* 282. 380–396.

Wiese, G., Healy, T. 1970. "Effect of particle size on colloid stability". *Transactions of the Faraday Society* 66. 490–499.

Witten, T. A., Sander, L. M. 1983. "Diffusion-limited aggregation". *Physical Review B* 27. 5686.

Yates, P. D., Franks, G. V., Jameson, G. J. 2008. "Orthokinetic heteroaggregation with nanoparticles: effect of particle size ratio on aggregate properties". *Colloids and Surfaces A: Physicochemical and Engineering Aspects* 326. 83–91.

Zhao, H., Maisels, A., Matsoukas, T., Zheng, C. 2007. "Analysis of four Monte Carlo methods for the solution of population balances in dispersed systems". *Powder Technology* 173. 38–50.

Zhou, Y., Franks, G. V. 2006. "Flocculation mechanism induced by cationic polymers investigated by light scattering". *Langmuir* 22. 6775–6786.

Zucca, A., Marchisio, D. L., Vanni, M., Barresi, A. A. 2007. "Validation of bivariate DQMOM for nanoparticle processes simulation". *AIChE Journal* 53. 918–931.

Appendix A

Computation of the far-field mobility matrix

$$
\begin{Bmatrix}
\mathbf{u}^\alpha - \mathbf{u}^\infty(\mathbf{x}^\alpha) \\
\mathbf{u}^\beta - \mathbf{u}^\infty(\mathbf{x}^\beta) \\
\vdots \\
\boldsymbol{\omega}^\alpha - \boldsymbol{\omega}^\infty(\mathbf{x}^\alpha) \\
\boldsymbol{\omega}^\beta - \boldsymbol{\omega}^\infty(\mathbf{x}^\beta) \\
\vdots \\
-\mathbf{e}^\infty \\
-\mathbf{e}^\infty
\end{Bmatrix}
= -
\begin{bmatrix}
a^{\alpha\alpha} & a^{\alpha\beta} & \dots & \tilde{b}^{\alpha\alpha} & \tilde{b}^{\alpha\beta} & \dots & \tilde{g}^{\alpha\alpha} & \tilde{g}^{\alpha\beta} \\
a^{\beta\alpha} & a^{\beta\beta} & \dots & \tilde{b}^{\beta\alpha} & \tilde{b}^{\beta\beta} & \dots & \tilde{g}^{\beta\alpha} & \tilde{g}^{\beta\beta} \\
\vdots & \vdots & \vdots & \vdots & \vdots & \vdots & \vdots & \vdots \\
b^{\alpha\alpha} & b^{\alpha\beta} & \dots & c^{\alpha\alpha} & c^{\alpha\beta} & \dots & \tilde{h}^{\alpha\alpha} & \tilde{h}^{\alpha\beta} \\
b^{\beta\alpha} & b^{\beta\beta} & \dots & c^{\beta\alpha} & c^{\beta\beta} & \dots & \tilde{h}^{\beta\alpha} & \tilde{h}^{\beta\beta} \\
\vdots & \vdots & \vdots & \vdots & \vdots & \vdots & \vdots & \vdots \\
g^{\alpha\alpha} & g^{\alpha\beta} & \dots & h^{\alpha\alpha} & h^{\alpha\beta} & \dots & m^{\alpha\alpha} & m^{\alpha\beta} \\
g^{\beta\alpha} & g^{\beta\beta} & \dots & h^{\beta\alpha} & h^{\beta\beta} & \dots & m^{\beta\alpha} & m^{\beta\beta}
\end{bmatrix}
\begin{Bmatrix}
\mathbf{F}_\alpha \\
\mathbf{F}_\beta \\
\vdots \\
\mathbf{T}_\alpha \\
\mathbf{T}_\beta \\
\vdots \\
\mathbf{s}_\alpha \\
\mathbf{s}_\beta \\
\vdots
\end{Bmatrix}
\tag{A.1}
$$

Indicating by n_i the generic component of the unit vector $\mathbf{n}_{\alpha\beta} = (\mathbf{x}_\beta - \mathbf{x}_\alpha)/|\mathbf{x}_\beta - \mathbf{x}_\alpha|$ and using $6\pi\eta a$ to make dimensionless the elements of the submatrices a and b and $6\pi\eta a^3$ for the remaining submatrices, the elements of the far-field mobility matrix $\mathcal{M}^\infty$ are given by (Durlofsky et al., 1987):

$$
\begin{cases}
a_{ij}^{\alpha\beta} = x_{\alpha\beta}^a n_i n_j + y_{\alpha\beta}^a (\delta_{ij} - n_{ij}) \\
b_{ij}^{\alpha\beta} = y_{\alpha\beta}^b \epsilon_{ijk} n_k \\
c_{ij}^{\alpha\beta} = x_{\alpha\beta}^c n_i n_j + y_{\alpha\beta}^c (\delta_{ij} - n_i n_j) \\
g_{ijk}^{\alpha\beta} = x_{\alpha\beta}^g (n_i n_j - \frac{1}{3}\delta_{ij}) n_k + y_{\alpha\beta}^g (n_i \delta_{jk} + n_j \delta_{ik} - 2 n_i n_j n_k) \\
h_{ijk}^{\alpha\beta} = y_{\alpha\beta}^h (n_i \epsilon_{jkl} n_l + n_j \epsilon_{ikl} n_l) \\
m_{ijkl}^{\alpha\beta} = \frac{3}{2} x_{\alpha\beta}^m (n_i n_j - \frac{1}{3}\delta_{ij})(n_k n_l - \frac{1}{3}\delta_{kl}) \\
\qquad + \frac{1}{2} y_{\alpha\beta}^m (n_i \delta_{jl} n_k + n_j \delta_{il} n_k + n_i \delta_{jk} n_l + n_j \delta_{ik} n_l - 4 n_i n_j n_k n_l) \\
\qquad + \frac{1}{2} z_{\alpha\beta}^m (\delta_{ij}\delta_{jl} + \delta_{jk}\delta_{il} - \delta_{ij}\delta_{kl} + n_i n_j \delta_{kl} + \delta_{ij} n_k n_l \\
\qquad + n_i n_j n_k n_l - n_i \delta_{jl} n_k - n_j \delta_{il} n_k - n_i \delta_{jk} n_l - n_j \delta_{ik} n_l
\end{cases}
\tag{A.2}
$$

with

$$
\begin{cases}
x_{11}^a = x_{22}^a = 1, & x_{12}^a = x_{21}^a = \frac{3}{2}r^{-1} - r^{-3}, \\
y_{11}^a = y_{22}^a = 1, & y_{12}^a = y_{21}^a = \frac{3}{4}r^{-1} + \frac{1}{2}r^{-3}, \\
y_{11}^b = -y_{22}^b = 0, & y_{12}^b = -y_{21}^b = -\frac{3}{4}r^{-2}, \\
x_{11}^c = x_{22}^c = \frac{3}{4}, & x_{12}^c = x_{21}^c = -\frac{3}{4}r^{-3}, \\
y_{11}^c = y_{22}^c = \frac{3}{4}, & y_{12}^c = y_{21}^c = -\frac{3}{8}r^{-3}, \\
x_{11}^g = -x_{22}^g = 0, & x_{12}^g = -x_{21}^g = \frac{9}{4}r^{-2} - \frac{18}{5}r^{-4}, \\
y_{11}^g = -y_{22}^g = 0, & y_{12}^g = -y_{21}^g = \frac{6}{5}r^{-4}, \\
y_{11}^h = y_{22}^h = 0, & y_{12}^h = y_{21}^h = -\frac{9}{8}r^{-3}, \\
x_{11}^m = x_{22}^m = \frac{9}{10}, & x_{12}^m = x_{21}^m = -\frac{9}{2}r^{-3} + \frac{54}{5}r^{-5}, \\
y_{11}^m = y_{22}^m = \frac{9}{10}, & y_{12}^m = y_{21}^m = \frac{9}{4}r^{-3} + \frac{36}{5}r^{-5}, \\
z_{11}^m = z_{22}^m = \frac{9}{10}, & z_{12}^m = z_{21}^m = \frac{9}{5}r^{-5}
\end{cases}
\tag{A.3}
$$

with $r = |\mathbf{x}_\beta - \mathbf{x}_\alpha|$ being the center-to-center distance between two particles.

Appendix B

Estimation of the parameters for the spring-like model

Four parameters are needed to tune the spring-like model by Becker, Briesen (2008), namely the tangential spring stiffness k_ζ, the torsional spring stiffness k_ϑ, the tangential maximum elongation ζ_{max} and the maximum torsion angle ϑ_{max}. The determination of k_ζ can be achieved by comparing the mechanical response of a linear chain of contacting particles to the one exhibited by a thin elastic rod with a circular section πb_0^2, with b_0 being the zero-load contact radius of a pair of colloidal particles, as estimated by the JKR theory. Let us imagine to test a thin rod of length L with a three point bending flexural test; the chain is initially aligned with the x direction and the force acts along the y direction. The expected shape is then given by:

$$y\left(x\right) = -\frac{F}{EI}\left(\frac{Lx^2}{4} - \frac{|x^3|}{6}\right) \tag{B.1}$$

where EI is the flexural rigidity, given by the product of the Young modulus E with the area moment of inertia I.
It is possible to relate the applied force F to the vertical displacement δ as:

$$\delta = |y(0) - y(L/2)| = \left|0 - \frac{-F}{EI}\left(\frac{LL^2/4}{4} - \frac{L^3/8}{6}\right)\right| = \frac{F}{EI}\frac{L^3}{24} \tag{B.2}$$

where a proportionality constant k_{rod} between δ and F can be identified as:

$$k_{rod} = \frac{24EI}{L^3} \qquad \text{with} \quad I = \frac{\pi}{4}b_0^4 \tag{B.3}$$

However, colloidal aggregates present a more complex structure, generally characterized by branches and internal loops. Therefore a parameter defining the single bond rigidity is needed. Pantina, Furst (2005) used the the single bond rigidity k_0 and related it to the whole aggregate rigidity k_{aggr} as:

$$k_{aggr} = k_0 \left(a/L\right)^3 \tag{B.4}$$

where a is the particle radius and L is a characteristic length scale of the aggregate. Equating Eq. (B.3) with Eq. (B.4) the single bond rigidity finally reads as:

$$k_0 = \frac{6\pi b_0^4 E}{a^3} \tag{B.5}$$

Therefore, in order to estimate the tangential rigidity of the single bond it suffices to compare Eq. (B.1) with the shape attained by a linear chain of particles when adopting the model by Becker, Briesen (2008), that reads as:

$$y_\alpha = -\frac{F}{8a^3 k_\zeta} \left(\frac{L x_\alpha^2}{4} - \frac{|x_\alpha^3|}{6} \right) \tag{B.6}$$

Equation (B.6) [1] gives the equilibrium position of each particle α as a function of the applied external load and the spring stiffness. Combining Eq. (B.6) with Eq. (B.1) and Eq. (B.3) the tangential spring stiffness is finally given by:

$$k_\zeta = \frac{k_{aggr}}{192} \left(\frac{a}{L} \right)^{-3}. \tag{B.7}$$

and by using Eq. (B.4) k_ζ finally becomes:

$$k_\zeta = \frac{k_0}{192} \tag{B.8}$$

The maximum spring elongation should be evaluated starting from the knowledge of the maximum bending moment that an aggregate can bear before an irreversible plastic deformation occurs. Thus:

$$\zeta_{max} = \frac{M_{cr}}{2a k_\zeta}. \tag{B.9}$$

However, given the inherent difficulty of such an estimation, for the present work it has been assumed that $\zeta_{max} = 0.10 \cdot a$.

The maximum torsional angle has been assumed to be equal to the central angle in a circumference of radius a subtended by an arc of length ζ_{max}. Therefore:

$$\vartheta_{max} \approx \sin(\vartheta_{max}) \approx \frac{\zeta_{max}}{a} \tag{B.10}$$

The torsional stiffness k_ϑ was obtained imposing that the maximum bending moment is equal to the maximum torsional couple ($k_\vartheta \vartheta_{max} = 2a k_\zeta \zeta_{max}$), thus

$$k_\vartheta = \frac{2a k_\zeta \zeta_{max}}{\vartheta_{max}} \tag{B.11}$$

---

[1]Equation (B.6) can be obtained by minimizing the elastic energy stored in a deformed linear chain as in the work by Becker, Briesen (2008)

Appendix C

Computation of the viscous dissipation terms

Indicating by α and β a pair of contacting particles and with $\mathbf{n}_{\alpha\beta} = (\mathbf{x}_\beta - \mathbf{x}_\alpha)/|\mathbf{x}_\beta - \mathbf{x}_\alpha| = (n_x, n_y, n_z)$ the unit vector connecting their center, the viscous force can be computed as:

$$\mathbf{F}_\beta^{diss} = -k_v \left[(\mathbf{u}_\beta - \mathbf{u}_\alpha) \cdot \mathbf{n}_{\alpha\beta} \right] \mathbf{n}_{\alpha\beta} \qquad \mathbf{F}_\beta^{diss} = -\mathbf{F}_\alpha^{diss} \qquad \text{(C.1)}$$

with k_v being the viscous damping constant. Given that $\mathbf{u}_\beta = \mathbf{u}^\infty(\mathbf{x}_\beta) - \boldsymbol{\Delta}\mathbf{u}_\beta$ and $\mathbf{u}_\alpha = \mathbf{u}^\infty(\mathbf{x}_\alpha) - \boldsymbol{\Delta}\mathbf{u}_\alpha$, Eq. (C.1) can be rewritten as

$$\mathbf{F}_\beta^{diss} = k_v \left[(\boldsymbol{\Delta}\mathbf{u}_\beta - \boldsymbol{\Delta}\mathbf{u}_\alpha) \cdot \mathbf{n}_{\alpha\beta} \right] \mathbf{n}_{\alpha\beta} - k_v \left[(\mathbf{u}^\infty(\mathbf{x}_\beta) - \mathbf{u}^\infty(\mathbf{x}_\alpha)) \cdot \mathbf{n}_{\alpha\beta} \right] \mathbf{n}_{\alpha\beta} \qquad \text{(C.2)}$$
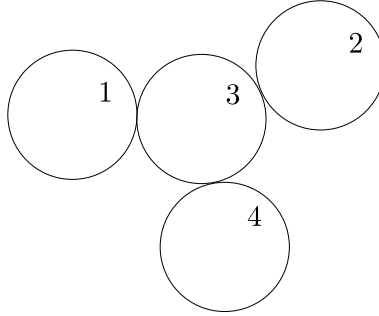

Figure C.1: Sample system composed by 4 primary particles used to illustrate the procedure for the computation of the viscous damping force

153

And in matrix formulation as

$$
\begin{Bmatrix}
F_{\beta,x}^{diss} \\
F_{\beta,y}^{diss} \\
F_{\beta,z}^{diss} \\
F_{\alpha,x}^{diss} \\
F_{\alpha,y}^{diss} \\
F_{\alpha,z}^{diss}
\end{Bmatrix}
= k_v
\begin{bmatrix}
n_x^2 & n_x n_y & n_x n_z & -n_z^2 & -n_x n_y & -n_x n_z \\
n_y n_x & n_y^2 & n_y n_z & -n_y n_x & -n_y^2 & -n_y n_z \\
n_z n_x & n_z n_y & n_z^2 & -n_z n_x & -n_z n_y & -n_z^2 \\
-n_x^2 & -n_x n_y & -n_x n_z & n_x^2 & n_x n_y & n_x n_z \\
-n_y n_x & -n_y^2 & -n_y n_z & n_y n_x & n_y^2 & n_y n_z \\
-n_z n_x & -n_z n_y & -n_z^2 & n_z n_x & n_z n_y & n_z^2
\end{bmatrix}
\begin{Bmatrix}
\Delta u_{\beta,x} \\
\Delta u_{\beta,y} \\
\Delta u_{\beta,z} \\
\Delta u_{\alpha,x} \\
\Delta u_{\alpha,y} \\
\Delta u_{\alpha,z}
\end{Bmatrix} -
$$

$$
-k_v
\begin{bmatrix}
n_x^2 & n_x n_y & n_x n_z \\
n_y n_x & n_y^2 & n_y n_z \\
n_z n_x & n_z n_y & n_z^2 \\
-n_x^2 & -n_x n_y & -n_x n_z \\
-n_y n_x & -n_y^2 & -n_y n_z \\
-n_z n_x & -n_z n_y & -n_z^2
\end{bmatrix}
\begin{Bmatrix}
u_{\beta,x}^\infty - u_{\alpha,x}^\infty \\
u_{\beta,y}^\infty - u_{\alpha,y}^\infty \\
u_{\beta,z}^\infty - u_{\alpha,z}^\infty
\end{Bmatrix}
\tag{C.3}
$$

and in a more compact notation as:

$$
\begin{Bmatrix}
\mathbf{F}_\beta^{diss} \\
\mathbf{F}_\alpha^{diss}
\end{Bmatrix}
= \delta_{\alpha\beta}
\begin{bmatrix}
k_{\alpha\beta} & -k_{\alpha\beta} \\
-k_{\alpha\beta} & k_{\alpha\beta}
\end{bmatrix}
\begin{Bmatrix}
\mathbf{\Delta u}_\beta \\
\mathbf{\Delta u}_\alpha
\end{Bmatrix}
+ \delta_{\alpha\beta}
\begin{Bmatrix}
\mathbf{J}_{\alpha\beta} \\
-\mathbf{J}_{\alpha\beta}
\end{Bmatrix}
\tag{C.4}
$$

where $\delta_{\alpha\beta}$ is equal to 1 for contacting particles and equal to 0 otherwise. This approach can be easily extended to the case of more than two contacting particles; for instance for the system of $n_p = 4$ particles depicted in Fig. C.1 we can write:

$$
\begin{Bmatrix}
\mathbf{F}_1^{diss} \\
\mathbf{F}_2^{diss} \\
\mathbf{F}_3^{diss} \\
\mathbf{F}_4^{diss}
\end{Bmatrix}
=
\begin{bmatrix}
+[k_{1,3}] & O & -[k_{1,3}] & O \\
O & +[k_{2,3}] & -[k_{2,3}] & O \\
-[k_{1,3}] & -[k_{2,3}] & +[k_{1,3}]+[k_{2,3}]+[k_{3,4}] & -[k_{3,4}] \\
O & O & -[k_{3,4}] & +[k_{3,4}]
\end{bmatrix}
\begin{Bmatrix}
\mathbf{\Delta u}_1 \\
\mathbf{\Delta u}_2 \\
\mathbf{\Delta u}_3 \\
\mathbf{\Delta u}_4
\end{Bmatrix}
\tag{C.5}
$$

$$
+
\begin{Bmatrix}
-\{J_{1,3}\} \\
-\{J_{2,3}\} \\
+\{J_{1,3}\}+\{J_{2,3}\}-\{J_{3,4}\} \\
-\{J_{3,4}\}
\end{Bmatrix}
$$

Or in a more compact notation:

$$
\mathbf{F}^{diss} = \mathcal{K} \cdot \mathbf{\Delta u} + \mathbf{J}.
\tag{C.6}
$$

Appendix D

Evaluation of the interval of quiescence

Indicating by $P(\tau)$ the probability that the interval of quiescence is larger than an arbitrary time interval τ, it is possible to state that IQ is greater than $\tau + d\tau$ if it is simultaneously greater than τ and none of the possible encounter events occurred in the time interval $[\tau; \tau + d\tau]$. In mathematical terms this reads as:

$$P(\tau + d\tau) = P(\tau)\left[1 - f_{tot}^e(t + \tau)\,d\tau\right] \tag{D.1}$$

Rearranging the terms in Eq. D.1, dividing by $d\tau$ and letting $d\tau \to 0$, the following differential equation is obtained:

$$\frac{dP(\tau)}{d\tau} = -P(\tau)\,f_{tot}^e(t + \tau) \tag{D.2}$$

whose solution, imposing the obvious initial condition $P(0) = 1$, is given by:

$$P(\tau) = \exp\left[-\int_0^\tau f_{tot}^e(t + \tau)\,d\tau'\right] = \exp\left[-f_{tot}^e\tau\right] \tag{D.3}$$

where the last identity follows from the fact that during the IQ no event occurs and the frequency f_{tot}^e can be assumed to be constant. Equation (D.3) represents the probability that IQ is larger than τ. Therefore, the cumulative probability function of the complementary event ($IQ < \tau$) is straightforwardly given by

$$F(\tau) = 1 - \exp\left(-f_{tot}^e\tau\right) \tag{D.4}$$